

ISBN: 978-90-393-6652-3

The studies described in this thesis were performed at the division of Cell Biology at the Faculty of Science of Utrecht University in Utrecht, The Netherlands.

This research is supported by the Dutch Technology Foundation STW, which is part of the Netherlands Organisation for Scientific Research (NWO) and partly funded by the Ministry of Economic Affairs (project number 11421) and by Nikon Instruments.

Cover: Maurice Boere
Layout: Bas Cloin

Printed by Gildeprint

Copyright © B.M.C. Cloin
All rights reserved.

Cellular cartography: mapping the neuronal microtubule network using super-resolution microscopy

Cellulaire cartografie:

het neuronale microtubulinetwerk in kaart gebracht met super-resolutiemicroscopie
(met een samenvatting in het Nederlands)

Proefschrift

ter verkrijging van de graad van doctor aan de Universiteit Utrecht op
gezag van de rector magnificus, prof.dr. G.J. van der Zwaan, ingevolge het
besluit van het college voor promoties in het openbaar te verdedigen op
woensdag 9 november 2016 des middags te 2.30 uur

door

Bastiaan Martinus Cornelis Cloin

geboren op 21 december 1982 te Eindhoven

Promotor: prof.dr. C.C. Hoogenraad

Copromotor: dr. L.C. Kapitein

Science is easy
- no scientist ever

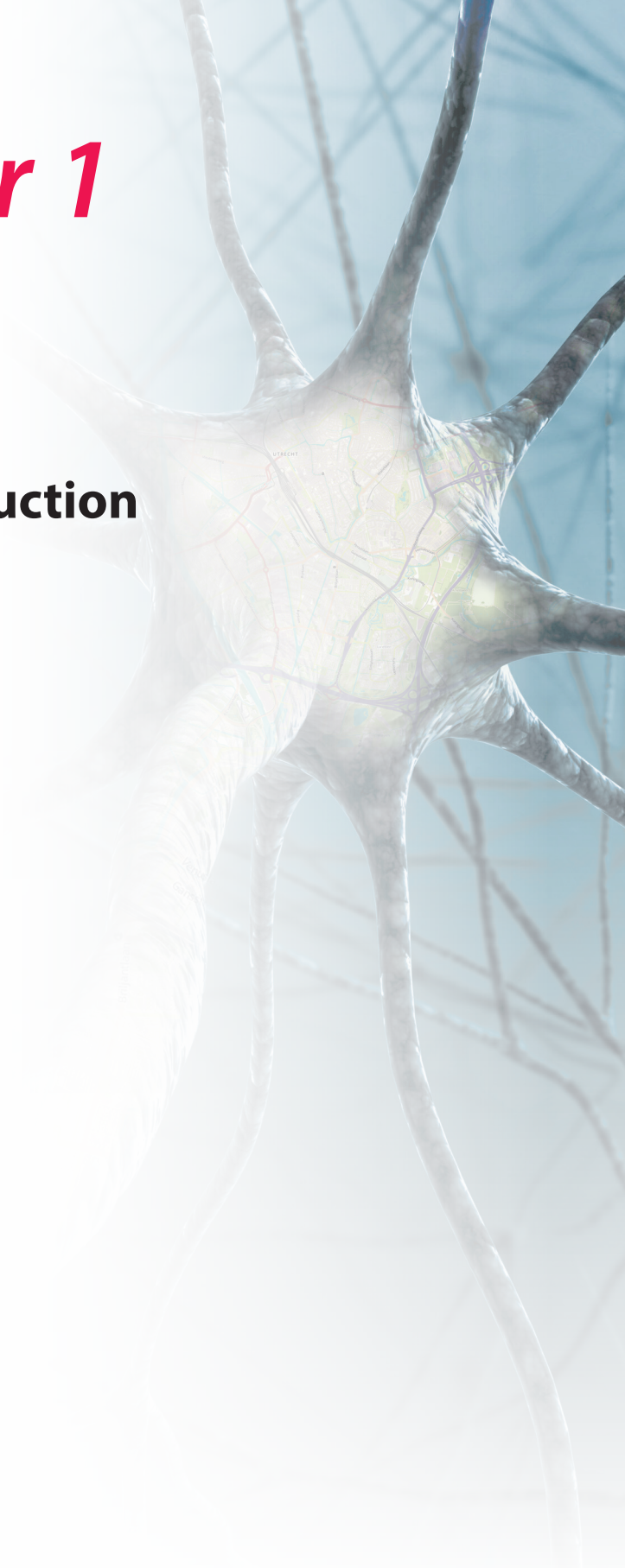
CONTENTS

Chapter 1	General introduction	9
Chapter 2	Single Molecule Localization Microscopy to study neuronal microtubule organization	25
Chapter 3	Efficient mCherry-based localization microscopy using a novel caging mechanism	47
Chapter 4	Resolving bundled microtubules using anti-tubulin nanobodies	69
Chapter 5	Microtubule minus-end binding protein CAMSAP2 controls axon specification and dendrite development	95
Chapter 6	Comparing depth-dependent astigmatism-based single-molecule localization using a deformable mirror and a cylindrical lens	141
Chapter 7	Motor-based nanoscopy reveals polarized microtubule bundles in neuronal dendrites	159
Chapter 8	General discussion	177
Addendum	Lay summary	194
	Lekensamenvatting	197
	Curriculum vitae	200
	List of publications	201
	Dankwoord	202



Chapter 1

General introduction



NEURONS

Approximately one hundred billion interconnected neurons, together with glia cells, compose the brain of an adult human. In these neurons, stimuli from in- and outside the body are translated into electrochemical signals. These signals are relayed from neuron to neuron and thereby spread over the brain to form meaningful patterns of activation that underlie our actions, thoughts, and memories.

To fulfill their function, neurons develop a highly specialized morphology. From the cell body, where most protein synthesis takes place, branched dendrites and a single axon emerge. With its dendrites, a neuron collects signals from other neurons, which are propagated to the soma and integrated at the axon initial segment. When the integrated signal crosses a certain threshold an action potential is generated, sending out a signal in an all or nothing fashion.

The electrochemical transmittance of signals between neurons takes place at contact points called synapses. A synapse is composed of a pre- and a post-synapse, located on axons and dendrites, respectively. Neurotransmitters are released at the pre-synapse by calcium-triggered exocytosis, and activate receptors on the post-synaptic side. Activated receptors allow the selective influx of ions resulting in an electric input signal for the post-synaptic neuron.

The pre- and post-synapse contain specific protein complexes, components of which are mostly translated in the soma and actively transported to their destination. Selective transport of cargo towards axons and dendrites is therefore essential for neuronal functioning, and transport defects can result in severe diseases. Impaired axonal transport, for instance, is implicated as a key player in neurodegenerative diseases, such as amyotrophic lateral sclerosis (ALS) and Alzheimer's disease [1].

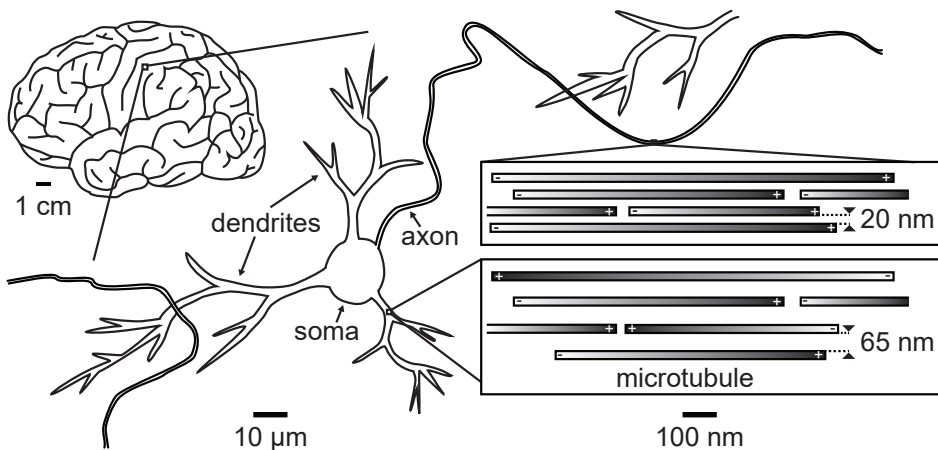


Figure 1: From brain to microtubule.

Schematic of a human brain with a zoom of one of the neurons showing the basic neuronal morphology. Insets show a zoom of the basic MT organization in the axon and dendrite, orientations and spacing are indicated.

Although the necessity of selective cargo transport is evident, the exact sorting mechanisms remain unclear. Long range intracellular transport mainly takes place over microtubules (MTs), and it is thought that the organization of these MTs and their properties influence the cargoes transported over them. Indeed, in neurons the microtubule organization is polarized in multiple ways and there is growing evidence for involvement of this polarized organization in selective transport.

MICROTUBULE NETWORK

The MT network is part of the cytoskeleton, which further consists of actin fibers and intermediate filaments. The cytoskeleton provides structural support and has a role in many cellular processes, such as cell migration, chromosome segregation during mitosis, and the formation of functional protrusions such as cilia, flagella, and microvilli. Due to their overall polarity, actin filaments and microtubules additionally are a substrate for unidirectional movement of molecular motors. Microtubules are the longest fibers of the cytoskeleton and are in general more ordered than actin fibers, making them most suited for transport far into the long neuronal protrusions.

Microtubules

Microtubules are hollow tube-like structures with an outer diameter of 25 nm and lengths in the order of microns. About 10 years after their discovery in the 1950's, it was found that MTs consist of around 13 protofilaments [2], and another 10 years later that these protofilaments are built up from 110kDa $\alpha\beta$ -tubulin heterodimers [3]. The head-to-tail arrangement of these heterodimers leads to an overall MT polarity with only α -tubulin exposed at one end, the minus-end, and only β -tubulin on the other, the plus-end. The α - and β -tubulin subunits are often heavily post-translationally modified.

Microtubules form spontaneously at high tubulin concentrations, but microtubule nucleation in cells usually starts with a minus-end template, the γ -tubulin ring complex (γ -TuRC), with γ -tubulin as the key player. The γ -TuRC is believed to cap the MT minus-end after nucleation preventing fast (de-)polymerization. The MT plus-end, on the other hand, is in a state of dynamic instability, continuously switching between periods of fast growth and shrinkage.

In most cell types the organization of MTs is governed by a MT organizing center (MTOC), often the centrosome. High concentrations of γ -tubulin in the centrosome provide fast MT nucleation and minus-end stabilization, resulting in a radial array of plus-end-out MTs. A radial MT organization is well suited for active transport between the perinuclear region, where most protein synthesis and sorting takes places, and the outer perimeter of the cell.

MTs are abundantly decorated with MT associated proteins (MAPs). Some MAPs bind specifically to the MT minus-end and can mediate anchoring of MTs to for instance the centrosome. The subset of MTs not connected to the centrosome also relies on minus-end binding proteins for stabilization, such as the CAMSAP-family [4]. The growing plus-end of MTs is tracked by plus-tip interacting proteins (+TIPs) that can influence the growth and

shrinkage characteristics of MTs and mediate anchoring of the MT plus-end to for instance actin or the cell cortex [5]. Other MAPs can bind everywhere on the MT lattice and have many roles, such as bundling parallel or antiparallel MTs, influencing kinase activity [6], and stabilizing MTs. The C-terminal tail of tubulin subunits is a hotspot for both binding of MAPs and PTMs, implying that MAPs can influence the distribution of PTMs and *vice versa* [7].

Microtubule based motor proteins

Motor proteins are a special class of microtubule binding proteins. Driven by energy derived from ATP-hydrolysis, these proteins can move processively over MTs towards either the minus-end, in the case of dynein, or the plus-end, in the case of most kinesin family members. Most processive dynein and kinesin motor proteins have two motor domains that alternate between MT-bound and unbound states. While one of the motor domains is bound to the MT, the other performs a directionally biased diffusional search for the next available binding site [8,9]. In this way, these motor proteins can take hundreds of steps before unbinding from the MT completely. Kinesins take steps of 8 nanometer [10], which is the spacing between two subsequent tubulin dimers, whereas dynein can take steps of 8, 16, 24 and 32 nanometers and adjust its step size to increasing load [11]. Next to two motor-containing polypeptides, motor proteins often have additional subunits that function in, for instance, the regulation of motor activity or cargo binding.

Motor proteins can actively transport all kinds of cargo, such as organelles, mRNA granules, and other piggy-backing motor proteins, towards their intracellular destination, sometimes hundreds of microns away. Different motors associate with different cargoes, which is believed to contribute to selective transport because these different motors might preferentially bind to, or avoid MTs with certain modifications or associated proteins. In addition to driving transport, several kinesin family members function as regulators of MT dynamics and as MT polymerizing and depolymerizing enhancers [12].

NEURONAL MICROTUBULE NETWORK

Neurons have a very distinct microtubule organization, reflecting their highly polarized morphology. In young neurons, as in many cell types, MT nucleation is governed by the centrosome resulting in a radial array of plus-end out MTs. When neurons grow older, however, the centrosome loses its role as MTOC [13] and MT organization is completely overhauled. In mature neurons, the MT organization differs between axons and dendrites, and this is implicated to play a role in directing cargo to the correct destination.

Selective transport in neurons was probed using a chemical heterodimerization system to couple normally stationary peroxisomes to specific motor proteins. In this way it was for instance shown that constitutively active forms of kinesin-family members KIF5 and KIF17 specifically target the axon, while dynein specifically targets dendrites [14]. It is hypothesized that MT associated proteins and post-translational modifications, as well as MT orientations underlie this selective targeting.

MAPs and PTMs

Without a functioning MTOC, MT nucleation in mature neurons happens in a γ -tubulin dependent manner throughout the cell. Minus-ends of these non-centrosomal MTs have to be stabilized to prevent fast depolymerization. It has been shown that in *Drosophila* S2 cells minus-end binding protein Patronin stabilizes MT minus-ends [15], and that mammalian homologs of Patronin, the CAMSAP family, protect minus-ends *in vitro* and in dividing celltypes [4]. It is not known, however, whether these proteins play a role in stabilizing MT minus-ends in neurons.

MAPs could influence selective transport in multiple ways. It is thought, for instance, that MT bundling by MAPs influences transport of organelles and vesicles by imposing steric constraints on MT spacing [16]. Most MTs in neurons occur in bundles with a characteristic and compartment specific MT spacing. MAP2 is exclusively found in dendrites and is responsible, together with MAP1B, for the 65 nm dendritic MT spacing, while tau, present in both axons and dendrites but highly enriched in the axon initial segment, bundles parallel axonal MTs with 20 nm spacing [17]. MAPs could also influence active transport by acting as roadblocks [18]. An increase in the expression of tau, for example, severely hinders kinesin-mediated axonal transport [19]. MAPs can also increase active transport by providing higher affinity binding sites for motor proteins, thereby increasing landing rates or run lengths. It was shown, for instance, that the MAP doublecortin-like kinase 1 promotes KIF1 mediated vesicle transport into dendrites [20].

Differences in PTMs between axons and dendrites also influence active transport. Two PTMs enriched in axons are detyrosination, the removal of the last C-terminal tyrosine residue from α -tubulin, and acetylation, the addition of an acetyl-group to lysine 40 of α -tubulin [17]. Tubulin acetylation and detyrosination both coincide with stable microtubules, although they do not completely colocalize [17]. It has been suggested that kinesin-1 has a preference for MTs marked by these modifications [21], but *in vitro* reconstitutions only showed very mild effects of detyrosination on kinesin-1 landing rate and no effects of acetylation [22]. Recently a strongly increased interaction of dynein with tyrosinated MTs compared to detyrosinated MTs was shown, resulting in increased dynein mediated transport over tyrosinated MTs [23].

Together these results suggest that MAPs and PTMs influence and regulate selective transport, although the exact mechanisms and cues remain elusive. Addressing these questions is severely hindered by the crowdedness of the MT network and the small inter-MT spacings in axons and dendrites.

Microtubule orientations

Since motor proteins move specifically towards either the plus- or the minus-end of MTs, the distribution of MT orientations is important for regulating active transport. MT orientations in neurons have been studied using a hook-decoration assay in combination with electron microscopy (EM) [24]. For axons it was shown that MTs are uniformly oriented with their plus-ends away from the soma. In dendrites, however, it was suggested that MTs are non-

uniformly oriented, with only half of their plus-ends pointing outward in the proximal part, and an increasing fraction of plus-end out MTs towards the distal part. However, due to extensive sample processing and the intrinsic small field of view of EM, this is based on only a few neurites.

These findings were reproduced for larger numbers using second harmonic generation microscopy (SHGM). An SHGM signal arises from uniformly oriented structures only, and was observed in axons but not in dendrites, both in brain slices and in primary cultured neurons [25]. Another indication for the differences in MT orientation comes from imaging MT plus-end binding proteins (EBs) that track the growing plus-ends of MTs. In dendrites comets move both retro- and anterogradely, while in axons only anterograde comets are observed [26]. Although comets only track growing MT plus-ends, this method can be extended to include normally stable MTs by cutting them and observing the direction of the EB-comets coming from the freshly created plus-ends. This method confirmed earlier results of mixed MT orientations in dendrites and uniform orientations in axons, but additionally indicated that dendrites have equal amounts of plus-end and minus-end out MTs all throughout the dendrite, and that minus-end out MTs are preferentially stabilized [27]. However, this method does not assess all microtubules, since cutting typically increased the number of comets by 5-10, much less than the number of MTs in a dendrite cross section [27].

Although the overall polarity of MTs in the different neuronal compartments is well established, it is not known whether there is local order in MT orientations. Grouping of same polarity MTs could have important implications for active transport. Transported cargos are generally in the order of hundreds of nanometers, allowing coupled motor proteins to interact with multiple nearby MTs, especially in the tight neuronal bundles. Local order would thereby promote unidirectional motility, but whether such order exists is currently unknown.

MICROSCOPY

By virtue of its sub-nanometer resolution, electron microscopy is well suited to study the dense neuronal MT network. In EM, a beam of electrons is scanned over the sample, and transmitted or backscattered electrons are collected as a measure for the electron density in the sample. Electron-dense structures, such as MTs, can be visualized directly; other structures can be stained with heavy metals to increase contrast. To overcome the very low specificity of classic heavy-metal stainings, immuno-gold labeling of proteins has been employed. However, the harsh fixation protocols and resin-embedding of EM samples results in severely hindered antibody penetration and low epitope availability. In addition, due to the extensive sample preparation, inherent small field of view, and use of thin slices, it is laborious to image large numbers of neurons, and most of our knowledge about the neuronal microtubule network is based on EM images of only a few neurons.

Currently, the most used method to study intracellular protein distributions and dynamics is fluorescence microscopy (FM). A fluorescent molecule can be brought to the excited singlet state by illumination with a wavelength within its absorbance spectrum. After typically a few nanoseconds the molecule returns to its ground state while emitting a photon

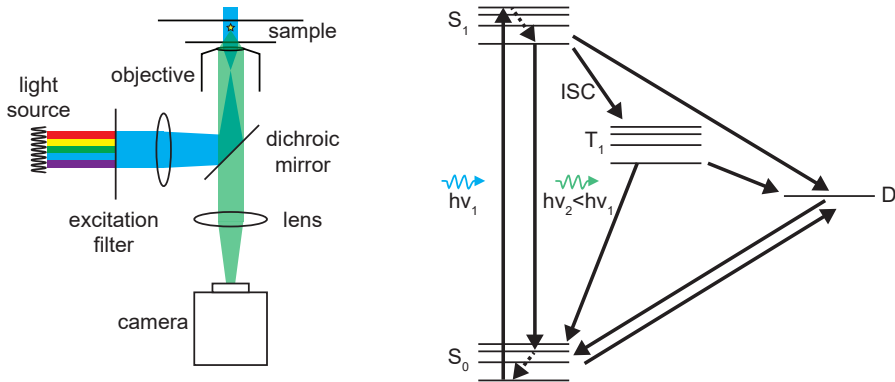


Figure 2: Schematic of fluorescence microscope and Jablonski-diagram.

Basic components of a fluorescence microscope (left panel) and Jablonski-diagram showing possible state transitions for a fluorescent molecule upon excitation (right panel). S_0 and S_1 are the singlet ground and first excited state, respectively, T_1 is the first excited triplet state, and D indicates a generic dark state. ISC stands for intersystem crossing. Squiggly arrows indicate photons, h is Planck's constant, and ν is the frequency.

that is 10-100 nm red-shifted with respect to the excitation light. The emitted photons are separated from the excitation light with wavelength-specific mirrors and filters, and collected using a digital camera. Proteins of interest (POIs) can be labeled with fluorescent molecules with extremely high specificity and sometimes with defined stoichiometry.

Although fluorescence microscopy greatly advanced the study of intracellular organization and dynamics, the attainable resolution is fundamentally limited by diffraction to approximately half the wavelength of the used light, i.e. in the order of hundreds of nanometers. To study the dense neuronal microtubule network in detail a higher resolution is needed. The search for higher resolution and high specificity resulted in multiple FM techniques that circumvent the diffraction limit, together coined super-resolution microscopy methods. These techniques use intricate illumination schemes and/or the reversible switching of fluorescent molecules to a non-fluorescent state to circumvent the diffraction limit. The technique with the highest spatial resolution is single molecule localization microscopy (SMLM).

Single molecule localization microscopy

The position of individually imaged fluorescent molecules can be determined with high precision in contrast to molecules imaged in ensembles, and this is exploited by SMLM. A fluorescent molecule, or fluorophore, is small enough to be approximated by a point source, an infinitely small light emitter. The image of a point source formed by a microscope is called the point spread function (PSF) and has a characteristic width d that depends on the wavelength of the light (λ) and the numerical aperture (NA) of the system:

$$d = \frac{1.22\lambda}{2NA}$$

The midpoint of the PSF corresponds to the position of the fluorophore, and can be found with nanometer accuracy by fitting the intensity distribution with a theoretical or experimentally determined model. The accuracy of this localization is mostly determined by the amount of photons collected and is theoretically unlimited.

A green light emitting point source, imaged with an NA of 1.4, results in a PSF with a width of approximately 220 nm. In a dense fluorescently labeled sample, hundreds of fluorophores can be present within this distance, resulting in overlapping PSFs. To achieve single molecule imaging in these densely labeled samples, most fluorophores are reversibly switched to a non-fluorescent state, or dark-state. Stochastically switching a small subset of molecules from the dark-state back to the fluorescent state allows single molecule localization. The fluorescent subset is subsequently either returned to the reversible dark-state or irreversibly photobleached, and the next subset of molecules is stochastically switched to the fluorescent state. This continues until a sufficient amount of fluorophores is localized to reconstruct a super-resolved image. This image is created by drawing the accurately determined positions of all fluorophores on a new image canvas, which will result in an image with an approximately ten-fold increase in resolution.

Labeling methods

Fluorescent tagging of proteins is usually done via immunolabeling with organic dyes or by fusing them to fluorescent proteins. The possibility of switching between dark and fluorescent states to achieve single molecule localization microscopy was shown almost simultaneously for both options [28,29].

Immunolabeling with organic dyes is usually done via a primary antibody that binds specifically to the POI, and a secondary antibody, covalently coupled to the dye, that binds to the primary antibody. Secondary antibodies are often polyclonal and can bind on multiple positions on the primary antibody. Additionally a secondary antibody is usually coupled to multiple dyes, resulting in a strongly amplified fluorescent signal from each POI. A drawback of this approach, however, is the relatively large distance between the POI and the dye of 20-30 nm. For conventional FM this distance between dye and POI is of little importance since it is well within the diffraction-limited resolution. In SMLM reconstructions, however, secondary labeled structures appear significantly larger than can be expected based on the true size of these structures and the localization precision. This makes it for example impossible to resolve individual MTs in the tight neuronal bundles. The distance between dye and POI can be reduced using dye-coupled primary antibodies, or by using nanobodies, the variable part of llama-derived heavy chain only antibody, which have a size in the order of 4 nm. It is not known, however, whether the tightly bundled neuronal MTs can be resolved with SMLM using these smaller probes.

A different approach to fluorescent labeling is the use of fluorescent proteins (FPs). After FPs are folded, a chromophore comprised of three amino acids is formed by a sequence of autocatalytic chemical reactions taking place in the middle of a stabilizing β -sheet barrel.

An FP is coupled to a POI by adding its genetic code before, after, or within its open reading frame. This can be done by directly editing the cell's genome, or by transient transfection using plasmids encoding both the POI and the FP. FPs are often directly coupled to the POI resulting in a small distance between POI and fluorophore. Since the first use of a (green) FP as a fluorescent label in cells in 1994 [30], FPs have undergone massive improvements in photostability, quantum yield, and folding speed, and also a whole spectral range of FPs is developed allowing for multicolor imaging. Importantly, many FPs have been developed that can switch between dark and fluorescent states (photoactivatable FPs) and/or change their spectral properties (photoconvertible FPs) upon irradiation with light of certain wavelengths, facilitating their use for SMLM.

Photophysics

Fluorescence in both organic dyes and FPs arises from electronic excitation of a conjugated system of electrons with overlapping pi-orbitals. On relaxation from the excited singlet state to the ground state a photon is emitted with a wavelength corresponding to the energy difference between these states. The spectral properties are mostly determined by the spatial extend of the conjugated system, the further it extends the more red-shifted are the emission and absorption spectra. A fluorophore is in a dark state when the conjugated pi-system is disrupted, which results in altered, or completely lacking, excitation and emission spectra. For example, a shortened conjugated pi-system can be formed with a correspondingly blue-shifted excitation and emission.

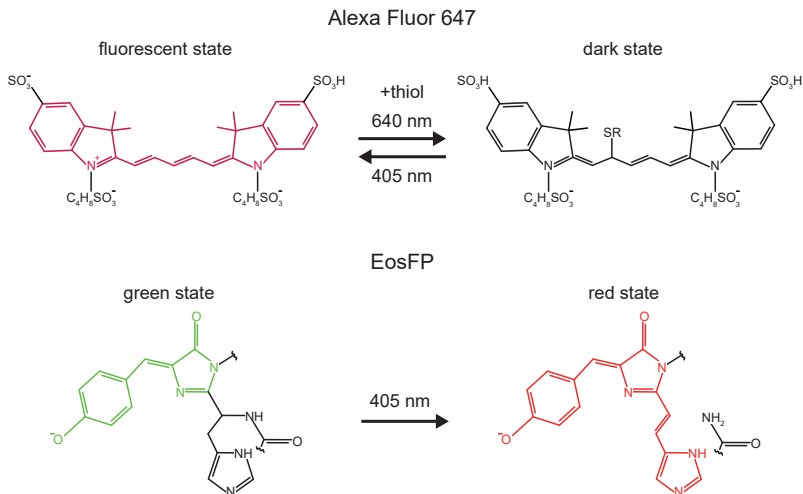


Figure 3: Fluorescent labels in different states.

AF647 shown in the fluorescent state and the reversible light-induced dark-state in the presence of a thiol (top). The thiol binds covalently to the methylene bridge of AF647 disrupting the conjugated pi-system. Green and red fluorescent state of EosFP (bottom). Illumination with 405 nm light induces a break between the chromophore and the backbone, irreversibly elongating the conjugated pi-system and thereby red-shifting the emission and excitation spectra.

1

For SMLM on densely labeled structures, fluorophores have to reside in a dark state 1.000 – 100.000 times longer than in the fluorescent state. Moreover, the contrast between the dark and fluorescent state should be large, and the amount of photons emitted while in the fluorescent state should be high to enable high localization precision. Based on these criteria, the most suitable organic dyes for SMLM are Alexa Fluor® 647 (AF647) and related far-red emitting dyes such as cyanine dye 5 (Cy5). These dyes can be reversibly switched to a light-induced dark state by high power laser illumination in the presence of reducing thiols, with a very low amount of irreversible photobleaching. The thiols are suggested to bind covalently to the polymethine bridge of the dyes, disrupting the conjugated pi-system responsible for the far-red fluorescence [31]. Interestingly, also a purely chemically induced dark-state can be efficiently populated in these dyes by incubation with tris(2-carboxyethyl)phosphine (TCEP), which also results in a covalent addition of the chemical to the dye's polymethine bridge [32]. The fluorophores switch back from dark to fluorescent spontaneously, but the return can be sped up considerably by illumination with near-UV light. Other dyes can be switched efficiently to and from a dark state in the presence of a combination of low concentrations of oxidizing and reducing agents, where the dark state corresponds to the reduced or oxidized state of the molecule [33].

In contrast to organic dyes, photoactivatable (PA) and photoconvertible (PC) FPs transition between states without the need for special buffer composition. In these FPs either the chromophore itself or residues close to the chromophore change upon illumination with certain wavelengths, resulting in a change in excitation and emission spectra.

In PAGFP, for instance, a non-fluorescent, neutral form of the chromophore is stabilized by the Glu222 residue. Upon illumination with near-UV light the chromophore transitions to an anionic fluorescent state, and at the same time Glu222 loses a carboxyl-group, resulting in stabilization of this anionic form [34]. In contrast, the reversible dark-to-green transition in Dronpa upon near-UV illumination is caused by a cis-trans isomerization of the chromophores tyrosine. Although the chromophore can in principle be fluorescent in both isoforms, the trans-form is less stabilized by hydrogen bonding with residues in the backbone, resulting in a non-fluorescent chromophore [35]. The dark-to-red conversion seen in, among others, PAMCherry, relies on the creation of an extra double bond in the chromophore that extends the conjugated pi-system from a near-UV absorbing precursor to the mature form of the red chromophore [36]. mEos-family members, the most used PC FPs, are derived from EosFP which transitions from green fluorescent to red fluorescent upon illumination with near-UV light. The near-UV illumination causes a break between the chromophore and the backbone, resulting in the extension of the conjugated system to the chromophores imidazole ring [37].

In spite of advances in specially engineered switching FPs, their brightness is usually lower than that of optimized non-switching FPs and switching rates rarely exceed 60% [38]. Interestingly, a recent study demonstrated a light-induced dark-state in the commonly used bright red FP mCherry when using a thiol-containing buffer [39]. Although this opens up the possibility to use conventional FPs for SMLM, the percentage of molecules returning to the fluorescent state was only 55%.

SMLM in the third dimension

A standard PSF enables accurate localization of molecules in the x- and y-direction. However, the shape of this PSF does not change significantly over hundreds of nanometers in the z-direction, making it difficult to obtain information about the z-position of a fluorophore. Moreover, the standard PSF is symmetric with respect to the focal plane making it impossible to determine whether a molecule is positioned above or below it. Z-information can however be encoded in a PSF by deliberately inducing aberrations to change its shape. For 3D SMLM, this is often done by introducing a cylindrical lens in the emission path, separating the x and y focal plane. This results in a PSF that is increasingly elongated for a fluorophore further away from the middle between the two focal planes, with opposite direction of the long axis above and below it. Fitting this astigmatic PSF with a 2D-Gaussian model directly reveals the x- and y-position of the molecule, whereas the z-position can be determined from the difference between width and length of the PSF with an accuracy of 50 – 100 nm over a range of approximately a micron.

When moving away from the coverslip deeper into the sample, 3D SMLM remains difficult, however, due to unwanted aberrations induced by the sample and the optical setup that distort the PSF. This decreases x-y-localization accuracy, but the effect on z-localization is more pronounced due to the stronger dependence on PSF shape. Unwanted aberrations can be removed using adaptive optical elements that can additionally be used to provide the astigmatic z-encoding. It is not clear, however, how these adaptive elements compare to conventional ways of inducing astigmatism, neither on the coverslip or deeper in samples.

SCOPE OF THIS THESIS

In this thesis, novel super-resolution technology is developed and used to better study (neuronal) MT networks.

Firstly, in Chapter 2 an optimized fixation and immunostaining protocol is described for SMLM of neuronal MTs.

In Chapter 3, a new mechanism for highly controlled photoactivation of the common red FP mCherry is described and used to obtain high quality SMLM images. Chapter 4 introduces novel nanobodies against tubulin, and it is shown that, using these nanobodies, individual MTs in tight neuronal bundles can now be resolved.

In Chapter 5 the optimized immunostaining protocol of Chapter 2, in conjunction with nanobodies against GFP, is used for dual color SMLM to show that the minus-end binding protein CAMSAP2 is an important player in the organization of the neuronal MT network. SMLM reconstructions demonstrate that CAMSAP2 is indeed found on the ends of neuronal MTs, and, based on imaging of over 90 neurons, that the centrosome loses its function as main MT organizing center during development.

A challenge for SMLM is imaging deeper into tissue, for instance in brain slices. Focusing deeper into these samples introduces optical aberrations that deteriorate the PSF. In Chapter 6 it is shown that using adaptive optics enhances SMLM in 2D and enables 3D localization with high precision deep in water-based samples.

In Chapter 7 a novel method to simultaneously determine MT orientations and obtain super-resolved MT images is introduced. Surprisingly, a local orientational order is found in dendritic MT arrays.

The thesis concludes with a general discussion in Chapter 8, which places the results of the earlier chapters in a broader perspective.

REFERENCES

- 1 Millicamps, S. & Julien, J.-P. Axonal transport deficits and neurodegenerative diseases. *Nat Rev Neurosci* 14, 161-176 (2013).
- 2 Ledbetter, M. C. & Porter, K. R. Morphology of Microtubules of Plant Cell. *Science* 144, 872-874 (1964).
- 3 Bryan, J. & Wilson, L. Are Cytoplasmic Microtubules Heteropolymers? *Proceedings of the National Academy of Sciences of the United States of America* 68, 1762-1766 (1971).
- 4 Jiang, K. et al. Microtubule Minus-End Stabilization by Polymerization-Driven CAMSAP Deposition. *Developmental Cell* 28, 295-309 (2014).
- 5 Akhmanova, A. & Steinmetz, M. O. Microtubule +TIPs at a glance. *Journal of Cell Science* 123, 3415-3419 (2010).
- 6 Mandelkow, E. & Mandelkow, E.-M. Microtubules and microtubule-associated proteins. *Current Opinion in Cell Biology* 7, 72-81 (1995).
- 7 Chakraborti, S., Natarajan, K., Curiel, J., Janke, C. & Liu, J. The emerging role of the tubulin code: From the tubulin molecule to neuronal function and disease. *Cytoskeleton*, (2016).
- 8 Carter, N. J. & Cross, R. A. Mechanics of the kinesin step. *Nature* 435, 308-312 (2005).
- 9 Roberts, A. J., Kon, T., Knight, P. J., Sutoh, K. & Burgess, S. A. Functions and mechanics of dynein motor proteins. *Nature reviews. Molecular cell biology* 14, 713-726 (2013).
- 10 Svoboda, K., Schmidt, C. F., Schnapp, B. J. & Block, S. M. Direct observation of kinesin stepping by optical trapping interferometry. *Nature* 365, 721-727 (1993).
- 11 Mallik, R., Carter, B. C., Lex, S. A., King, S. J. & Gross, S. P. Cytoplasmic dynein functions as a gear in response to load. *Nature* 427, 649-652 (2004).
- 12 Vicente, J. J. & Wordeman, L. Mitosis, microtubule dynamics and the evolution of kinesins. *Experimental Cell Research* 334, 61-69 (2015).
- 13 Nguyen, M. M., Stone, M. C. & Rolls, M. M. Microtubules are organized independently of the centrosome in *Drosophila* neurons. *Neural Development* 6, 38-38 (2011).
- 14 Kapitein, L. C. et al. Mixed Microtubules Steer Dynein-Driven Cargo Transport into Dendrites. *Current Biology* 20, 290-299 (2010).
- 15 Goodwin, S. S. & Vale, R. D. Patronin Regulates the Microtubule Network By Protecting Microtubule Minus Ends. *Cell* 143, 263-274 (2010).
- 16 Shahpasand, K., Ahmadian, S. & Riazi, G. H. A possible mechanism for controlling processive transport by microtubule-associated proteins. *Neuroscience Research* 61, 347-350 (2008).
- 17 Kapitein, L. C. & Hoogenraad, C. C. Which way to go? Cytoskeletal organization and polarized transport in neurons. *Molecular and Cellular Neuroscience* 46, 9-20 (2011).
- 18 Sato-Harada, R., Okabe, S., Umeyama, T., Kanai, Y. & Hirokawa, N. Microtubule-associated Proteins Regulate Microtubule Function as the Track for Intracellular Membrane Organelle Transports. *Cell Structure and Function* 21, 283-295 (1996).

- 19 Baas, P. W. & Qiang, L. Neuronal microtubules: when the MAP is the roadblock. *Trends in cell biology* 15, 183-187 (2005).
- 20 Lipka, J., Kapitein, L. C., Jaworski, J. R. & Hoogenraad, C. C. Microtubule-binding protein doublecortin-like kinase 1 (DCLK1) guides kinesin-3-mediated cargo transport to dendrites. *The EMBO Journal* 35, 302-318 (2016).
- 21 Cai, D., McEwen, D. P., Martens, J. R., Meyhofer, E. & Verhey, K. J. Single Molecule Imaging Reveals Differences in Microtubule Track Selection Between Kinesin Motors. *PLoS Biology* 7, e1000216 (2009).
- 22 Kaul, N., Soppina, V. & Verhey, K. J. Effects of alpha-Tubulin K40 Acetylation and Detyrosination on Kinesin-1 Motility in a Purified System. *Biophysical journal* 106, 2636-2643 (2014).
- 23 McKenney, R. J., Huynh, W., Vale, R. D. & Sirajuddin, M. Tyrosination of α -tubulin controls the initiation of processive dynein-dynactin motility. *The EMBO Journal* (2016).
- 24 Baas, P. W., Deitch, J. S., Black, M. M. & Banker, G. A. Polarity orientation of microtubules in hippocampal neurons: uniformity in the axon and nonuniformity in the dendrite. *Proceedings of the National Academy of Sciences* 85, 8335-8339 (1988).
- 25 Dombeck, D. A. et al. Uniform polarity microtubule assemblies imaged in native brain tissue by second-harmonic generation microscopy. *Proceedings of the National Academy of Sciences of the United States of America* 100, 7081-7086 (2003).
- 26 Stepanova, T. et al. Visualization of Microtubule Growth in Cultured Neurons via the Use of EB3-GFP (End-Binding Protein 3-Green Fluorescent Protein). *The Journal of Neuroscience* 23, 2655-2664 (2003).
- 27 Yau, K. W. et al. Dendrites In Vitro and In Vivo Contain Microtubules of Opposite Polarity and Axon Formation Correlates with Uniform Plus-End-Out Microtubule Orientation. *The Journal of Neuroscience* 36, 1071-1085 (2016).
- 28 Rust, M. J., Bates, M. & Zhuang, X. Sub-diffraction-limit imaging by stochastic optical reconstruction microscopy (STORM). *Nat Meth* 3, 793-796 (2006).
- 29 Betzig, E. et al. Imaging Intracellular Fluorescent Proteins at Nanometer Resolution. *Science* 313, 1642-1645 (2006).
- 30 Chalfie, M., Tu, Y., Euskirchen, G., Ward, W. & Prasher, D. Green fluorescent protein as a marker for gene expression. *Science* 263, 802-805 (1994).
- 31 Dempsey, G. T. et al. Photoswitching Mechanism of Cyanine Dyes. *Journal of the American Chemical Society* 131, 18192-18193 (2009).
- 32 Vaughan, J. C., Dempsey, G. T., Sun, E. & Zhuang, X. Phosphine quenching of cyanine dyes as a versatile tool for fluorescence microscopy. *J Am Chem Soc* 135, 1197-1200 (2013).
- 33 Vogelsang, J., Cordes, T., Forthmann, C., Steinhauer, C. & Tinnefeld, P. Controlling the fluorescence of ordinary oxazine dyes for single-molecule switching and superresolution microscopy. *Proceedings of the National Academy of Sciences* 106, 8107-8112 (2009).

- 34 Shcherbakova, D. M. & Verkhusha, V. V. Chromophore chemistry of fluorescent proteins controlled by light. *Current opinion in chemical biology* 20C, 60-68 (2014).
- 35 Heilemann, M., Dedecker, P., Hofkens, J. & Sauer, M. Photoswitches: Key molecules for subdiffraction-resolution fluorescence imaging and molecular quantification. *Laser & Photonics Reviews* 3, 180-202 (2009).
- 36 Subach, F. V. et al. Photoactivation mechanism of PAmCherry based on crystal structures of the protein in the dark and fluorescent states. *Proceedings of the National Academy of Sciences* 106, 21097-21102 (2009).
- 37 Nienhaus, K., Nienhaus, G. U., Wiedenmann, J. & Nar, H. Structural basis for photo-induced protein cleavage and green-to-red conversion of fluorescent protein EosFP. *Proceedings of the National Academy of Sciences of the United States of America* 102, 9156-9159 (2005).
- 38 Durisic, N., Laparra-Cuervo, L., Sandoval-Alvarez, A., Borbely, J. S. & Lakadamyali, M. Single-molecule evaluation of fluorescent protein photoactivation efficiency using an in vivo nanotemplate. *Nat Meth* 11, 156-162 (2014).
- 39 Winterflood, C. M. & Ewers, H. Single-Molecule Localization Microscopy using mCherry. *Chemphyschem* 15, 3447-3451 (2014).

Chapter 2

Single Molecule Localization Microscopy to study neuronal microtubule organization

Bas M. C. Cloin¹, Casper C. Hoogenraad¹, Marina Mikhaylova¹,
Lukas C. Kapitein¹

Immunocytochemistry and Related Techniques (2015); 101 Neuromethods; 389 - 408

ABSTRACT

The highly complex and polarized morphology of neurons is established by the cytoskeleton, a network of protein polymers, such as F-actin and microtubules, and associated proteins that provide shape and strength. In addition to providing structural support, microtubules serve as tracks for long-range active transport driven by dynein and kinesin motor proteins. To better understand how microtubule organization underlies the establishment and maintenance of neuronal architecture, better mapping of the neuronal microtubule network and its associated proteins is essential.

Different fluorescence microscopy techniques are commonly used to explore the organization of the microtubule cytoskeleton. The resolution of these techniques is, however, limited by diffraction to approximately 250 nanometers, which makes it not suitable for nanoscale mapping of microtubule properties. Super-resolution microscopy techniques that rely on single molecule localization (Single Molecule Localization Microscopy; SMLM) combine high protein specificity, multi-color imaging, and a resolution in the order of 5-50 nanometers, making it an ideal tool to study the neuronal cytoskeleton and its properties.

In this chapter, we will discuss the theory behind SMLM, labeling strategies for the fluorescent probes, describe a workflow and a detailed protocol for fixation and immunostaining of neuronal microtubules, and provide some tips for successful super-resolution imaging, data analysis and image reconstruction.

INTRODUCTION

Neurons are highly specialized cells that form long processes to establish connections in the nervous system. Neuronal processes are classified based on their morphology, function, and protein composition as either dendrite or axon. Pyramidal neurons have multiple highly branched dendrites that conduct electrical stimulations received from other neurons to the cell body, and a single axon that sends signals away from the cell body. The axons of neurons in the cortex and hippocampus usually reach lengths of hundreds of microns. To establish and maintain such complex and elongated architecture, neurons employ cytoskeletal motor proteins to drive active transport of cellular building blocks to specific destinations. These motor proteins can move directionally along either of two types of cytoskeletal biopolymers: actin filaments and microtubules (MTs). Actin facilitates motility of motor proteins of the myosin superfamily, whereas MTs serve as tracks for two families of motor proteins, kinesin and dynein, which move in opposite directions along the microtubule. In neurons, long range transport is predominantly microtubule-based.

Microtubules are hollow tubes with a diameter of 25 nanometer and consist of 13 protofilaments which form through head-to-tail polymerization of α - and β -tubulin heterodimers, resulting in long biopolymers with a well-defined polarity. Microtubule functions are tightly regulated by several factors: the intrinsic GTPase activity of tubulins; association with microtubule-interacting proteins (including microtubule associated proteins (MAPs), microtubule severing proteins, microtubule plus-end tracking proteins; and posttranslational modifications of tubulin such as acetylation, tyrosination, detyrosination, and polyglutamylation [1-3]. In mature neurons, axonal microtubules have a uniform orientation with the fast growing plus end directed away from the cell body, while microtubules in proximal dendrites have mixed polarity [4].

To determine whether motor proteins distinguish between axons or dendrites, we recently developed a well-controlled intracellular transport assay [5,6]. This assay employs a chemical heterodimerization system in which the addition of the cell-permeable small molecule rapalog induces the binding of two protein domains, FRB and FKBP. With FRB fused to motor proteins and FKBP targeted to immobile organelles, rapalog addition can acutely recruit specific motor proteins to immobile cargo (i.e. peroxisomes), which from then on report the activity of the motor. These experiments revealed that the minus-end directed motor protein dynein can drive selective transport into dendrites, whereas multiple kinesin motors selectively enter axons. The molecular basis for this striking selectivity is poorly understood, but the specific differences in microtubule organization between axons and dendrites appear to impose selectivity. Interestingly, the selectivity of kinesin 1 for driving axonal transport can be altered by treating neurons with low doses of paclitaxel, a microtubule stabilizing drug. After paclitaxel treatment, kinesin 1-driven peroxisomes also target dendrites [5].

For understanding the structural basis of polarized neuronal transport it is necessary to study the subcellular differences in the organization of the microtubule network, such as the orientation and density of the microtubules, and their posttranslational modifications

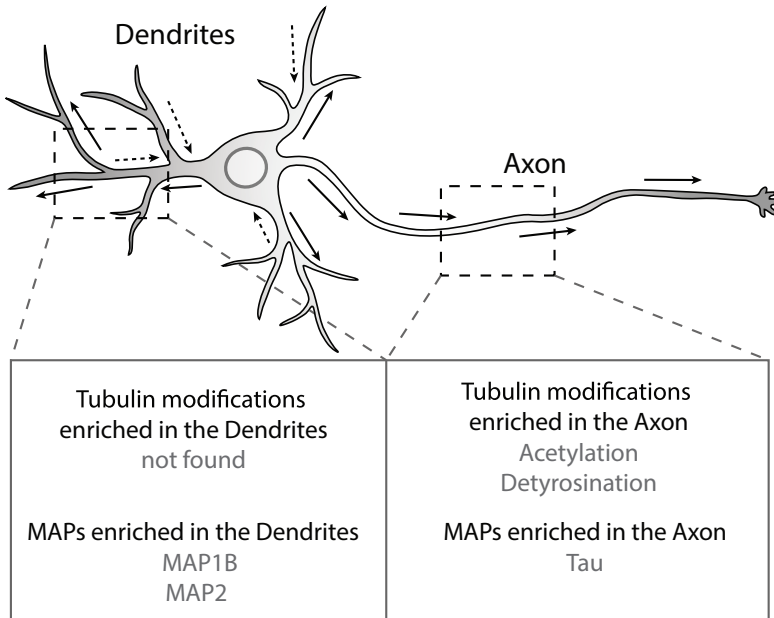


Figure 1: Schematic representation of a neuron showing neurite morphology.

Arrows indicate orientations of microtubules, plus-end outward in the axon, and microtubules with mixed polarization in dendrites. Cytoskeletal properties specific for axon or dendrite are depicted in the box below.

(PTMs) and associated proteins (MAPs), that could affect the stability of the network and provide selectivity for transport driven by specific motor proteins (Figure 1) [4].

Immunocytochemical staining of individual proteins visualized by fluorescence microscopy is often used to examine the cytoskeleton and its properties. Advantages include very high protein specificity, possibility to label several different proteins or structures at the same time by using multiple colors, and the relatively simple protocols for fixation and staining of samples. Spatial resolution obtained by conventional fluorescence microscopy is, however, limited by the diffraction of light. Light emitted by a fluorophore (or more general, a point-source) is diffracted at the interfaces they encounter from source to image plane. At the image plane, this causes the light to spread into a pattern with finite size instead of converging back to one point. The pattern or image created by a microscope of a point-source is called the Point Spread Function (PSF).

The PSF is usually shaped like an Airy pattern which consists of a bright spot, the Airy disk, surrounded by alternating dark and bright concentric rings. When two fluorescent molecules are separated by less than half the width of the Airy disk, the individual molecules

cannot be distinguished (Figure 2A). The theoretical resolution, defined as half the width of the Airy disk, is determined by the wavelength of the light (λ) and the numerical aperture (NA) of the system according to the formula [7]:

$$d = \frac{1.22\lambda}{2NA}$$

Because in this case the resolution limiting factor is the diffraction of light, this is called the diffraction-limit. For instance, for green light with a wavelength of 500nm and an NA of 1.4 the theoretical resolution is around 220 nanometers.

Considering that neuronal microtubules are mostly arranged in dense bundles with spacings that are often much smaller than the diffraction limit [4], conventional fluorescence microscopy is often not suitable to determine properties on the scale of individual microtubules. An alternative to fluorescence microscopy for examining the cytoskeleton and its properties is electron microscopy (EM). In EM, a beam of electrons is used to visualize structures. Electrons, just as photons, can be described by a wave with a certain wavelength. The wavelength of electrons is much smaller than that of photons which leads to a subnanometer theoretical resolution. EM can be used to visualize individual microtubules, even in the dense neuronal bundles [8]. However, EM lacks the high protein specificity needed for simultaneous immunolabeling of PTMs and MAPs associated with (parts of) particular microtubules.

During the last decade, different fluorescence microscopy techniques have emerged that allow diffraction-unlimited imaging [9-12]. In particular, Single Molecule Localization Microscopy (SMLM) offers a high resolution of 5-50 nanometers, combined with the high protein specificity associated with multi-color fluorescence microscopy, and is therefore very well suited to study the properties of the dense neuronal cytoskeleton. In contrast to EM, SMLM requires no embedding or sectioning of the sample. Also, SMLM can be done on a relatively standard fluorescence microscope equipped with laser illumination and a sensitive (EM-CCD) camera.

SMLM microscopy is a collective term for a number of techniques, among others PALM (Photoactivated Localization Microscopy) [13], STORM (Stochastic Optical Reconstruction Microscopy) [9], dSTORM (direct STORM) [14] and Ground-State Depletion and Single-Molecule return (GSDIM) [12], that all use active control over fluorophore activity to sequentially sample many different subsets of clearly resolved individual fluorophores. Each fluorophore then shows up as a single spot in an acquired image. The midpoint of this spot corresponds to the position of the fluorophore and can be determined by fitting with a theoretical or experimentally determined approximation of the PSF. A super-resolved image can then be created by plotting the positions of all localized fluorophores in a new image, thereby effectively eliminating the blurring caused by diffraction, as well as the blurring caused by out of focus light. The resolution of this reconstructed image is therefore no longer diffraction-limited, but only limited by the error in the localization of the fluorophores, and by the labeling density.

The error (σ) in the localization of a fluorophore arises from photon shot noise, pixilation noise due to the finite size of camera pixels, and noise from background fluorescence [15,16]. In the case of bright fluorophores and a sensitive camera the localization error is dominated by shot noise and depends on the number of photons according to:

$$\sigma \sim \frac{1}{\sqrt{N}}$$

This implies that by collecting enough photons the localization error can be made arbitrarily small.

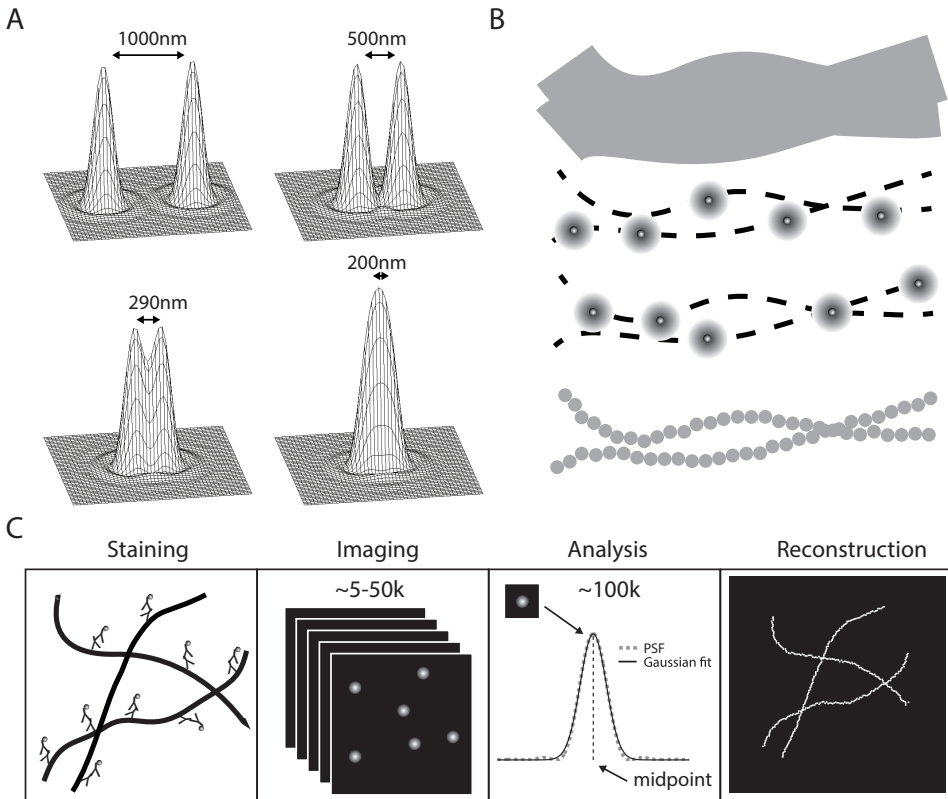


Figure 2: Principle of SMLM.

A) PSFs of AF647 molecules at different spacing. When the spacing becomes smaller, the PSFs of the two fluorophores cannot be discriminated.

B) Upper panel: schematic of two closely spaced fluorescently labeled microtubules with diffraction-limited resolution (290nm). Middle panel: when most fluorophores have been brought to a dark state, the PSFs of the few molecules in the fluorescent state can be detected separately. Lower panel: super-resolved image of the microtubules created by plotting the accurately determined positions of many fluorophores, collected over several thousand frames.

C) Workflow of SMLM.

The other factor determining the resolution of a reconstructed super-resolution image is the labeling density. According to the Nyquist sampling criterion, the resolution will not exceed twice the distance between localized fluorophores (for instance in [17]). Therefore, a structure that has a low labeling density cannot be resolved with high accuracy. Protocols for staining of samples for super-resolution microscopy should be optimized to achieve a high labeling density, for instance by a lower dilution of antibodies or longer incubation steps, while at the same time background labeling should be minimal. Another factor to keep in mind is that if the structure of interest is not well preserved on the nanometer scale, for instance due to fixation artifacts, it will never be resolved at high resolution.

Because SMLM is based on the analysis of single fluorophore PSFs, only one fluorophore per diffraction-limited area should emit light to ensure that its PSF can be correctly imaged and fitted. However, in a sample where the structure of interest is densely labeled, hundreds of fluorophores reside within a diffraction limited area and when they all emit light at the same time their PSFs blur into one irresolvable spot (Figure 2A). The breakthrough needed for SMLM was a method to switch fluorophores between a non-fluorescent (dark) state and the light-emitting fluorescent state. Active control over fluorophores allows the PSF of the small subset of fluorophores in the fluorescent state to be imaged without hindrance of fluorescence from neighboring fluorophores. Through imaging of these few fluorophores, they are either irreversibly photobleached or converted back to a dark state, upon which a new random subset of dye molecules is switched to the fluorescent state. This continues until the PSFs of all (or most) fluorophores are imaged and localized.

The first two documented SMLM methods either used specially engineered fluorescent proteins that can be switched once from a non-fluorescent to the fluorescent state using photoactivation (PALM/FPALM) [13,18], or probes labeled with both a reporter-dye, that is brought to a dark state with intense laser illumination, and an activator-dye that, when excited, brings the reporter-dye back to the fluorescent state (STORM) [9]. Later, more methods have become available, such as exciting conventional organic dyes with high power laser illumination under reducing buffer conditions resulting in reversible on-off-switching (dSTORM [14]; GSDIM [19]), the reductive caging of organic dyes using NaBH_4 rendering the dyes photoactivatable with 405 nanometer light [20], and the use of fluorescent proteins that can be reversibly switched from dark to fluorescent states, or from green- to red-fluorescent states (for instance [21,22]). In the remainder of this chapter, we will focus on dSTORM. Here, the switching from the fluorescent state to long lived dark states and back, usually called 'blinking', is achieved by chemical and/or photoinduced transitions. Often used chemicals to induce a transition from the fluorescent to a long lived dark state include thiols, such as β -mercaptoethylamine (MEA) and β -mercaptoethanol (β ME).

The most important selection criteria for fluorophores used in SMLM are blinking kinetics and brightness in the fluorescent state. Suitable fluorophores reside more than a thousand times longer in a dark-state than in the fluorescent state (duty ratio < 0.001), and emit thousands of photons in the time spent in the fluorescent state to allow precise localization. Spectrally

separated suitable fluorophores are Alexa Fluor® 647, Alexa Fluor® 568, and Atto 488 (see [23] for a detailed description). It is important to remember that the blinking characteristics depend heavily on buffer conditions such as thiol-concentration and pH.

A super-resolved image is built up by plotting all fluorophore localizations in a new image with arbitrary pixel size. Many localizations are necessary to reconstruct the continuous microtubule structure (Figure 2B). Because each acquired image can only contain the PSFs of a small number of fluorophores, a large number of images is collected. Using open access (for instance QuickPalm, RapidSTORM), self-developed, or commercially available software (for instance MetaMorph, NIS Elements, etc.), the PSFs in every acquired image are found and fitted with a mathematical function matching the PSF (usually a Gaussian curve). The midpoint of the PSF, and thereby the location of the fluorophore, is determined from the fit-parameters.

As explained, the final resolution of the image obtained using SMLM is not only determined by the fluorophore properties and fitting procedures. Instead, labeling density and structure preservation are also of crucial importance for successful nanoscopy. Here we provide a detailed protocol for labeling and imaging of neuronal microtubules and demonstrate that the microtubule organization can be mapped using SMLM giving rise to new knowledge for unraveling structural bases of polarized active transport.

EQUIPMENT, MATERIALS, AND SETUP

Materials and reagents for antibody labeling

- AffiniPure Donkey Anti-Mouse IgG (H+L) (Jackson ImmunoResearch Europe)
- Monoclonal Anti- α -Tubulin, clone B-5-1-2 (Sigma)
- Alexa Fluor® 647 (AF647) Carboxylic acid succinimidyl ester 1 mg (Life Technologies)
- Dimethyl sulfoxide (DMSO), 100 ml (Sigma)
- D-PBS (Dulbecco's, Sigma-Aldrich)
- 1M NaHCO₃ (pH 8.3)
- Gel filtration columns (NAP-5 columns; GE Healthcare)

Materials and reagents for immunocytochemistry

- Light-tight plastic box
- Parafilm (Sigma-Aldrich)
- 16% PFA EM-grade (Sigma-Aldrich)
- D-PBS (Dulbecco's, Sigma-Aldrich)
- Extraction buffer: 80mM PIPES, 7mM MgCl₂, 1mM EGTA, 0.3% Triton-X (Sigma-Aldrich), 150mM NaCl, 5 mM glucose, 0.25% glutaraldehyde (Electron Microscopy Sciences), adjust to pH 6.9
- Fixative: PFA 4%, sucrose 4% in D-PBS
- Permeabilization buffer: 0.3% Triton-X in D-PBS

- Blocking buffer: 2% w/v BSA, 0.2% gelatin, 10mM glycine, 50mM NH_4Cl in D-PBS (sterile filtered)
- Post-fixation buffer: PFA 2 % in D-PBS

Materials and reagents for imaging

- Microscope slides with single cavity (Globe Scientific)
- Imaging buffer: 50mM MEA (cysteamine; Sigma-Aldrich), 5% w/v glucose, 560 μg /ml glucose oxidase (Sigma-Aldrich), 40 μg /ml catalase (Sigma-Aldrich) in D-PBS. Prepare freshly.

Setup

- Standard fluorescence microscope equipped with high NA (~ 1.4) objective for efficient photon collection. An inverted microscope is more commonly used for this type of experiments because of possibility to illuminate and image in total internal reflection fluorescence (TIRF) mode but it is possible to use upright microscope as well.
- Fluorescence filters for imaging of Alexa Fluor[®] 647: excitation 640 nm, emission (imaging) 670 nm.
- Imaging laser-emitting light with wavelength around 640 nm. Laser intensity in the focal plane should be in the order of kW/cm^2 . This can be quite easily achieved with a laser power around 50 mW.
- Activation laser emitting light with wavelength around 405 nm. This can be a low power laser; intensity in the focal plane should be in the order of W/cm^2 . Dichroic mirror for combining the two laser beams. Normally a longpass dichroic mirror is used with cutoff wavelength around 600 nm.
- EMCCD camera with high quantum efficiency (~ 90 % at 670 nm) and capable of achieving frame rates in the order of 30–50 frames per second.
- Software for SMLM reconstruction: e.g., QuickPalm, RapidSTORM, MetaMorph, NIS Elements.
- PC for controlling the setup, storing the acquired images, and running SMLM analysis and reconstruction software.

PROCEDURES

Neuronal cultures

Rat hippocampal primary neurons are prepared at embryonic day 19 and plated on 19 mm coverslips coated with poly-L-lysine and laminin at a density of 75,000 cells per 19 mm coverslip (265 cells per mm^2). A detailed procedure for preparing and culturing dissociated hippocampal neurons is described previously [6].

Antibody labeling

Key factors in super-resolution imaging include the fluorescent properties of the dye, as well as high affinity and small size of the probe. Antibodies against α -tubulin or β -tubulin are frequently used to visualize microtubules in mammalian cells. Fluorescent labeling can be achieved by using a secondary antibody labeled with a fluorophore or by immunostaining with directly conjugated primary antibody. The advantages of custom labeling of primary antibody are flexible choice of fluorescent dye (desired markers are not always commercially available), control of labeling density (physical-chemical interactions between multiple fluorophores attached to the same antibody molecule might interfere with stochastic activation) and accelerated immunostaining procedures. We optimized the protocol for conjugation of amino-reactive groups to secondary anti-mouse antibody and monoclonal anti- α -tubulin antibody (Molecular Probes, Life technologies; 10). As an alternative, the secondary anti-mouse antibody conjugated to AF647 can be also purchased from Molecular probes (Life technologies). A step by step procedure of antibody – dye conjugation is given below and additional information can be found in Note 1:

1. Prepare the aliquots of AF647 dye. Dissolve one dye pack in 500 μ l of anhydrous DMSO, make 10 aliquots and remove DMSO by lyophilisation and store tubes at -20°C . We usually perform multiple labeling procedures at the same time. Less volume aliquots can be prepared for a smaller scale experiments.
2. For conjugation, dissolve one aliquot of dye in 50 μ l of anhydrous DMSO. Keep at room temperature.
3. For labeling of secondary antibody: mix 50 μ l secondary antibody (1.25 mg/ml in PBS) with 6 μ l of 1M NaHCO_3 and 3.5 μ l AF647. For labeling of primary antibody: 30 μ l of mouse anti- α -tubulin (Sigma, clone B-5-1-2), 6 μ l of AF647, 3.5 μ l of NaHCO_3 and 20.5 μ l of D-PBS. Mix well and incubate the reaction for 1 to 1.5 hours at room temperature, wrapped in aluminium foil, on a shaking platform.
4. During the incubation time, equilibrate NAP-5 gel filtration column by passing three column volumes of D-PBS. Alternatively, Sephadex[®] G-25 or BioGel[®] P-30 columns can be used.
5. Starting from this step avoid direct light. Add 140 μ l of D-PBS to the reaction, gently mix.
6. Apply whole sample to the centre of pre-equilibrated NAP-25 column.
7. Allow the sample to enter the column and then wash with 550 μ l of D-PBS.
8. Add 300 μ l of D-PBS and collect the eluent into 1.5 mL tube. Unbound dye will remain in the column.
9. Determine the labeling efficiency (LE), which is derived by dividing the concentration of the bound AF647 by the concentration of the antibody

$$LE = \frac{c_{dye}}{c_{IgG}}$$

with c_{dye} the concentration of the dye and c_{IgG} the concentration of the antibody.

The concentrations can be calculated using Beer-Lambert's law:

$$c = \frac{OD}{\epsilon}$$

where c is the concentration, OD the optical density, and ϵ the extinction coefficient. The OD and ϵ of dyes is determined at the absorbance maximum (650 nanometer for AF647). OD is measured using a photometer, ϵ can be found in the manufacturer's datasheet ($239,000 \text{ cm}^{-1}\text{M}^{-1}$ for AF647; Molecular Probes). For IgG the OD is measured at 280 nanometer; ϵ_{IgG} at 280 nanometer is equal to $203,000 \text{ cm}^{-1}\text{M}^{-1}$ (24). To calculate IgG concentration, a correction factor has to be included in the Beer-Lambert's law to account for the absorbance of the dye at 280 nanometer:

$$c_{\text{IgG}} = \frac{OD_{\text{IgG}} - OD_{\text{dye}, 280}}{\epsilon}$$

In case of AF647, the OD at 280 nanometer is equal to 0.03 times the OD at 650 nanometer (Molecular Probes).

10. Aliquot the labeled antibody (10-20 μl) and store at -80°C .

Fixation and immunostaining of primary neurons

Strong fixation of the structure of interest is important for high image quality. Often methanol is used as a fixative in protocols for immunostaining of microtubules. Incubating cells with methanol cause dehydration of the cells and precipitation of proteins. Methanol fixation yields good results for conventional diffraction-limited microscopy. However, methanol causes denaturation of proteins, largely due to weakening of the hydrophobic interactions favoring unfolding of globular proteins. This causes artifacts in the cellular structure which affect the quality of EM [25,26] and SMLM images.

Other commonly used fixatives, such as paraformaldehyde (PFA) and glutaraldehyde (GA) serve as crosslinkers. They covalently link protein residues intra- and intermolecularly and provide better preservation of (microtubule) structure. GA is a stronger fixative than PFA but PFA penetrates better into the cells and acts faster [27]. Therefore a combination of PFA and GA is frequently used.

Tubulin is present in cells in soluble form and in polymerized form (microtubules). The soluble tubulin fraction will also be immobilized after fixation with a crosslinking reagent increasing the background staining. Removing soluble tubulin before fixation greatly reduces this background. This can be done by permeabilizing the cell membrane which enables diffusion of soluble protein out of the cell before adding the fixative, or by permeabilization and slow fixation with GA at the same time. This process is called 'extraction' and is routinely used for preparation of samples for EM [28].

Here we provide a detailed protocol for fixation and immunostaining of hippocampal primary neurons (see also Note 2). Note that neurons need to be handled gently. Exchanging

the medium and buffers in the wells should be done with great care. Always pipette slowly and via the side of the well, never directly onto the neurons. While the neurons are not fixed it is best to only add preheated buffers (37°C).

Extraction and fixation

1. Remove the medium from the neurons and *gently* add 1ml of preheated D-PBS (37°C) via the side of the well.
2. Remove the D-PBS and add 1ml extraction buffer preheated to 37°C. Incubate the neurons for 90 seconds in extraction buffer. This will permeabilize the cells and allows enough time for the soluble tubulin fraction to diffuse out of the cells. If the neurons are incubated with extraction buffer for (much) longer they can be completely washed away from the coverslip (Notes 4.4).
3. Remove the extraction buffer from the well and add 1ml of preheated fixation buffer (37°C). Incubate the neurons with the fixation buffer for ten minutes at room temperature.
4. Remove the fixation buffer and wash the neurons three times with D-PBS for five minutes to remove the leftover fixative.

Further permeabilizing and blocking

5. Exchange the D-PBS with 1ml permeabilization buffer and incubate for ten minutes. Triton X-100 is a detergent that disrupts the cell membrane. This allows antibodies to easily enter and access the antigens.
6. Remove the permeabilization buffer and wash the neurons three times with 1ml D-PBS for five minutes to completely remove the Triton X-100.
7. Exchange the D-PBS with 1ml of blocking buffer. The blocking buffer contains reagents that will hinder the antibodies to bind unspecifically to other proteins. This promotes binding of antibodies only to their epitopes.

Fluorescent Immunostaining

In fluorescent immunostaining antibodies are used to label the structure of interest with fluorophores. Usually this is done in a two-step process. The first step is to label a specific protein with a primary antibody with high affinity. The second step is adding a fluorescently labeled polyclonal secondary antibody with high affinity for the primary antibody. This procedure can also be done with a primary antibody directly conjugated to fluorophores. Here we provide a detailed procedure for fluorescent immunostaining of microtubules using a mouse antibody with high affinity for α -tubulin, followed by staining with a secondary anti-mouse antibody coupled to AF647.

To protect the fluorescently labeled secondary antibodies from light we perform the antibody incubation steps in a dark immunostaining chamber. For ease of handling put a Parafilm layer in the (plastic) box. At this stage the neurons are less fragile because they are

fixed, but still proceed with care (Note 4). The coverslips can be transferred back to the wells for washing. Use a needle or a second pair of tweezers to prevent the coverslip from sliding over the Parafilm during the pick-up.

8. Dilute mouse anti- α -tubulin antibody in blocking buffer to a final concentration of 1:400. Put a 70-100 μ l drop on the Parafilm layer. Use tweezers to put the coverslip onto the drop *with the neurons facing downwards*. The neurons can be incubated with the primary antibody for two hours at room temperature, or overnight at 4°C. For directly labeled anti- α -tubulin antibody skip steps 8. and 9.
9. Add fresh D-PBS to the wells before transferring the coverslips. Transfer coverslips back to the wells. Wash the neurons three times with D-PBS for five minutes to remove non-bound antibodies.
10. Dilute the secondary antibody to a final concentration of 1:400. Again apply a 70-100 μ l drop on the Parafilm and put the coverslip on the drop *with the neurons facing downwards*. The neurons can be incubated with the secondary antibody for two hours at room temperature, or overnight at 4°C.
11. Add fresh D-PBS to the wells before transferring the coverslips. Wash the neurons three times with D-PBS for five minutes to remove non-bound antibodies.
12. Post-fix with 2% PFA in D-PBS. Post-fixation is used to crosslink the antibodies to the structure of interest and to each other. This decreases the likelihood of dissociation over time. Leave the neurons in the post-fixation buffer for ten minutes (Note 3).
13. Wash the neurons three times with D-PBS for five minutes to remove excess PFA.

Mounting

SMLM is done under conditions that promote fluorophore transitions to and from long-lived dark states and requires the fluorophores to be in a liquid buffer during imaging. This can be achieved by mounting the coverslips either in open imaging chambers, or on top of indented microscope slides. The advantage of indented microscope slides is that the volume is smaller so less buffer is required, and that the reservoir is closed preventing evaporation of the imaging buffer and reducing the influx of oxygen. The composition of the imaging buffer depends on the used fluorophores. For AF647, by far the best fluorophore for SMLM, the imaging buffer described in the Materials section is used.

To mount the coverslip on an indented slide, add 100 μ l imaging buffer to the indentation and put the coverslip onto the indentation with the neurons facing downwards. Use a vacuum suction device to remove excess buffer. Make sure the coverslip is securely in place and that there are no air bubbles under the coverslip.

Imaging

Secure the sample on the microscope stage and select a position to image. It is good practice to limit light exposure of the sample to a minimum to prevent unwanted photobleaching. Once the sample is positioned acquire a conventional image to serve as a comparison for the super-resolved image.

For successful super-resolution imaging, make sure that imaging settings are optimal (for additional information see Note 5):

- **Set exposure time.** To achieve the highest signal-to-noise-ratio, the exposure-time should be close to the average on-time of the used fluorophores. A shorter exposure time will decrease the number of photons from the fluorophore with respect to the readout noise of the camera. A longer exposure time will increase the background noise by collecting more photons not originating from the fluorophore. Also the chance of having two fluorophores in the fluorescent state per diffraction limited area increases with longer exposure times. For AF647 the exposure time is set to 20-30 milliseconds.
- **Set laser power.** High laser powers are necessary to bring the fluorophores quickly to the dark state and to ensure the collection of many photons from the small subset of fluorophores in the fluorescent state. Powers in the order of kW/cm^2 in the sample plane are preferable.
- **Set number of images.** The number of images to acquire depends on the density of the structure of interest, the density of labeling, and the number of detectable PSFs per image. Usually between 5,000 and 50,000 images are acquired.
- **Bring fluorophores to dark state.** Expose the sample to the laser light to bring most fluorophores to the dark state.
- **Start image acquisition.** During acquisition, check that the PSFs in each image are sparse enough to not overlap each other. Over time the number of PSFs per image will decrease due to irreversible photobleaching. This can be compensated for by actively stimulating fluorophores in the dark state to switch to the fluorescent state using photoactivation with 405 nm light. Start out by activating with little 405 nm light, intensity in the order of W/cm^2 , and increase the intensity gradually by ramping up the power.

Analysis/reconstruction

A super-resolved SMLM image is created by plotting all the fluorophore positions in a new image (Note 6). The positions of the fluorophores are determined by fitting all PSFs in the acquired images and determining the midpoints. Fitting of the PSF and determination of the midpoint is done by dedicated software algorithms. Most SMLM software packages consist of separate parts for the detection and fitting of fluorophores and for the reconstruction of a super-resolved image. Several packages are freely available, such as QuickPALM [29], RapidSTORM [30] and μ Manager [31].

Parameters concerning the detection and fitting of the fluorophores include the size of the PSF and the pixel size in the images acquired by the camera. The size of the PSF (for instance expressed in the standard deviation of the Gaussian fit) is used for an accurate detection of fluorophores. Spots in the acquired images that are much smaller or larger than the given PSF size can be excluded based on this difference in size. The size of the PSF

can be approximated by making a number of cross sections from PSFs, fitting a Gaussian curve to them and determining the width. The actual pixel size of the acquired images is important for conversion of the location of fluorophores in pixels to nanometers, and should be calibrated using a sample with a structure of known dimensions, for instance lines with equal spacing.

The output of the fitting process is a table containing information about all localizations, such as x- and y-coordinates (in pixels and in nanometers), a measure for the brightness of the fluorophore, the number of the image it was found in, a measure for the symmetry of the PSF, etc. This information is used during the reconstruction of the super-resolved image. The x- and y-coordinates are used to determine the position in the super-resolved image. The brightness of the PSF can be used as intensity measure for the point plotted in the super-resolved image and/or the width of this point.

Reconstruction is usually done via a second part of the software. Parameters that can be varied in the reconstruction include the pixel size of the super-resolved image, and a cutoff value for localization accuracy of fluorophores included in the reconstruction. The pixel size of the super-resolved image can be chosen arbitrarily. The choice depends on the average localization error, the number of localizations per unit area, and the structure that is being imaged. Because the pixel size can be freely chosen it should not limit resolution. According to the Nyquist criterium, the pixel size should be at least twice as small as the smallest structural details. This implies that for an image with a resolution of 20 nanometer, the pixel size should be at most 10 nanometer. In case the number of localizations per unit area is low, a small pixel size entails an image with large distances between neighboring points and therefore a very non-continuous structure. The pixel size should therefore be tuned for each reconstruction. Usually a pixel size between 5 and 30 nanometers gives optimal super-resolved image quality.

A last important point is drift correction (Note 6). The high localization accuracy, together with the relatively long imaging time, makes SMLM vulnerable for drift of the sample with respect to the objective during image acquisition. Sample drift causes incorrect fluorophores localizations and should be corrected for. There are in general two ways to correct sample drift. Firstly, drift can be monitored from frame to frame with the use of fiducial markers, small particles adhered to the coverslip that can be localized with great accuracy (in the same way the fluorophores are localized). Assuming the fiducial markers are not moving with respect to the sample, every shift in the position of these fiducial markers observed in the acquired images is due to sample drift. The shift in position of a set of fiducial markers in each image can be used to correct the localizations of the fluorophores in that image.

A second, elegant method for drift correction is based on the correlation of intermediate super-resolved reconstructions [32]. For this method, the total number of acquired frames is divided in subsets with an equal number of frames, and a super-resolved image is created from the localizations of each subset. Drift is then determined by calculating the correlation

between the intermediate reconstructions of the subsequent subsets as function of a shift in pixels. The shift in pixels giving rise to the highest correlation coefficient is considered to be the drift between the two intermediate reconstructions. The drift per acquired image is then approximated by assuming that the drift in this time period is linear, and dividing the total drift over the number of frames in a subset. Correlation-based drift correction is included in most software packages and gives very good results in samples with well-defined structures, such as microtubules in neurons.

An example of successfully resolved neuronal microtubules is shown in Figure 3, where densely packed microtubules can be resolved individually.

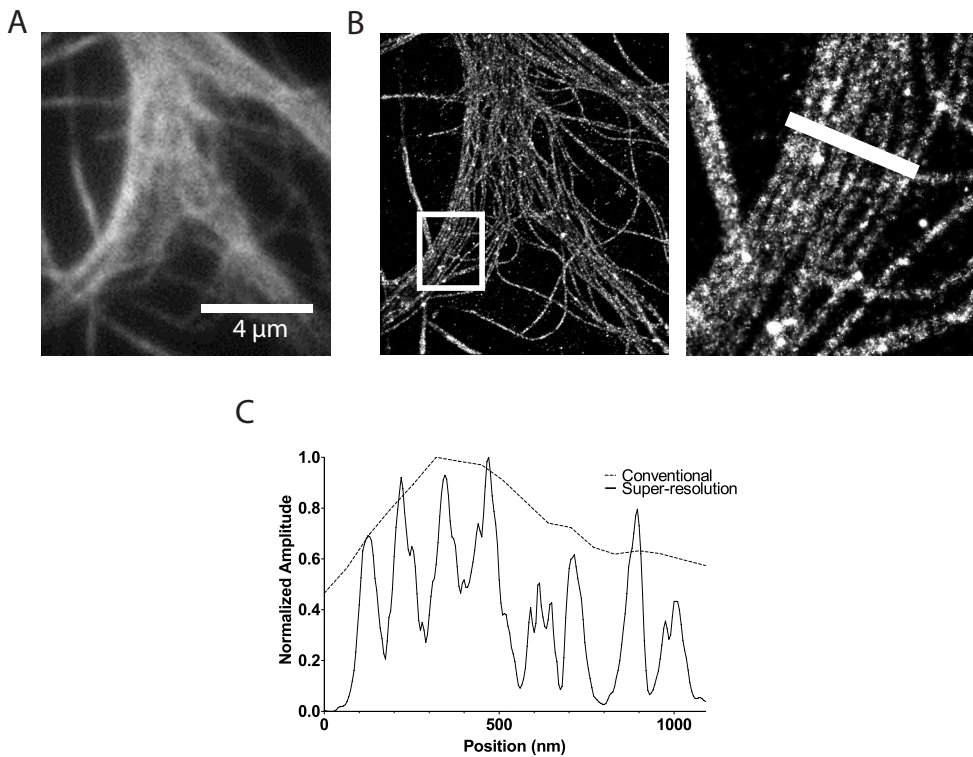


Figure 3: Representative example of the microtubule network in a proximal branch of a DIV4 hippocampal primary neuron stained with a primary antibody against α -tubulin and visualized via a secondary antibody labeled with AF647.

A) Widefield overview.

B) Super-resolved SMLM image. Enlarged view of the area in the white box shown in lower panel.

C) Intensity profile of the cross section marked by the white line in B). Dashed line corresponds to the widefield image, continuous line indicates the profile of the super-resolved image. Note that individual microtubules can only be distinguished in the reconstructed SMLM image.

Notes and troubleshooting

1. Low labeling efficiency of the antibody

- AF647 Carboxylic acid succinimidyl ester is moisture-sensitive. Always use freshly dissolved dye for the conjugation.
- Antibody or buffers that contain primary amines (e.g., Tris or glycine) are not compatible with AF647 Carboxylic acid succinimidyl ester because they react with the NHS-ester moiety and compete with the intended reaction. If this is the case, the antibody should be dialyzed into D-PBS.
- Low concentrations of sodium azide ($\leq 3\text{mM}$ or 0.02%) or glycerol (below 10%) will not significantly affect the labeling reaction. However, if the concentrations are higher, the labeling reaction mix should be diluted or antibody diluent should be replaced by D-PBS.

2. Dim microtubule staining

- Increase the concentration of primary and/or secondary antibody.
- Antibody labeling efficiency can be too low. Label antibodies with higher number of fluorophores.
- Not all microscopes are equipped with the right filter sets for imaging of AF647. Make sure the excitation and emission filters are suited for exciting and imaging at 650 and 670 nanometer, respectively.
- Note that the human eye is not sensitive to the light emitted by AF647, while most CCD cameras are. A staining that looks dim by eye can appear very bright on screen.

3. Neuronal morphology looks affected after staining procedure

- Neurons should be handled with great care, especially before fixation. Pipetting should be done via the sides of the wall and buffers added before fixation should be preheated to 37°C .
- Extraction can remove not only the soluble tubulin from the cell, but also the polymerized microtubules. Extraction should be done carefully, and extraction time should be optimized to remove soluble tubulin from the cells while not interfering with the microtubule network.
- Note that older neurons (more than DIV8) have much more bundled microtubules that can be challenging to resolve.

4. Diffusing fluorophores

- The binding of antibodies to the tubulin is reversible. Use a stronger post-fixation to slow down the unbinding of antibodies. A stronger fixation can be achieved by increasing the PFA-concentration, or by incubating longer. Also make sure the post-fixation buffer is freshly made.

- Not all antibodies will bind to their targets. The unbound fraction of antibodies in the sample can be reduced by prolonging the washing steps.

5. Fluorophores are not blinking

- Fresh MEA is important for the transition of AF647 to a long lived dark state. MEA is not very stable, even in solution, and defreezing an aliquot of 1M MEA stock shortly before imaging is preferable.
- Removing oxygen from the sample by the oxygen scavenging system decreases the chance of the fluorophores to irreversibly photobleach. If the fluorophores seem to bleach too rapidly, try with fresh oxygen scavenger system.
- Blinking characteristics of dyes are pH-dependent. The pH of the buffer can be optimized per sample for best results.
- In optimal buffer conditions most fluorophores reside in a long lived dark state at any time. In case the fraction of fluorophores in the fluorescent state is (too) low only few will be visible per acquired image. To increase the number of molecules in the fluorescent state, increase the amount of photoactivation with 405 nm light.

6. Super-resolved image is not clear

- Drift correction is important for a clear super-resolved image because of the relatively long time it takes to acquire all images. An important parameter for optimal correlation-based drift correction is the number of frames per intermediate reconstruction. Too many frames can result in noticeable non-linear drift within the intermediate reconstructions thereby compromising optimal correction of this drift. Too few frames can result in intermediate reconstructions with not enough localizations to form a structure clear enough for calculation of the correlation coefficient. A value between 500 and 3,000 frames usually gives satisfactory results.
- Fluorophore localizations with high error can blur the super-resolved image. The cut off value for localization error can be used select only fluorophores with a satisfactory localization precision.
- A super-resolved image that is too 'dotty' can be enhanced by increasing the pixel size. This will result in a larger spot for each localization and therefore a more continuous structure.

AUTHOR CONTRIBUTIONS:

B.M.C.C. and M.M. optimized protocols, wrote the manuscript and prepared figures with advice from C.C.H. and L.C.K.

REFERENCES

- 1 Hirokawa N., Takemura R. (2005) Molecular motors and mechanisms of directional transport in neurons. *Nat Rev Neurosci* 6, 201-214.
- 2 Witte H., Bradke F. (2008) The role of the cytoskeleton during neuronal polarization. *Curr Opin Neurobiol.* 18, 479-487.
- 3 Janke C., Kneussel M. (2010) Tubulin post-translational modifications: encoding functions on the neuronal microtubule cytoskeleton. *Trends Neurosci* 33, 362-372.
- 4 Kapitein L.C., Hoogenraad C.C. (2011) Which way to go? Cytoskeletal organization and polarized transport in neurons. *Mol Cell Neurosci* 46, 9-20.
- 5 Kapitein L.C., et al. (2010) Probing intracellular motor protein activity using an inducible cargo trafficking assay. *Biophys J* 99, 2143-2152.
6. Kapitein L.C., Yau K.W., Hoogenraad C.C. (2010) Microtubule dynamics in dendritic spines. *Methods Cell Biol.* 97, 111-132.
- 7 Hecht E. (2001) *Optics* (4th Edition), Addison-Wesley.
- 8 Sharp D.J., Yu W., Baas P.W. (1995) Transport of dendritic microtubules establishes their nonuniform polarity orientation. *J Cell Biol* 130, 93-103
- 9 Rust M.J., Bates M., Zhuang X. (2006) Sub-diffraction-limit imaging by stochastic optical reconstruction microscopy (STORM). *Nat Methods* 3, 793-795.
- 10 Bates M., Jones S.A., Zhuang X. (2013) Preparation of photoswitchable labeled antibodies for STORM imaging. *Cold Spring Harb Protoc* 2013, 540-541.
- 11 Klar TA, Hell SW. Subdiffraction resolution in far-field fluorescence microscopy. *Opt Lett.* 1999 Jul 15;24(14):954-6.
- 12 Fölling J., et al. (2008) Fluorescence nanoscopy by ground-state depletion and single-molecule return. *Nat Methods.* 5, 943-945.
- 13 Betzig E., et al. (2006) Imaging intracellular fluorescent proteins at nanometer resolution. *Science.* 313, 1642-1645.
- 14 Heilemann, M., et al. (2008) Subdiffraction-Resolution Fluorescence Imaging with Conventional Fluorescent Probes. *Angew Chem Int Ed* 47, 6172-6176.
- 15 Thompson R.E., Larson D.R., Webb W.W. (2002) Precise nanometer localization analysis for individual fluorescent probes. *Biophys J.* 82, 2775-2783.
- 16 Rieger B., Stallinga S. (2014) The lateral and axial localization uncertainty in super-resolution light microscopy. *Chemphyschem.* 15, 664-670.
- 17 Pawley, J. (2006) Points, pixels, and gray levels: digitizing image data. *Handbook of biological confocal microscopy*, Springer US, pp. 59-79.
- 18 Hess S.T., Girirajan T.P., Mason M.D. (2006) Ultra-high resolution imaging by fluorescence photoactivation localization microscopy. *Biophys J* 91, 4258-4272.
- 19 Testa I., et al (2010) Multicolor fluorescence nanoscopy in fixed and living cells by exciting conventional fluorophores with a single wavelength. *Biophys J* 99, 2686-2694.

- 20 Vaughan J.C., Jia S., Zhuang X (2012). Ultrabright photoactivatable fluorophores created by reductive caging. *Nat Methods* 9, 1181-4.
- 21 Stiel A.C., et al. (2008) Generation of monomeric reversibly switchable red fluorescent proteins for far-field fluorescence nanoscopy. *Biophys J* 95, 2989-97.
- 22 McKinney S.A. (2009). A bright and photostable photoconvertible fluorescent protein. *Nat Methods*. 6, 131-133.
- 23 Dempsey G.T., et al. (2011) Evaluation of fluorophores for optimal performance in localization-based super-resolution imaging. *Nat Methods* 8, 1027-1036.
- 24 Johnstone A.P, Thorpe R. (1988) *Immunochemistry in Practice*. Wiley-Blackwell.
- 25 Hoetelmans R.W. et al. (2001) Effects of acetone, methanol, or paraformaldehyde on cellular structure, visualized by reflection contrast microscopy and transmission and scanning electron microscopy. *Appl Immunohistochem Mol Morphol* 9, 346-351.
- 26 Schnell U. (2012) Immunolabeling artifacts and the need for live-cell imaging. *Nat Methods* 9, 152-158.
- 27 Kiernan J. A. (2000) Formaldehyde, formalin, paraformaldehyde and glutaraldehyde: what they are and what they do.” *Microscopy Today* 1, 8-12.
- 28 Auinger S., Small J.V. (2008) Correlated light and electron microscopy of the cytoskeleton. *Methods Cell Biol* 88, 257-72.
- 29 Henriques R., et al (2010). QuickPALM: 3D real-time photoactivation nanoscopy image processing in ImageJ. *Nat Methods* 7, 339-340.
- 30 Wolter S, et al. (2012) rapidSTORM: accurate, fast open-source software for localization microscopy. *Nat Methods* 9, 1040-1041.
- 31 Edelstein A., et al (2010), Computer Control of Microscopes Using μ Manager. *Current Protocols in Molecular Biology* 14.20.1-14.20.17.
- 32 Mlodzianoski M.J., et al. (2011) Sample drift correction in 3D fluorescence photoactivation localization microscopy. *Opt Express*. 19, 15009-15019.

¹Cell Biology, Department of Biology, Faculty of Science, Utrecht University, 3584 CH Utrecht, the Netherland. ²Department of Chemistry, KU Leuven, Celestijnenlaan 200F, Heverlee 3001, Belgium. ³NMR spectroscopy, Department of Chemistry, Faculty of Science, Utrecht University, 3584 CH Utrecht, the Netherland. ⁴Institute of Physics, Faculty of Physics, Astronomy and Informatics, Nicolaus Copernicus University, Grudziadzka 5, 87-100 Torun, Poland. [#]Present address: Center for Molecular Neurobiology Hamburg, 20251 Hamburg, Germany

Chapter 3

Efficient mCherry-based localization microscopy using a novel caging mechanism

Bas M. C. Cloin¹, Elke De Zitter², Vincent Gielen², Gert E. Folkers³,
Marina Mikhaylova^{1,#}, Bartosz Krajnik^{2,4}, Casper C. Hoogenraad¹, Luc Van
Meervelt², Peter Dedecker², Lukas C. Kapitein¹

Submitted

ABSTRACT

Single-molecule localization microscopy (SMLM) depends on the controlled switching of fluorophores between dark states and fluorescent states, facilitating repetitive sparse sampling and nanometric localization of individual fluorophores. Photoconvertible fluorescent proteins are often used as probes for SMLM, as they enable highly specific labeling and control over the active emitter density. Nevertheless, for most photo-convertible fluorescent proteins the conversion efficiency is only around 50%, leaving half of the fluorophores undetected. Here we show that mCherry can be brought to a purely chemically-induced reversible dark-state that allows highly efficient SMLM with up to 80% of fluorophores switching to the red state. Incubating with β -mercaptoethanol (β ME) quenches the fluorescence peak at 610 nm and introduces a fluorescence peak at 460 nm, which can be reversed by illumination with near UV light or by β ME washout. X-ray crystallography and NMR spectroscopy revealed that β ME can convert mCherry to a blue fluorescent protein both by reducing the chromophore and by covalently attaching to the C $_{\beta}$ of the chromophores tyrosine. Our strategy for mCherry-based SMLM using chemical caging followed by highly efficient photoactivation should be widely applicable, given the many existing model systems with stably expressing mCherry fusion proteins.

INTRODUCTION

Fluorescent proteins have greatly advanced the study of intracellular organization and dynamics. For example, the discovery of red fluorescent proteins (RFPs) has enabled multicolor imaging when combined with the original green fluorescent protein (GFP), whereas the development of photoconvertible proteins whose fluorescence emission can be either activated or altered has not only enabled studying protein dynamics and turnover, but also diffraction-unlimited imaging through single-molecule localization. Single-molecule localization microscopy (SMLM [1]) depends on the switching of fluorophores between dark states and fluorescent states, which facilitates repetitive sparse sampling and nanometric localization of individual fluorophores. In contrast to synthetic fluorophores where blinking is often induced by transient interactions between the dye and buffer components such as reducing agents, blinking in FPs is typically achieved through the use of photoactivatable variants whose emission spectrum changes upon exposure to specific wavelengths, which is largely independent of buffer conditions. For example, photoactivatable GFP (PA-GFP) switches from dark to green fluorescent upon exposure to near UV light, whereas mEos3.2 switches from green fluorescent to red fluorescent in the same conditions. Nevertheless, for most photoswitchable fluorescent proteins the switching efficiency is only around 50% [2], leaving half of the fluorophores undetected.

Interestingly, also conventional FPs, such as GFP and YFP, can be used for SMLM, because they will blink either spontaneously or in specific conditions [3,4]. Recently, also SMLM with a conventional red FP has been achieved by exploiting a light-induced dark-state of mCherry in the presence of the reducing agent β -mercaptoethylamine [5]. Unfortunately, using a light-induced dark-state provides limited control over the blinking kinetics and will lead to premature photobleaching of many molecules before the start of the single-molecule image acquisition, resulting in sub-optimal SMLM images. Here we show that mCherry can be brought to a purely chemically-induced reversible dark-state from which up to 80% of the fluorophores can be recovered to the fluorescent state, allowing for highly efficient SMLM. Incubating with β -mercaptoethanol (β ME) quenches the fluorescence peak at 610 nm and introduces a fluorescence peak at 460 nm, which can be reversed by illumination with near UV light or by β ME washout. Spectroscopic characterization of this process provided insights into the kinetics of this process, whereas X-ray crystallography and NMR spectroscopy revealed that β ME can convert mCherry to a blue fluorescent protein both by reducing the chromophore and by covalently attaching to the C _{β} of the chromophore's tyrosine. We demonstrate that chemical caging can be used for mCherry-based SMLM, which should be widely applicable, given the many existing mCherry fusion proteins.

RESULTS AND DISCUSSION

The effect of β ME on RFPs was first observed in fixed COS-7 cells expressing mCherry-tubulin. The bright red fluorescence in these cells was largely quenched after addition of 286 mM (2% v/v) β ME (Figure 1A). Illuminating the sample with near UV light from a mercury lamp recovered

$58 \pm 4\%$ of the initial red fluorescence (Figure 1B), demonstrating that mCherry-tubulin can be chemically caged by β ME and subsequently photoactivated to recover the red fluorescent state. However, the 405 nm light used for photoactivation could also damage the mCherry, suggesting that the uncaging efficiency could be improved by optimizing the UV intensity.

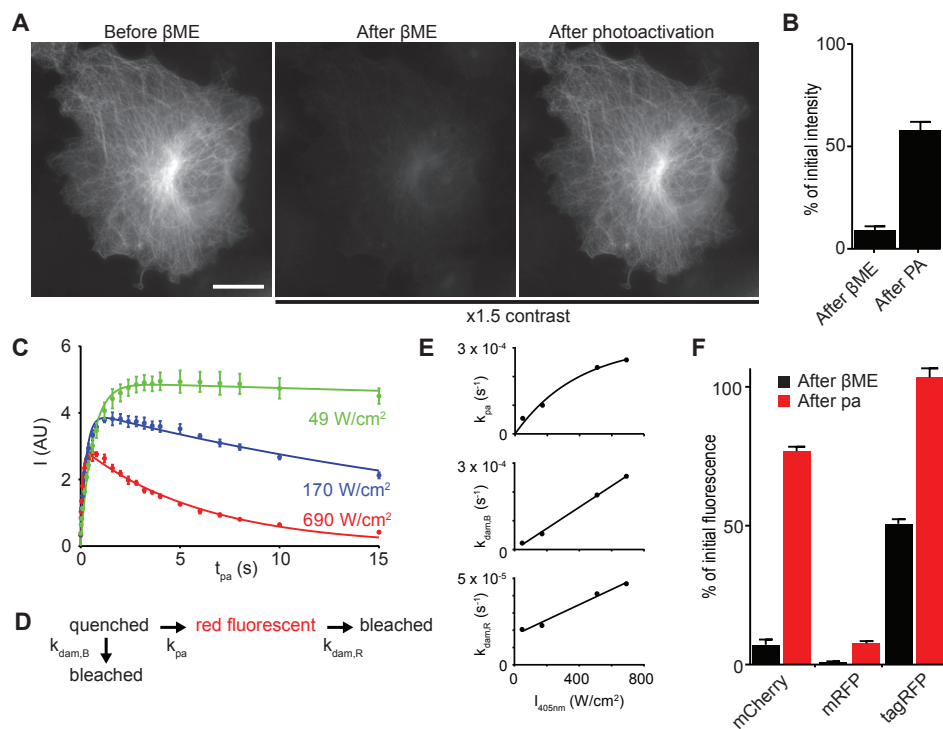


Figure 1: RFPs can be caged by β ME and uncaged by near UV light

A) Widefield images of a fixed COS-7 cell transfected with mCherry-tubulin, showing the initial fluorescence signal (left), the fluorescence signal after adding 286 mM β ME (middle), and the fluorescence signal after photoactivation with violet light (right). The image contrast in the center and right subpanel is 1.5 times that of the left subpanel. Scale bar is 20 μ m.

B) Quantification of the fluorescence signal of widefield images of COS-7 cells transfected with mCherry-tubulin after adding β ME and after photoactivation as percentage of the initial fluorescence. The fluorescence signal after photoactivation is 58% of the initial signal. $N = 2$ samples, $n = 21$ positions.

C) Fluorescence intensity of purified mCherry molecules in the presence of 286 mM β ME after photoactivation, as a function of photoactivation exposure times for three 405 nm laser intensities. Solid lines indicate fits with a model incorporating both photoactivation and photodamage. (See supplement, $n = 6$ measurements per timepoint).

D) Schematic of the model used for fitting data in C).

E) Rates of photoactivation and photodamage as function of 405 nm laser intensity, obtained from the fits described in C). Solid lines represent exponential (k_{pa}) or linear ($k_{dam,R}$ and $k_{dam,B}$) fits.

F) Quantification of the fluorescence signal of purified mCherry, mRFP and TagRFP molecules from TIRF imaging. Black and red bars indicate the percentage of initial fluorescence after adding 286 mM β ME and after photoactivation with low 405 nm laser intensity, respectively. $N = 4, 2,$ and 2 samples, $n = 40, 24,$ and 20 measurements for mCherry, mRFP, and tagRFP, respectively.

To test this, purified mCherry was non-specifically adsorbed onto glass coverslips, quenched by incubation with 286 mM β ME in PBS and subsequently activated by different exposure periods (0-15 s) at different intensities of 405 nm laser light (Figure 1C). At the lowest intensity, we observed that uncaging first increased and then saturated with increasing exposure time. At higher intensities, longer exposures resulted in less fluorescence and also the maximum achievable fluorescence intensity was lower at increasing activation intensities.

The data was fitted with a model describing a photo-induced transition from a caged to a fluorescent state and photo-damaging pathways from both the caged state and the fluorescent state, with rates k_{pa} , $k_{dam,B}$, and $k_{dam,R}$, respectively (Figure 1D). As expected, the photoactivation rate and the photodamage rates increased with increasing 405 nm laser intensity (Figure 1E). The linear fit of $k_{dam,B}$ approximately went through the origin, implying no photodamage without 405 nm light. In contrast, the fit of $k_{dam,R}$ had an offset, which can be explained by recaging of photoactivated molecules. Fitting with a model that directly incorporated recaging of photoactivated molecules resulted in ambiguous fits (data not shown). The photoactivation rate also increased with laser intensity, but to a lesser extent at higher laser powers. Together, these results explain why the amount of molecules returning to the fluorescent state is highest when low photoactivation intensities are used. Employing these activation settings, we found that mCherry, mRFP, and tagRFP were caged by β ME to $7.1 \pm 0.4\%$, $1.3 \pm 0.5\%$ and $50.5 \pm 0.2\%$ of the original intensity, respectively, whereas the return percentages using near-UV illumination were $77 \pm 2\%$, $10.4 \pm 2.8\%$, $103 \pm 3\%$ (mean \pm SEM, Figure 1F).

We next tested whether the observed photoactivation of chemically caged mCherry could be used for SMLM. Indeed, mCherry-based localization microscopy using fixed COS7 cells expressing mCherry-tubulin in a buffer containing 143 mM β ME resulted in an improved resolution with a high density of emitters contributing to the super-resolution reconstruction. mCherry molecules could either be photoactivated in the presence of β ME (Figure 2A, B), or returned spontaneously after washout of β ME during acquisition of the first thousands of frames (Figure 2C, D). To directly compare conventional RFPs with the green-to-red photoconvertible protein mEos3.2, cells were transfected with mEos3.2-tubulin and the early endosome marker mRFP-clathrin (Figure 2E-G). These easily discernible structures allow discriminating between mRFP or mEos3.2 signals, while testing them in exactly the same conditions. These experiments revealed that the localization precision of mRFP is only slightly worse than that of mEos3.2 (mode of 6.3 nm versus 7.8 nm, Figure 2F, G). Thus, β ME-based caging enables RFP-based localization microscopy.

During photoactivation of mCherry-tubulin expressing and β ME-quenched cells, we noted a faint blue fluorescence. To investigate this further, we recorded the fluorescence emission spectrum of purified mCherry in the presence of increasing β ME concentrations, and found that addition of β ME reduced the emission peak at 610 nm, while a peak at 460 nm appeared, indicating blue fluorescence (Figure 3A). The intensity decrease at 610 nm upon addition of β ME and as a function of the β ME concentration followed the expected behavior for a reversible bimolecular reaction ($I = I_0 / (1 + K_{eq} [\beta ME])$), yielding a K_{eq} of 0.10 mM^{-1} (Figure 3B).

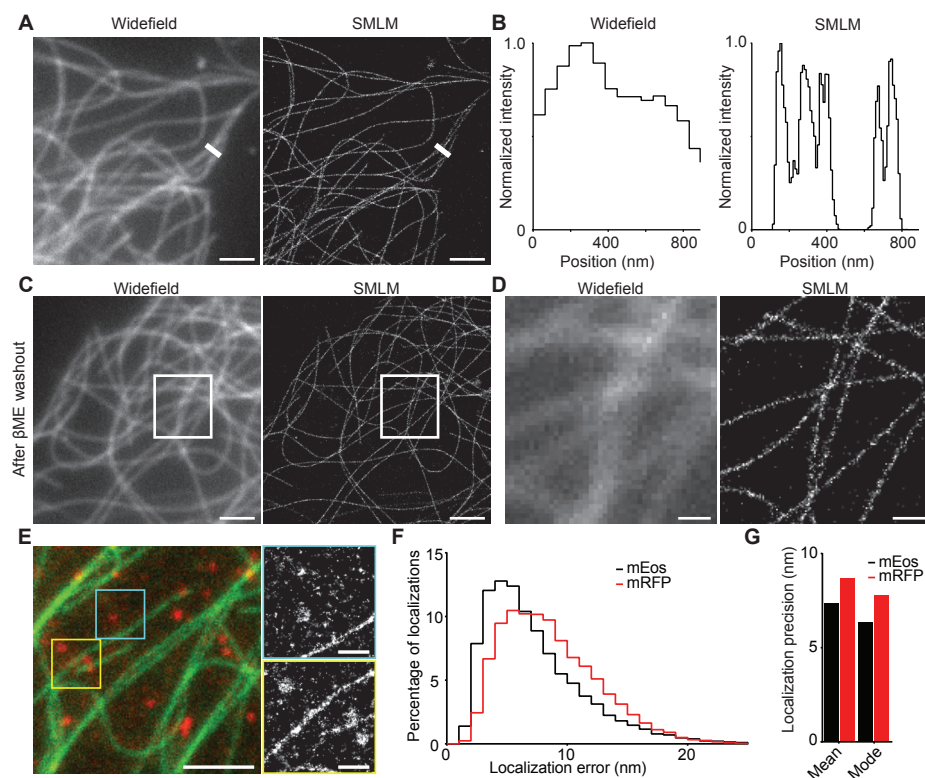


Figure 2: Gradual uncaging enables super-resolution imaging

- A) Widefield image of a COS-7 cell transfected with mCherry-tubulin (left panel) and SMLM reconstruction of the same area (right panel). SMLM was performed after addition of 143 mM β ME. Scalebars are 2 μ m.
- B) Normalized intensity profiles along the white lines in A).
- C) Widefield image of a COS-7 cell transfected with mCherry-tubulin (left panel) and SMLM reconstruction of the same area. SMLM was performed after addition and washout of 286 mM β ME, with no 405 nm activation during the first ~3000 frames (right panel). Scalebars are 2 μ m.
- D) Zooms of the boxed regions in C). Scalebars are 500 nm.
- E) Widefield image of a COS-7 cell transfected with mRFP-clathrin and mEos3.2-tubulin (left panel) and SMLM reconstruction of the boxed regions (right panels). Scale bars are 3 and 1 μ m, respectively.
- F) Histogram of localization errors of mEos3.2 (black line) and mRFP (red line), based on regions in the SMLM reconstruction where a clear distinction could be made between localizations of mRFP-clathrin and mEos3.2-tubulin.
- G) Mean and mode of the localization error distribution shown in F). $N = 4$ SMLM reconstructions, $n = 23878$ and 13064 localizations for mEos3.2 and mRFP, respectively.

In addition to the emission spectrum, the absorbance spectrum of mCherry was also strongly altered upon addition of 286 mM β ME. The absorbance peak at 590 nm decreased over time and a peak at 410 nm appears (Figure 4C, D), which could be reversed by photoactivation with a 405 nm laser. These results indicate that β ME converts mCherry molecules from a red fluorescent state to a blue fluorescent photoconvertible state with absorption maximum at 410 nm and fluorescence emission maximum at 460 nm.

To characterize the spontaneous return of mCherry to the red fluorescent state without photoactivation, coverslips with non-specifically adsorbed mCherry molecules were incubated with 286 mM β ME in PBS for 20 minutes and then washed extensively with PBS to remove the β ME. Upon β ME washout, the red fluorescence of mCherry returned over the course of an hour, with an average recovery of $83\% \pm 3\%$ of the initial intensity and a single-exponential time constant of $7.0 \cdot 10^2$ s (Figure 3E-G).

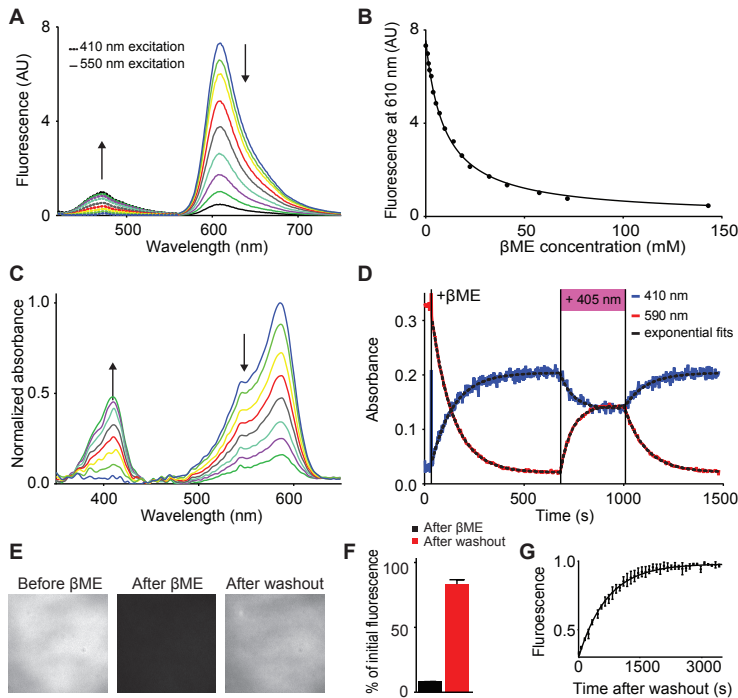


Figure 3: β ME transforms mCherry into a blue fluorescent protein

- A)** Fluorescence spectra of *in-vitro* mCherry-molecules incubated with various β ME concentrations, excited with 405nm light (dotted lines) and 561nm light (solid lines). Arrows indicate increasing β ME concentration.
- B)** Quantification of mCherry fluorescence intensity at 610 nm as function of β ME concentration. Solid line represents a fit of the fluorescence intensity according to an equation for a reversible bimolecular reaction $I = I_0 / (1 + K_{eq} \cdot [\beta\text{ME}])$, yielding $K_{eq} = 0.10 \text{ mM}^{-1}$ ($N = 1, n = 4$).
- C)** Absorbance spectra of *in-vitro* mCherry-molecules over time after addition of 286 mM β ME. Arrows indicate increasing time.
- D)** Absorbance of purified mCherry-molecules at 410 nm (black line) and 590 nm (red line) as function of time. Addition of 286 mM β ME and exposure to 405 nm light is indicated. Dotted black lines represent fits for one phase decay: $I = \text{Plateau} + (I_0 - \text{Plateau}) \cdot \exp(-t/t_{1/2})$. Values for $t_{1/2}$ are 111 s⁻¹ and 106 s⁻¹ after β ME, 65 s⁻¹ and 60 s⁻¹ during 405 nm illumination, and 109 s⁻¹ and 108 s⁻¹ after 405 nm illumination, for absorbance at 410 nm and 590 nm, respectively.
- E)** Fluorescence images of purified mCherry-molecules on a coverslip before addition of 286 mM β ME, after addition of β ME, and 1.5h after washout of β ME.
- F)** Quantification of the fluorescence signal after addition of 286 mM β ME ($8\% \pm 0.1\%$) and 1.5h after washout ($83\% \pm 3\%$) (mean \pm SEM; $N = 2, n = 44$ regions).
- G)** Kinetics of fluorescence return after β ME washout. Fluorescence intensity is normalized to the final value. The solid line represents a fit for one phase dissociation of β ME and mCherry yielding $t_{1/2} = 4.8 \cdot 10^2$ s (95% confidence interval $4.6 \cdot 10^2 - 5.1 \cdot 10^2$; $N = 3$).

The β ME-induced blue fluorescent state that we observed resembles the blue intermediate state reported in the maturation pathway of RFPs [6] and also matches the absorption and emission spectra reported for mTagBFP [7]. Interestingly, exposure to near-UV light was found to accelerate the transition from the blue intermediate state to the final red state for dsRed [6], for mCherry-derived fluorescent timers and for photoactivatable PAmCherry [8,9]. We therefore hypothesized that the addition of β ME returns the RFP chromophore to a state similar to the blue intermediate state. The structure of the blue intermediate chromophore has been elucidated using x-ray crystallography [10] and *ab initio* QM/MM calculations [11] and based on the reported differences in structure between the red fluorescent and blue fluorescent chromophore, we envisioned (at least) two ways for β ME to interact with the chromophore to return it to the blue state (Figure 4A). One option is that β ME binds directly to the C_{β} of the tyrosine. The other option is a reduction of the chromophore without β ME being covalently bound to the chromophore. In both cases the double bond between the tyrosine C_{α} and C_{β} would be removed, resulting in the formation of an mTagBFP-type chromophore, with the shortening of the conjugated π -system leading to the blue-shift of the absorption and emission wavelengths.

To investigate the structural changes caused by β ME, we crystallized mCherry and soaked it in a β ME-containing solution just before flash freezing. Absorption measurements

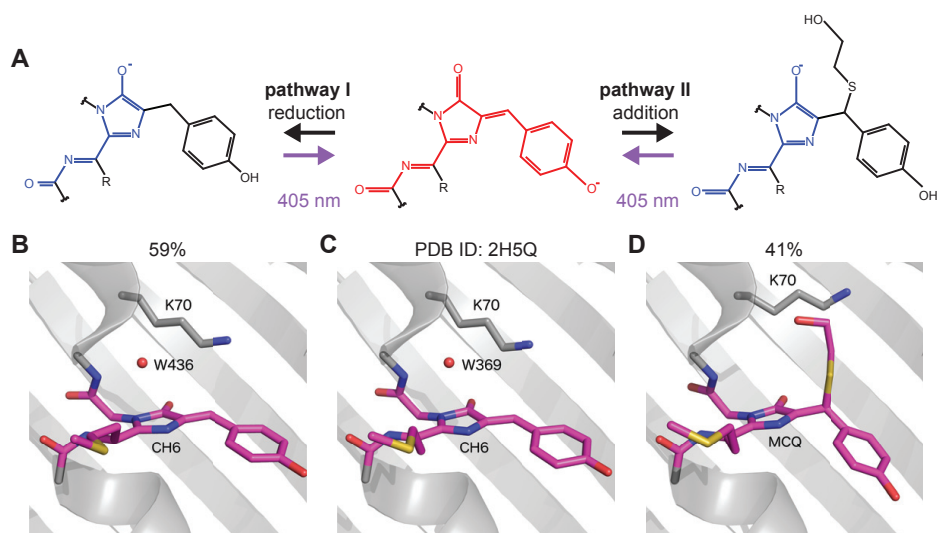


Figure 4: mCherry caging occurs through Michael addition of β ME to the chromophore.

A) Two hypothesized pathways for β ME-induced conversion of the RFP chromophore from the red fluorescent form to the blue fluorescent form. Pathway I is via reduction of the double bond between the C_{α} and C_{β} of the tyrosine. In pathway II, β ME is covalently attached to the C_{β} of the tyrosine through a Michael addition, removing the double bond between the C_{α} and C_{β} of the tyrosine.

B-D) Crystal structures of mCherry. C depicts the structure found in the PDB (ID: 2H5Q), whereas B) and D) depict the structures obtained after soaking a crystal in β ME. The structure in B has 59% occupancy in the crystal, versus 41% occupancy for D).

demonstrated that crystallized mCherry shows a similar blue-shift in absorbance spectrum as non-crystallized mCherry, and loses its red/purple color after soaking (Figure S1A-C). The crystal structure was determined with a resolution of 1.55 Å and had the typical β -barrel shape as seen in other fluorescent proteins. Whereas most amino acid residues were nicely defined in the electron density maps, the region around the chromophore in the center of the barrel was initially less clear. We were able to model two different chromophore types in this electron density: a chromophore closely resembling that of untreated mCherry (with occupancy of 59%), and a variant in which β ME adds to the C_β of the tyrosine via its mercapto-group (with occupancy of 41%) (Figure 4B-D). Although clear evidence for these two types was found during structure refinement, peaks in the $F_o - F_c$ difference map suggest the existence of alternative conformations of the free β ME-tail (Figure S1D, E). Moreover, the electron density suggests the existence of alternative chromophore structures in which the OH group of the added β ME moiety further reacts with the imidazolinone ring to form cyclic structures. However, as different cyclization reaction products can be envisioned that are difficult to distinguish unambiguously in the x-ray data, we refrained from modeling these explicitly.

While the crystal structure occupancies suggest that only about 41% of the mCherry molecules contain a β ME adduct, the purple color of the crystal fully disappears and the absorbance completely shifts to near UV wavelengths (Figure S1A-C). As a result, our data suggest that the remaining 59% does not correspond to the native mCherry chromophore, but rather to a chromophore in which the tyrosine C_β is in the reduced state, albeit with non-optimal bond angles for the C_β sp^3 -hybridised carbon atom. However, such deviations from model values are often observed in fluorescent protein chromophores. Further support for this model comes from our 2D [$^1H, ^{13}C$] HSQC measurements using $^{13}C/^{15}N$ tyrosine, methionine, glycine labeled mCherry (Figure S2). Upon addition of β ME, an extra peak emerged in the ^{13}C - 1H spectrum close to the characteristic C_β resonance for tyrosine. This indicates that the double bond between the C_α and C_β is converted to a standard single bond, resulting in blue-shifted absorption and emission. This peak most likely corresponds to the reduced state, because the covalent attachment of β ME to the C_β that was observed in the crystal structure is expected to induce a non-traceable shift away from the characteristic tyrosine C_β resonance.

In summary, we have shown that mCherry can be chemically brought to a blue fluorescent state by β ME and returned to the red fluorescent state by photoactivation with near-UV light or by β ME washout. The crystallographic data unambiguously showed the appearance of electron density that can only be explained by the formation of a new covalent bond at the C_β atom of tyrosine 67, resulting in a blue fluorescent chromophore. Covalent addition of thiols has been previously reported for cyanine dyes [12], although in that case the addition required irradiation with light, whereas here quenching occurs in the absence of light. Other groups have observed a similar spontaneous addition of thiol compounds [13] and phosphine [14] to fluorophores, but to our knowledge this has not been previously shown for fluorescent proteins. We propose that the covalent modification of the chromophore occurs via a Michael addition through the SH group of β ME. Reversibility of Michael additions has been shown for

different addends and adducts [15,16]. For example, reversible Michael addition of a thiol to a fluorescent probe was shown to blue-shift the absorbance and fluorescence spectra allowing the measurement of glutathione concentration inside living cells [17].

It is important to note that the additional covalent bond with BME was present in about 40% of mCherry molecules in the crystal, whereas the whole crystal changed color upon soaking in β ME. This suggests that the quenching of the other 60% of the molecules is achieved by reducing the double bond between the tyrosine's C_α and C_β , consistent with the appearance of the characteristic tyrosine C_β resonance in the NMR spectrum. Remarkably, irradiation with near UV light could reverse both the reduction and the addition, given that the maximum recovery is about 77%.

The mechanisms described here facilitate the use of conventional RFPs in SMLM. The localization accuracy is comparable to mEos3.2, but the number of fluorophores that contribute to the super-resolved image is almost twofold higher. Also, the purely chemical transition to a dark-state using β ME decouples imaging laser power and duty ratio, allowing for optimizing imaging conditions for single molecule detection. This is also an advantage compared to using a light-induced dark state, as reported for mCherry in the presence of β -mercaptoethylamine [5]. Given the many existing mCherry-based model systems, our strategy for mCherry-based SMLM using chemical caging followed by highly efficient photoactivation should be widely applicable.

MATERIALS AND METHODS

Microscopy

All microscopy was performed on a Nikon Ti-E microscope equipped with a 100x Apo TIRF (NA 1.49) objective and a Perfect Focus System. Excitation was done either with a mercury lamp or via a custom illumination pathway with a 15 mW 405 nm diode laser (Power Technology) and a 100mW 561 nm DPSS laser (Cobolt Jive). Fluorescence was detected using either an Andor DU-897D EMCCD with an additional 2.5x Optovar to achieve an effective pixel size of 64 nm, or an Andor NEO 5.5 sCMOS with an effective pixel size of 65 nm. All components were controlled by Micromanager software [18]. For intensity measurements as function of photoactivation time an additional diffuser (Optotune LSR-C-3010) was inserted between a pair of lenses with focal distance of 75 mm in the illumination pathway for even illumination in TIRF mode.

For SMLM, samples were continuously illuminated with 561 nm light in combination with increasing 405 nm intensity to keep the amount of molecules in a fluorescent state constant. Typically 5000-15000 frames were recorded with exposure times of 40-60 ms.

Cell culture, transfection and fixation of cells

COS-7 cells were cultured in DMEM/Ham's F10 (50%/50%) containing 10% Fetal Calf Serum (FCS) and 1% penicillin/streptomycin at 37°C and 5% CO₂. Prior to transfection, COS-7 cells

were plated on 18 mm glass coverslips for at least 2 days. COS-7 cells were transfected with Eugene6 (Roche) according to manufacturer's protocol.

For images of fixed cells before β ME, after β ME, and after photoactivation, cells were transfected for 2 days with mCherry- α -tubulin, and then extracted and fixed using PEM80 with 0.3% Triton-X100 and 0.25% GA for 90 seconds and then PBS with 4% PFA for 20 minutes. Coverslips were mounted in imaging chambers in PBS and positions for imaging were stored. A widefield image was made per position first in PBS, then after incubation with 286 mM β ME for 10 minutes, and finally after photoactivation for 8 s using a mercury lamp and a standard BFP2-filtercube (Chroma).

For SMLM imaging of mCherry- α -tubulin, after two days of transfection, the growth medium was exchanged with PBS containing 1 μ M Taxol, preheated to 37°C, for 1 minute, then extracted with PEM80 (80 mM PIPES, 1 mM EGTA, and 5 mM MgCl₂, adjusted to pH 6.9) containing 1% Triton-X100 and 1 μ M Taxol, preheated to 37°C, for 2 minutes. The cells were then washed quickly three times with PEM80 and fixed with PBS containing 4% PFA and 0.25% GA for 20 minutes at RT. Samples were mounted in an imaging chamber filled with PBS, multiple positions were selected for SMLM imaging and widefield images at these positions were made. The PBS was then exchanged for PBS containing 143 mM β ME, and SMLM imaging was started.

For dual color SMLM imaging of clathrin-mRFP and mEos3.2-tubulin, after one day of transfection, cells were fixed using PBS containing 4% PFA and 0.5% GA for 20 minutes, quickly washed 3 times with PBS and mounted on an indented slide with imaging buffer. (PBS containing 5% glucose, 560 μ g/ml glucose oxidase, 40 μ g/ml catalase, 50 mM MEA, and 143 mM β ME)

Protein production

mCherry and tagRFP were cloned by PCR from pmCherry-N1 (Clontech), and pTagRFP-N (Eurogene), respectively, and inserted into linearized pET-SUMO via TA-ligation (Champion™ pET SUMO Expression System, Invitrogen). mRFP flanked by BamHI/XhoI was cloned by PCR, restricted and inserted into a linearized pET28a-6xHis vector. The identity of constructs was confirmed by sequencing analysis and the plasmids were re-transformed into E.coli BL21(DE3). Protein expression was induced for 3 hours at 37°C with 0.5 mM IPTG. Cells were pelleted by centrifugation at 4600x g. mCherry and tagRFP expressing cells were lysed in PBS containing 0.5% Triton X-100 and protease inhibitor cocktail (Roche), sonicated for 15 min and kept on ice for another 30 minutes mRFP expressing cells were lysed in PBS supplemented with protease inhibitor cocktail (Roche) and Lysozyme combined with five rounds of 1 minute sonication. Bacterial extracts were prepared by centrifugation at 4600x g, 4 °C for 30 min and soluble protein was isolated with Probond resin (Invitrogen) according to a standard protocol. Purified protein was eluted from the beads by Imidazole gradient (150-300 mM), dialyzed into PBS, concentrated to 1 mg/ml, aliquoted and stored at -80 °C.

Quantification of the fluorescence signal return percentage in cells

Images of 22 cells divided over two samples were analysed. The integrated fluorescence intensity was measured in non-saturated parts of the images before adding β ME, after incubation with 286 mM β ME, and after photoactivation with violet light. Background intensity levels were determined from a part of the image outside of the cells and subtracted from all measurements. The fluorescence intensity before adding β ME was set to 100%.

In-vitro experiments

For measurements of intensity as function of photoactivation time, lane samples were created by attaching plasma cleaned glass coverslips to microscope slides using double sided tape. Purified RFPs were diluted in PBS and non-specifically adsorbed to the coverslips during 10 minutes incubation. After extensive washing with PBS to remove unbound molecules, 286 mM β ME in PBS was added and the lanes were sealed. Imaging took place after ~ 20 minutes. For each time point, the mean of the average intensity of 6 images was calculated. The data was fitted with a model describing photoactivation from the quenched state and photobleaching from both the quenched and red fluorescent state with rates k_{pa} , $k_{dam,B}$, and $k_{dam,R}$, respectively:

$$R = \frac{e^{-t \cdot k_{dam,R}} (1 - e^{-t \cdot (k_{pa} - k_{dam,R} + k_{dam,B})}) \cdot Q_0 \cdot k_{pa}}{k_{pa} - k_{dam,R} + k_{dam,B}}$$

where R is the amount of red fluorescent molecules after photoactivation and Q_0 the amount of quenched molecules before photoactivation. Q_0 is assumed constant for all photoactivation intensities and recaging was not included.

For washout experiments, the lanes samples were washed extensively with PBS after 20 minutes incubation with β ME and sealed with vacuum grease. Every ~ 60 seconds an image was made and the average intensity calculated. The graph shows the mean \pm SEM for $N = 3$ samples. The fitted model represents one phase dissociation of β ME and mCherry:

$$I = I_0 + (Plateau - I_0) \cdot (1 - e^{-K_{eq} \cdot t})$$

To determine the return percentage, RFPs were non-specifically adsorbed to plasma cleaned 25 mm coverslips and mounted in imaging rings. In total 5 frames were made per position with an exposure time of 100 ms using 561 nm laser light. Three images were made before β ME was added, 1 image after addition, and 1 image after photoactivation with 405 nm laser light. The percentages of fluorescence after adding β ME and after photoactivation are relative to the last image before adding β ME. $N = 4, 2,$ and 2 samples, $n = 40, 24,$ and 20 measurements for mCherry, mRFP, and tagRFP, respectively.

SMLM Localization and Rendering Algorithms

Single-molecule localization software was written in Java as an ImageJ plugin, called Detection of Molecules (DoM). Each image in an acquired stack was convoluted with the two-dimensional Mexican hat kernel matching the microscope's point spread function (PSF) size. The intensity

histogram of the convolved image was fitted to a Gaussian distribution and used to calculate the threshold intensity value (mean value of the fit plus three standard deviations). The maximum intensity values within individual spots were chosen as initial positions for the peaks' fitting performed on the original image. We used unweighted nonlinear least squares fitting with Levenberg-Marquardt algorithm to the assumed asymmetric two-dimensional Gaussian PSF.

Only fits with a calculated width within $\pm 30\%$ of the measured PSF's standard deviation were accepted. Localizations within one pixel distance in a number of successive frames were considered to arise from the same molecule. In this case the weighted mean was calculated for each coordinate, where weights were equal to inverse squared localization precision. The resulting table with molecule coordinates and precision was used to render the final localization image with 10-20 nm pixelsize. Each molecule was plotted as a 2D Gaussian of the integrated intensity equal to one and with standard deviations equal to the localization precision.

Comparison of localization precision

In dual color SMLM images of clathrin-mRFP and mEos3.2-tubulin, regions were selected by eye that clearly contained mainly clathrin-mRFP or mainly mEos3.2-tubulin. Using a custom R-script, the distribution of the localization precision of localizations in these regions was determined and mean and mode were calculated. Localizations with an estimated error larger than 32 nm were discarded.

Fluorescence spectroscopy

Fluorescence spectra as function of β ME percentage were recorded using a fluorescence spectrophotometer (Cary Eclipse, Agilent Technologies). Purified mCherry was diluted in PBS and pipetted in a 40 μ l Quartz cuvette. β ME concentration was increased from 0 to 143 mM. Four fluorescence spectra with both 550 nm and 410 nm excitation were recorded per β ME concentration and averaged. Fluorescence intensity at 610 nm was fitted with an expression for a reversible bimolecular reaction:

$$I = \frac{I_0}{1 + k_{eq} \cdot [\beta ME]}$$

Absorbance was measured over time using a miniature deuterium-tungsten halogen lamp (Ocean Optics DT-MINI-2-GS) in-line with a miniature spectrophotometer (Ocean Optics USB-4000). Purified mCherry was pipetted in a 1 ml cuvette and after the absorbance measurement was started 286 mM BME was added. Measurements were continued until the absorbance reached a steady state. An unfocused 405 nm diode laser (Coherent CUBE, 100 mW) was aimed from top to bottom through the cuvette to photoactivate the quenched mCherry-molecules until again a steady state was reached. The photoactivation was then stopped and measurements continued for approximately 6 minutes. Both the absorption at 410 nm and 590 nm are fitted with separate single exponential functions for the three regimes.

Crystallography

For crystallization, a pRSetb plasmid containing the mCherry gene was transformed into JM109(DE3) E.coli cells (Promega). A single colony was inoculated in 1 l LB medium containing ampicillin. mCherry was expressed after 4 days at 20°C. Cells were harvested by centrifugation at 5000 rpm for 10 minutes and resuspended in TN buffer (100 mM Tris, 300 mM NaCl, pH 7.4). Afterwards, they were lysed using a French pressure cell, and the cellular debris was spun down for 20 minutes at 8500 rpm. Afterwards, the cellular extract was loaded onto a HisTrap FF Crude column (GE Healthcare) coupled to an Aktra Prime system (GE Healthcare). Elution was performed using TN buffer supplemented with 500 mM imidazole. Then a size-exclusion chromatography was run on a HiLoad Superdex 200pg 16/600 column (Ge Healthcare) coupled to an Akta Purfier 10 system (GE Healthcare) with 0.1x TN buffer. Finally the protein was concentrated using a Vivaspin 10.000 MWCO column.

mCherry crystals were grown in sitting drops containing 1 μ l of protein solution (10 mg/ml), 1 μ l of precipitant (0.2 M $\text{MgCl}_2 \cdot 6\text{H}_2\text{O}$, 0.1 M Tris pH 8.5, 25% PEG 4000) and 0.5 μ l of β ME (2 M), equilibrated against a 100 μ l reservoir of precipitant. As the solution regained its colour after several days, the crystals were soaked in a drop containing 1 μ l PEG 400 (40%) and 1 μ l β ME (5 M) just before flash freezing in liquid nitrogen. Upon soaking, the crystals immediately lost their color and this absence of color remained until X-ray diffraction.

X-ray diffraction data were collected on a Pilatus detector with a wavelength of 1.00 Å (12.4 keV) under a 100 K nitrogen stream at the X60DA beamline of SLS at the PSI, Switzerland. The data were indexed and integrated using XDS v. January 22, 2015 [19] and scaled and merged using Aimless [20]. The structure was solved by molecular replacement using Phaser v.2.5.6 [21] and the coordinates of mCherry (PDB ID: 2H5Q) as a model. Structure refinement was carried out using Phenix.refine v.1.9 [22] and Coot v.0.7.2 [23]. After the first refinement cycle the original mCherry chromophore (PDB ligand ID: CH6) was modelled in the difference map. In subsequent refinement cycles, a modified version of the chromophore, being the Michael addition product of the chromophore and β ME, was added to the model. The dictionary file of the CH6 chromophore was prepared using eLBOW[24]. For the additional fragment in the other chromophore type (MCQ), an initial dictionary file was created using JLigand [25] and was manually changed using mean values of angles and dihedrals obtained from the Cambridge Crystallographic Database (CSD [26]). The occupancy factor of CH6 was coupled to that of K70 and water molecule 436 and converged to 59%, while the occupancy factor of MCQ was linked to that of the alternative conformation of K70 and converged to 41%. Water molecules were included in the model if they were in hydrogen bonding distance with chemically reasonable groups, appeared in $F_o - F_c$ maps contoured at 3.0 σ , and had B-factors less than 80 Å².

Data collection and refinement statistics can be found in Table S1. The structure was deposited in the PDB with accession code 5FHV. Images were created using the PyMOL Molecular Graphics System (Version 1.8 Schrödinger, LLC.).

Crystal absorption measurements

Absorption spectra from single mCherry crystals were recorded using a home-built optical setup equipped with two objectives: a 10x Plan Apo objective (Nikon, NA 0.45) and a 10x Plan S objective (Olympus, NA 0.4). Depending on the working mode, the first objective was used to either focus white light on the crystal, or else to illuminate the full field of view of the second objective, with the latter being responsible for the collection of the transmitted light and imaging of the sample surface. Transmitted light was split with a non-polarizing beamsplitter and guided towards an optical fiber collimator and high resolution color CMOS detector (DCC1645C), preceded with a tube lens. Imaging capability allowed for the precise beam positioning and collection of reliable reference absorption spectra (Ocean Optics DT-MINI-2-GS and USB4000). Both illumination and transmitted light was guided with a premium grade multimode optical fiber (Ocean Optics, QP600-1-UV-BX) with a core diameter of 600 μm . The crystallization buffer solution containing one mCherry crystal was sandwiched between two coverslips. Subsequently, the sample was placed between the objectives and mounted on the micrometer XYZ stage (Newport) that allowed for precise positioning within a travel range of 25 mm.

NMR spectroscopy

The pET Sumo mCherry plasmid was transformed in BL21(DE3)Rosetta2, a fresh colony was inoculated in 2 ml LB and cultured for 6 hour at 37 °C. Cells were, after removal of the LB medium by centrifugation, transferred to 50 ml minimal medium [27], containing 4g/l ^{12}C glucose and 1g/l ^{14}N NH_4Cl and cultured overnight at 30 °C. Cells were transferred to 250 ml minimal medium containing ^{12}C glucose and ^{14}N NH_4Cl supplemented with 100 mg/l of each amino acid. Glycine, Methionine and Tyrosine (Cortecnet) were $^{13}\text{C}/^{15}\text{N}$ labeled, all the other amino acids were not isotope enriched. mCherry expression was induced for 4 hours at 30 °C by the addition of 0.5 mM IPTG, when the culture reached an OD600 of 0.7. Purification was performed as described before [27] using metal affinity chromatography followed by sumo-tag removal by ULP1 according to instructions (Invitrogen). After overnight protease digestion, metal affinity chromatography was performed to separate the sumo tag from the essentially pure mCherry. The final sample was buffer exchanged by ultrafiltration to NMR buffer containing 50 mM NaPO_4 , 100 mM NaCl pH 7.0 and 7.5% D_2O at a final concentration of 100-200 μM mCherry.

2D [$^1\text{H},^{15}\text{N}$] and [$^1\text{H},^{13}\text{C}$]-HSQC spectra of mCherry were recorded at 298 K in the presence or absence of βME on a Bruker Avance 600 MHz spectrometer equipped with a TXI probe with z-gradients. Spectra were processed using Topspin 2.1 and analysis was performed using Sparky [28].

ACKNOWLEDGEMENTS

This research was supported by the Dutch Technology Foundation STW and the Foundation for Fundamental Research on Matter (FOM), which are part of the Netherlands Organisation for Scientific Research (NWO). Additional support came from NWO (NWO-ALW-VIDI to L.C.K.) and the European Research Council (ERC Starting Grant to L.C.K.). We also acknowledge support by the Research-Foundation Flanders FWO via grants 1521915N, 1502314N, and 1525113N. M.M. is recipient of a European Molecular Biology Organization (EMBO) Long-Term Fellowship (EMBO ALTF 884-2011), Marie Curie IEF (FP7-PEOPLE-2011-IEF) and DFG Emmy-Noether Grant (MI 1923/1-1). E.D.Z and V.G. thank the IWT Flanders for a doctoral fellowship. B.K. thanks the financial support from the Mobility Plus programme (1068/MOB/2013/0) founded by the Polish Ministry of Science and Higher Education. E.D.Z. and L.V.M. thank the staff of the beamline X60DA at the Swiss Light Source (Villigen, Switzerland) for their assistance with the data collection.

AUTHOR CONTRIBUTIONS

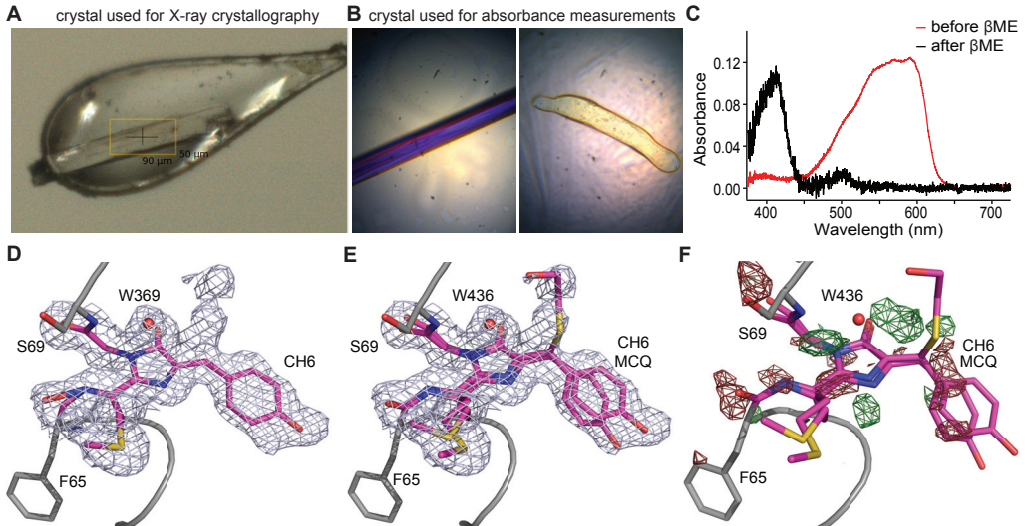
B.M.C.C. and L.C.K. initiated the research, designed experiments for figures 1 and 2, and wrote the manuscript. B.M.C.C. performed experiments and analyzed data for figures 1 and 2. B.M.C.C. and V.G. performed experiments and analyzed data for figure 3.

REFERENCES

- 1 Patterson, G., Davidson, M., Manley, S. & Lippincott-Schwartz, J. Superresolution Imaging using Single-Molecule Localization. *Ann Rev of Phys Chem* 61, 345-367 (2010).
- 2 Durisic, N., Laparra-Cuervo, L., Sandoval-Alvarez, A., Borbely, J. S. & Lakadamyali, M. Single-molecule evaluation of fluorescent protein photoactivation efficiency using an in vivo nanotemplate. *Nat Meth* 11, 156-162 (2014).
- 3 Folling, J. et al. Fluorescence nanoscopy by ground-state depletion and single-molecule return. *Nat Meth* 5, 943-945 (2008).
- 4 Biteen, J. S. et al. Super-resolution imaging in live *Caulobacter crescentus* cells using photoswitchable EYFP. *Nat Meth* 5, 947-949 (2008).
- 5 Winterflood, C. M. & Ewers, H. Single-Molecule Localization Microscopy using mCherry. *Chemphyschem* 15, 3447-3451 (2014).
- 6 Verkhusha, V. V., Chudakov, D. M., Gurskaya, N. G., Lukyanov, S. & Lukyanov, K. A. Common Pathway for the Red Chromophore Formation in Fluorescent Proteins and Chromoproteins. *Chem Biol* 11, 845-854 (2004).
- 7 Subach, O. M. et al. Conversion of red fluorescent protein into a bright blue probe. *Chem Biol* 15, 1116-1124 (2008).
- 8 Subach, F. V. et al. Photoactivation mechanism of PAmCherry based on crystal structures of the protein in the dark and fluorescent states. *Proc Natl Acad Sci* 106, 21097-21102 (2009).
- 9 Subach, F. V. et al. Photoactivatable mCherry for high-resolution two-color fluorescence microscopy. *Nat Meth* 6, 153-159 (2009).
- 10 Subach, O. M. et al. Structural characterization of acylimine-containing blue and red chromophores in mTagBFP and TagRFP fluorescent proteins. *Chem Biol* 17, 333-341 (2010).
- 11 Bravaya, K. B., Subach, O. M., Korovina, N., Verkhusha, V. V. & Krylov, A. I. Insight into the Common Mechanism of the Chromophore Formation in the Red Fluorescent Proteins: The Elusive Blue Intermediate Revealed. *J Am Chem Soc* 134, 2807-2814 (2012).
- 12 Dempsey, G. T. et al. Photoswitching Mechanism of Cyanine Dyes. *J Am Chem Soc* 131, 18192-18193 (2009).
- 13 Peng, H. et al. Thiol Reactive Probes and Chemosensors. *Sensors (Basel, Switzerland)* 12, 15907-15946 (2012).
- 14 Vaughan, J. C., Dempsey, G. T., Sun, E. & Zhuang, X. Phosphine quenching of cyanine dyes as a versatile tool for fluorescence microscopy. *J Am Chem Soc* 135, 1197-1200 (2013).
- 15 van Axel Castelli, V. et al. Rates and Equilibria of the Michael-Type Addition of Benzenethiol to 2-Cyclopenten-1-ones. *J Org Chem* 64, 8122-8126 (1999).

- 16 Allen, C. F. H. & Happ, G. P. The thermal reversibility of the Michael reaction: I. Nitriles. *Canadian Journal of Chemistry* 42, 641-649 (1964).
- 17 Chen, J., Jiang, X., Carroll, S. L., Huang, J. & Wang, J. Theoretical and Experimental Investigation of Thermodynamics and Kinetics of Thiol-Michael Addition Reactions: A Case Study of Reversible Fluorescent Probes for Glutathione Imaging in Single Cells. *Org Lett* 17, 5978-5981 (2015).
- 18 Edelstein, A., Amodaj, N., Hoover, K., Vale, R. & Stuurman, N. in *Current Protocols in Molecular Biology* (John Wiley & Sons, Inc., 2001).
- 19 Kabsch, W. XDS. *Acta Crystallogr Sect D-Biol Crystallogr* 66, 125-132 (2010).
- 20 Evans, P. R. & Murshudov, G. N. How good are my data and what is the resolution? *Acta Crystallographica Section D: Biological Crystallography* 69, 1204-1214 (2013).
- 21 McCoy, A. J. et al. Phaser crystallographic software. *J Appl Crystallogr* 40, 658-674 (2007).
- 22 Afonine, P. V. et al. Towards automated crystallographic structure refinement with phenix.refine. *Acta Crystallogr Sect D-Biol Crystallogr* 68, 352-367 (2012).
- 23 Emsley, P., Lohkamp, B., Scott, W. G. & Cowtan, K. Features and development of Coot. *Acta Crystallographica Section D: Biological Crystallography* 66, 486-501 (2010).
- 24 Moriarty, N. W., Grosse-Kunstleve, R. W. & Adams, P. D. electronic Ligand Builder and Optimization Workbench (eLBOW): a tool for ligand coordinate and restraint generation. *Acta Crystallogr Sect D-Biol Crystallogr* 65, 1074-1080 (2009).
- 25 Lebedev, A. A. et al. JLigand: a graphical tool for the CCP4 template-restraint library. *Acta Crystallogr Sect D-Biol Crystallogr* 68, 431-440 (2012).
- 26 Allen, F. The Cambridge Structural Database: a quarter of a million crystal structures and rising. *Acta Crystallographica Section B* 58, 380-388 (2002).
- 27 Folkers, G. E., van Buuren, B. N. M. & Kaptein, R. Expression screening, protein purification and NMR analysis of human protein domains for structural genomics. *J Struct Funct Genomics* 5, 119-131.
- 28 Goddard, T. & Kneller, D. Sparky 3. University of California, San Francisco.

SUPPLEMENTARY FIGURES

**Figure S1: Information about the crystallography**

- A) Color picture of the (near) colorless mCherry crystal just before the start of the X-ray experiment.
- B) Color pictures of the mCherry crystal used for absorption measurements before (left panel) and after (right panel) soaking in β ME. The odd shape of the crystal after soaking in β ME is due to β ME-induced dissolution since the absorption experiments were performed at room temperature (in contrast to the crystallography, where the crystal is flash-frozen after addition of β ME).
- C) Absorption spectra of the crystals in B. The red line corresponds to the crystal before soaking in β ME and the black line to the crystal after soaking in β ME. The same absorbance shift is observed as for non-crystallized mCherry after soaking in β ME.
- D) $2F_o - F_c$ map contoured at 0.5 r.m.s.d. together with the mCherry crystal structure as found in the PDB (ID: 2H5Q). An extra electron density is present near the C_β of the chromophore's tyrosine.
- E) $2F_o - F_c$ map contoured at 0.5 r.m.s.d. together with the two mCherry structures modeled in the electron density as described.
- F) $F_o - F_c$ difference map contoured at 3 r.m.s.d., positive peaks in green, negative peaks in red. The map shows that the model does not completely cover the electron density. Different cyclisation reaction products can be fit in the positive electron density, but cannot clearly be distinguished from each other.

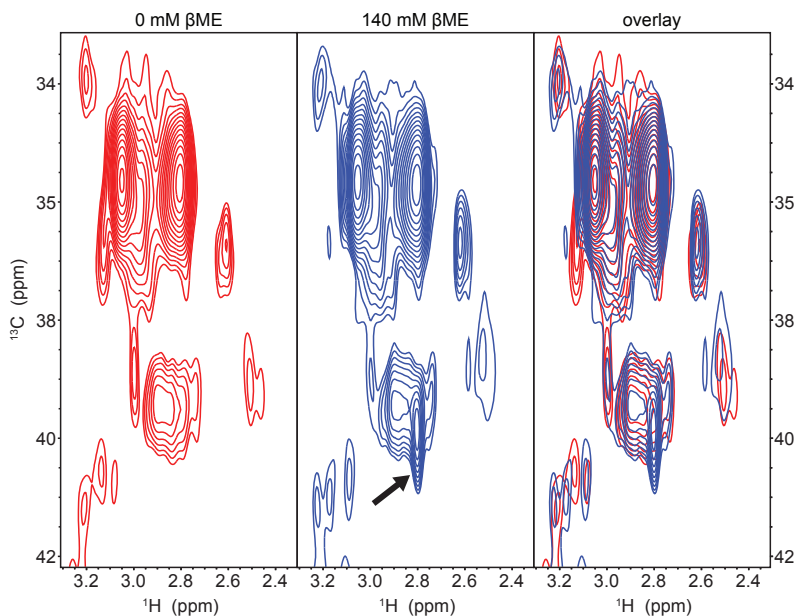


Figure S2: NMR spectra of mCherry with and without β ME

^{13}C - ^1H HSQC-spectra of purified mCherry molecules without β ME (left panel), with 143 mM β ME (middle panel) and overlay (right panel). The arrow in the middle panel indicates an extra peak present in the spectrum in the presence of 143 mM β ME at 39.9 ppm ^{13}C and 2.8 ppm ^1H , corresponding closely to the reported chemical shifts of the C_β of tyrosine (39.3 ± 2.7 ppm ^{13}C and 2.9 ± 0.5 ppm ^1H ; data from Biological Magnetic Resonance Data Bank). This indicates that the double bond between the C_α and C_β could also be reduced after addition of β ME, without the formation a covalent adduct.

Table S1: Data collection and refinement statistics

Space group	$P 2_1$
Unit cell parameters	
a, b, c (Å)	48.783 43.244 61.234
α, β, γ (°)	90 111.52 90
Resolution range (Å)	45.38 – 1.55 (1.58 – 1.55) [*]
R_{merge} (%)	5.3 (49.9)
$CC_{1/2}$ (%)	99.9 (76.7)
$\langle I/\sigma(I) \rangle$	14.0 (2.1)
No. of reflections	113930 (5098)
No. of unique reflections	34495 (1686)
Multiplicity	3.3 (3.0)
Completeness (%)	99.4 (99.0)
$R_{\text{work}}/R_{\text{free}}^{\text{s}}$ (%)	15.68/18.77
RMSD from ideal	
Bond lengths (Å)	0.006
Bond angles (°)	1.269
Average isotropic B-factors (Å ²)	
Main chain	13.03
Side chain	17.81
Water molecules	28.98
Ligands (BME, PGE, P6G)	35.84
Ramachandran plot [#] (%)	
Residues in favored regions	98.7
Residues in allowed regions	1.3
Outliers	0.0
Rotamer [#] outliers	1.0

* Values in parentheses are for the highest resolution shell.

^s R_{free} is calculated using a random 5% of data excluded from the refinement.

[#]Ramachandran and rotamer analysis was carried out using Molprobit.

¹Cell Biology, Department of Biology, Faculty of Science, Utrecht University, Padualaan 8, 3584 CH Utrecht, The Netherlands. ²Randall Division of Cell and Molecular Biophysics, King's College London, Guy's Campus, London SE1 1UL, United Kingdom. ³Department of Neuro- and Sensory Physiology, University of Göttingen, Humboldtallee 23, 37073 Göttingen, Germany. ⁴Institut Curie, Research Center, 26, rue d'Ulm, 75248, Paris, France. ⁵CNRS UMR144, 26, rue d'Ulm, Paris, France. ⁶Translational Research Department, Institut Curie, 26, rue d'Ulm, 75248, Paris, France. ⁷RG Neuroplasticity, Leibniz Institute for Neurobiology, Brennekestr. 6, 39118 Magdeburg, Germany. ⁸Inserm, U836, 38000, Grenoble, France. Univ. Grenoble Alpes, Grenoble Institut des Neurosciences, 38000, Grenoble, France. ⁹present address: Freie Universität Berlin, Institut für Chemie und Biochemie, Thielalle 63, 14195 Berlin, Germany. ¹⁰present address: University Medical Center Hamburg-Eppendorf, UKE, Center for Molecular Neurobiology, ZMNH, Falkenried 94, 20251 Hamburg, Germany

* These authors contributed equally to this work

Chapter 4

Resolving bundled microtubules using anti-tubulin nanobodies

Marina Mikhaylova^{1,7,10}, **Bas M. C. Cloin**^{1*}, Kieran Finan^{2*}, Robert van den Berg^{1*}, Jalmar Teeuw¹, Marta M. Kijanka¹, Mikolaj Sokolowski¹, Eugene A. Katrukha¹, Manuel Maidorn³, Felipe Opazo³, Sandrine Moutel^{4,5,6}, Marilyn Vantard⁸, Frank Perez^{4,5}, Paul M.P. van Bergen en Henegouwen¹, Casper C. Hoogenraad¹, Helge Ewers^{2,9}, Lukas C. Kapitein¹

ABSTRACT

Microtubules are hollow biopolymers of 25 nm diameter and are key constituents of the cytoskeleton. In neurons, microtubules are differently organized between axons and dendrites, but their precise organization in different compartments is not completely understood. Super-resolution microscopy techniques, such as single-molecule localization microscopy, can detect specific structures at an increased resolution, but the extremely small spacing between neuronal microtubules poses novel challenges, because most existing labelling strategies increase the effective microtubule diameter by 20-40 nanometer and will thereby blend neighbouring microtubules into one structure. Here we developed single-chain antibody fragments (nanobodies) against tubulin to achieve super-resolution imaging of microtubules with a decreased apparent diameter. To test the resolving power of these novel probes, we generated microtubule bundles with a known spacing of 50-70 nm and successfully resolved individual microtubules. Individual bundled microtubules could also be resolved in different mammalian cells, including hippocampal neurons, allowing novel insights into fundamental mechanisms of microtubule organization in cell- and neurobiology.

INTRODUCTION

Microtubules are hollow biopolymers of 25 nm diameter and are key constituents of the cellular cytoskeleton, the mechanical framework of dynamic polymers and associated proteins that directs cell shape and facilitates intracellular transport [1]. The exact spatial organization of microtubules and their bundling is of central importance to a number of fundamental cellular processes such as mitosis, cell polarization and the outgrowth of cellular processes, for example in neurons [1]. Conventional fluorescence microscopy allows selective labeling of microtubule modifications and associated proteins, but cannot resolve individual microtubules within tightly bundled microtubule arrays. Electron microscopy, in contrast, allows resolving individual microtubules, but is very labor intensive, while high-density labeling of specific proteins has remained challenging. Single-molecule localization microscopy (SMLM) provides selectivity at an increased resolution, but the extremely small spacing between neuronal microtubules (20-70 nm) [2] poses novel challenges, because existing labeling strategies typically increase the apparent microtubule diameter by 20-40 nanometers and will thereby blend neighboring microtubules into one structure [3]. It is therefore widely assumed that despite all progress in super-resolution microscopy, electron microscopy is still the only technique that allows insight into complex microtubule structures [4]. Here, we use both computer simulations and experimental approaches to explore how labelling strategy affects SMLM imaging of microtubules. We developed single-chain antibody fragments (nanobodies) against tubulin and achieved super-resolution imaging of microtubules with a decreased apparent diameter, allowing to optically resolve bundled microtubules.

RESULTS

Simulations of microtubules with different labels

To explore the effect of label size and fluorescent probe positioning on resolving ability, we first performed numerical simulations to examine how labeling density, localization precision and fluorophore positioning affect the apparent microtubule width (determined as the full width at half maximum (FWHM) from Gaussian fits to intensity profiles integrated over 512 nm of microtubule length) (Figure 1A). Using a maximum localization uncertainty of 8 nm, we found that the apparent microtubule width was ~31 nm for a fluorophore positioned directly at the microtubule surface (probe position of 0 nm, Figure 1B). Placing the fluorophore further away increased the FWHM by double the displacement, i.e. 41 nm for a fluorophore position of 5 nm. A more stringent precision cutoff resulted in decreased FWHM (Figure 1C) and the FWHM decreased from 63 nm for a probe position of 15 nm and precision cutoff at 13 nm to 27 nm with fluorescent probes directly on the microtubule lattice and a precision cutoff of 3 nm.

To examine how label size affects the probability of resolving closely spaced microtubules, pairs of randomly picked profiles were superimposed with a set distance between the

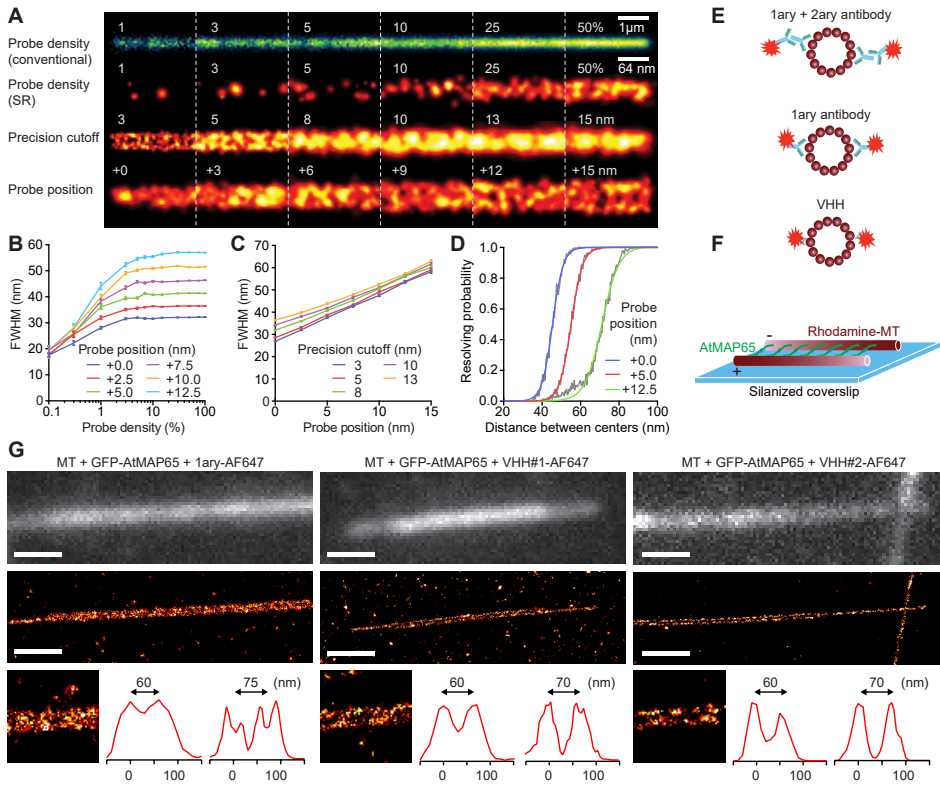


Figure 1: Smaller labels allow resolving bundled microtubules.

- A)** Simulations of conventional (top) and single-molecule localization based microtubule images for different probe densities, localization precision cutoffs and probe positions (distance between target molecule and fluorophore). Unless specified otherwise, probe position is 2.5 nm and precision cutoff is 8 nm. Probe density is 100% and 50% for the third and fourth row, respectively. A Gaussian localization accuracy distribution with $\text{mean} \pm \text{SD}$ of 7.5 ± 2.5 nm is used.
- B)** FWHM of Gaussian fits to microtubule cross sections integrated over 512 nm length as a function of probe density and for different probe positions. Error bars represent SEM. Each point is the average of 150 FWHMs measured on 512 nm long MT (but empty stretches along the MT were not included).
- C)** MT FWHM versus probe position for different cutoffs of the localization accuracy distribution.
- D)** Estimation of resolving power for staining of microtubules with probes at increasing distance from the microtubule. Probe density is 7%, localization precision cutoff threshold is 13 nm. 250 profiles per distance.
- E)** Illustration of the different labeling strategies compared in this study.
- F)** Scheme of the *in vitro* microtubule bundling assay to test the resolving power of different microtubule labeling strategies. Rhodamine-labeled microtubules are assembled into planar bundles with defined spacing formed by the microtubule-bundler GFP-AtMAP65-1.
- G)** Conventional (top) and SMLM (middle and bottom left) images and representative line scans (bottom right) of *in vitro* microtubule bundles stained with a fluorescently labeled primary anti- α -tubulin antibody (1ary-AF647) or two novel tubulin nanobodies (VHH#1 and VHH#2) conjugated to AF647. More examples are provided in Figure S3.

microtubule centers and the resulting profile was analyzed. If the lowest intensity between the two microtubule centers was <75% of the intensity of the lowest peak, the microtubules were considered to be resolved and the resolving probability was calculated as the fraction of resolvable cases out of 250. As expected, decreasing label size results in increasing the resolving probability (Figure 1D). For example, given a labeling density of 7% and a precision cutoff of 13 nm, the probability of resolving microtubules with centers spaced 55 nm apart increased from 0.03 to 0.49 to 0.97 for probes positioned at 12.5 nm, 5 nm and 0 nm from the microtubule lattice, respectively (data taken from fit).

Generation and characterization of tubulin nanobodies

Conventional staining strategies often use a combination of primary antibodies binding a specific epitope, followed by a fluorescently-tagged secondary antibody that recognizes the primary antibody, resulting in significant displacement of the fluorescent probe from the target (Figure 1E). Typically, smaller labels have been obtained by directly conjugating a fluorophore to the primary antibody, or by using antibody fragments. Antibody fragments derived from heavy-chain only camelid antibodies (nanobodies) are now emerging as promising alternatives, because of their small size (~15 kDa, ~4 nm), as well as ease of selection and production. Previous work has demonstrated the usage of nanobodies to create smaller labels for SMLM. Overexpression of GFP-tubulin and subsequent labeling with an anti-GFP nanobody conjugated to a fluorescent dye significantly decreased the effective diameter of individual microtubules [3]. However, this strategy requires over-expression of GFP-tubulin to very high levels, which will perturb cytoskeletal organization and is not possible in many biological systems.

To experimentally assess the effect of label size on resolving power, we created three novel labels for SMLM of endogenous tubulin, complementing the existing strategies using conventional antibodies. First, we developed two different nanobodies against tubulin. One was derived from two rounds of phage display selection using a universal synthetic library of humanized nanobodies (VHH#1) and the other using an MRC7 cell library (VHH#2) (Figure S1A and B; see Methods section for details), similarly selected in two rounds of phage display. Immunoblotting with VHH#1 or VHH#2 on lysates of HEK293 cells overexpressing GFP- α -tubulin or GFP- β -tubulin revealed that both nanobodies react with the endogenous tubulin as well as GFP- β -tubulin (Figure S2A and B). Conjugation of Alexa Fluor® 647 (AF647) to the nanobodies did not interfere with their binding properties (Figure S2C; Figure S3 and S4). As a second approach, recombinant human-derived single chain variable fragments (scFvs) directed against α - and β -tubulin were purified and also coupled to AF647 [5]. All bacterially expressed and purified labels were relatively pure and stable over long periods of time (Figure S2A).

Resolving microtubule bundles *in vitro*

To test the SMLM resolving power of the different microtubule labels, we established an *in vitro* bundling assay using polymerized microtubules in combination with the microtubule bundler AtMAP65-1, which promotes the formation of a planar network of antiparallel

microtubules with a single dimer spacing in between (Figure 1F) [6]. Silanized coverslips were used to stably attach the microtubule bundles to the coverslip surface to allow for subsequent staining procedures. As a control, we performed SMLM on non-stained samples to which fluorescently-tagged tubulin (conjugated to HiLyte™ Fluor 647) was added in to the polymerization mix. In this condition, most bundles could be clearly resolved with an average spacing of 65 ± 2 nm (SEM, $n = 56$, Figure S3A). Both VHH#1 and VHH#2 conjugated to AF647 efficiently decorated the bundles and in most cases the individual microtubules could be clearly distinguished when the microtubule centers were 60-70 nm apart (Figure 1G and Figure S3B). In contrast, when a conventional primary anti- α -tubulin antibody directly coupled to AF647 was used, such bundled microtubules could often not be resolved.

Comparative analysis of microtubule labels in adherent cells

When we tested our nanobodies on microtubules in cells, we found that we could resolve microtubules that were spaced down to 40 nm (Figure 2A). To quantitatively compare the nanobody approach to the other staining methods in cells, we labeled microtubules in fixed Ptk2 and COS-7 cells using different tubulin labels conjugated to AF647. We determined the FWHM from a Gaussian fit to intensity profiles perpendicular to the microtubule averaged over 512 nm length to rule out possible profile artifacts that could arise from low labeling density (Figure 1B). We found that individual microtubules were densely labeled with the most common diameter (average mode \pm SEM) varying from 39.3 ± 0.8 nm (VHH#2, $N = 10$ datasets with in total $n = 1365$ profiles) to 54.0 ± 1.2 and 61.7 ± 0.8 nm (directly conjugated primary anti-tubulin antibody, $N = 10$, $n = 2462$, and primary anti-tubulin + secondary-AF647, $N = 10$, $n = 2460$, respectively) ((Figure 2B and Figure S4A and S4B; see Methods section for details and Figure S5A for statistical testing). Because in the rendering of the SMLM images we rejected all localizations with localization precision ≥ 13 nm, these values suggest that fluorophores coupled to primary antibodies are on average ~ 12.5 nm displaced from the microtubule lattice (Figure 1C). Strikingly, this distance is reduced to < 2.5 nm for VHH#2.

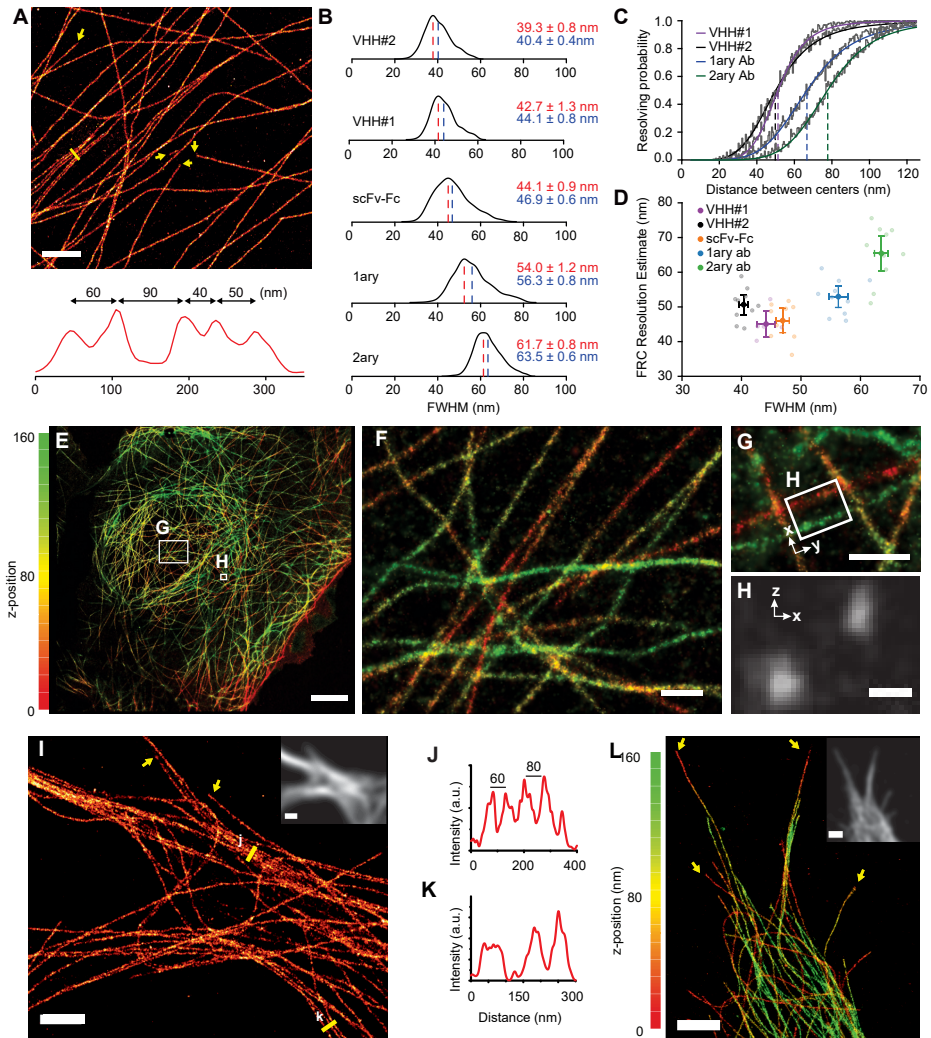
Figure 2: Resolving bundled microtubules in cells using tubulin nanobodies

A) SMLM reconstruction of a Ptk2 cell stained with VHH#1 and intensity profile of closely spaced microtubules along the yellow line. Yellow arrows indicate microtubule ends. A larger field of view of the same cell can be found in Figure S4B.

B) Histograms of microtubule FWHM for different probes. scFvs: mixture of human single chain antibody fragments (scFvs) recognizing α - and β -tubulin. For representative images, see Figure S4A. (From top to bottom: $n = 1365$, 547, 352, 2462, 2460 profiles from $N = 10, 5, 9, 10, 10$ different acquisitions). Mean (blue) and mode (red) value are indicated \pm SEM (using N).

C) Estimation of resolving power for different labels obtained by combining arbitrarily selected line profiles at increasing distance between centers.

D) Scatter plot of FRC resolution estimate versus microtubule FWHM for images of microtubules in COS-7 cells stained with different labels. Error bars depict 95% confidence intervals.



E) Overview 3D-SMLM reconstruction of a U2OS cell stained with AF647-labeled VHH#1. The z-depth is color-coded according to the scale on the left of the image. Scale bar is 5 μm .

F) Magnified image of the inset in E). Color code is the same as in E). Scale bar is 500 nm.

G) Area containing parallel microtubules at different depth in the cell. Color code is the same as in E). Scale bar is 800 nm.

H) Collapsed cross section (z-x) of the volume depicted in G). Scale bar is 100 nm.

I-K) SMLM reconstruction of microtubule bundles labeled with VHH#1 in the dendrites of a hippocampal primary neuron. Yellow arrows indicate microtubule ends and yellow lines were used for line scans across densely packed microtubule bundles J),K). Inset shows the diffraction-limited fluorescence image. Scale bar is 2 μm .

L) 3D-SMLM reconstruction of a hippocampal primary neuron labeled with VHH#1. The Z-depth is color-coded according to the scale on the left of the image. Yellow arrows indicate microtubule ends. Inset shows the diffraction-limited fluorescence image. Scale bar is 2 μm .

To translate the observed microtubule FWHM into a resolution estimate, we again analyzed composite profiles obtained by superimposing two randomly picked profiles with a set distance between the microtubule centers (Figure 2C). Based on cumulative probability plots obtained for the VHH#1, VHH#2, primary and primary-secondary antibody labelings, ~50% of all bundled microtubules with 25 nm lattice-to-lattice spacing (corresponding to 50 nm between peaks) will be resolved by the nanobody labels, whereas the directly conjugated primary antibodies or the sandwich labeling will only resolve ~20% and ~5% of all microtubule pairs, respectively. Consistent with the *in vitro* bundling results, VHHs are expected to resolve more than 90% of microtubule pairs with a lattice-to-lattice spacing of 60 nm, which is the typical spacing of tightly bundled microtubules in neuronal dendrites [2].

To further quantify the gain in resolution, we used the Fourier Ring Correlation resolution measure (FRCrm) as an independent, quantitative estimate of resolution that accounts for both localization precision and probe density [7]. Whereas direct application of the available FRC ImageJ-plugin to our data yielded highly variable results, this could be circumvented by data preprocessing to average different localizations emerging from the same fluorophore emitting over multiple frames (Figure S5B). As expected, smaller apparent diameters also resulted in better FRCrm resolution estimates, with the exception of VHH#2, whose lower labeling density resulted in a worse FRCrm compared to VHH#1, despite its smaller FWHM. For VHH#1, the average FRCrm was 45 ± 4 nm (Figure 2D). These results demonstrate that our novel anti-tubulin nanobodies provide improved resolution.

Tubulin nanobody for 3D-SMLM in U2OS cells and neurons

To test how anti-tubulin nanobodies performed in 3D-SMLM, we labeled microtubules in U2OS cells with VHH#1 and performed 3D-SMLM using the biplane approach [8]. We found that microtubules could easily be resolved in *z*-direction (Figure 2E-H) at distances of 100 nm. Finally, we used the VHH#1 nanobody to perform SMLM on microtubules in primary hippocampal neurons (Days *in vitro*, DIV1) and could successfully resolve individual microtubules in neurites (Figure 2I-L). The cross sections across densely packed microtubule bundles indicate a center-to-center spacing of 60 to 80 nm, consistent with earlier results using electron microscopy on cross sections [2]. In several cases, ends of individual microtubules could be clearly identified (Figure 2I and L, arrows). Thus, tubulin nanobodies can be used to resolve neuronal microtubule bundles.

DISCUSSION

We have introduced novel labels for microtubules that allow using SMLM to resolve previously inaccessible functional details of microtubule organization such as bundling, both *in vitro* and in fixed cells. These labels nicely complement the recently introduced live-cell marker for tubulin [8] that allows nanoscopy using STED (Stimulated Emission Depletion) microscopy and SIM (Structured Illumination Microscopy) in living cells, but does not remain bound to microtubules upon fixation (Figure S6). Microtubules are key components of many complex

cytoskeletal assemblies and their organization, polymerization, motility and interactions with motor proteins are controlled by a plethora of posttranslational modifications and modulating proteins, such as microtubule polymerases, severing proteins and bundlers. Therefore, our ability to resolve individual microtubules in such cytoskeletal assemblies paves the way towards a deeper understanding of the mechanisms underlying microtubule organization and function, both in health and disease.

METHODS

VHH#1 selection

VHH#1 was selected from a novel library of 3×10^9 humanized nanobodies. Briefly, commercial biotinylated tubulin (Cytoskeleton) was diluted to obtain a 10–20 nM solution (1 mL final) and efficient recovery of biotinylated tubulin was confirmed on 50 μ L streptavidin-coated magnetic beads (Dyna). Fractions of bound and unbound samples were compared by Western blot using streptavidin-HRP. Adequate amounts of beads and biotinylated antigen were incubated for 2 h with the phage library (10^{13} phages diluted in 1 mL of PBS containing 0.1% Tween-20 and 2% nonfat milk). Phages were previously adsorbed on empty streptavidin-coated magnetic beads to remove nonspecific binders. Phages bound to tubulin-coated beads were recovered on a magnet and washed 10 times (round 1) or 20 times (round 2) using PBS containing Tween-20 0.1%. Bound phages were eluted using 500 μ L triethylamine (TEA, 100 mM) for 10 min. Eluted phages were neutralized using 1M Tris pH 7.4. Elution was repeated once more. *E. coli* (TG1) were infected with the eluted phages. Round 2 was carried out using 10^{12} phages as input. After round 2, 40 bacteria clones were picked at random and used to produce nanobodies in the culture medium. Nanobody specificity was analyzed by immunofluorescence as described before [5] and nanobodies staining microtubules were analyzed further.

VHH#1 expression and purification

For production of VHH#1, WK6 *E. coli* containing the plasmid pHEN2-VHH#1- His_6 -cMyc₃ were grown in 2 L of 'Terrific Broth' (17 mM KH_2PO_4 , 72 mM K_2HPO_4 , 12 g/L tryptone, 24 g/L yeast extract, 0.4% glycerol) containing 2 mM MgCl_2 , 0.1% glucose, and 100 μ g/mL ampicillin with shaking at 37°C until the *E. coli* had an OD_{600} of 0.6–0.9. IPTG was then added to a concentration of 0.5 mM, and the flasks were shaken at 28°C overnight (~16 h). In order to extract the nanobody from the periplasmic space, cells were centrifuged (5000 x g, 10 min), resuspended in 24 mL of TES buffer (0.2 M Tris pH 8.0, 0.5 mM EDTA, 0.5 M sucrose) and shaken for 1 h at 4°C. The cell-TES mixture was then diluted by the addition of 36 mL of TES/4 buffer (50 mM Tris pH 8.0, 0.125 mM EDTA, 0.125 M sucrose), and shaken for 1 h at 4°C. The cells were then pelleted (5000 x g, 10 min), and the nanobody-containing supernatant removed. The His_6 -tagged VHH#1 was then purified using HisPur cobalt-agarose resin (Thermo Scientific) following manufacturer's instructions. The eluted protein

was concentrated ~10-fold using 'Vivaspin' columns (3 kDa MWCO; General Electric). SDS PAGE and Coomassie-staining of the resulting gels revealed the nanobody to be >90% pure. VHH#1 was dialyzed overnight against PBS at 4°C to remove any residual imidazole. The 2 L of culture yielded ~50 mg of pure nanobody. The stability of VHH#1 was analyzed by immunoblotting of a sample stored at 4°C for more than four month. 2 µg of VHH#1 were used for coomassie staining and about 100 ng for immunoblotting using anti-VHH serum 976 (1:2000, [9]) or mouse monoclonal anti-c-myc antibody (1:5000, Abcam) recognizing the carboxy-terminal myc-tag of VHH#1.

VHH#2 selection

The VHH phage display library was generated from llamas immunized with MCF7 cells [9]. Two rounds of selection were performed as described [9]. For selection of VHHs against tubulin, the bovine brain tubulin (Cytoskeleton) was directly coated onto 96-well NUNC Maxisorp plates (Thermo Scientific) in a series of dilutions (0; 0.1; 1; 5 µg in PBS) by incubation for 30 min at RT and then overnight at 4°C. Phages retrieved from the phage-glycerol stock were preincubated with 2% milk-PBS for 30 min at RT, and added to the tubulin-coated wells and kept at RT on a shaker for 2h. Afterwards wells were washed extensively with 0.05% Tween-20 in PBS. Bound phages were eluted with 100 µl/well of 0.1M triethylamine followed by recovery via infection of *E.coli* TG1. Phages from the first round were subjected to the second round of selection with 0, 0.1, 1 or 5 µg of coated tubulin. *E.coli* TG1 were infected with the phages from the second selection and plated on LB-Agar plates supplemented with ampicillin. 96 random colonies were picked for testing. Expression of VHHs targeted to the bacterial periplasm was induced by addition of 1 mM IPTG at 37°C overnight. To obtain the periplasmic fraction, bacterial pellets were resuspended in 10 volumes of PBS (pH 7.4) containing protease inhibitor cocktail (Roche), subjected to two freeze/thaw cycles, and spun down for 15 min at 4600 rpm. Periplasm was collected as supernatant fraction. Specificity of VHHs for tubulin was determined by ELISA.

VHH#2 expression and purification

For efficient bacterial expression, four of the most successful and divergent VHH sequences were directly subcloned from pUR8100 into modified pET28a-EPEA vector using SfiI/NotI restriction sites. pET28a-EPEA was created inserting AAACAAAGYQDYEPEA – STOP sequence (NotI/XhoI) in front of the C-terminal 6xHis-myc sequence which allows purification with Capture Select C-tag matrix (Life Technologies). Although all of the constructs were expressed and purified, from now on, we focused on one of the VHH sequences showing the best performance during protein production and labeling (Clone H, i.e. VHH#2).

For protein production, an overnight culture of *E. coli* BL21(DE3) transformed with pET28a-VHH#2-EPEA was grown in LB supplemented with kanamycin till $OD_{600} \approx 0.8$ and induced with 0.5 mM Isopropyl β-D-1-thiogalactopyranoside (IPTG) for 4 h at 25°C or at 20°C overnight. VHHs were purified from the periplasmic fraction in PBS (pH 7.4)

containing 0.5% Triton-X100, protease inhibitor cocktail (Roche) and 0.5 mM TCEP and purified using Capture Select C-tag matrix according to the manufacturer's instructions (Life Technologies). Bound VHH was eluted from the beads in buffer containing 2 M MgCl₂, 20 mM Tris-HCL (pH 7.0) and immediately dialyzed against PBS (pH 7.4). Impurities were removed by size exclusion chromatography performed on an ÄKTA FPLC system (ÄKTA purifier, GE Healthcare, UK) using a Superdex 75 gel filtration column. Fractions containing VHH#2 were pooled and upconcentrated to 1-1.5 µg/µl.

Cell culture and immunostaining

COS-7, MRC5 or Ptk2 cells were plated on 19 mm diameter glass coverslips or 8-well Labtek chambers (Thermo scientific) respectively and cultured in DMEM/Ham's F10 (50/50%) medium supplemented with 10% FCS and 1% penicillin/streptomycin for 2-3 d. Culturing of primary neurons was described before [10]. Briefly, hippocampal primary neurons were prepared from embryonic day 18 rat brains. Cells were plated on coverslips coated with poly-L-lysine (30mg/ml) and laminin (2mg/ml) at a density of 40,000/well. Hippocampal cultures were grown in Neurobasal medium (NB) supplemented with B27, 0.5 µM glutamine, 12.5 µM glutamate and penicillin/streptomycin. For optimal microtubule imaging, cells were pre-extracted and fixed in extraction buffer containing 80mM PIPES (pH 6.9), 7mM MgCl₂, 1mM EGTA, 0.3% Triton-X100 (Sigma-Aldrich), 150mM NaCl, 5 mM glucose, 0.25% glutaraldehyde (Electron Microscopy Sciences) for 90 s at 37°C and then in PBS with 4% PFA and 4% sucrose for 10 min at 37°C. After fixation, cells were washed 2 times in PBS and cells were further permeabilized for 10 min in PBS with 0.25% Triton-X100. Cells were then washed 3 times in PBS, quenched for 10 min with 50mM NH₄Cl in PBS, washed again and incubated with Image-IT (Molecular Probes) for 30 min at RT. After 3 washes with PBS, blocking buffer 1 (used for staining with antibody and VHH#2) containing 2% w/v 2% w/v BSA-c[™] (Aurion) [11], 0.2% w/v gelatin, 10 mM glycine, 50 mM NH₄Cl in PBS (pH 7.4) or blocking buffer 2 (used for VHH#1, also works for VHH#2) containing 10% FHS (Gibco, Life Technologies) and 0.1% Triton-X-100 in PBS (pH 7.4) was added for 30-45 min. Primary antibodies or VHHs were diluted in corresponding blocking buffer and were incubated overnight at 4°C (antibody) or one-two days at RT (VHHs). For the secondary antibody labeling, coverslips were washed from the primary antibody and anti-mouse antibody conjugated to AF647 were diluted in a same blocking buffer and added for 1-1.5 hours at RT. Antibody were α-tubulin (Sigma-Aldrich, clone B-5-1-2, T5168) conjugated to AF647 (dilution 1:100), AF647 conjugated goat anti-mouse IgG (H+L) secondary antibody (Molecular Probes[®], Life Technologies[™], dilution 1:500). VHH#1 and VHH#2 were diluted to about 10 µg/ml. All coverslips were extensively washed with PBS shortly before imaging, post-fixed in PBS with 4% PFA and 0.25% GA for 10 min at RT and again extensively washed with PBS. For co-staining with F-actin marker, neurons already labeled with VHH#1-AF647 were washed in PBS and incubated with AF568 Phalloidin from Molecular probes (Life Technologies[™], 1:200 in PBS) for 20 min, extensively washed in PBS and mounted for imaging. For live staining with SiR-tubulin [8], 100 nM of the

probe was added to the growth medium and incubated for 1 hour at 37°C, 5% CO₂. MRC5 cells expressing plus-end microtubule marker EB3-GFP were used for the life imaging. COS7 cells were fixed with standard pre-extraction/fixation protocol (see above), mixture of 3% PFA and 1% glutaraldehyde for 10 min at 37°C or 4% PFA for 10 min at 37°C. Fixed cells were extensively washed in PBS and processed for imaging.

Ptk2 cells were fixed at 37°C using pre-warmed PEM buffer (15 mM PIPES pH 7, 1 mM MgCl₂, 10 mM EGTA) containing 0.1% Triton X-100 and 0.4% glutaraldehyde for 10 min. They were washed 3 times with PBS, incubated with PBS containing 50 mM NH₄Cl for 10 minutes, washed twice with PBS, incubated with freshly-prepared PBS with 0.1 mg/ml sodium borohydride for 5 min, washed three times with PBS, incubated with Image-IT blocking solution (Life Technologies™) for 30 min, washed three times with PBS, and then incubated with blocking buffer 2. Labeled VHH#1 nanobody was then added to a final concentration of 600 nM, and the cells incubated overnight at 25°C (note that similar labeling was obtained with a four hour incubation). The cells were then washed three times with PBS containing 0.1% Triton X-100, and twice with PBS and processed for imaging.

***In vitro* microtubule bundling assay**

Rhodamine labeled MTs were prepared from stabilized seeds as described earlier [12] and stored at -80°C. HiLyte™ Fluor 647-tubulin was purchased from Cytoskeleton and HiLyte™ Fluor 647-MT seeds were made in a same way like Rhodamine-MT seeds. The seeds were quickly transferred into a 37°C water bath, incubated for 5 min and kept in the dark at RT for 24 h. Labeled MTs were diluted 1:30 in PEM80 (80 mM PIPES, pH 6.9, 2 mM MgCl₂, 1 mM EGTA) containing 10 μM of Taxol (Sigma). Then 50 μl of this dilution was mixed with 0.2 ng of recombinant purified GFP-AtMAP65-1 [6] and incubated for 20 min at RT to allow formation of bundles. Imaging flow chambers were assembled using microscope slides and coverslips connected with double-sided tape. Before each experiment coverslips were plasma cleaned for 10 min, coated for 1 min with 0.4% diethylenetriamine (DETA) diluted in H₂O and baked for 1 hour at 200°C. MTs with and without GFP-AtMAP65-1 were washed into the flow channels and kept in dark. After 20 minutes, unbound microtubules were washed out with PEM80 containing 1 μM Taxol. For the immunostainings, attached Rhodamine-MTs were first fixed for 3 minutes with 4% PFA and 0.25% GA in PEM80, washed with PEM80 containing 1 μM Taxol, quenched for 10 min with 50 mM NH₄Cl in PBS, washed again and unspecific binding of proteins to the surface was blocked with blocking buffer 1 for 30 min at RT. Samples intended for staining with VHH#1 were in addition blocked with Image-IT for 30 minutes and then blocked with blocking buffer 2 (see above). Primary AF647-labeled anti-α-tubulin antibody (1:20), VHH#1 (10 ng/μl) or VHH#2 (10 ng/μl) were diluted in corresponding blocking buffer, added to the flow channels and incubated in RT for 2 h in the dark. Stained samples were post-fixed for 3 min with 4% PFA and 0.25% glutaraldehyde in PEM80, washed with PEM80 and imaged immediately.

SMLM imaging

Imaging of fixed cells stained with MT probes conjugated to AF647 was performed using 10-100 mM MEA, 5% w/v glucose, 560 mg/ml glucose oxidase, 40 mg/ml catalase in PBS. Imaging mixture for *in vitro* MT samples contained 100 mM mercaptoethylamine (MEA), 5% w/v glucose, 560 mg/ml glucose oxidase, 40 mg/ml catalase in PEM80 containing 1 μ M Taxol.

SMLM microscopy [13-15] was performed on a Nikon Ti microscope equipped with a 100x Apo TIRF objective (NA. 1.49), a Perfect Focus System and an additional 2.5x Optovar to achieve an effective pixel size of 64 nm. Evanescent or oblique laser illumination was achieved using a custom illumination pathway with a 15 mW 405 nm diode laser (Power Technology), a 50 mW 491 nm DPSS laser (Cobolt Calypso), and a 40 mW 640 nm diode laser (Power Technology). Fluorescence was detected using an Andor DU-897D EMCDD camera. All components were controlled by Micromanager software [16]. For SMLM imaging of AF647, the sample was continuously illuminated with 640 nm wavelength light. In addition, the sample was illuminated with 405 nm light at increasing intensity to keep the number of fluorophores in the fluorescent state constant. Typically 5,000 – 15,000 frames were recorded per acquisition with exposure times of 30-40 ms.

SMLM imaging of Ptk2 cells was performed as described [17]. Imaging chambers were filled with Buffer TN (50 mM Tris-HCl pH 8, 10 mM NaCl) containing 10% glucose, 10 mM MEA (pH adjusted to 8 with KOH; Sigma), 40 μ g/mL catalase (Sigma, C40-100MG), and 0.5 mg/mL glucose oxidase (Sigma, G2133-50KU), and sealed with a coverslip. Imaging was performed using a standard Nikon NSTORM microscope, using a 647 nm laser adjusted to provide total internal reflection-based illumination. Videos were acquired using an iXon EMCCD (Andor) and a 100 Hz frame rate, with a typical acquisition containing 50,000-100,000 frames. A 488-nm laser was sometimes used to increase the rate at which the AF 647 molecules exited the dark state; however this was typically not necessary. Acquisitions were then processed to create super-resolution images using custom-written software [3] (Figure 2 and Figure S4B). For 3D-SMLM, we use the biplane method as described [3,18].

SMLM Localization and Rendering Algorithms

For Figure 1 and Figures S3 and S4A, we used localization software written in Java as an ImageJ plugin, called Detection of Molecules (DoM). Each image in an acquired stack was convoluted with the two-dimensional Mexican hat kernel matching the microscope's point spread function (PSF) size. The intensity histogram of the convolved image was fitted to a Gaussian distribution and used to calculate the threshold intensity value (mean value of the fit plus three standard deviations). The maximum intensity values within individual spots were chosen as initial positions for the peaks' fitting performed on the original image. We used unweighted nonlinear least squares fitting with Levenberg-Marquardt algorithm to the assumed asymmetric two-dimensional Gaussian PSF.

Only fits with a calculated width within $\pm 30\%$ of the measured PSF's standard deviation were accepted. Localizations within one pixel distance in a number of successive frames were considered to arise from the same molecule. In this case the weighted mean was calculated for each coordinate, where weights were equal to inverse squared localization precision. The resulting table with molecule coordinates and precision was used to render the final localization image with 5 nm pixel size for MT FWHM analysis, and 10 or 20 nm pixel size otherwise. Each molecule was plotted as a 2D Gaussian with integrated intensity equal to one and with standard deviations equal to the localization precision. SMLM-localization and rendering of 3D-data into images was done as described before [3].

Analysis of superresolution images

To estimate the FWHM of the microtubules, line region of interests (ROI) were drawn by hand on the microtubules in the reconstructed image. A custom-made ImageJ macro was then used to generate an intensity profile perpendicular to the ROI, integrating the intensity values over a length of 500 nm. A Gaussian distribution was fitted to the intensity profile, from which the FWHM was derived as $FWHM = 2\sqrt{2\log 2} \times \sigma$.

In order to calculate the probability of separately resolving two microtubule profiles, all profiles used for FWHM calculation were normalized along the y-axis to an area under the curve of 1 and centered on the x-axis on the mean derived from the Gaussian distribution fit. To allow for subpixel shifts, bicubic interpolation was applied to the intensity profiles. Two profiles were randomly selected and positioned with their centers a distance between 5 and 125 nm apart from each other. The profiles were summed, and the dip in intensity between the two peaks was calculated. If this dip was greater than 25% of the intensity of the lowest peak, the two profiles were considered to be resolved. After 250 iterations with different randomly selected profiles, the distance between the means was increased by 0.5 nm and the procedure was repeated. At each position, the ratio between resolved and non-resolved sets of intensity profiles was used to calculate the resolving probability. All analysis was performed in the open source software package R.

An independent estimate of image resolution was obtained using Fourier Ring Correlation (FRC), as described previously [7]. In short, particle tables generated by DoM were converted to tables with only x- and y-coordinates for each localization remaining. The FRC plug-in for ImageJ created by the Delft University of Technology Quantitative Imaging Group was then used to obtain a resolution estimate. To obtain consistent results, it was essential to perform frame-to-frame fluorophore linking (see above, Figure S5).

Additional information about methods used for purification and labeling of the antibody fragments F2C and SIIB, ELISA assay, determination of nanobody specificity, conjugations of fluorophores as well as microtubule labeling simulations can be found in the Supplementary Information.

ACKNOWLEDGEMENTS

We thank Amol Aher for preparing stabilized MT seeds, Jérémie Gaillard for AtMAP65 purification, Rachid El Khoulati for providing the pET28a-EPEA vector, Roderick Tas for technical support, and Elly van Donselaar for advice.. This research is supported by the Dutch Technology Foundation STW, which is part of the Netherlands Organisation for Scientific Research (NWO). Additional support came from NWO (NWO-ALW-VICI to C.C.H and NWO-ALW-VIDI to L.C.K.) and the European Research Council (ERC Starting Grant to L.C.K.), CTMM (Mammoth project to MK and PvBeH). M.M. is recipient of a European Molecular Biology Organization (EMBO) Long-Term Fellowship (EMBO ALTF 884-2011) and Marie Curie IEF (FP7-PEOPLE-2011-IEF). The Swiss National Fund (H.E., K.F.). F.O. acknowledges the support from the Deutsche Forschungsgemeinschaft Center for Molecular Physiology of the Brain/Excellence Cluster 171, Göttingen, Germany. Support to MV came from CNRS (Centre National de la Recherche Scientifique).

AUTHOR CONTRIBUTIONS

HE and LK conceived the project (independently). Marina M developed VHH#2, together with MK, MS and PvBeH, who provided the MRC7 library. KF, HE, FP and SM developed VHH#1. Manuel M and FO produced scFvs. MM, BMCC, RvdB, and KF performed experiments and analyzed data. BMCC performed experiments and analyzed data for Figures 1G, S3, and S4A, and partly prepared and analyzed data for Figure 2B,C. JT and EK developed simulations. MV contributed AtMAP65. CH, HE and LK supervised the project.

REFERENCES

- 1 Kapitein, L. C. & Hoogenraad, C. C. Which way to go? Cytoskeletal organization and polarized transport in neurons. *Mol Cell Neurosci* 46, 9-20 (2011).
- 2 Chen, J., Kanai, Y., Cowan, N. J. & Hirokawa, N. Projection domains of MAP2 and tau determine spacings between microtubules in dendrites and axons. *Nature* 360, 674-677 (1992).
- 3 Ries, J., Kaplan, C., Platonova, E., Eghlidi, H. & Ewers, H. A simple, versatile method for GFP-based super-resolution microscopy via nanobodies. *Nat Methods* 9, 582-584 (2012).
- 4 Royle, S. J. Super-duper resolution imaging of mitotic microtubules. *Nat Rev Mol Cell Biol* 16, 67 (2015).
- 5 Nizak, C. et al. Recombinant antibodies against subcellular fractions used to track endogenous Golgi protein dynamics in vivo. *Traffic* 4, 739-753 (2003).
- 6 Gaillard, J. et al. Two microtubule-associated proteins of Arabidopsis MAP65s promote antiparallel microtubule bundling. *Mol Biol Cell* 19, 4534-4544 (2008).
- 7 Nieuwenhuizen, R. P. et al. Measuring image resolution in optical nanoscopy. *Nat Methods* 10, 557-562 (2013).
- 8 Lukinavicius, G. et al. Fluorogenic probes for live-cell imaging of the cytoskeleton. *Nat Methods* 11, 731-733 (2014).
- 9 Kijanka, M. et al. Rapid optical imaging of human breast tumour xenografts using anti-HER2 VHHs site-directly conjugated to IRDye 800CW for image-guided surgery. *European journal of nuclear medicine and molecular imaging* 40, 1718-1729 (2013).
- 10 Kapitein, L. C., Yau, K. W. & Hoogenraad, C. C. Microtubule dynamics in dendritic spines. *Methods Cell Biol* 97, 111-132 (2010).
- 11 Kijanka, M. Development of HER2-targeted nanobodies for molecular optical imaging and therapy of breast cancer PhD thesis, Utrecht University, dspace.library.uu.nl/handle/1874/298483 (2014)
- 12 Mohan, R. et al. End-binding proteins sensitize microtubules to the action of microtubule-targeting agents. *Proc Natl Acad Sci U S A* 110, 8900-8905 (2013).
- 13 Betzig, E. et al. Imaging intracellular fluorescent proteins at nanometer resolution. *Science* 313, 1642-1645 (2006).
- 14 Heilemann, M. et al. Subdiffraction-resolution fluorescence imaging with conventional fluorescent probes. *Angew Chem Int Ed Engl* 47, 6172-6176 (2008).
- 15 Rust, M. J., Bates, M. & Zhuang, X. Sub-diffraction-limit imaging by stochastic optical reconstruction microscopy (STORM). *Nat Methods* 3, 793-795 (2006).
- 16 Edelstein, A., Amodaj, N., Hoover, K., Vale, R. & Stuurman, N. Computer control of microscopes using microManager. *Current protocols in molecular biology* / edited by Frederick M. Ausubel ... [et al.] Chapter 14, Unit14 20 (2010).

- 17 Dempsey, G. T., Vaughan, J. C., Chen, K. H., Bates, M. & Zhuang, X. Evaluation of fluorophores for optimal performance in localization-based super-resolution imaging. *Nat Methods* 8, 1027-1036 (2011).
- 18 Juette, M. F. et al. Three-dimensional sub-100 nm resolution fluorescence microscopy of thick samples. *Nat Methods* 5, 527-529 (2008).

SUPPLEMENTARY FIGURES

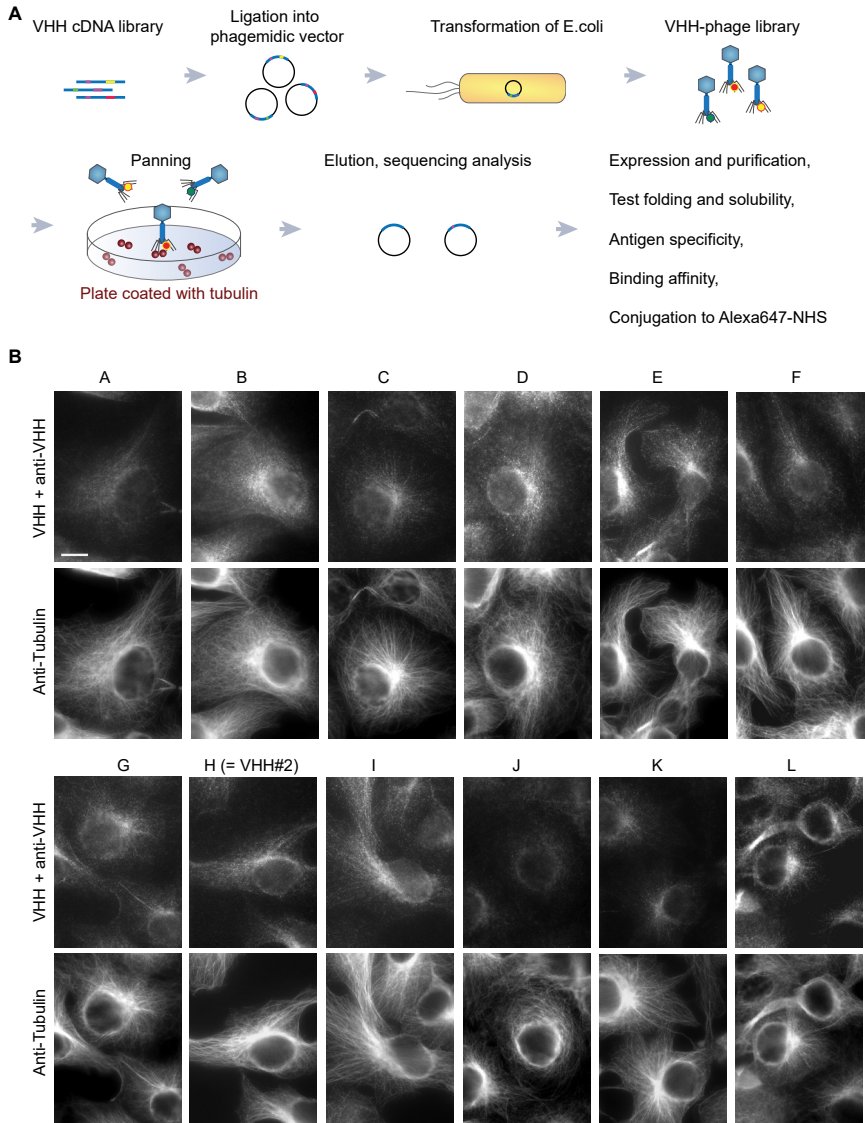


Figure S1: Nanobody selection.

A) Schematic workflow for production of tubulin nanobodies and steps required for selection and quality control of binders. For the details see Materials and methods.

B) Widefield images of COS-7 cells stained with the periplasm obtained from E. coli expressing different VHH sequences (named A-L). VHHs derived from two rounds of panning were tested by ELISA. Then the periplasmic fraction containing the strongest binders was applied on fixed COS-7 cells. Binding of VHHs was detected by immunostaining with polyclonal anti-VHH antibody and by co-localization with microtubules co-stained with mouse anti- α -tubulin antibody. VHH clone H is the same as VHH#2. Scale bars are 5 μ m.

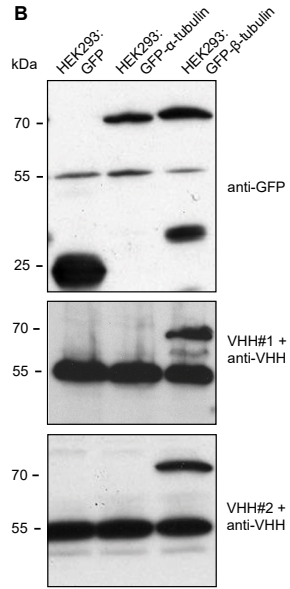
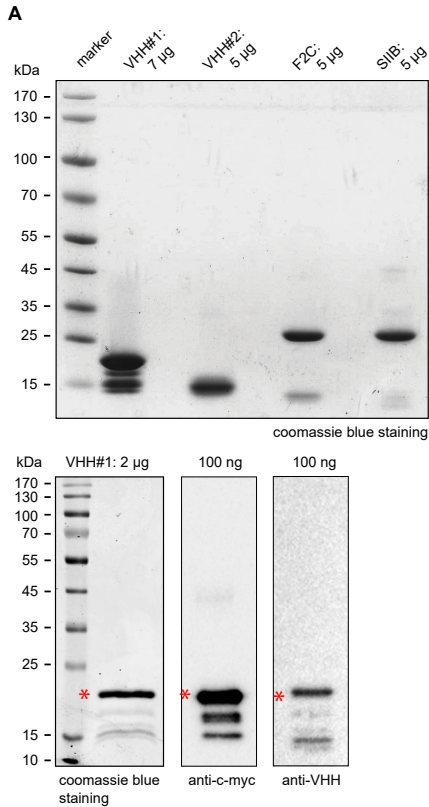


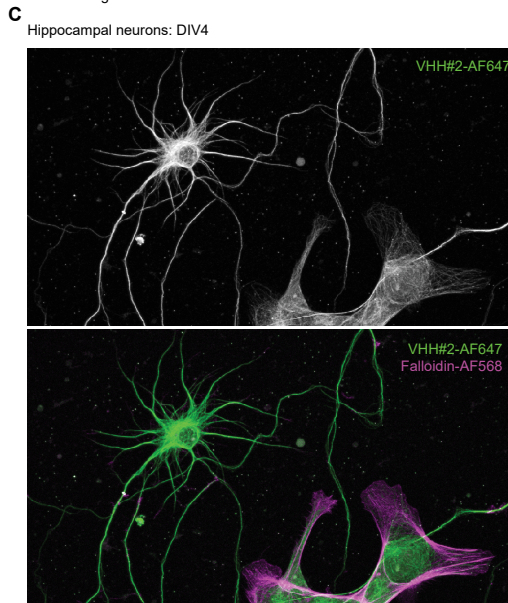
Figure S2: Biochemical properties of tubulin-binding probes.

A) Upper panel: Coomassie blue stained SDS-PAGE gel with purified VHH#1, VHH#2 and the antibody fragments F2C and SIIB. The smallest probe VHH#2 migrates at 15 kDa, followed by VHH#1 (20 kDa) and the antibody fragments (about 30 kDa). 5-7 µg of protein were loaded per lane. **Lower panel:** Coomassie blue stained SDS-PAGE gel with purified VHH#1 stored for more than four

months at 4°C and corresponding immunoblots with anti-VHH and anti-myc antibody. Red star indicates intact VHH#1-myc-6xhis band

B) Immunoblot showing that both tubulin nanobodies are directed against beta-tubulin. Lysates were prepared from HEK293 cells transfected with empty GFP plasmid, GFP-α-tubulin or GFP-β-tubulin, and stained with VHH#1, or VHH#2 followed by incubation with anti-VHH rabbit antibody. As a positive control for expression of GFP proteins, the same membranes were developed with anti-GFP rabbit antibody. VHH#1 and VHH#2 recognize the endogenous and overexpressed GFP-β-tubulin, but not GFP-α-tubulin.

C) Confocal image of DIV4 hippocampal neurons stained with VHH#2 directly labeled with AF647 and co-stained with F-actin marker Phalloidin-AF568. Note, that conjugation to AF647-NHS does not interfere with the epitope binding. Scale bar is 10 µm.



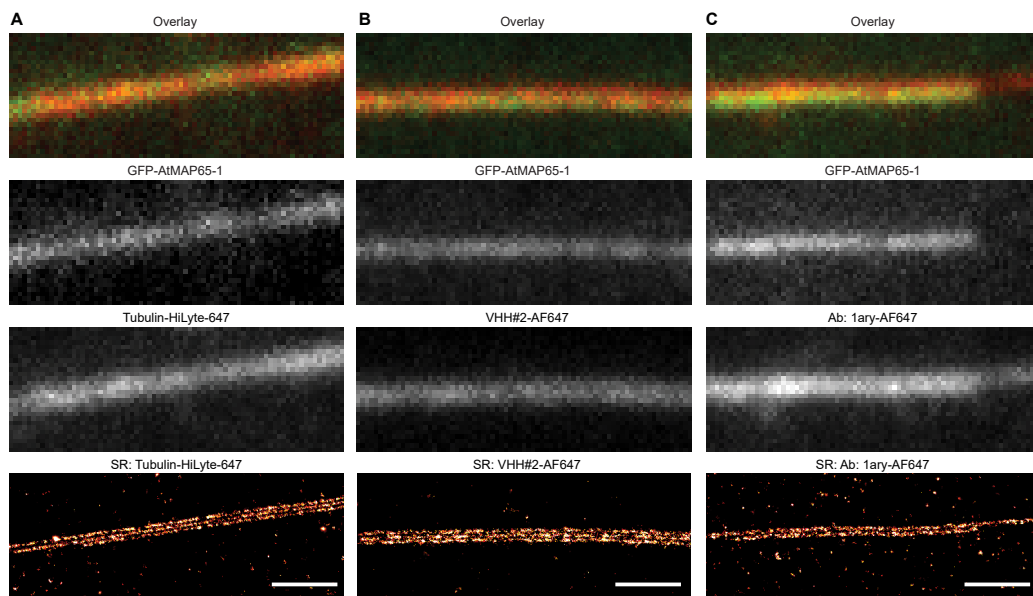


Figure S3: Examples of *in vitro* microtubule bundles resolved by dSTORM.

A-C) GFP-AtMAP65-1 bundled microtubules copolymerized with tubulin-HiLyte647 A), or copolymerized with Rhodamine-tubulin (channel is not shown) and labeled with VHH#2-AF647 B) or a conventional primary antibody (1ary) labeled with Alexa647 C). Bottom row shows SMLM reconstructions. Scale bar is 1 μm . Ab stands for antibody.

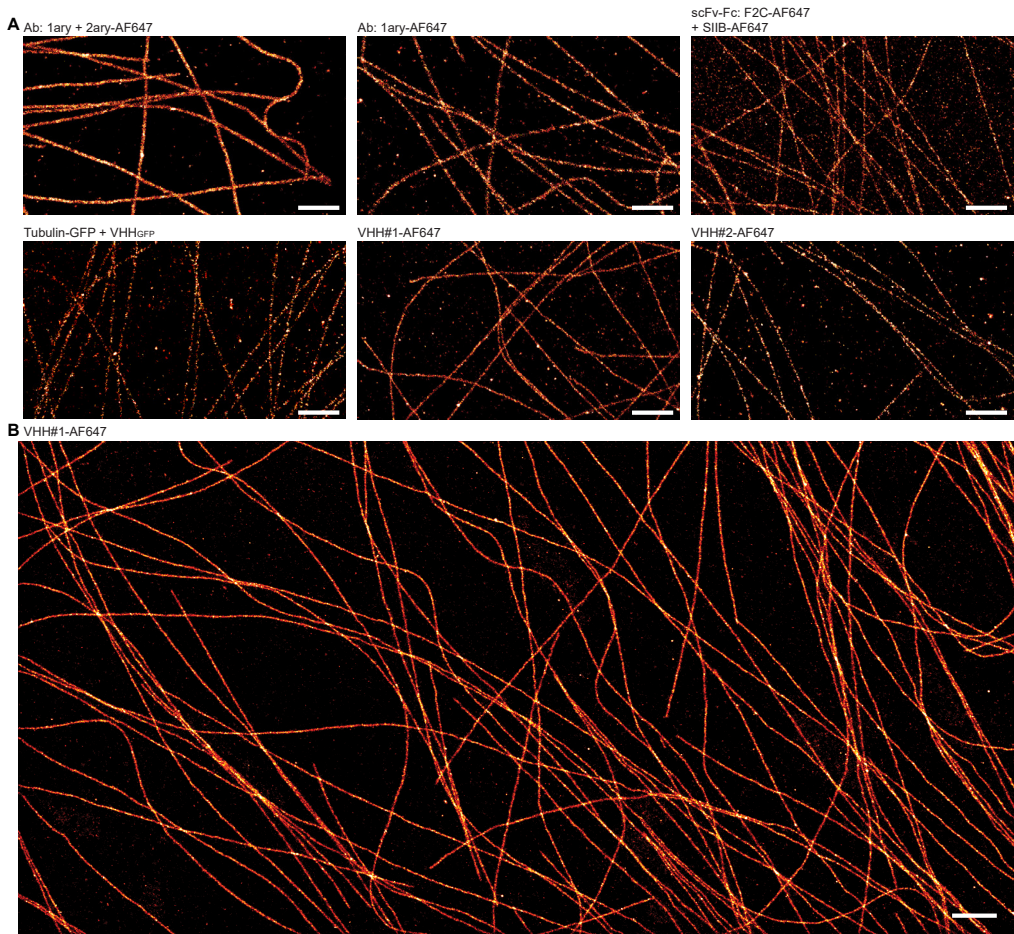


Figure S4: Examples of cellular stainings

A) Representative images of COS7 cells stained with different labels and quantified in Figure 2E). Scale bars are 1 μm . Ab stands for antibody.

B) Large field of view SMLM reconstruction of microtubules in a Ptk2-cell (also shown in Figure 2D). Scale bar is 1 μm .

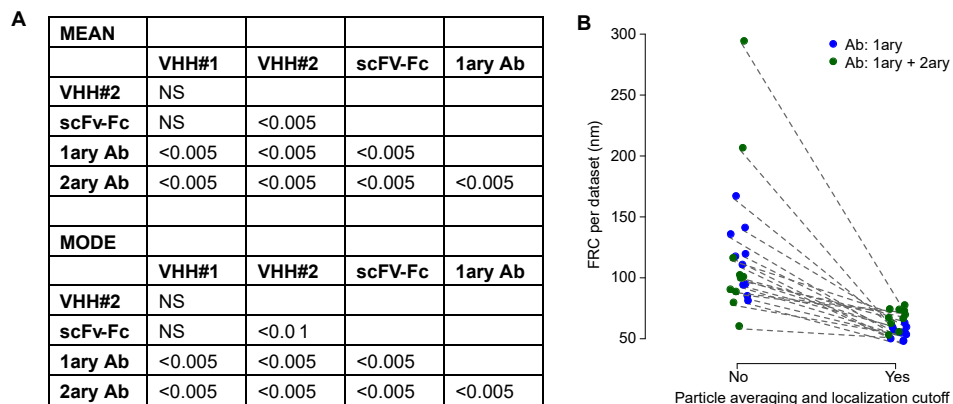


Figure S5: Significance and FRC correction effects

A) *p*-values for comparing the mean values and mode values. This was tested using the Welch Two Sample *t*-test (two-sided), and using the Bonferroni correction for testing of multiple conditions.

B) Effect of frame-to-frame fluorophore linking on the FRC resolution estimate.

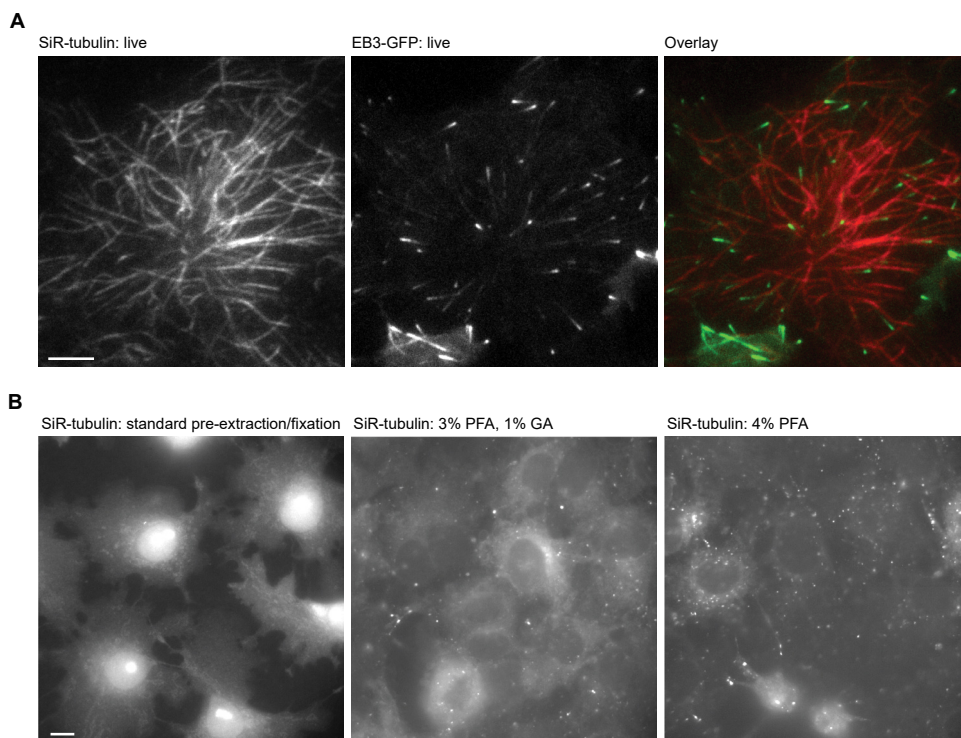


Figure S6: SiR Tubulin does not remain bound to microtubules upon fixation.

A) Still image from a live-cell recording of a MRC5 cells expressing EB3-GFP and incubated with SiR tubulin.

B) Example images of cells incubated with SiR tubulin before fixation using the indicated protocol. Scale bars are 5 μ m. GA stands for glutaraldehyde.

SUPPLEMENTARY METHODS

Purification and labeling of the antibody fragments F2C and SIIB

Human-derived single chain variable fragments (scFvs) were previously selected and characterized [1]. The antibody fragments were cloned in a custom designed plasmid (His_{14x}-ZZ-SUMO-F2C or -SIIB) and transformed into SHuffle E. coli strain for cytoplasmic expression. Bacteria were grown at 20°C in Terrific Broth medium containing 4 mM MgCl₂ and 100 µg/ml kanamycin until OD₆₀₀ reached ~1.5. Expression was induced with 0.5 mM IPTG. Flasks were shaken at 160 rpm for ~16 h at 20°C. EDTA was added to a final concentration of 0.5 mM and cultures were finally centrifuged at 6000 x g for 10 min. Bacterial pellets were resuspended in binding buffer (50 mM HEPES, 500 mM NaCl, 5 mM MgCl₂, 20 mM imidazole, 10% glycerol) supplemented 0.25 mM of PMSF before disruption by sonication on ice. Suspension was centrifuged for 60 min at 12.000 g and 4°C. Supernatants were filtered (0.45 µm pore size) and incubated for one hour at room temperature with complete His-Tag purification resin (Roche) followed by several washes as recommended by the supplier. Elution was achieved using 500 mM imidazole in binding buffer. To remove the histidine-tag, His_{14x}-ZZ-SUMO-scFvs proteins were incubated for 1 hour at room temperature with yeast-derived His_{6x}-SUMO protease (Ulp1). After specific cleavage of the SUMO-domain, antibody fragments were desalted and passed through a HisTrap 1 ml column using Äkta HPLC system to remove unwanted cleaved fragments and His_{6x}-SUMO protease. The high purity (>90%) and the untagged nature of purified scFvs were analyzed via SDS-PAGE. Antibody fragments were conjugated to AF647 using succinimidyl ester chemistry. The stock of fluorophore was dissolved in anhydrous DMSO at a final concentration of 10 µg/µl. The coupling reaction was performed in freshly prepared 100 mM NaHCO₃ buffer (pH 8.0). The reactive fluorophore was added in 6 fold molar excess to the scFvs containing solution while mixing for 1.5 h at room temperature and protected from light. Unconjugated reactive fluorophores were quenched by adding an excess of hydroxylamine (~150 mM) with subsequent mixing for 15 minutes at room temperature. Antibody fragments were efficiently separated from uncoupled dye molecules using a 14 cm column (BioRad) packed with superfine G25 sephadex resin. Elution fractions were tested by immunostainings, the best fractions were pooled and stored at 4°C adding to 0.05% sodium azide or in 50% glycerol at -20°C.

ELISA assay for determining specificity of VHHs for tubulin

A flat-bottom 96-well plate (Maxisorp) was coated with 0.1 µg of bovine brain tubulin, washed with PBS and pre-blocked with 2% milk-PBS for 30 min at RT. 10 µl of periplasm fractions in 100 µl 2% milk-PBS was added to the wells and incubated for 90 min at RT. The plate was washed twice with PBS and the primary rabbit polyclonal anti-VHH antibody ([2], 1:2000) was added for 1 h at RT in 2% milk-PBS. Plate was again washed twice with PBS and incubated with secondary donkey anti-rabbit-PO antibody (Dako, 1:5000) for 1 h at RT. After final washing steps, 100 µl/well OPD+H₂O₂ was added and the plate was incubated for 30 min at RT. The reaction was stopped with 50 µl/well of H₂SO₄ and relative VHHs presence was analyzed by measuring optical density at λ= 490 nm with an Ultramark spectrophotometer (Biorad). Monoclonal anti-α-tubulin antibody (Sigma) was used as positive control. 14 colonies showing the strongest signal were selected for further study and VHH DNA was isolated and sequenced using an M13 reverse primer.

Determination of the tubulin subunit detected by VHH#1 and VHH#2.

HEK293 cells were plated on 10 cm² dishes and cultured in DMEM/Ham's F10 (50/50%) medium supplemented with 10% FCS and 1% penicillin/streptomycin for 2 days. Cells were transfected using MaxPEI (PolyEthylenImine, Sigma) with 10 µg of pDNA encoding for empty EGFP, β-tubulin(2C)-EGFP or α-tubulin-EGFP in β-actin vectors and grown for 48h at 37°C and 5% CO₂. Following transfection, dishes were washed with 1 ml of PBS and extracted with 500 µl extraction buffer (PBS pH 7.4, 1% TritonX-100, 2mM Ca²⁺, protease inhibitor cocktail). Cell suspensions were frozen at -80°C, thawed, incubated on ice for 2 h, and finally spun down at 13.000 rpm for 15 min. Obtained supernatants samples were loaded on 12% SDS-PAGE gels, and transferred for 90 min at 15V via semi-dry western blotting onto a PVDF membrane. The membrane was blocked with 5% milk-PBS for 1h, and incubated with VHH#1 or VHH#2 (2 µg/ml) for 4h at RT on a shaker. After PBS wash, membranes were incubated in either home-made primary rabbit anti-VHH serum 976 (1:2000 in milk-PBS; [2]) or rabbit anti-GFP antibody (1:5000 in PBS; Abcam) overnight at 4°C. Next day, another cycle of PBS wash was performed, and HRP-conjugated secondary goat anti-rabbit antibodies (Dako) were added for 60 min at RT, blots were extensively washed and processed for developing.

Conjugation of fluorophores to antibodies and VHHs

Conjugation of AF647 (Alexa Fluor® 647 Carboxylic acid, Succinimidyl Ester, Molecular Probes, Life technologies) to monoclonal anti- α -tubulin antibody (Sigma) was performed according to the protocol described before [3,4]. Some modifications were introduced for labeling of VHH. Conjugation reaction was performed in freshly prepared 100 mM NaHCO₃ buffer (pH 8.0) where the ratio of VHH:fluorophore was 1:5 for VHH#1 and 1:3 for VHH#2. Samples were incubated for 1-6 h at RT in the dark and labeled VHH was separated from non-conjugated dye by passing through a NAP25 column (GE Healthcare). Eluted VHH-AF647 was upconcentrated to 0.5-0.7 $\mu\text{g}/\mu\text{l}$, labeling efficiency was measured as described before [3]. The absorption spectrum of the preparations revealed a labeling ratio of 1.5 fluorophores per VHH#1 and 0.3 fluorophores per VHH#2. Sodium azide was then added to the mixture to a final concentration of 0.05%, and the proteins were stored at 4°C.

Microtubule labeling simulations

Generative model

Images of *in silico* microtubules were synthesized from a generative 3D model. First the main axis (backbone) of straight microtubule with a specified length was marked. The backbone segment was populated with tubulin heterodimers forming a regular 25 nm diameter 3-start helix consisting of 13 straight protofilaments. The coordinates of tubulin subunits were spaced 8 nm apart from each other along the protofilament.

Tubulin subunits were randomly labeled with fluorophores to achieve the desired probe density. If a tubulin molecule was marked as labeled, the fluorophore coordinates were generated and added to the model. The position of the fluorophore was determined by addition of the offset distance m extending outwards from the surface (i.e. in the radial direction) to the coordinates of the corresponding tubulin. A small rotation by angle φ (uniformly distributed on the interval from 10° till -10°) in the plane perpendicular to the microtubule axis was added to simulate flexibility in the binding of the antibody probe to the antigen.

To simulate widefield images, the positions of fluorophores were projected onto a 2D plane and convoluted with a 2D isometric Gaussian kernel with a standard deviation equal to that of the point spread function of the microscope. This produced a continuous 2D distribution of intensity. Further the intensity was integrated over the area of each pixel of the future image. The final pixel intensity value was drawn from the Poisson distribution with the mean equal to the integrated intensity value from the previous step, to account for the shot noise of light registration.

Simulated super-resolution microscopy images of microtubules were generated using the same rendering algorithm as for the real SMLM dataset reconstruction (see above). To account for the uncertainty in the localization of fluorescent signal during “virtual” SMLM acquisition, each fluorophore position was shifted by random displacement of magnitude d drawn from a Gaussian localization accuracy distribution with mean \pm SD of 7.5 ± 2.5 nm. If the displacement magnitude d was above a specified precision cutoff threshold t , its random value is generated again until it is below the threshold, so the probe density remains constant. An angle of displacement direction θ was drawn from a uniform random distribution covering the full 360° for each of the fluorophores. The new position of the fluorophore was used to render its image.

Dataset

The generative model was transcribed into a Matlab code and run in GNU Octave version 3.8.2 on Mac OS X 10.10.0, Intel Core i7 2.8 GHz, 16GB RAM. A dataset of images was generated where the model parameters (probe density, position of the probe and precision cutoff) varied in a wide range. The values for probe density were chosen at 0.1%, 0.3%, 1%, 5%, 7%, 10%, 15%, 30%, 50%, 75% and 100%. The values for mean probe position were chosen at 0.0, 2.5, 5.0, 7.5, 10.0 and 12.5 nm. The values for the precision cutoff threshold were chosen at 3, 5, 8, 10, and 13 nm. For each combination of the three parameters a microtubule with a contour length of 80 μm was generated. The generated microtubule was centered within the field of view before being rendered into a widefield and super-resolution image. The widefield images were generated with a pixel size of 64 nm and the standard deviation of microscope's point spread function equal to 1.8 pixels (=115.2 nm). The super-resolution images were generated with a pixel size of 4 nm. All microscopy images were exported to local storage in 16-bit gray scale TIFF image format. Intensities were uniformly scaled prior to export to take advantage of the full dynamic range of the image format.

Analysis of simulated images

The super-resolution images were sampled with a window 512 nm long (in axial direction) and 400 nm wide. The window was placed at non-overlapping intervals along the entire microtubule, resulting in 150 samples per microtubule. Empty regions (i.e. summed intensity of zero) were rejected from the analysis. This situation was particularly common for the low (<3%) probe density. An intensity line profile was derived from a sampled region by averaging the intensities along the axial direction. A 1D Gaussian function with four parameters (background level, peak amplitude, peak position, and peak width) was fitted to the intensity line profile using a Levenberg-Marquardt nonlinear regression algorithm. The regression algorithm was run for a maximum of 1000 iterations or until convergence was achieved with an accuracy of 10^{-3} . The mean and standard error of the FWHM were computed for each condition in the dataset. The FWHM was calculated from the fitted peak width as described. The analysis of the resolving probability of two microtubules was performed as described above.

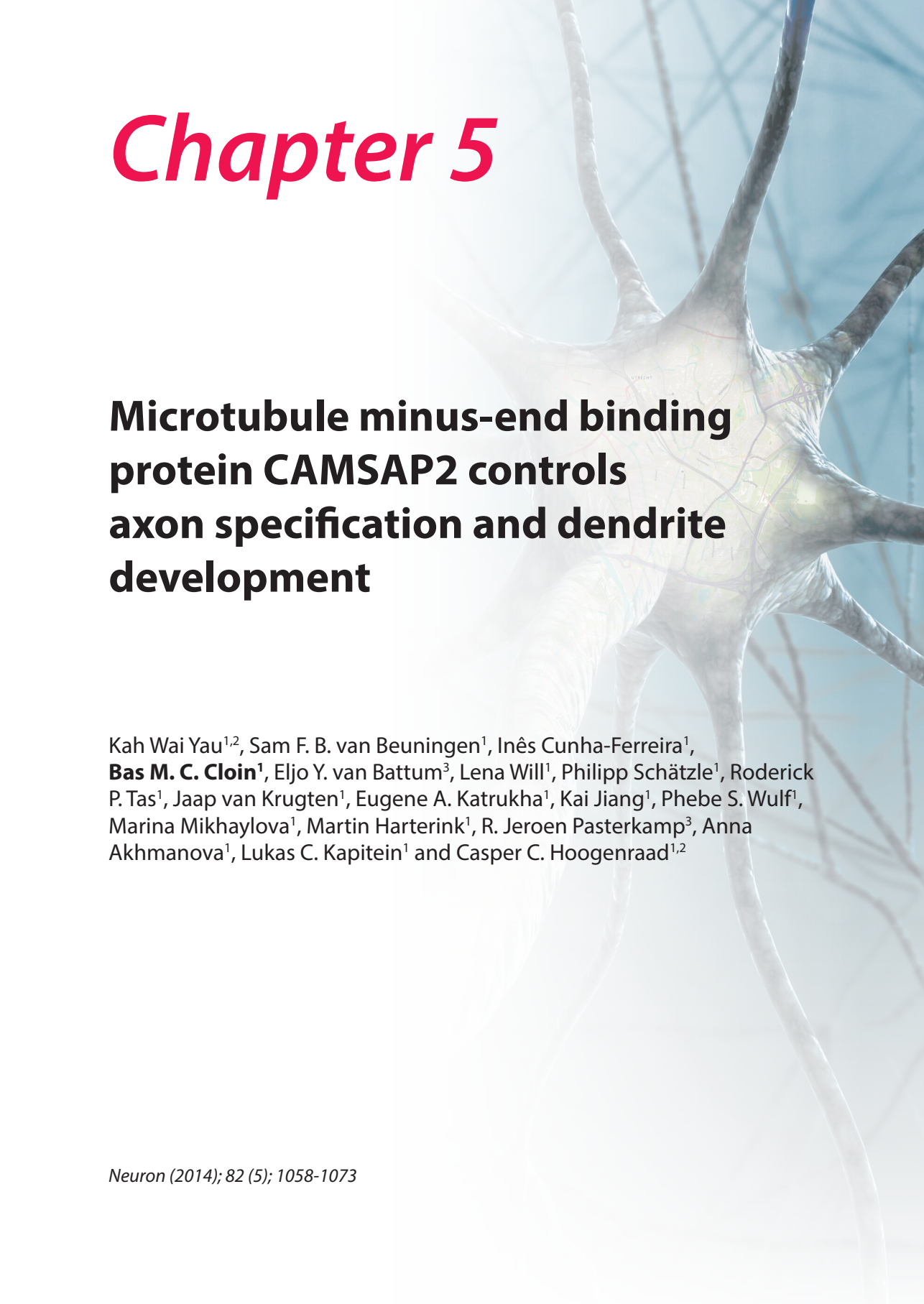
SUPPLEMENTARY REFERENCES

- 1 Nizak, C. et al. Recombinant antibodies against subcellular fractions used to track endogenous Golgi protein dynamics in vivo. *Traffic* 4, 739-753 (2003).
- 2 Kijanka, M. et al. Rapid optical imaging of human breast tumour xenografts using anti-HER2 VHHs site-directly conjugated to IRDye 800CW for image-guided surgery. *European journal of nuclear medicine and molecular imaging* 40, 1718-1729 (2013).
- 3 Cloin, B. M., Hoogenraad, C. C., Mikhaylova, M. & Kapitein, L. C. in *Immunocytochemistry and Related Techniques* Vol. 101 (eds A Merighi & L Lossi) 389-408 (Springer, 2015).
- 4 Yau, K. W. et al. Microtubule minus-end binding protein CAMSAP2 controls axon specification and dendrite development. *Neuron* 82, 1058-1073 (2014).

¹Cell Biology, Faculty of Science, Utrecht University, 3584 CH, Utrecht, The Netherlands.

²Department of Neuroscience, Erasmus Medical Center, 3015 GE Rotterdam, The Netherlands. ³Department of Translational Neuroscience, Brain Center Rudolf Magnus, University Medical Center Utrecht, 3584 CG, Utrecht, The Netherlands

Chapter 5



Microtubule minus-end binding protein CAMSAP2 controls axon specification and dendrite development

Kah Wai Yau^{1,2}, Sam F. B. van Beuningen¹, Inês Cunha-Ferreira¹, **Bas M. C. Cloin**¹, Eljo Y. van Battum³, Lena Will¹, Philipp Schätzle¹, Roderick P. Tas¹, Jaap van Krugten¹, Eugene A. Katrukha¹, Kai Jiang¹, Phebe S. Wulf¹, Marina Mikhaylova¹, Martin Harterink¹, R. Jeroen Pasterkamp³, Anna Akhmanova¹, Lukas C. Kapitein¹ and Casper C. Hoogenraad^{1,2}

ABSTRACT

In neurons, most microtubules are not associated with a central microtubule-organizing center (MTOC) and therefore both the minus and plus-ends of these noncentrosomal microtubules are found throughout the cell. Microtubule plus-ends are well established as dynamic regulatory sites in numerous processes, but the role of microtubule minus-ends has remained poorly understood. Using live-cell imaging, high-resolution microscopy and laser-based microsurgery techniques, we show that the CAMSAP/Nezha/Patronin family protein CAMSAP2 specifically localizes to noncentrosomal microtubule minus-ends and is required for proper microtubule organization in neurons. CAMSAP2 stabilizes noncentrosomal microtubules and is required for neuronal polarity, axon specification and dendritic branch formation *in vitro* and *in vivo*. Furthermore, we found that noncentrosomal microtubules in dendrites are largely generated by γ -Tubulin-dependent nucleation. We propose a two-step model in which γ -Tubulin initiates the formation of noncentrosomal microtubules and CAMSAP2 stabilizes the free microtubule minus-ends in order to control neuronal polarity and development.

INTRODUCTION

Neurons are polarized cells that critically depend on the microtubule (MT) cytoskeleton for their development and function. Mutations in different Tubulin genes cause a range of nervous system abnormalities and several neurological and neurodegenerative diseases have been linked to altered MT-based transport processes [1,2]. MTs, which serve as tracks for long-distance transport to axons and dendrites, are polarized structures with two distinct ends, the plus and minus-ends [3]. Most plus-ends are highly dynamic, whereas minus-ends are believed to be much more stable. Control of MT plus-end dynamics, often by plus-end associated proteins, has recently been shown to play an important role in determining neuronal polarity and in regulating dendritic spine morphology and synaptic plasticity [4]. In contrast, little is known about the functions of neuronal MT minus-ends and potential minus-end associated proteins.

In many cell types, most MT minus-ends are anchored and stabilized at a MT-organizing center (MTOC), most often the centrosome [5]. However, neuronal cells do not rely entirely on centrosomal MT nucleation. *Drosophila* neurons lacking an active centrosomes display a normal MT network and have proper axon outgrowth and neuronal organization [6,7]. In addition, electron microscopy studies in sympathetic rat neurons show that most neuronal MTs are not anchored by the centrosome and do not form large radial arrays [8]. More recent experiments found that during neuronal development the centrosome loses its function as an MTOC [9]. Noncentrosomal MTs can be generated by two distinct mechanisms: severing of pre-existing MTs or local nucleation at noncentrosomal sites, such as cortical γ -Tubulin complexes [10-12]. Depletion of the MT severing enzymes katanin and spastin was found to alter axonal growth in young neurons [13]. MT nucleation at noncentrosomal sites has been reported to occur on Golgi membranes [14]. Additionally, a recent study in *Drosophila* neurons reports that Golgi outposts in dendrites locally nucleate MTs and shape dendrite morphology [15].

Regardless of the precise mechanisms of noncentrosomal MT formation, in a sequential step the newly generated MT minus-end must be stabilized in order to prevent depolymerization [10,16]. Recently, a MT minus-end binding protein, called Patronin, was found to protect MT minus-ends in *Drosophila* cells from depolymerization [17]. Three mammalian homologs of Patronin, calmodulin-regulated spectrin-associated protein 1-3 (CAMSAP1-3) have been identified [18]. CAMSAP3/Nezha localizes at MT minus-ends close to adherent junctions in epithelial cells [19]. Moreover, CAMSAP3/Nezha and CAMSAP2 cooperate in determining the overall growth pattern of MTs in epithelial cells [20] and recent *in vitro* experiments revealed that CAMSAP proteins associate with growing MT minus-ends and regulate their dynamics [21]. Nevertheless, whether these proteins also contribute to the establishment and maintenance of noncentrosomal MT arrays in developing and mature neurons has remained unresolved.

In this study we use a combination of cell-biological approaches, quantitative/high-resolution microscopy, laser microsurgery, *in utero* electroporation and organotypic slice cultures to determine the role of CAMSAP2 during neuronal polarity and development.

We show that CAMSAP2 localizes to the MT minus-ends in axon and dendrites, stabilizes noncentrosomal MTs and is required for axon specification, dendritic branch formation and BDNF-induced dendritic outgrowth. Together, these results reveal a new mechanism for stabilizing neuronal MTs and reveal a critical role for CAMSAP2 in axon specification and dendrite development.

RESULTS

Distinct CAMSAP2-decorated structures are present in hippocampal neurons

Little is known about the expression and distribution of the CAMSAP minus-end binding protein family in neurons. According to the *in situ* hybridization data from the Allen Mouse Brain Atlas and proteomics dataset from the Human Protein Atlas project, CAMSAP2 is the most abundant family member in the hippocampus. Consistent with these data, Western blot analysis of the three CAMSAP family members in the developing and mature hippocampus revealed that CAMSAP2 is the most abundant family member whereas CAMSAP1 and 3 could not be detected (Figure 1A). The CAMSAP2 antibody is specific for CAMSAP2, as it does not recognize the other CAMSAP family members (Figure 1B). Immunocytochemistry of mature hippocampal neurons at *in vitro* day 21 (DIV 21) with CAMSAP2 antibodies revealed a variety of small clusters and distinct (punctated) stretches, scattered throughout the cell body, axon and dendritic shaft as revealed by the axonal marker Tau and dendritic marker MAP2 (Figure 1C). Similar results were obtained by immunostaining of two other CAMSAP2 antibodies and by low level expressing of GFP-tagged CAMSAP2 in neurons (Figure 1D and Figure S1). CAMSAP2 stretches were found within the soma, axon and dendritic shaft (Figure 1C and Figure S1). CAMSAP2 was absent from the actin-rich dendritic spines, showing minimal overlap with the synaptic marker Bassoon (Figure 1F and Figure S1) and lacked a significant degree of colocalization with the diffuse γ -Tubulin protein (Figure 1E and Figure S2A).

Next, we analyzed endogenous CAMSAP2 in different stages of developing hippocampal neurons (from DIV 0-14) by immunostaining. The centrosome of young neurons (DIV 0-1),

Figure 1: CAMSAP2 distribution in mature hippocampal neurons

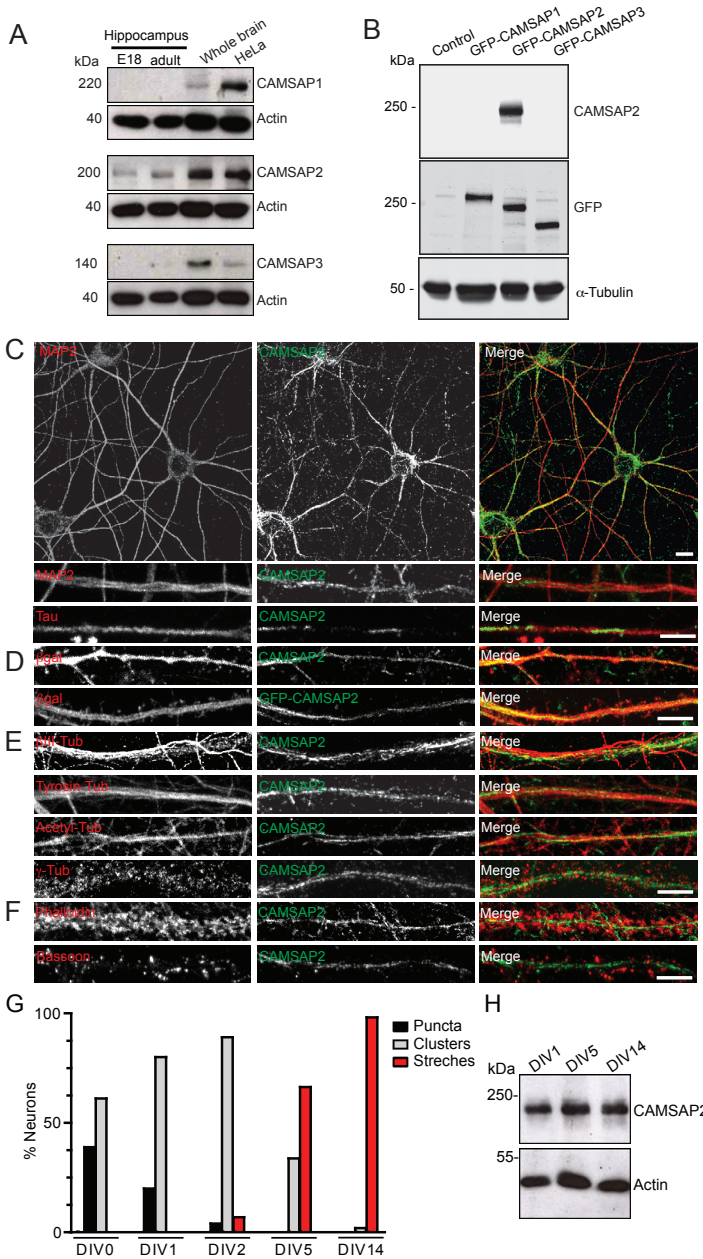
A) Extracts of whole hippocampus and brain of E18 embryos and adult rats were analyzed by western blot with indicated antibodies. HeLa cell extracts were used as a positive control.

B) HEK293 human cells transiently expressing indicated GFP-CAMSAP proteins were analyzed by western blot with CAMSAP2 and GFP antibodies. α -Tubulin was used as a loading control.

C) Representative confocal images of hippocampal neurons (DIV 21) stained for both endogenous MAP2 (red) or Tau (red) and CAMSAP2 (green). Dendritic segment is shown enlarged in the bottom row.

D) Representative images of dendritic segments of hippocampal neuron (DIV 21) expressing β -Galactosidase (red) to highlight neuronal morphology and either stained for endogenous CAMSAP2 (green, top) or co-transfected with GFP-CAMSAP2 (green, bottom).

E,F) Double staining in hippocampal neurons (DIV21) for endogenous CAMSAP2 (green) with markers (red) for neuronal MTs (β III-Tubulin), MT modifications (acetylated-Tubulin and tyrosinated-Tubulin), γ -Tubulin (E), actin (Phalloidin) and synapses (Bassoon) (F).



G) Quantification of CAMSAP2 stretches throughout neuronal development. CAMSAP2 structures were divided into 3 categories: (1) Puncta (approximately $\leq 1\mu\text{m}$), (2) Clusters (approximately $> 1\mu\text{m}$ and $< 10\mu\text{m}$) and (3) Stretches (approximately $\geq 10\mu\text{m}$). At least 100 neurons were analyzed per developmental stage.

H) Extracts of hippocampal neurons were prepared at the indicated time points and probed by Western blot for CAMSAP2 and actin antibodies.

detected by immunostaining for Centrin or γ -Tubulin, did not overlap with CAMSAP2 (Figure S2B). Interestingly, the size of the CAMSAP2-decorated structures changed during neuron development: CAMSAP2-positive puncta ($\leq 1\mu\text{m}$) and small clusters ($> 1\mu\text{m}$ and $< 10\mu\text{m}$) were clearly visible in young hippocampal neurons at $< \text{DIV } 5$ but less in mature cells, whereas long CAMSAP2 stretches ($\geq 10\mu\text{m}$) were abundantly present in mature neurons at $> \text{DIV } 14$ (Figures 1G and Figure S2). The total CAMSAP2 expression levels were unchanged during neuronal development (Figure 1H). Thus, distinct CAMSAP2-decorated structures are present in hippocampal neurons and the length of these structures changes during neuron development.

CAMSAP2 localizes to microtubule minus-ends in hippocampal neurons

To further study the subcellular distribution of CAMSAP2, we performed dSTORM (direct STochastic Optical Reconstruction Microscopy) imaging using neuron cultures stained for endogenous CAMSAP2 [22,23]. In dSTORM reconstructions, CAMSAP2 stretches detected using conventional microscopy were often found composed of multiple shorter puncta or clusters of variable size (Figure 2A-C). On average, 1.1 ± 0.3 CAMSAP2 puncta per μm^2 were observed in primary dendrites. To directly test whether CAMSAP2 localizes to MT ends in hippocampal neurons, we next optimized dSTORM imaging to resolve individual MTs within the crowded neuronal MT cytoskeleton. Whereas methanol fixation was required for immunolabeling of endogenous CAMSAP2, this was incompatible with sharp dSTORM imaging of MTs. In contrast, individual and continuous neuronal MTs, as well as many MT ends, could be clearly resolved using an optimized alternative fixation procedure that was compatible with GFP-based immunolabeling of GFP-CAMSAP2 (Figure 2D,E). Dual-color dSTORM imaging revealed that many individual MT ends were decorated with ~ 2 -4 GFP-CAMSAP2 puncta, which appeared as stretches in diffraction-limited images (Figure 2F). Localization to MT ends was also observed with overexpressed GFP-CAMSAP3 in hippocampal neurons, except that the stretches were typically shorter and more continuous (Figure 2G). These data demonstrate that CAMSAP2 localizes to the ends of MTs in neurons.

Figure 2: CAMSAP2 localizes to microtubule minus-ends in hippocampal neurons

A) Conventional widefield image (left) and dSTORM reconstruction (right) of a methanol-fixed neuron stained for endogenous CAMSAP2 with Atto488. Scale bar is $5\mu\text{m}$.

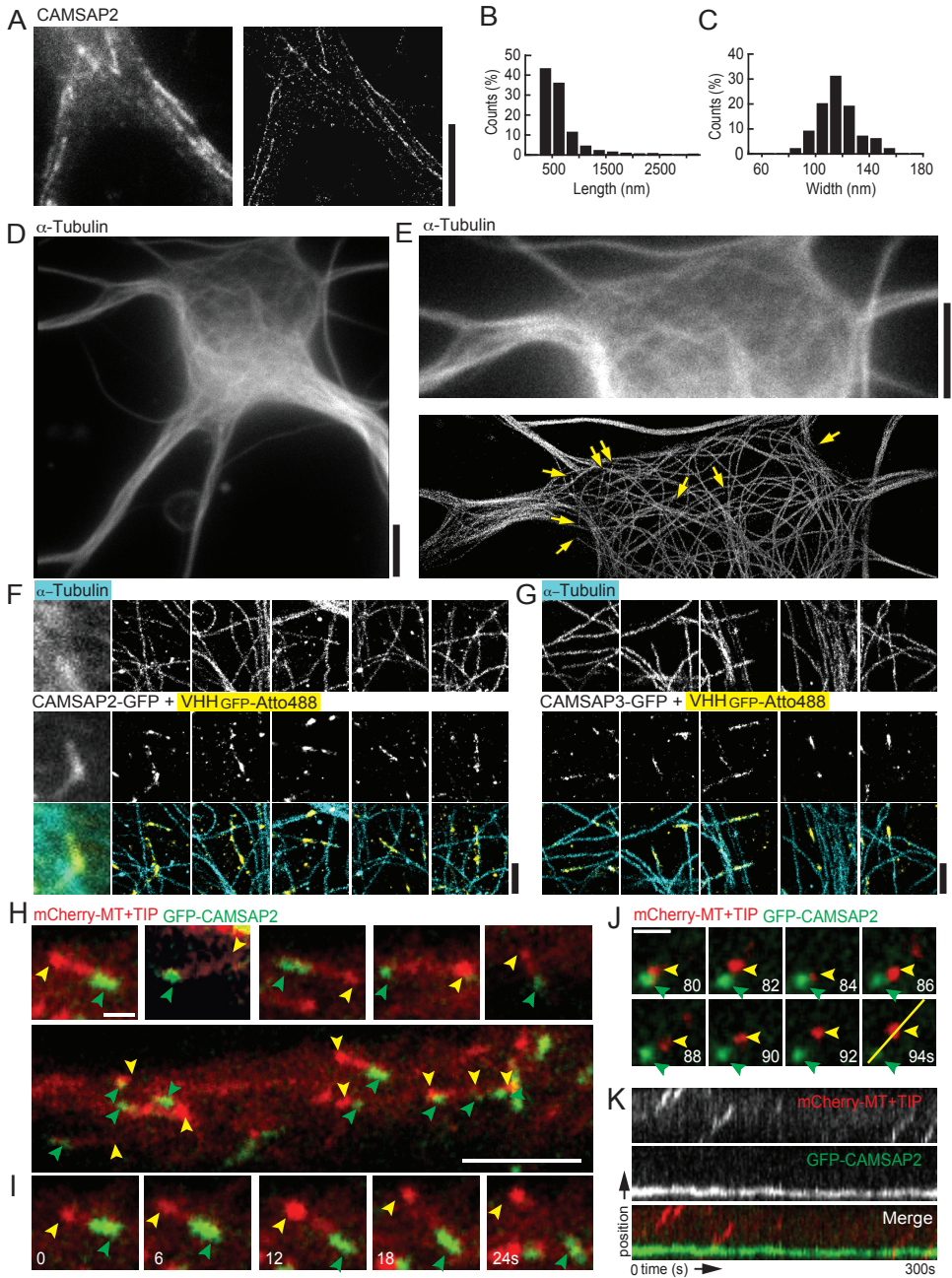
B) Distribution of stretch lengths including 316 stretches from 7 neurons.

C) Distribution of stretch widths (FWHM) based on Gaussian fitting (88 stretches from 7 neurons).

D) Conventional widefield image of a DIV 5 neuron fixed using glutaraldehyde (GA) and paraformaldehyde (PFA), and stained with an AlexaFluor647-labeled antibody against α -Tubulin.

E) Zoom of D (top) and corresponding dSTORM reconstruction (bottom), where multiple MT ends can be clearly observed.

F,G) Zooms from different DIV 5 neurons overexpressing CAMSAP2-GFP (F) or CAMSAP3-GFP (G), fixed with GA and PFA, and stained with an AlexaFluor647-labeled α -Tubulin antibody (top row) and a Atto488-labeled nanobody (VHH) against GFP (middle row). First two columns show conventional images and corresponding dSTORM reconstructions, followed by additional examples of CAMSAP2 decorated MT ends. Bottom row shows merge. Scale bars is $5\mu\text{m}$, except F,G, $1\mu\text{m}$.



H) Representative image of a dendritic segment from an hippocampal neuron (DIV 1) expressing mCherry-MT+TIP marker (red) and GFP-CAMSAP2 (green). Top row shows various examples. Yellow arrowheads indicate the MT plus-end, green arrowheads indicate the GFP-CAMSAP2 positive MT minus-end. Scale bars are 1 and 5 μ m.

I, J) Stills from TIRFM time-lapse recording of DIV 1 (**I**) and DIV 5 (**J**) neuron similar to **H**). Scale bar is 1 μ m.

K) Kymograph of the yellow line (2.5 μ m) shown in **J**).

To determine whether CAMSAP2 localizes to MT minus-ends, we expressed GFP-CAMSAP2 in COS7 cells together with mCherry- α -Tubulin and analyzed MT dynamics using TIRF microscopy. Consistent with previous observations [20], GFP-CAMSAP2 was specifically localized to one end of noncentrosomal MTs (Figure S3). The other end of these MTs alternated between rapid periods of growth and shrinkage, which is characteristic of MT plus-ends suggesting that CAMSAP2 indeed enriches near the MT minus-end (Figure S3B and Movie S1). In addition, CAMSAP2 and the MT plus-end marker mCherry-MT+TIP were distributed differently along noncentrosomal MTs. The two proteins were localized at the opposite ends of the MT with the displacement of plus-end comets away from the GFP-CAMSAP2 signal (Figure S3C and Movie S2), demonstrating that CAMSAP2 localizes to MT minus-ends and allows MT extension and shortening by plus-end dynamics. Similar results were obtained in hippocampal neurons, where GFP-CAMSAP2 specifically localizes to noncentrosomal MTs ends and MT plus-ends repeatedly emanated from stable CAMSAP2 stretches in the cell body (Figure 2H,I and Movie S3) and primary dendrites (Figure 2J,K and Movie S4). These results demonstrate that CAMSAP2 labels the minus-ends of noncentrosomal MTs in neurons.

Small CAMSAP2 clusters are transformed to extended stretches

To characterize the dynamics of CAMSAP2-positive structures in primary dendrites of mature neurons, we examined the fluorescence recovery after photo-bleaching (FRAP) of GFP-CAMSAP2 stretches. On average, GFP-CAMSAP2 fluorescence recovered to $33\pm 1\%$ of pre-bleached intensity after ~ 10 minutes with an average recovery half-time of 206 ± 20 s (Figure 3A). This recovery of CAMSAP2 is remarkably slow and incomplete when compared to the MT-associated protein MAP2, which recovered to $77\pm 1\%$ of pre-bleached intensity after ~ 10 minutes with an average recovery half-time of 106 ± 6 s. Interestingly, while a small recovery was observed along the length of the stretch, strong signals appear at the outmost edges of these structures (Figure 3B,C and Movie S5), suggesting that CAMSAP2 dynamics is increased at specific *foci*. To explore this phenomenon in more detail, GFP-CAMSAP2 recovery was monitored for extended periods (>30 min) in several stretches along the dendrite (Figure 3D-F and Movie S6). CAMSAP2 stretches are highly dynamic along the dendritic shaft and recover as small clusters that typically grow from one side towards either the proximal or distal site of the dendrite (Figure 3E,F). The elongating CAMSAP2 stretches occasionally pause or shrink before continuing growing into longer stretches (Figure 3E,F). These results demonstrate that small CAMSAP2 clusters are transformed to extended stretches. This data suggests that in neurons, MT minus-ends can slowly grow and be stabilized by accumulation of CAMSAP2, explaining the existence of very long stretches in older neurons.

CAMSAP2 depletion reduces microtubule density in neurons

To examine the function of CAMSAP2 in neuronal cells, we next used RNAi to suppress endogenous CAMSAP2 in developing (DIV 5) and mature (DIV 21) hippocampal neurons and analyzed the MT cytoskeleton. The efficiency of CAMSAP2 protein depletion was tested

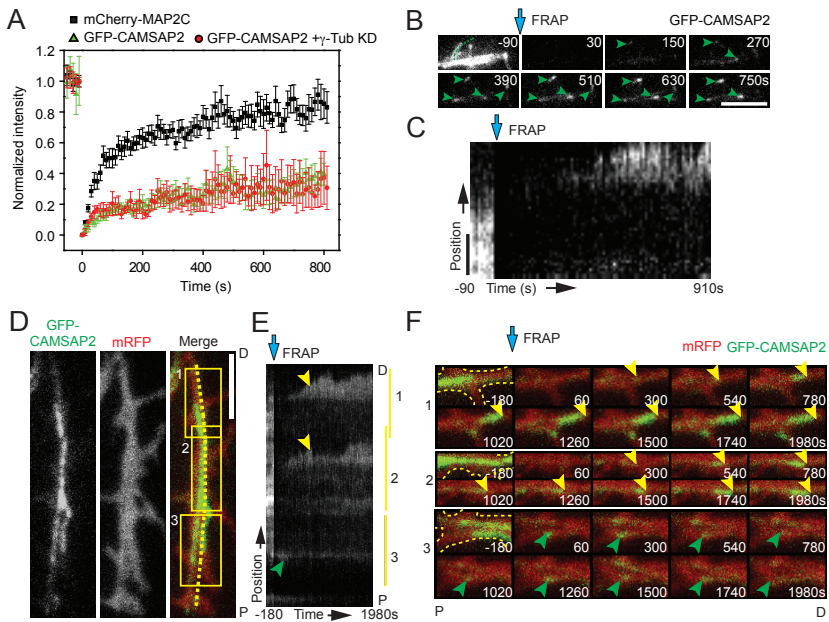


Figure 3: Elongating CAMSAP2 clusters form extended stretches in neurons

A) FRAP experiment intensity time traces of mCherry-MAP2C and pSuper ($n=12$, black squares), GFP-CAMSAP2 and pSuper ($n=8$, green triangles) or GFP-CAMSAP2 and γ -Tubulin shRNA ($n=5$, red circles). FRAP was performed on GFP-CAMSAP2 stretches at $t=0$. Error bars represent SEM.

B) Stills from a TIRFM time-lapse recording of a neuron transfected with GFP-CAMSAP2. Green arrowheads point out recovery of specific points after photo-bleaching. Scale bar is $5 \mu\text{m}$.

C) Kymograph of a TIRFM time-lapse recording corresponding to the dashed green line in B). Blue arrows indicates the FRAP ($t=0$). Scale bar is $1 \mu\text{m}$.

D) Still frame from TIRFM time-lapse recording of a DIV 24 hippocampal neuron expressing mRFP (red) and GFP-CAMSAP2 (green). D indicates the distal end and P the proximal end of the dendrite.

E) Kymograph from the TIRFM time-lapse recording in D). Green arrow heads indicate GFP-CAMSAP2 elongating towards the cell body, yellow arrowheads indicate GFP-CAMSAP2 growing away from the cell body.

F) Still frames corresponding to the boxed regions of the TIRFM time-lapse recording in D).

by introducing two independent CAMSAP2 shRNAs into neuronal cultures by lentiviral transduction. Western blot analysis revealed that both CAMSAP2 shRNAs reduced the levels of CAMSAP2 by $\sim 85\%$ (Figure 4A). Immunostaining experiments confirmed that CAMSAP2 intensity was strongly decreased in neurons expressing CAMSAP2 shRNA (Figure 4B and Figure S4A-D). The level of polymerized MTs in neurons was analyzed by Tubulin pre-extraction, followed by measurement of endogenous MAP2 fluorescent staining intensity in CAMSAP2 shRNA expressing neurons compared to the non-transfected neurons in the same field of view (Figure 4C). In DIV 5 neurons expressing CAMSAP2 shRNA, the MAP2 staining was reduced by $\sim 80\%$ compared to control cells (Figure 4E). This reduction greatly exceeded the effect of the potent MT-depolymerizing drug nocodazole (40% reduction (Figure 4F)) suggesting that in the latter case the remaining MT network was stabilized by CAMSAP2.

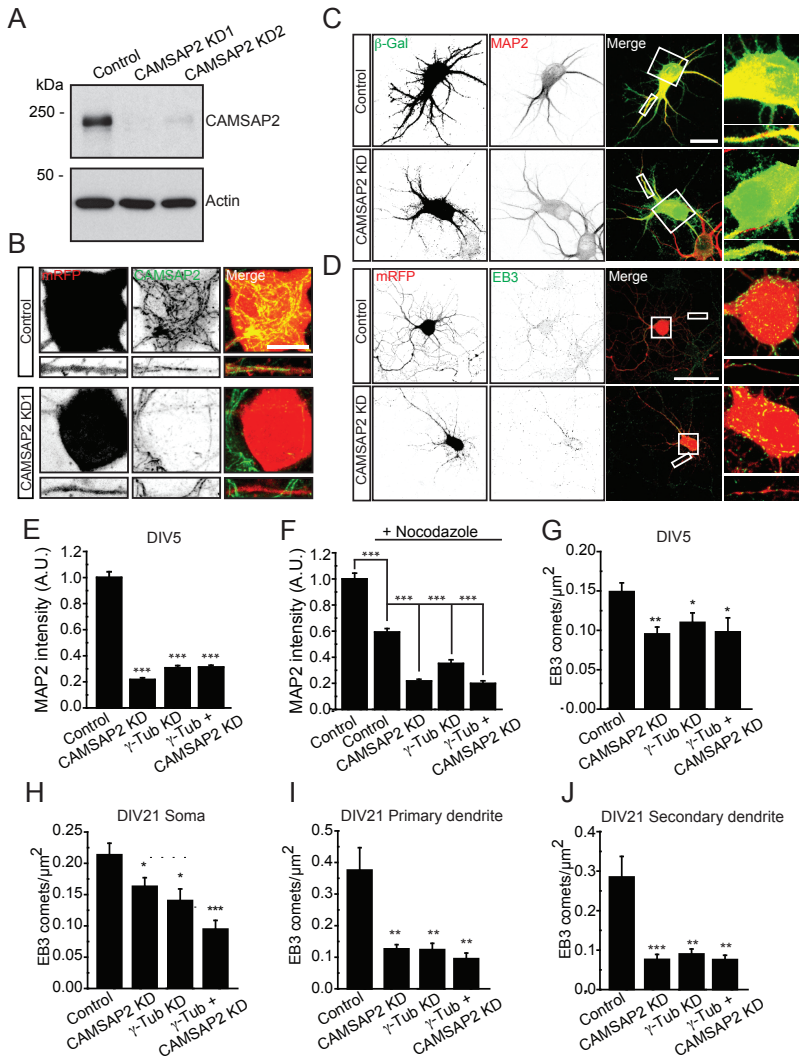
In addition, the number of growing MT plus-ends was analyzed by immunostaining for endogenous EB3 upon knockdown of CAMSAP2. All control and shRNA expressing neurons showed the characteristic comet-like MT plus-end patterns [4], but the number of comets was markedly decreased in cells depleted of CAMSAP2 (Figure 4D). In young neurons at DIV 5, a decrease of ~30% of EB3 comets in axons, dendrites and soma was found in CAMSAP2 shRNA expressing neurons compared to control cells (Figure 4G). In mature neurons at DIV 21, the number of EB3 comets in the soma was only reduced by ~20% in CAMSAP2 knockdown cells (Figure 4H), while the number of comets in the primary and secondary dendrites was decreased by ~70% (Figure 4I,J). Live-cell imaging of EB3-GFP labeled growing MT plus-ends confirmed these results: the number of EB3-GFP comets was decreased in CAMSAP2 knockdown neurons, but other parameters, such as the average growth velocity and the direction of displacement (retrograde *versus* anterograde) were not affected (data not shown). These data demonstrate that CAMSAP2 is important to establish and maintain the MT network in developing and mature neurons.

CAMSAP2 and γ -Tubulin are both required for noncentrosomal microtubules

Because both CAMSAP2 and γ -Tubulin associate with MT minus-ends, we next investigated the relationship between γ -Tubulin and CAMSAP2 in neurons. We used RNA interference (RNAi) to suppress endogenous γ -Tubulin in hippocampal neurons and analyzed the subcellular distribution and dynamics of CAMSAP2. Immunostaining experiments confirmed that γ -Tubulin was strongly downregulated in the cytoplasm of shRNA expressing neurons (Figure S4E,F). Similar to the knockdown of CAMSAP2, the intensity of MAP2 and EB3 in γ -Tubulin depleted neurons was markedly decreased (Figure 4E-J), which is consistent with a role for γ -Tubulin in the nucleation of noncentrosomal MTs [9]. γ -Tubulin knockdown also reduced the intensity of CAMSAP2 by ~70% compared to control cells (Figure S4G,H). A similar decrease in CAMSAP2 staining was obtained by depleting two other subunits within the γ -Tubulin ring complex (γ -TuRC), γ -Tubulin complex-associated proteins GCP2 and GCP6 (Figure S4G,H). Importantly, simultaneous depletion of γ -Tubulin and CAMSAP2 showed no additive effect in the reduction of MT density (Figure 4E-J), suggesting that the two proteins mostly operate in the same pathway.

Figure 4: CAMSAP2 stabilizes microtubules in neurons

- A) Extracts of DIV 25 hippocampal neurons sequentially infected at DIV 15 and DIV 20 with pSuper control, CAMSAP2-shRNA1 (KD1) and CAMSAP2-shRNA2 (KD2) lentivirus. Samples were analyzed by Western blot with indicated antibodies.
- B) Representative images of hippocampal neurons transfected (DIV22) with mRFP (red) and pSuper (control) or CAMSAP2-shRNA1 (KD1) and stained for CAMSAP2 (green). Scale bar is 10 μ m.
- C) Hippocampal neurons transfected at DIV 1 with β -Galactosidase (green) and pSuper or CAMSAP2-shRNA, pre-extracted, fixed and stained for MAP2 (red) at DIV 5. Scale bar is 20 μ m.
- D) Hippocampal neurons at DIV 1 transfected with mRFP (red) and pSuper or CAMSAP2-shRNA, fixed and stained for EB3 (green) at DIV 5. Scale bar is 50 μ m.



E) Diagram showing the normalized mean intensity of MAP2 in dendritic regions from DIV 5 neurons expressing control pSuper ($n=26$), CAMSAP2-shRNA ($n=23$), γ -Tubulin-shRNA ($n=20$) or both CAMSAP2-shRNA and γ -Tubulin-shRNA ($n=20$). AU, arbitrary unit

F) Diagram showing the normalized mean intensity of MAP2 in dendritic regions from neurons, which have been untreated ($n=26$) or treated with 30mM nocodazole transfected as in E ($n=19$, $n=15$, $n=13$, $n=15$ respectively). AU, arbitrary unit

G) Diagram showing the average number of EB3 comets/ mm^2 in DIV 5 neurites transfected as in E) at DIV 1 ($n=11$, $n=11$, $n=11$, $n=12$ respectively).

H) Diagram showing the average number of EB3 comets/ mm^2 in DIV 21 soma transfected as in E) at DIV 16 ($n=16$, $n=19$, $n=10$, $n=12$ respectively).

I) Diagram showing the average number of EB3 comets/ mm^2 in DIV 21 primary dendrites transfected as in E) at DIV 16 ($n=16$, $n=19$, $n=10$, $n=12$ respectively).

J) Diagram showing the average number of EB3 comets/ mm^2 in DIV 21 secondary dendrites transfected as in E) ($n=16$, $n=19$, $n=10$, $n=12$ respectively). Error bars represent SEM. * $P<0.05$, ** $P<0.01$ *** $P<0.001$ (T-test).

To test whether GFP-CAMSAP2 localization to minus-ends directly depends on γ -Tubulin, we next used laser-based microsurgery to generate new MT ends (Figure 5A) and measure GFP-CAMSAP2 dynamics in control and γ -Tubulin depleted cells. Upon laser-induced severing, GFP-CAMSAP2 was rapidly recruited to the newly generated MT minus-ends in both COS7 cells and neurons (Figure 5B-G). Interestingly, repetitive MT plus-end growth and shrinkage was also observed from newly formed CAMSAP2 clusters (Figure 5B-E and Movie S7), indicating that CAMSAP2 binding protects both sides of the decorated MT segments from depolymerization, consistent with *in vitro* observations [21]. The dynamics of GFP-CAMSAP2 accumulation upon laser-induced severing in γ -Tubulin knockdown neurons was indistinguishable from control cells (Figure 5F,G and Movie S8), indicating that CAMSAP2 can localize to MT minus-ends independent of γ -Tubulin. FRAP experiments with GFP-CAMSAP2 stretches in primary dendrites of γ -Tubulin knockdown neurons showed that although the number of events was reduced due to the decrease in overall MT density, the recovery rate and recovery levels were similar to the control cells (Figure 3A). The finding that γ -Tubulin depletion affects the number of CAMSAP2-decorated MT minus-ends but not the CAMSAP2 behavior is consistent with the *in vitro* data showing that CAMSAP accumulates on free, growing MT minus-ends, which are expected to lack γ -Tubulin [17,21]. Together, these data suggest that CAMSAP2 likely acts independently of γ -Tubulin at the molecular level, but might act downstream after the generation of *de novo* noncentrosomal neuronal MT by γ -Tubulin.

CAMSAP2 is required for dendrite development and BDNF-induced dendritic growth

Stable MTs are important for both dendrite development and maintenance [3]. To determine whether CAMSAP2 controls normal dendrite morphology, we examined the effect of CAMSAP2 knockdown on dendrites in developing (DIV 5) and mature (DIV 20) hippocampal neurons using the two CAMSAP2 shRNAs. In both cases, we observed a marked change in dendrite morphology (Figure 6A,B). Dendritic length was decreased by ~30% in CAMSAP2 knockdown DIV 5 neurons compared to the control (Figure 6C). Moreover, knockdown of CAMSAP2 decreased the number of dendritic branches and total dendritic complexity, whereas the number of primary dendrites was not significantly changed (Figure 6C,D). A similar morphological phenotype was observed in mature neurons (Figure 6B,F,G), indicating that CAMSAP2 is important for both dendritic development and maintenance. To obtain further insight in how CAMSAP2 regulates dendrite development, we determined whether the minimal CAMSAP2 domain required for minus-end binding (CC2-CC3-CKK, Figure S5) is sufficient to rescue the dendritic phenotype. Neurons were co-transfected at DIV 16 with CAMSAP2-shRNA and full-length GFP-CAMSAP2 or GFP-CC2-CC3-CKK for 4 days. This experiment showed that GFP-CAMSAP2 can restore the knockdown phenotype, while GFP-CC2-CC3-CKK expression was unable to rescue the CAMSAP2 phenotype (Figure 6K,L). These findings show that the minimal CAMSAP2 minus-end binding domain is not sufficient to restore dendrite morphology suggesting that additional domains of CAMSAP2 are critical for CAMSAP2 function.

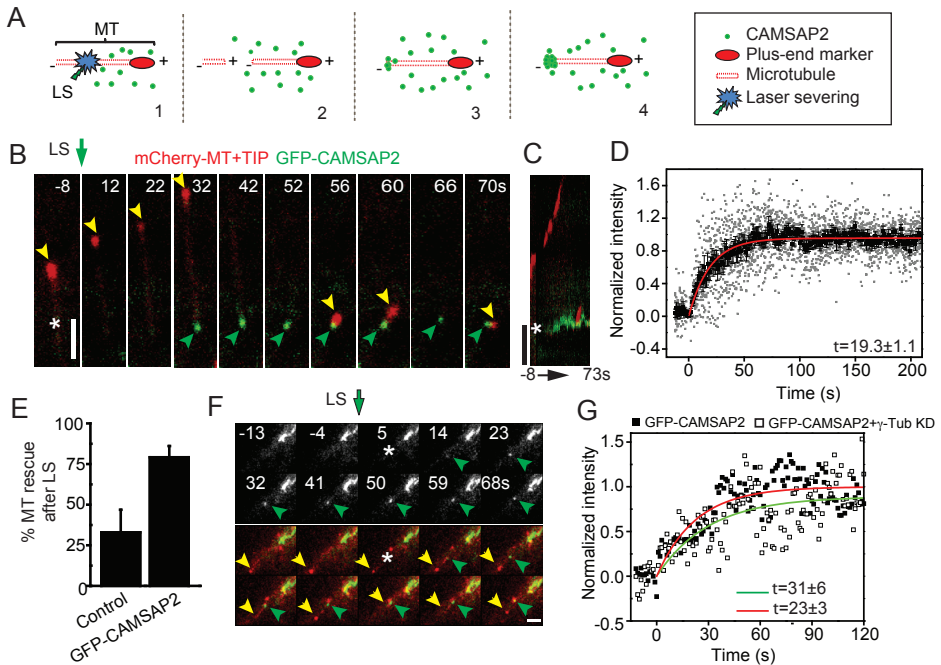


Figure 5: CAMSAP2 can localize to microtubule minus-ends independent of γ -Tubulin

- A)** Schematic representation of MT laser-induced severing.
- B)** Stills from a TIRFM time-lapse recording of a COS-7 cell expressing mCherry-MT+TIP (red) and GFP-CAMSAP2 (green). The yellow arrowheads indicate the MT plus-end marker, Green arrowheads indicate GFP-CAMSAP2 accumulating on MT minus-ends. Asterisk indicates the location of laser-induced severing at t=0.
- C)** Kymograph of the time-lapse recording shown in B). Scale bars are 2 μm.
- D)** GFP-CAMSAP2 intensity time trace of individual MT minus-ends (gray squares) and average trace (black squares) (n=10). Single exponential fit of the data average points is shown in red.
- E)** Quantification of the percentage of MTs that are rescued after laser-induced severing after expression of GFP-CAMSAP2 (n=4-6).
- F)** Representative time-lapse recording of a hippocampal neuron (DIV 1) expressing GFP-CAMSAP2 (green) and mCherry-MT+TIP (red). Green arrowheads indicate GFP-CAMSAP2 accumulation, yellow arrowheads indicate MT plus-end and the asterisk indicate the area of laser-induced severing. Scale bar is 1 μm.
- G)** GFP-CAMSAP2 intensity time trace (black squares) of a TIRFM time-lapse recording, single exponential fit of the data points is shown in red. The white squares correspond to the intensity time trace of neurons transfected with GFP-CAMSAP2 and γ -Tubulin shRNA, single exponential fit of the data points is shown in green. Error bars represent SEM.

To further examine the role of CAMSAP2 in dendrite development, we compared the effect of brain-derived neurotrophic factor (BDNF) in control and CAMSAP2 knockdown cells. BDNF causes dendritic growth in hippocampal neurons [24]. The control DIV 22 neurons cultured in the presence of 50 ng/ml BDNF for 3 days acquired ~41% additional dendrites (Figure 6I,J). In contrast, BDNF-induced dendrite formation did not occur in neurons expressing CAMSAP2 shRNA (Figure 6I,J). Together, these data demonstrate that CAMSAP2 is required for normal dendrite morphology and BDNF-induced dendritic growth.

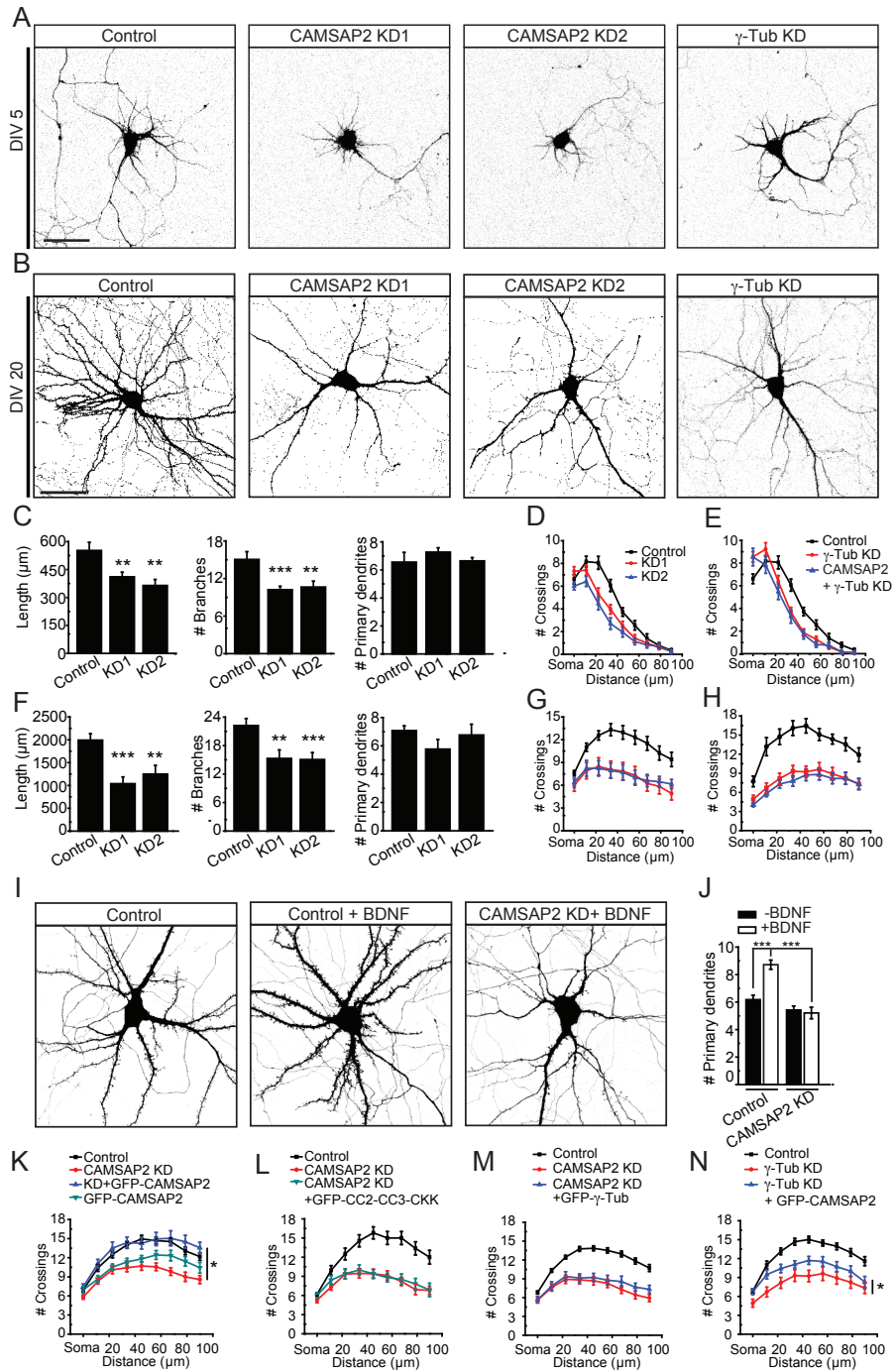
Similar to knockdown of CAMSAP2, γ -Tubulin depletion also strongly reduced dendritic complexity in young and mature neurons (Figure 6E,H). Next, we tested whether CAMSAP2 acts up- or downstream of γ -Tubulin in regulating dendrite morphology. While overexpression of GFP-CAMSAP2 partly restored the dendritic complexity in γ -Tubulin depleted neurons (Figure 6N), GFP- γ -Tubulin expression was unable to rescue the CAMSAP2 phenotype (Figure 6M). These data suggest that CAMSAP2 expression is to some extent able to stabilize dendritic MTs and reverse the effects of γ -Tubulin knockdown. Together these results demonstrate that CAMSAP2 and γ -Tubulin are important to maintain noncentrosomal MT arrays and dendrite morphology and that these factors might act sequentially: γ -Tubulin initiates the formation of *de novo* noncentrosomal MTs while CAMSAP2 stabilizes them.

Neuronal activity activation affects the distribution of CAMSAP2 in dendrites

Previous studies have shown that neuronal activity modulates the stability of the MT arrays in dendrites [25]. For instance, transient glutamate receptor activation suppresses MT growth and density [26]. We next determined whether glutamate stimulation affects the distribution of CAMSAP2-decorated MT minus-ends in dendrites. Upon treatment with 50 μ M glutamate for 5 min, the staining of CAMSAP2 stretches was markedly decreased and replaced by a more diffuse cytoplasmic signal within the dendrites, which could be blocked by the NMDA receptors antagonist APV (Figure S6A,B). In contrast, blocking either AMPA-type and kainate receptors (CNQX) or metabotropic glutamate receptors (AIDA) did not prevent the decrease

Figure 6. CAMSAP2 is required for dendrite morphology

- A) Representative images of DIV 5 hippocampal neurons transfected at DIV 1 with mRFP and control pSuper, CAMSAP2-shRNA1 (KD1), CAMSAP2-shRNA2 (KD2) or γ -Tubulin-shRNA.
- B) Representative images of DIV 20 hippocampal neurons transfected at DIV 16 with β -Galactosidase alone or with CAMSAP2-shRNA1, CAMSAP2-shRNA2 or mRFP and γ -Tubulin-shRNA. Scale bars are 50 μ m.
- C) Quantification of dendrite morphology. Number of dendrites, branches and total dendrite distance are determined from DIV 5 neurons transfected with control pSuper (n=18), CAMSAP2-shRNA1 (n=22) or CAMSAP2-shRNA2 (n=17).
- D) Sholl analysis corresponding to the data used in C)
- E) Sholl analysis of DIV 5 neurons transfected at DIV 1 with mRFP and control pSuper (n=18), γ -Tubulin-shRNA (n=22) or the combination of γ -Tubulin-shRNA and CAMSAP2-shRNA1 (n=17).
- F) Quantification of the number of dendrites, branches and total dendrite distance are determined from DIV 20 neurons transfected with control pSuper (n=25), CAMSAP2-shRNA1 (n=13) or CAMSAP2-shRNA2 (n=13).
- G) Sholl analysis corresponding to the data in F)
- H) Sholl analysis of DIV 22 neurons transfected at DIV 18 with mRFP and control pSuper (n=11), γ -Tubulin-shRNA (n=13) or the combination of γ -Tubulin-shRNA and CAMSAP2-shRNA1 (n=15).
- I) Representative images of DIV 22 neurons transfected with mRFP and pSuper control or CAMSAP2-shRNA1 at DIV 18 and untreated or treated with 50 ng/ml BDNF for 3 days.
- J) Quantification of the number of primary dendrites untreated (n=28) and treated with 50 ng/ml BDNF for 3 days and transfected control pSuper (n=50) or CAMSAP2-shRNA1 (n=29-32 treated) at DIV 18. Neurons were fixed at DIV 22.
- K) Sholl analysis of DIV 21 neurons transfected at DIV 17 with pSuper (n=40), CAMSAP2-shRNA (n=30), GFP-CAMSAP2 (n=21) or CAMSAP2-shRNA and GFP-CAMSAP2 (n=16).
- L) Sholl analysis of DIV 21 neurons transfected at DIV17 with pSuper (n=16), CAMSAP2-shRNA (n=15), CAMSAP2-shRNA and GFP-CC2-CC3-CKK (n=15).



M) Sholl analysis of DIV 21 neurons transfected at DIV 17 with control pSuper ($n=48$), CAMSAP2-shRNA ($n=28$) or CAMSAP2-shRNA1 and GFP- γ -Tubulin ($n=18$).

N) Sholl analysis of DIV 21 neurons transfected at DIV 17 with control pSuper ($n=34$), γ -Tubulin-shRNA ($n=13$) or γ -Tubulin-shRNA and GFP-CAMSAP2 ($n=24$). Error bars represent SEM. * $P<0.05$ ** $P<0.01$ *** $P<0.001$ (T-test).

in CAMSAP2 intensity at the dendrites (Figure S6B). We next determined whether a protocol to induce chemical LTD affects CAMSAP2 localization. Bath application of 50 μ M NMDA for 5 min markedly decreased the intensity of the CAMSAP2-positive stretches in dendrites (Figure S6A,C). In mature hippocampal neuronal cultures, signaling through NMDA receptors mainly occurs through either NR2A- or NR2B containing receptors. Using shRNA constructs that reduce the expression of NR2A and/or NR2B, we found that the knockdown of NR2B rather than NR2A blocked the NMDA-dependent CAMSAP2 redistribution (Figure S6A,C). Next we investigated GFP-CAMSAP2 dynamics upon NMDA stimulation. Consistent with the immunohistochemical data, NMDA stimulation induced a strong and rapid decrease in the intensity of the CAMSAP2-positive stretches in dendrites (Figure S6D). This effect started within the first minute after NMDA stimulation and persisted until GFP-CAMSAP2 signals fully disappeared, \sim 10 minutes after treatment (Figure S6E). Together, these data demonstrate that neuronal activity affects the distribution of CAMSAP2 in dendrites, which could explain the observed decrease in MT density after NMDA receptor stimulation [26].

CAMSAP2 is required for microtubule stabilization during neuronal polarization

It is well known that the MT cytoskeleton is also important during early neuronal development and changes in MT stability markedly affect neuronal polarity [27]. To investigate whether CAMSAP2 is directly involved in neuronal polarization, we first analyzed the distribution of endogenous CAMSAP2 in hippocampal neurons at early stages of development. Upon plating, hippocampal neurons first form lamellipodia around the cell body (stage 1) followed by the formation of several processes about six hours later, the minor neurites (stage 2). After 20h-48h in culture one neurite starts to grow out quickly and becomes the axon (stage 3), which can initially be labeled with the axonal marker Tau and later on with axon initial segment (AIS) markers, such as Ankyrin G, β IV-Spectrin and sodium channels (pan-Nav). As reported previously [9], distinct centrosomal components disappeared from the MTOC during neuronal development and dispersed throughout the cytoplasm at later stages (Figure S7), consistent with a shift from centrosomal to noncentrosomal nucleation. Indeed, dSTORM imaging revealed that, whereas in DIV1 cells many microtubules emanated radially from the centrosome, DIV5 neurons had a non-axonal microtubule organization with many free CAMSAP-decorated minus ends the centrosome (Figure 2 and Figure S8).

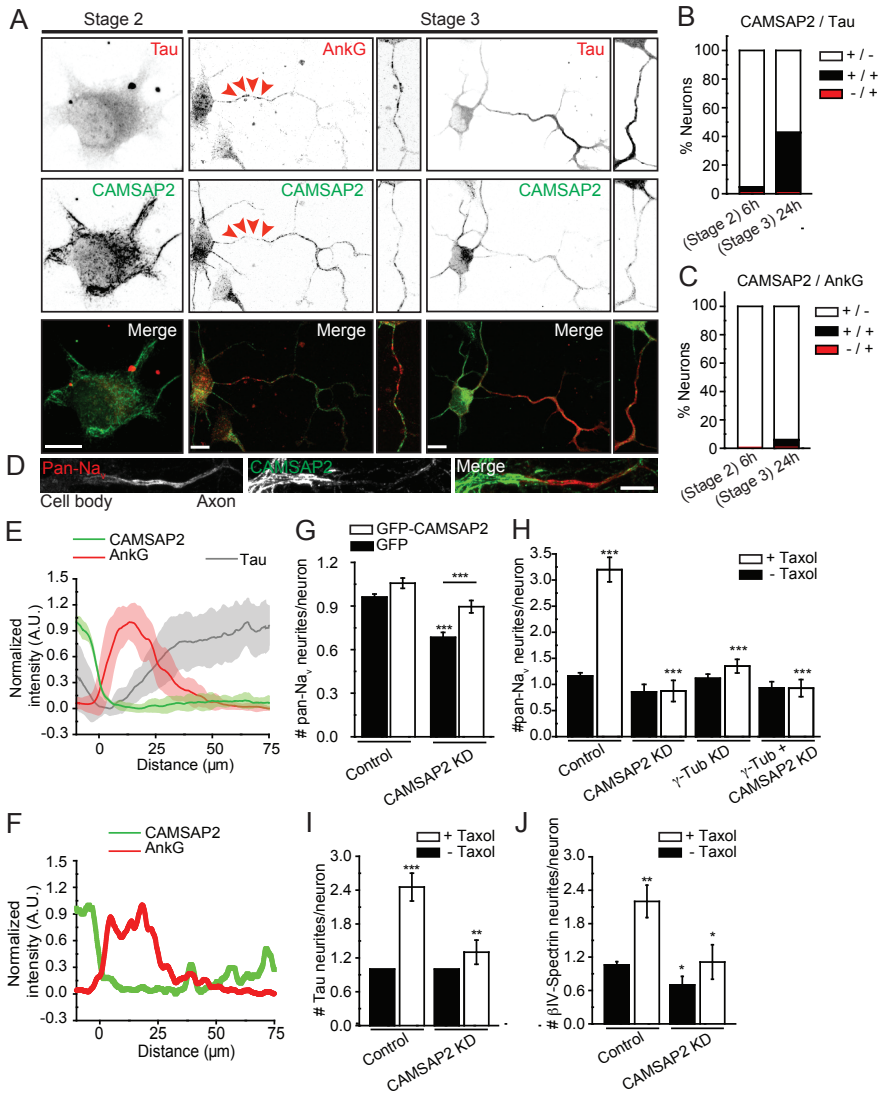
Figure 7. CAMSAP2 is required for axon formation and neuronal polarization

A) Representative images of DIV 1 hippocampal neurons double stained for endogenous Tau (red) and CAMSAP2 or endogenous Ankyrin G (red) and CAMSAP2 (green). Scale bars are 10 μ m.

B) Diagram showing the percentage of neurons at DIV 0.25 and DIV 1 with neurites positive for endogenous CAMSAP2+ / Tau+, CAMSAP2+ / Tau-, CAMSAP2- / Tau+ (n=150).

C) Diagram showing the percentage of neurons at DIV 0.25 and DIV 1 with neurites positive for endogenous Ankyrin G+ / Tau+, Ankyrin G+ / Tau-, Ankyrin G- / Tau+ (n=150).

D) Representative image of an axonal segment from DIV 21 neuron stained for CAMSAP2 and axon initial segment marker, pan-Nav. Scale bar is 10 μ m.



E,F Profiles of CAMSAP2 (green), Ankyrin G (red trace) and Tau (grey trace) fluorescence intensity in the axon of neurons at DIV 7. Examples of average intensity traces of at least 19 neurons for each dual staining **E** and representative single intensity traces **F**. AU, arbitrary unit. Error bars represent SD.

G Diagram showing the number of pan-Nav positive neurites per neuron in cortex neurons at DIV 4. Cells are electroporated before plating with pSuper control (n=180), pSuper control and GFP-CAMSAP2 (n=105), CAMSAP2-shRNA (n=180) or CAMSAP2-shRNA and GFP-CAMSAP2 (n=105) and stained for endogenous pan-Nav and CAMSAP2.

H Diagram showing the number of pan-Nav positive neurites per neuron in hippocampal neurons at DIV 5, transfected at DIV 1 with mRFP and pSuper control (n=35) or CAMSAP2-shRNA (n=21 untreated, n=16 treated), γ-Tubulin-shRNA (n=17 untreated, n=20 treated), CAMSAP2-shRNA and γ-Tubulin-shRNA (n=15 untreated, n=14 treated) and untreated (n=37) or treated with 10nM Taxol for 48 hours.

I,J Diagram showing the number of Tau or βIV-Spectrin positive neurites per neuron in hippocampal neurons DIV 5, transfected with mRFP and pSuper control (n=11) or CAMSAP2-shRNA (n=10 untreated, n=10 treated) and untreated (n=17) or treated with 10nM Taxol for 48hours. Error bars represent SEM, *P<0.05, **P<0.01 ***P<0.001 (T-test).

At 6h, all morphologically unpolarized neurons stained positively for endogenous CAMSAP2, showing puncta and small clusters in the soma and minor neurites (Figure 7A) and stained negatively for axonal marker Tau and the earliest AIS marker Ankyrin G (Figure 7B,C). Thus, CAMSAP2 is already expressed in stage 2 cells before the neurons form an axon and polarize. At 24h, polarized neurons maintained CAMSAP2 expression within the soma, neurites and Tau-positive axon (Figure 7A-C). Interestingly, CAMSAP2 was present at low levels at the AIS region, but enriched in the proximal part of the soma to the axon (Figure 7A). Closer inspection indicated that CAMSAP2 was abundant in the soma and in the first part of the axons but not in the AIS and was also present as small clusters and distinct stretches in the proximal axonal compartment directly after the AIS (Figure 7D). The high levels of CAMSAP2 at proximal part of the axon, right before the start of the AIS was consistent across the neuronal population and maintained throughout neuronal development (Figure 7E,F).

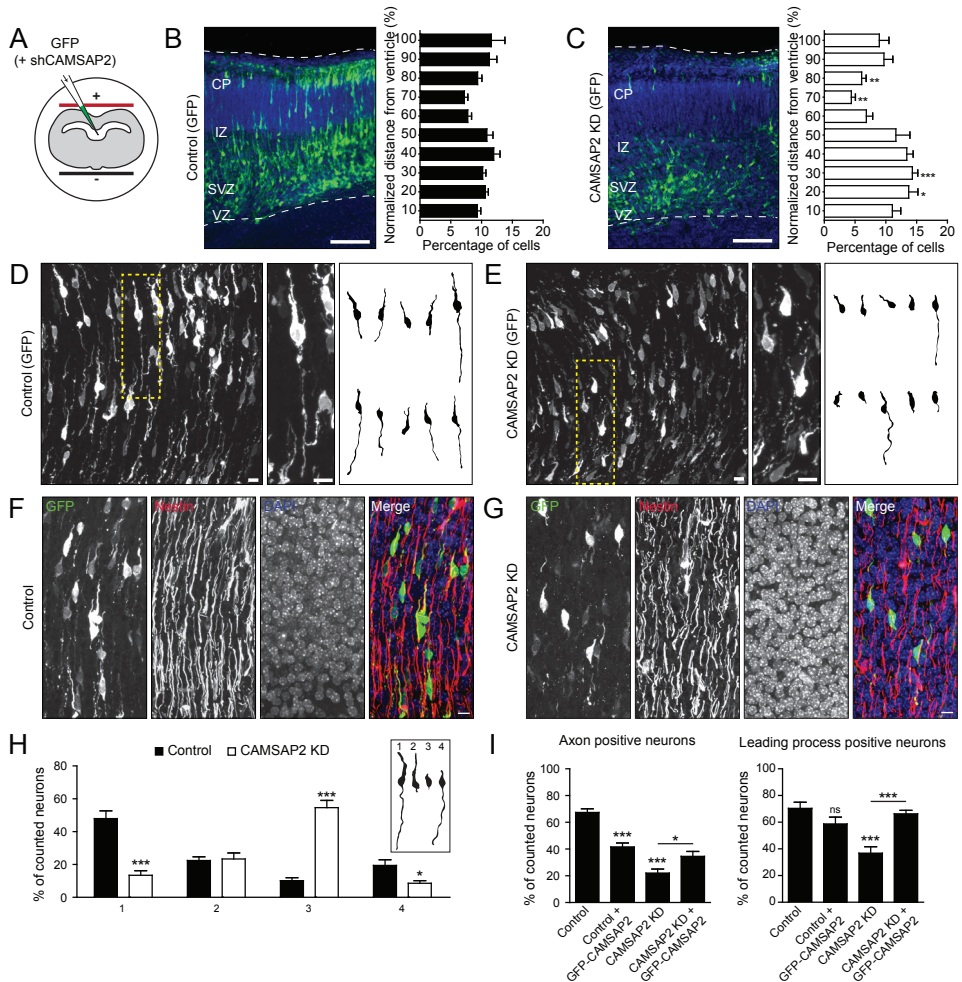
To determine whether CAMSAP2 is involved in neuronal polarization, we knocked down CAMSAP2 before polarization in stage 1-2 neurons. Directly after dissection, primary cortical neurons were electroporated to deliver CAMSAP2 shRNA. At DIV 4, we determined the number of polarized neurons using the AIS marker pan-Nav and found a reduced fraction of polarized cells compared to control cells (Figure 7G), indicating that CAMSAP2 contributes to neuronal polarization. To further test whether CAMSAP2 plays a role in MT stabilization during axon initiation and specification, we used the MT-stabilizing drug taxol to induce multiple axon formation [28]. In the presence of low concentrations of taxol (10 nM) for 2 days, the number of pan-Nav positive processes per cell was increased more than three-fold in control neurons (Figure 7H). However, such taxol-induced axonal processes did not emerge in neurons expressing CAMSAP2 shRNA. The same phenotype was also observed after γ -Tubulin depletion (Figure 7H) Similar results were obtained by analyzing the axon specific marker Tau and AIS marker β IV-Spectrin (Figure 7I,J). These *in vitro* data suggest that CAMSAP2 is required for axon specification.

CAMSAP2 is required for axon formation and neuronal polarity *in vivo*

In the developing neocortex after terminal cell division, highly polarized neurons with a trailing process (future axon) and an unipolar leading process (future apical dendrite) are formed during neuronal migration [29]. To investigate the effect of CAMSAP2 depletion in newborn neurons in the neocortex, we first performed *ex vivo* electroporation followed by organotypic slice cultures. E14.5 mouse embryos were subjected to intracranial electroporation to introduce GFP and CAMSAP2 shRNA plasmids selectively into neuronal precursors in the ventricular zone (VZ) (Figure 8A). Cortical slices were then prepared and cultured for 3 days,

Figure 8: CAMSAP2 is required for axon initiation and neuronal polarity *in vivo*

A) Schematic cross section of the *ex vivo* electroporation procedure: E14.5 intact mouse embryo head were injected in the lateral ventricle with GFP alone or together with two CAMSAP2 shRNAs (shRNA1/2), electroporated and followed by immediately slicing of the brains before subjecting them to organotypic slice culture for 4 days.



B,C Maximum intensity projection of ex vivo neuronal migration of GFP positive neurons electroporated with either GFP only (B) or GFP and CAMSAP2 shRNAs (C). Bar diagram shows the normalized migration distribution along the radial axis from the ventricle. CP, cortical plate; IZ, intermediate zone; SVZ, subventricular zone; VZ, ventricular zone; scale bars, 100μm; *P<0.05, **P<0.01, ***P<0.001, comparing corresponding bins using a Mann-Whitney U Test.

D,E Neuron morphology (E17.5) of in utero electroporated (E14.5) mouse embryo brains. Morphology (maximum intensity projection) shown of neurons electroporated with either GFP only (D) or GFP and CAMSAP2 shRNAs (E). Middle panel contains a zoom of a typical neuron. Right panel contains individual traces of representative neurons found in the specific condition. Scale bars: 10 μm

F,G Maximum intensity projection of GFP and Nestin staining (E17.5) of in utero electroporated (E14.5) mouse embryo brains. Brains were electroporated with either GFP only (F) or GFP and CAMSAP2 shRNAs (G). Scale bars are 10 μm.

H Quantification of the different (GFP positive) neuronal cell morphologies found in the E17.5 brain after in utero electroporation (E14.5). *P<0.05, **P<0.01, ***P<0.001, comparing control versus shCAMSAP2 using a Mann-Whitney U Test.

I Quantification of the axon positive and GFP positive neurons (left graph) as well as the quantification of the leading process positive and GFP positive neurons (right graph) found in the E17.5 brain after in utero electroporation (E14.5). Comparing control versus control and GFP-CAMSAP2, control versus shCAMSAP2, and shCAMSAP2 versus shCAMSAP2 and GFP-CAMSAP2 using a Mann-Whitney U Test. *P<0.05, **P<0.01, ***P<0.001.

to allow the labeled neurons to polarize and migrate to the cortical plate (CP) in a manner highly similar to that observed *in vivo*. Control GFP-positive neurons migrated to the CP (Figure 8B), while many CAMSAP2 depleted neurons accumulated in the (sub)ventricular zone (SVZ/VZ) and failed to migrate properly (Figure 8C), indicating that CAMSAP2 knockdown impairs neuronal migration in a cell-autonomous manner.

We next performed *in utero* electroporation for detailed analysis of neuronal morphogenesis. Following electroporation at E14.5, embryos were allowed to develop for 3 days (E17.5), at which point the morphology of GFP-positive migrating neurons was examined. In littermate controls, most GFP-positive migrating neurons possessed stereotypical bipolar morphologies consisting of a leading process and a long trailing-edge axon (Figure 8D). In contrast, cells expressing GFP and CAMSAP2 shRNA failed to form a distinguishable axon and the leading edge process (Figure 8E). Moreover, whereas GFP-positive axons projecting through the IZ were observed in control animals, such structures were not seen in CAMSAP2 shRNA expressing animals (Figure 8D,E). In contrast, the radial glial cell fibers, expressing nestin, were not affected by CAMSAP2 shRNA expression (Figure 8E,G). Quantification revealed that ~80% of control neurons possessed a morphologically discernable leading process compared to ~30% of CAMSAP2 depleted cells (Figure 8H,I). Moreover, whereas ~70% of control cells in the IZ possessed axons, only ~20% of CAMSAP2 knockdown cells had discernible axons (Figure 8H,I). Together, these findings demonstrate that CAMSAP2 is critical for axon formation and the establishment of neuronal polarity in the developing neocortex.

DISCUSSION

Recent studies have identified different MT-mediated processes involved in regulating neuron polarization, development and function [3,30]. MT minus-end dynamics has remained one of the least well-understood properties of the MT cytoskeleton in neurons. Especially, the mechanisms stabilizing the free noncentrosomal MT minus-ends have remained elusive. In this study, we demonstrate that by stabilizing minus-ends of noncentrosomal MTs, CAMSAP2 contributes to MT organization in developing and mature neurons playing an important role in axon specification and dendritic branch formation *in vitro* and *in vivo*. In addition, similar to the widely used plus-end binding proteins to track growing MTs [4,31], the endogenous or fluorescently tagged CAMSAP2 provides a new molecular tool to identify noncentrosomal minus-ends and probe the MT organization in neuronal cells.

CAMSAP2 stabilizes noncentrosomal minus-ends in neurons

Neuronal development and differentiation require sophisticated architectural changes, which may be incompatible with a large MT network emanating from a single MTOC [11,12]. Indeed, it has been shown that the centrosome loses its function as an MTOC during early neuronal development and that noncentrosomal MT arrays within axonal and dendritic processes acquire distinct organization patterns at later developmental stages [9,32]. In this study, we show that CAMSAP2 accumulates at neuronal MT minus-ends and plays a key

role in stabilizing noncentrosomal MT arrays in axons and dendrites. We also found that small CAM SAP2 structures can grow and transformed into extended stretches. The dynamic behavior of CAM SAP2 in neurons is likely explained by our recent data showing that CAM SAP proteins decorate growing MT minus-ends [21]. Although it is generally believed that MT minus-ends do not to grow [16], the numerous elongating CAM SAP2 stretches in various parts of the dendrites instead suggests that MT minus-end growth events frequently occur in hippocampal neurons. Since the length of the CAM SAP2 structures markedly changes during neuron differentiation, this might indicate that MT minus-end growth is developmentally regulated. Moreover, the need for MT minus-end growth to generate long CAM SAP2 stretches implies that CAM SAP proteins likely act on free MT minus-ends that are not capped by γ -Tubulin or other factors. Indeed, we found that when already existing MTs are severed, CAM SAP2 is able to accumulate at the newly created MT minus-ends independently of γ -Tubulin.

CAM SAP2 is dynamic at the outmost edges of a bleached stretch, while CAM SAP2 is stably present along the length of the stretch. Once localized at the minus-ends, CAM SAP2 could act as a critical minus-end recognition signal involved in the recruitment and assembly of other factors to one specific MT end, similar to EB proteins at the plus-ends [33]. Our finding that the minimal CAM SAP2 minus-end binding domain (CC2-CC3-CKK) is not sufficient to restore dendrite morphology, suggests that other domains and potential binding partners are involved in CAM SAP2 functions in neurons. Additional studies are required to investigate such mechanisms and for the identification of CAM SAP2 binding partners.

CAM SAP2 is required for axon specification and neuronal polarization

Axon formation during neuronal polarization is associated with increased MT stability [27,30]. Here we show that neurons lacking CAM SAP2 fail to initiate axon formation and show impaired neuronal polarization during *in vitro* and *in vivo* development. The defects in neuronal migration upon CAM SAP2 depletion might be caused by the lack of polarization in the developing neocortex. Since CAM SAP2 stabilizes the neuronal MT arrays, these data suggest that noncentrosomal MT stabilization plays critical role during the specification of axonal fate in early neuronal development. In addition, the complete block of taxol-induced axon formation in CAM SAP2 depleted neurons implies that instable MTs and subsequent decreased MT density is sufficient to block axon specification. We found that CAM SAP2 was present in the soma and small processes of neurons at early stages of neuron development (stage 2), before neuronal polarization and axon formation. In polarizing stage 3 neurons, CAM SAP2 staining is reduced at the AIS, but enriched in the soma and in the proximal part of the axon, suggesting that there are no MT minus-ends in the AIS and that most MTs are continuous throughout the AIS. High levels of CAM SAP2 at the first part of the axon may create a local pool of stabilized MT minus-ends and promote plus-end out oriented MT growth in axons. Interestingly, the increase in CAM SAP2 at the first part of the axon is maintained throughout neuronal development. Local MT stability at the site of axon

formation has been reported to cause polarized membrane flow [34]. Consistently, MT-based motor proteins such as kinesin-1/KIF5 show a higher affinity for stabilized MTs and have been found to transport several vesicular carriers into the axon [35]. Future work will be needed to resolve the molecular interplay between CAMSAP2 and axonal transport during neuronal polarization. In addition, signaling molecules involved in the regulation of MT dynamics in axon formation and polarity processes should be reassessed for their potential role in regulating CAMSAP2 activity [36].

CAMSAP2 and γ -Tubulin are required for dendrite development

We further demonstrated that CAMSAP2 stabilizes noncentrosomal MTs in dendrites. Since dendritic outgrowth occurs after the centrosome loses its function as an MTOC [9], noncentrosomal MT assembly and stabilization is most likely an essential process during later stages of neuronal development. Indeed, both stable MAP2 positive and dynamic EB3 positive MTs were reduced upon CAMSAP2 knockdown. CAMSAP2-decorated MTs were enriched in primary dendrites, consistent with the large fraction of minus-end-out MTs in this part of the dendrite [31,32]. In the absence of CAMSAP2, dendritic branching was reduced and BDNF-induced dendrite development was inhibited. Similar to mechanisms governing neuronal polarization, we propose that dendritic branches are formed and maintained by noncentrosomal MTs that are stabilized by CAMSAP2. Our finding that γ -Tubulin knockdown also strongly reduces the MT population in dendrites suggests that many noncentrosomal MTs are generated by local nucleation. A distinct mechanism to generate noncentrosomal MTs is by severing of pre-existing MTs [10-12]. Depletion of katanin and spastin has been shown to modulate axon growth in young neurons [13], but changes in dendrite outgrowth and morphology have so far not been reported. Moreover, in *Drosophila* class IV dendritic arborization (da) neurons, mutations in the two major MT-severing proteins spastin and katanin do not induce noticeable dendrite phenotypes [37]. In contrast, the complexity of the dendritic arbor in these neurons depends on the presence of Golgi outposts, which were shown to behave as MTOCs [15]. Since we observed a decrease in γ -Tubulin at the centrosome at early stages of development without an overall change in total protein levels suggests that similar to other systems γ -Tubulin regulates local microtubule nucleation throughout the neuron in a centrosome independent manner. Therefore, we hypothesize that γ -Tubulin-dependent MT nucleation and CAMSAP2-dependent stabilization are two key features of MT organization during dendritic development. We propose a two-step model in which γ -Tubulin initiates the formation of noncentrosomal MTs and CAMSAP2 subsequently stabilizes the newly formed free MT minus-ends.

In summary, we demonstrate that the CAMSAP/Nezha/Patronin family protein CAMSAP2 specifically stabilizes noncentrosomal MT minus-ends and plays an important role in the development and maintenance of neuronal structure. As changes in MT organization are important for many neuronal functions, including plasticity and regeneration, we anticipate that more neuronal processes that involve CAMSAP2 will be revealed in the future.

MATERIALS AND METHODS

Antibodies and reagents

The following antibodies were used in this study: rabbit anti-EB3 (02-1005-07) [31], mouse anti- γ -Tubulin (T6557, Sigma), rabbit anti-CAMSAP1 (Novus Biologicals, NBP1-26645), rabbit anti-CAMSAP2 (17880-1-AP, Proteintech; NBP1-21402, Novus Biologicals; HPA0273, Sigma), rabbit anti-CAMSAP3 (Abgent, AP18323a). Details of other antibodies and reagents are in the Supplementary Materials and Methods.

DNA constructs

The CAMSAP2 expression constructs and their deletion mutants were generated by a PCR-based strategy using the human CAMSAP2 cDNA (IMAGE clone 40124603). The mCherry-MT+TIP construct contains the general MT + tip localization signal (SxIP motif) of human MACF2 (E5455-R5497; NP_899236) recognized by MT end binding (EB) proteins. The following shRNAs were created and used in this study: γ -Tubulin-shRNA (5'-ggaggacatcttcaaggac), CAMSAP2-shRNA1, (KD1, 5'-ttgcatgtgctcaacagt) and CAMSAP2-shRNA2 (KD2, 5'-attccagaagaatcgggtg). For details see Supplementary Materials and Methods.

Primary hippocampal neuron cultures, transfection and nucleofection

Primary hippocampal and cortical cultures were prepared from embryonic day 18 (E18) rat brains and transfected using Lipofectamine 2000 (Invitrogen) or the Amaxa Rat Neuron Nucleofector kit (Lonza), respectively.

Live-cell imaging and laser-induced severing

Simultaneous dual color time-lapse live cell imaging and TIRFM was performed on a Nikon Eclipse TE2000E microscope with Coolsnap and QuantEM cameras (Roper Scientific). Neurons were maintained at 37°C with 5% CO₂ (Tokai Hit). A Teem Photonics 532 nm Q-switched pulsed laser is used for laser-induced severing. The FRAP experiments were performed on a TIRF microscope system using the ILas2 system (Roper Scientific). For details see Supplementary Materials and Methods.

Ethics statement

All animal experiments were performed in compliance with the guidelines for the welfare of experimental animals issued by the Government of the Netherlands. All animal experiments were approved by the Animal Ethical Review Committee (DEC) of the Erasmus Medical Center and Utrecht University.

ACKNOWLEDGEMENTS

We thank Dr. Rasband for sharing β IV-Spectrin antibodies, N.T. Keijzer for cloning shRNA-constructs, Dr. F. Polleux and Dr. J. Courchet for sharing the cortical migration excel macro and A.M.A. Chiotto for assisting with imaging and analyzing EB3 antibody stainings. This work was supported by the Netherlands Organization for Scientific Research (NWO-ALW-VICI, CCH, AA; NOW-ALW-VIDI, LCK; NWO-ALW-VENI, MH), the Foundation for Fundamental Research on Matter ((FOM) CCH, LCK, AA)), which is part of the NWO, the Netherlands Organization for Health Research and Development (ZonMW-TOP, CCH), the European Science Foundation (ESF-EURYI, CCH) and European Molecular Biology Organization - Young Investigators Program (EMBO-YIP, CCH).

AUTHOR CONTRIBUTIONS

Super-resolution experiments for figures 2A-G and S8 were performed and analyzed by B.M.C.C. or by students under supervision of B.M.C.C.

REFERENCES

- 1 Millecamps, S. & Julien, J. P. Axonal transport deficits and neurodegenerative diseases. *Nat Rev Neurosci* 14, 161-176 (2013).
- 2 Franker, M. A. & Hoogenraad, C. C. Microtubule-based transport - basic mechanisms, traffic rules and role in neurological pathogenesis. *J Cell Sci* 126, 2319-2329 (2013).
- 3 Conde, C. & Caceres, A. Microtubule assembly, organization and dynamics in axons and dendrites. *Nat Rev Neurosci* 10, 319-332 (2009).
- 4 Jaworski, J. et al. Dynamic microtubules regulate dendritic spine morphology and synaptic plasticity. *Neuron* 61, 85-100 (2009).
- 5 Bettencourt-Dias, M. & Glover, D. M. Centrosome biogenesis and function: centrosomes brings new understanding. *Nat Rev Mol Cell Biol* 8, 451-463 (2007).
- 6 Basto, R. et al. Flies without centrioles. *Cell* 125, 1375-1386 (2006).
- 7 Nguyen, M. M., Stone, M. C. & Rolls, M. M. Microtubules are organized independently of the centrosome in *Drosophila* neurons. *Neural Dev* 6, 38 (2011).
- 8 Baas, P. W. & Lin, S. Hooks and comets: The story of microtubule polarity orientation in the neuron. *Dev Neurobiol* 71, 403-418 (2011).
- 9 Stiess, M. et al. Axon extension occurs independently of centrosomal microtubule nucleation. *Science* 327, 704-707 (2010).
- 10 Bartolini, F. & Gundersen, G. G. Generation of noncentrosomal microtubule arrays. *J Cell Sci* 119, 4155-4163 (2006).
- 11 Kuijpers, M. & Hoogenraad, C. C. Centrosomes, microtubules and neuronal development. *Mol Cell Neurosci* 48, 349-358 (2011).
- 12 Stiess, M. & Bradke, F. Neuronal polarization: the cytoskeleton leads the way. *Dev Neurobiol* 71, 430-444 (2011).
- 13 Yu, W. et al. The microtubule-severing proteins spastin and katanin participate differently in the formation of axonal branches. *Mol Biol Cell* 19, 1485-1498 (2008).
- 14 Efimov, A. et al. Asymmetric CLASP-dependent nucleation of noncentrosomal microtubules at the trans-Golgi network. *Dev Cell* 12, 917-930 (2007).
- 15 Ori-McKenney, K. M., Jan, L. Y. & Jan, Y. N. Golgi outposts shape dendrite morphology by functioning as sites of acentrosomal microtubule nucleation in neurons. *Neuron* 76, 921-930 (2012).
- 16 Dammermann, A., Desai, A. & Oegema, K. The minus end in sight. *Curr Biol* 13, R614-624 (2003).
- 17 Goodwin, S. S. & Vale, R. D. Patronin regulates the microtubule network by protecting microtubule minus ends. *Cell* 143, 263-274 (2010).
- 18 Baines, A. J. et al. The CKK domain (DUF1781) binds microtubules and defines the CAMSAP/ssp4 family of animal proteins. *Mol Biol Evol* 26, 2005-2014 (2009).
- 19 Meng, W., Mushika, Y., Ichii, T. & Takeichi, M. Anchorage of microtubule minus ends to adherens junctions regulates epithelial cell-cell contacts. *Cell* 135, 948-959 (2008).

- 20 Tanaka, N., Meng, W., Nagae, S. & Takeichi, M. Nezha/CAMSAP3 and CAMSAP2 cooperate in epithelial-specific organization of noncentrosomal microtubules. *Proc Natl Acad Sci U S A* 109, 20029-20034 (2012).
- 21 Jiang, K. et al. Microtubule minus-end stabilization by polymerization-driven CAMSAP deposition. *Dev Cell* In Press (2014).
- 22 Heilemann, M. et al. Subdiffraction-resolution fluorescence imaging with conventional fluorescent probes. *Angew Chem Int Ed Engl* 47, 6172-6176 (2008).
- 23 Rust, M. J., Bates, M. & Zhuang, X. Sub-diffraction-limit imaging by stochastic optical reconstruction microscopy (STORM). *Nat Methods* 3, 793-795 (2006).
- 24 Cheung, Z. H., Chin, W. H., Chen, Y., Ng, Y. P. & Ip, N. Y. Cdk5 is involved in BDNF-stimulated dendritic growth in hippocampal neurons. *PLoS Biol* 5, e63 (2007).
- 25 Halpain, S. & Greengard, P. Activation of NMDA receptors induces rapid dephosphorylation of the cytoskeletal protein MAP2. *Neuron* 5, 237-246 (1990).
- 26 Kapitein, L. C. et al. NMDA receptor activation suppresses microtubule growth and spine entry. *J Neurosci* 31, 8194-8209 (2011).
- 27 Witte, H. & Bradke, F. The role of the cytoskeleton during neuronal polarization. *Curr Opin Neurobiol* 18, 479-487 (2008).
- 28 Witte, H., Neukirchen, D. & Bradke, F. Microtubule stabilization specifies initial neuronal polarization. *J Cell Biol* 180, 619-632 (2008).
- 29 Barnes, A. P. & Polleux, F. Establishment of axon-dendrite polarity in developing neurons. *Annu Rev Neurosci* 32, 347-381 (2009).
- 30 Hoogenraad, C. C. & Bradke, F. Control of neuronal polarity and plasticity--a renaissance for microtubules? *Trends Cell Biol* 19, 669-676 (2009).
- 31 Stepanova, T. et al. Visualization of microtubule growth in cultured neurons via the use of EB3-GFP (end-binding protein 3-green fluorescent protein). *J Neurosci* 23, 2655-2664 (2003).
- 32 Baas, P. W., Black, M. M. & Banker, G. A. Changes in microtubule polarity orientation during the development of hippocampal neurons in culture. *J Cell Biol* 109, 3085-3094 (1989).
- 33 Jiang, K. et al. A Proteome-wide screen for mammalian SxIP motif-containing microtubule plus-end tracking proteins. *Curr Biol* 22, 1800-1807 (2012).
- 34 Bradke, F. & Dotti, C. G. Neuronal polarity: vectorial cytoplasmic flow precedes axon formation. *Neuron* 19, 1175-1186 (1997).
- 35 Kapitein, L. C. & Hoogenraad, C. C. Which way to go? Cytoskeletal organization and polarized transport in neurons. *Mol Cell Neurosci* 46, 9-20 (2011).
- 36 Arimura, N. & Kaibuchi, K. Neuronal polarity: from extracellular signals to intracellular mechanisms. *Nat Rev Neurosci* 8, 194-205 (2007).
- 37 Lee, H. H., Jan, L. Y. & Jan, Y. N. Drosophila IKK-related kinase Ik2 and Katanin p60-like 1 regulate dendrite pruning of sensory neuron during metamorphosis. *Proc Natl Acad Sci U S A* 106, 6363-6368 (2009).

LEGENDS TO SUPPLEMENTARY MOVIES

Movie S1. GFP-CAMSAP2 localizes to MT minus-ends in COS-7 cells

This video corresponds to Figure S3B. COS-7 cells were transfected with GFP-CAMSAP2 (green) and mCherry- α -Tubulin (red). Series of growth and shrinkage of the MT can be seen in respect to the GFP-CAMSAP2 stretch. Total time is 1 minute and 19 seconds. 1 second per frame. Movie is speeded up 15 times.

Movie S2. GFP-CAMSAP2 localizes to MT minus-ends in COS-7 cells

This video corresponds to Figure S3C. COS-7 cells were transfected with GFP-CAMSAP2 (green) and mCherry-MT+TIP (red). Repetitive growth of the comet from the GFP-CAMSAP2 stretch is clearly observed. Total time is 1 minute. 2 seconds per frame. Movie is speeded up 15 times.

Movie S3. GFP-CAMSAP2 localizes to MT minus-ends in neurons

This video corresponds to Figure 2H. Rat hippocampal neurons were transfected with GFP-CAMSAP2 (green) and mCherry-MT+TIP (red). This movie shows several individual MTs that have GFP-CAMSAP2 localized to the MT minus-end. Total time is 5 minutes. 1 second per frame. Movie is speeded up 30 times.

Movie S4. MT plus-end marker originates from CAMSAP2 in neurons

This video corresponds to Figure 2J. Rat hippocampal neurons were transfected with GFP-CAMSAP2 (green) and mCherry-MT+TIP (red). MT plus-end marker mCherry-MT+TIP originates from CAMSAP2. Total time is 44 seconds. 2 seconds per frame. Movie is speeded up 30 times.

Movie S5. GFP-CAMSAP2 recovers at one end of CAMSAP2 stretches in neurons

This video corresponds to Figure 3B. Rat hippocampal neurons were transfected with GFP-CAMSAP2. FRAP was performed at time point $t=1:30$ (m:s). GFP-CAMSAP2 recovers specifically on MT minus-ends. Total time is 15 minutes. 10 seconds per frame. Movie is speeded up 150 times.

Movie S6. CAMSAP2 clusters grow into extended stretches in neurons

This video corresponds to Figure 3F, which is related to Figure 1G-I. Rat hippocampal neurons were transfected with GFP-CAMSAP2 (green) and mRFP (red). FRAP was performed at time point $t=3:00$ (m:s). GFP-CAMSAP2 specifically recovers at the MT minus-end. Multiple recoveries can be observed which reveal that CAMSAP2 stretches in dendrites enlarge towards both the proximal and distal regions. Total time is 40 minutes. 20 second per frame. Movie is speeded up 600 times.

Movie S7. GFP-CAMSAP2 accumulates on newly formed MT minus-ends

This video corresponds to Figure 5B. COS-7 cells were transfected with GFP-CAMSAP2 (green) and mCherry-MT+TIP (red). MT was laser-induced severed at time point $t=44s$, the asterisk points the area of laser-induced severing. GFP-CAMSAP2 accumulates onto the newly formed MT minus-end over time and the MT continues to be dynamic. Total time is 1 minute and 55 seconds. 1 second per frame. Movie is speeded up 15 times.

Movie S8. GFP-CAMSAP2 accumulates on newly formed MT minus-ends in neurons

This video corresponds to Figure 5F. Rat hippocampal neurons were transfected with GFP-CAMSAP2 (green) and mCherry-MT+TIP (red). MT was laser-induced severed at time point $t=13s$, the asterisk points the area of laser-induced severing. GFP-CAMSAP2 accumulates onto the newly formed MT minus-end over time and the MT continues to be dynamic. Total time is 1 minute and 33 seconds. 1 second per frame. Movie is speeded up 30 times.

Movies are available online

<http://dx.doi.org/10.1016/j.neuron.2014.04.019>



SUPPLEMENTARY FIGURES

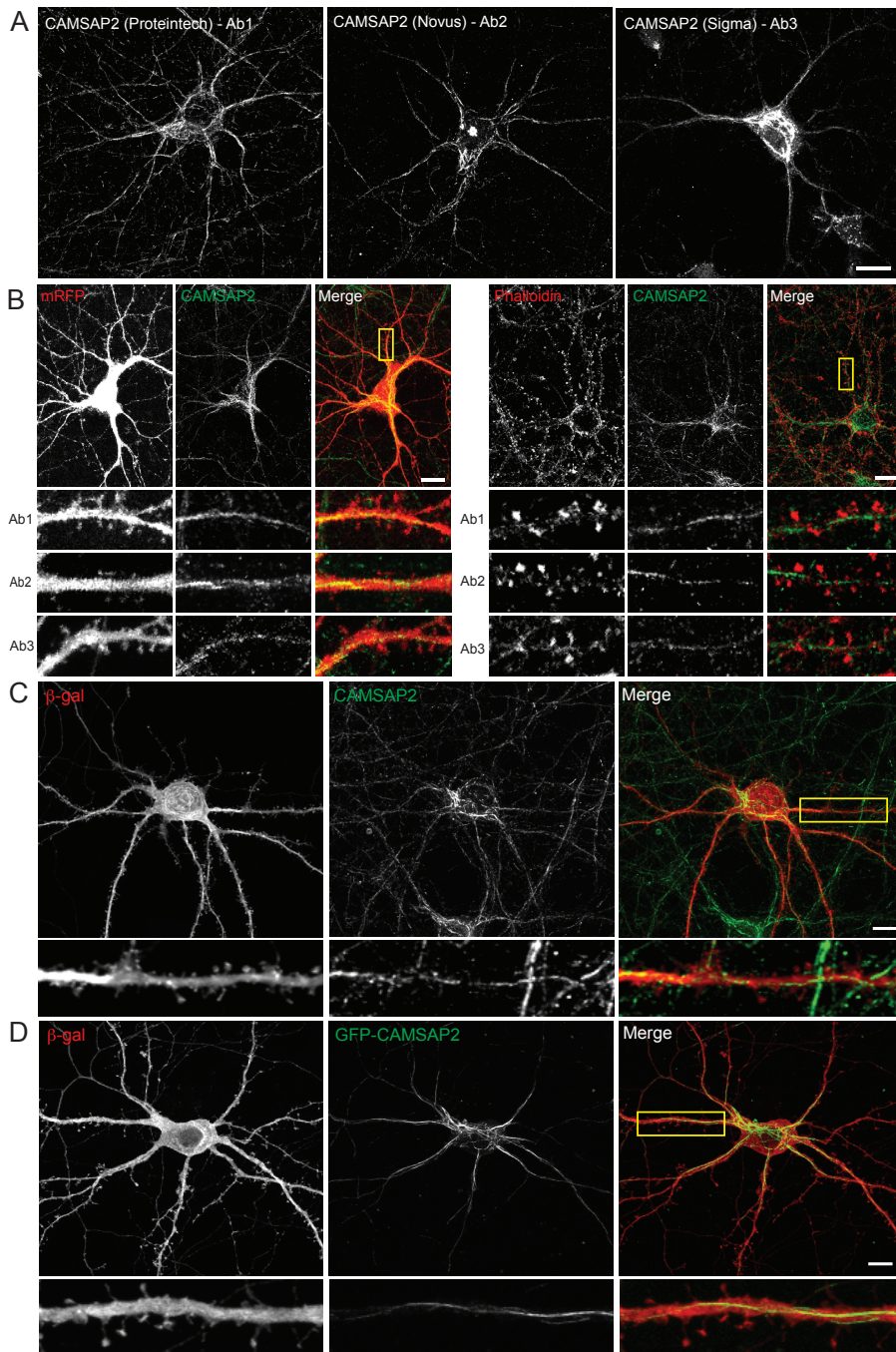


Figure S1 (related to Figure 1C-F): Three independent CAMSAP2 antibodies label small clusters and distinct stretches in hippocampal neurons

A) DIV 21 neurons immunostained with CAMSAP2 antibodies from three different companies. CAMSAP2 antibodies are purchased from Proteintech (Bioconnect) (CAMSAP2 antibody 1), Novus Biologicals (CAMSAP2 antibody 2) and Sigma (CAMSAP2 antibody 3). CAMSAP2 antibody 1 is the most used in this study and labels small clusters and distinct stretches throughout the neurons. This signal was strongly decreased after knockdown of CAMSAP2 with two CAMSAP2 shRNAs. In addition to typical CAMSAP2 clusters and stretches, CAMSAP2 antibody 2 labels the nucleolus and CAMSAP2 antibody 3 labels the Golgi apparatus in hippocampal neurons. Antibodies 2 and 3 probably cross react, since CAMSAP2 depletion did not decrease the nucleolus and Golgi staining, respectively.

B) Left panel shows neurons that are transfected at DIV 19 with mRFP fixed at DIV 21 and stained for CAMSAP2 with 3 different antibodies as described in A). Right panel shows neurons fixed at DIV 21, double stained for 3 different CAMSAP2 antibodies with phalloidin.

C) Neurons are transfected with β -Galactosidase (red), fixed at DIV 22 and stained for endogenous CAMSAP2 (green).

D) Neurons are transfected with β -Galactosidase (red) and GFP-CAMSAP2 (green) and fixed at DIV 22. Scale bars are 10 μ m.

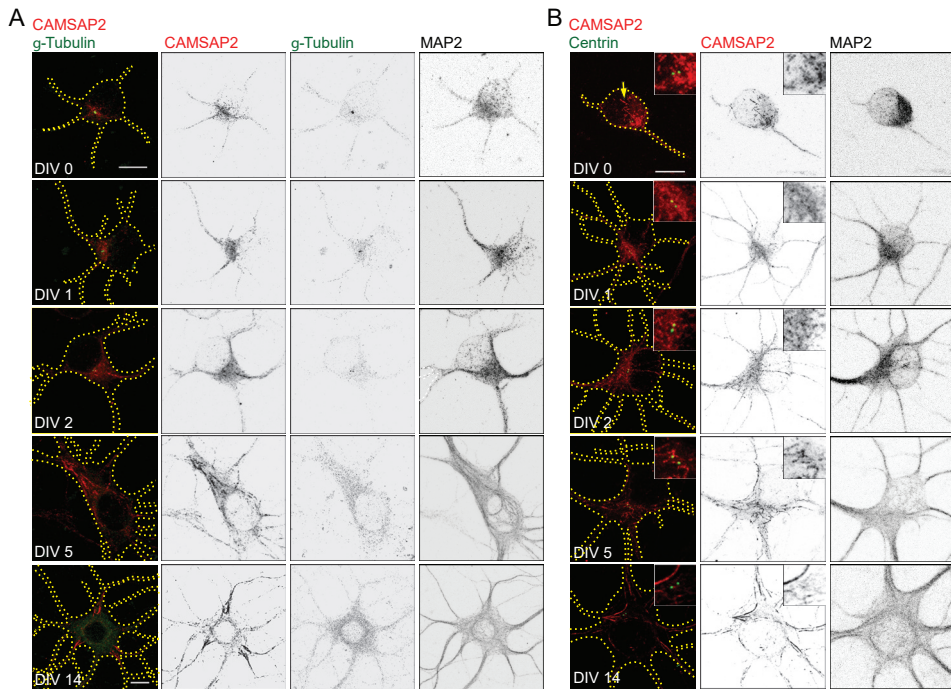


Figure S2 (related to Figure 1C-H): Endogenous CAMSAP2 expression and distribution in hippocampal neurons throughout development

A) Maximum intensity confocal projections representing the distribution and dynamics of CAMSAP2 and γ -Tubulin throughout development. Hippocampal neurons were fixed at the indicated time points and immunostained for CAMSAP2 (red), γ -Tubulin (green) and MAP2. All images were acquired with the same light intensity and exposure time. Individual neurons are outlined by dashed lines that represent the cell outline as judged by CAMSAP2, γ -Tubulin and MAP2 signals. Scale bar is 10 μ m.

B) Maximum intensity confocal projections representing the distribution and dynamics of CAMSAP2 around the centrioles throughout development. Hippocampal neurons were fixed at the indicated time points and immunostained for CAMSAP2 (red), Centrin (green) and MAP2. All images were acquired with the same light intensity and exposure time. Insets depict the indicated centriole areas (2.5x magnification). Individual neurons are outlined by dashed lines that represent the cell outline as judged by CAMSAP2 and MAP2 signals. Scale bar is 10 μ m. Note that CAMSAP2 stretches are present in areas devoid of the centrosome already from DIV0 (marked with an arrow).

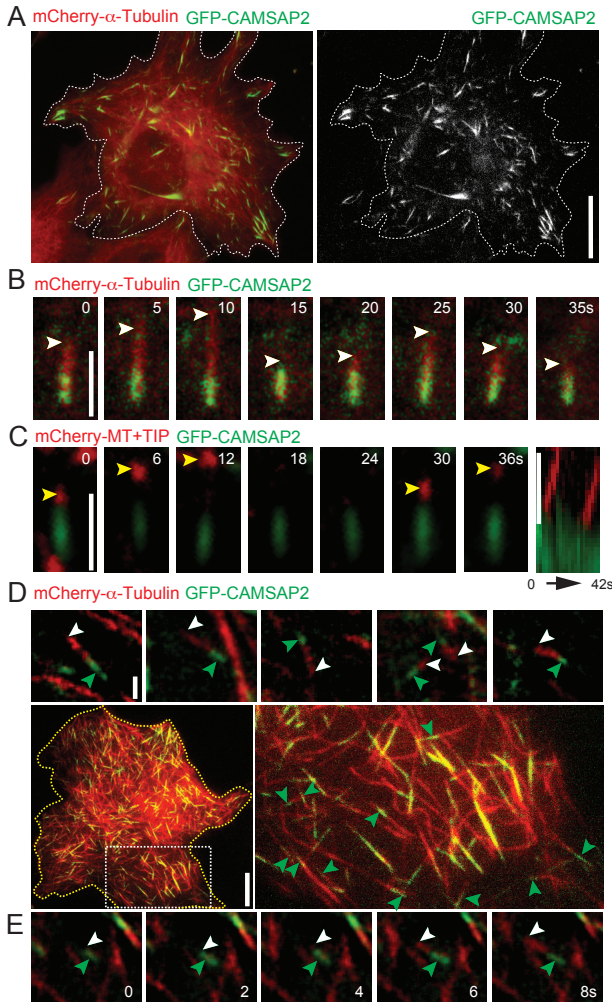


Figure S3 (related to Figure 2H-K):
CAMSAP2 localizes to microtubule minus-ends in COS7 cells

A) An example of a COS7 cell transfected with mCherry- α -Tubulin (red) and GFP-CAMSAP2 (green). Scale bar is 10 μ m.

B) Stills from TIRFM time-lapse recordings of a COS7 cell expressing mCherry- α -Tubulin (red) and GFP-CAMSAP2 (green). The white arrowheads indicate the growing MT plus-end. Scale bar is 2 μ m.

C) Stills from TIRFM time-lapse recordings of a COS7 cell expressing mCherry-MT+TIP (red) and GFP-CAMSAP2 (green). The yellow arrowheads indicate the MT plus-end marker. The kymograph corresponds to the time-lapse recording. Scale bar is 2 μ m.

D) An example of a COS7 cells are transfected with mCherry- α -Tubulin (red) and GFP-CAMSAP2 (green). Top row shows stills (low-pass filtered) from a TIRFM time-lapse recording of the COS7 cell shown in the bottom row. The white arrowheads indicate the fast growing MT plus-ends, green arrow heads indicate the MT minus-ends positive for GFP-CAMSAP2. The middle row shows a COS7 cell outlined with a dashed yellow line. Scale bars are 1 and 10 μ m.

E) TIRFM time-lapse recording stills (low-pass filtered) from an area in the inset shown in D).

Figure S4 (related to Figure 4A,B): Knockdown efficiency of CAMSAP2- and γ -Tubulin-shRNAs

A) Representative images of hippocampal neurons transfected with fill β -Galactosidase (red) and control or CAMSAP2-shRNA1 (KD1) using Lipofectamine 2000 (L2K). Representative examples of the soma and dendrite are shown. Neurons are transfected at DIV 16 and fixed at DIV 20.

B) Normalized intensities of CAMSAP2 for control neurons ($n=14$) or neurons transfected with either of the two different CAMSAP2 shRNAs ($n=18$ for CAMSAP2-shRNA1 (KD1), $n=6$ for CAMSAP2-shRNA2 (KD2)) at DIV16 for 4 days. AU, arbitrary units.

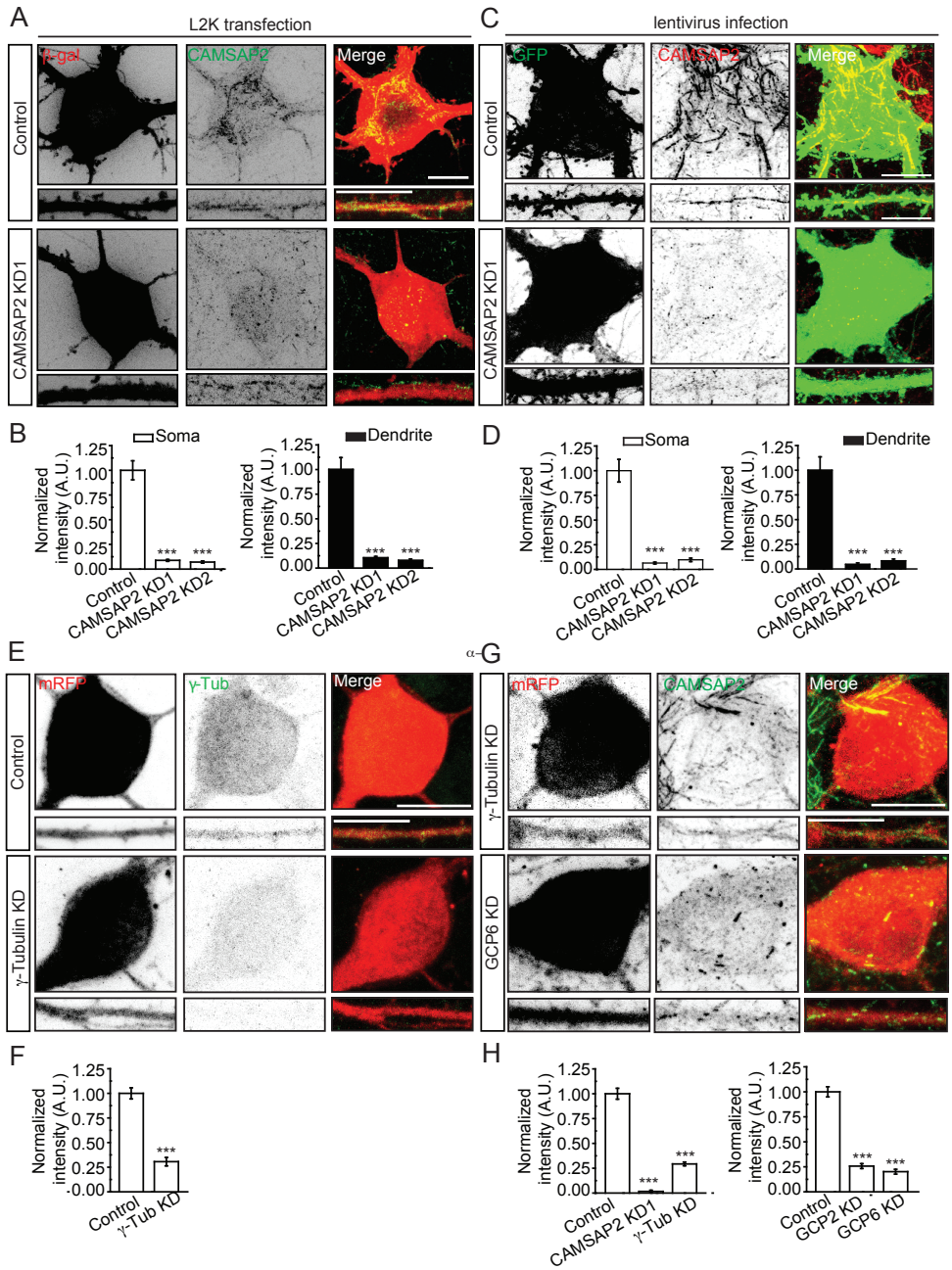
C) Representative images of hippocampal neurons (DIV21) infected with lentivirus expressing MARCKS-GFP (green) and control or CAMSAP2-shRNA1 (KD1). Neurons are stained for endogenous CAMSAP2.

D) Normalized intensities of CAMSAP2 for control neurons ($n=19$) and neurons infected with control, CAMSAP2-shRNA1 ($n=23$) or GFP-CAMSAP2-shRNA2 ($n=16$). AU, arbitrary units.

E) Confocal maximum intensity projection images of the fill mRFP (red) and endogenous γ -Tubulin (green).

Representative examples of the soma and dendrite are shown. Neurons are transfected at DIV 16 and fixed at DIV 20.

F) Normalized intensities of γ -Tubulin for control neurons ($n=18$) or neurons transfected with γ -Tubulin shRNAs ($n=9$) at DIV17 and fixed at DIV21. AU, arbitrary units.



G) Confocal maximum intensity projection images of the fill mRFP (red) and endogenous CAMSAP2 (green), where representative examples of the soma and dendrite are shown. Neurons are transfected at DIV 16 and fixed at DIV 20. **H**) Normalized intensities of CAMSAP2 for control neurons ($n=11$) or neurons transfected with γ -Tubulin shRNAs ($n=11$), GCP2 shRNA ($n=11$) or GCP6 shRNA ($n=11$) at DIV17 for 4 days. AU, arbitrary units. Error bars represent SEM. *** $P<0.001$. Scale bars are 10 μ m.

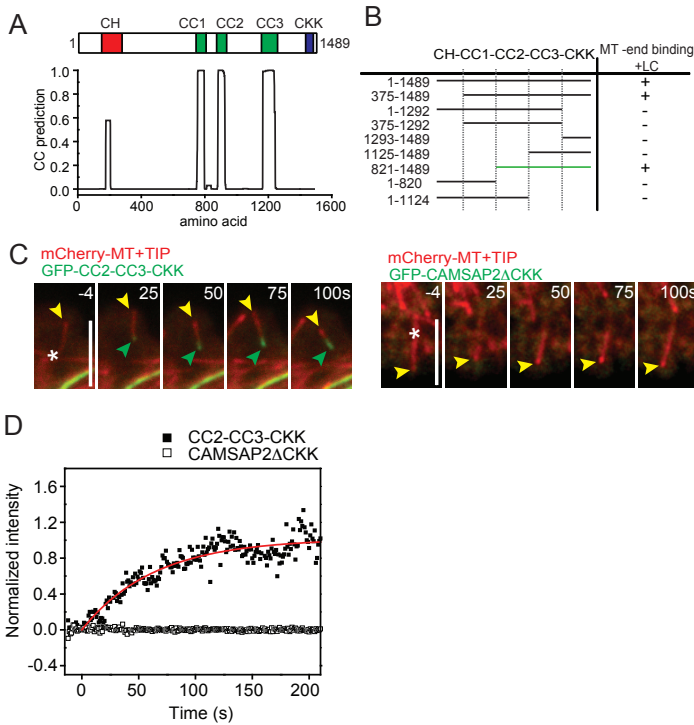


Figure S5 (related to Figure 6K): CAMSAP2 mutants accumulate on new microtubule minus-ends

A) Coiled coil prediction diagram of CAMSAP2 protein. N-terminal CH domain is indicated in red, the central coiled coil domains are indicated in green and the C-terminal CKK domain is indicated in blue.

B) Mapping of the minimal MT minus-end binding domain of CAMSAP2. The mutant indicated with a green line consists of the minimal domains required for MT minus-end binding after laser-induced severing of the MT.

C) Left row shows merge stills from a TIRFM time-lapse recording where a COS-7 cell is transfected with mCherry-MT+TIP (red) and GFP-CC2-CC3-CKK (green), CAMSAP2 mutant (821-1489). Yellow arrow heads indicate the MT plus-end marker. Green arrow heads indicate GFP-CC2-CC3-CKK accumulation on the MT minus-end after laser-induced severing. Right row shows merge stills from a TIRFM time-lapse recording where a COS-7 cell is transfected with mCherry-MT+TIP (red) and GFP-CAMSAP2ΔCKK (green), CAMSAP2 mutant (1-1292). Yellow arrow heads indicate the MT plus-end marker. Asterisk indicates the area of laser-induced severing. MT is laser-induced severed at $t=0$. Both time-lapse recordings are low-pass filtered. Scale bars are 5 μm .

D) Intensity time traces corresponding to the stills in C). The black squares represent the intensity time trace of the left row in C). The white squares represent the intensity time trace from the bottom right in C). Single exponential fit of the black squares is shown in red.

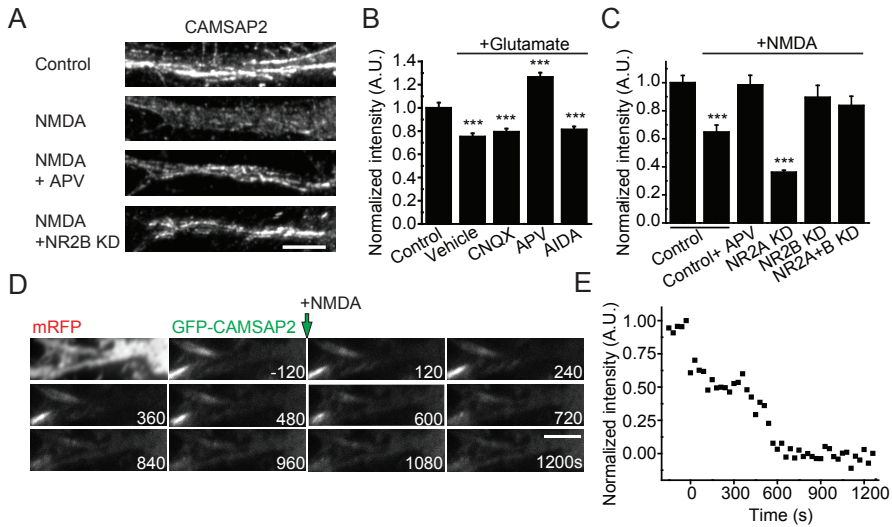


Figure S6 (related to Figure 6): Neuronal activity affects the distribution of CAMSAP2 in dendrites

A) Dendritic regions of hippocampal neurons at DIV 22 with endogenous CAMSAP2 staining treated with 50 μ M NMDA for 5 min and recovered for 25 min. From top to bottom representative control, NMDA treatment, APV and NMDA treatment and NR2B KD and NMDA treatment are shown. Scale bars are 5 μ m.

B) Diagram showing the normalized mean intensity of CAMSAP2 in dendritic regions from neurons, which have been untreated ($n=20$), treated with 50 μ M glutamate for 5 min (and recovered for 25min) alone ($n=16$) or combined with either 10 μ M CNQX ($n=19$), 100 μ M APV ($n=19$) or 50 μ M AIDA ($n=19$). AU, arbitrary unit. *** $P<0.001$ (T-test).

C) Diagram showing the normalized mean intensity of CAMSAP2 in dendritic regions from neurons, which have been untreated ($n=11$), treated with 50 μ M NMDA for 5 min (and recovered for 25min) alone ($n=9$) or combined with either 100 μ M APV ($n=12$), NR2A shRNA ($n=13$), NR2B shRNA ($n=7$) or NR2A/B shRNAs ($n=9$). AU, arbitrary unit. *** $P<0.001$ (T-test).

D) Stills from TIREM time-lapse recordings of a dendritic segment of a hippocampal neuron (DIV 15) expressing GFP-CAMSAP2 and mRFP to highlight the morphology. The first image is an average projection from the mRFP channel showing the dendritic region. At $t=0$ neurons are treated with 50 μ M NMDA bath application. Scale bar is 5 μ m.

E) Intensity time trace of GFP-CAMSAP2 corresponding to the time-lapse recording in D).

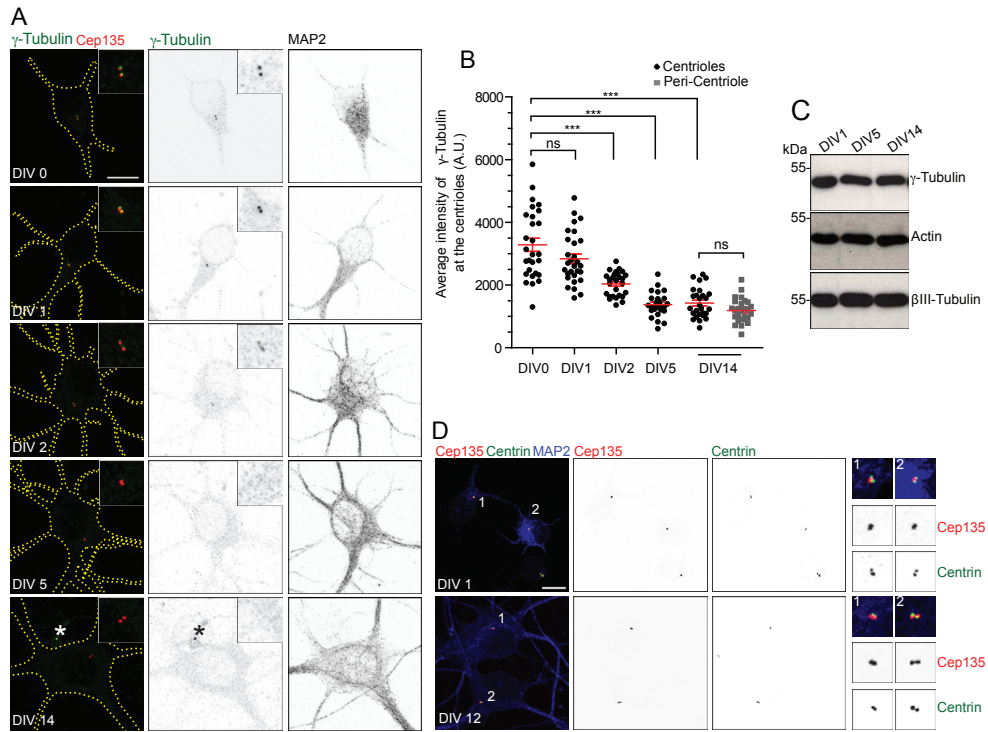


Figure S7 (related to Figure 7A): Endogenous γ -Tubulin expression and distribution in hippocampal neurons throughout differentiation

A) Maximum intensity confocal projections representing the distribution and dynamics of γ -Tubulin at centrioles throughout differentiation. Hippocampal neurons were fixed at the indicated time points and immunostained for γ -Tubulin (green), Cep135 (centriole marker, in red) and MAP2. All images were acquired with the same light intensity and exposure time. Insets depict the indicated centriole areas (2.5x magnification). Individual neurons are outlined by dashed lines that represent the cell outline as judged by γ -Tubulin and MAP2 signals. Scale bar is 10 μ m. Note that although γ -Tubulin is absent from centrioles in DIV 14, it is detected at centrioles of the surrounding glia cells (marked with an asterisk).

B) Quantification of endogenous γ -Tubulin levels at both centrioles throughout hippocampal neuron differentiation. Centriolar γ -Tubulin was measured at the indicated time points. At least 26 hippocampal neurons were analyzed per developmental time point (DIV 0-14). Represented is the average intensity of γ -Tubulin at the centrioles. The average intensity of γ -Tubulin in the peri-centriolar area is also represented for DIV 14. Note that the total levels of γ -Tubulin at DIV5 and DIV14 at the centriole do not differ from the ones measured at the peri-centriolar area. The statistical difference between sample distribution of DIV0 and the other stages was evaluated with a Mann-Whitney test (***, $p < 0.001$; ns, not statistically significant).

C) γ -Tubulin protein is expressed at constant levels throughout neuron differentiation. Extracts of hippocampal neurons were prepared at the indicated time points and probed by Western blot for γ -Tubulin, actin (loading control) and β III-Tubulin (loading control) antibodies.

D) Cep135, used in A) is a bona-fide centriolar marker in hippocampal neurons. Maximum intensity confocal projections representing the localization of Cep135 at both centrioles in hippocampal neurons throughout differentiation. Hippocampal neurons were fixed at the indicated time points and immunostained for Cep135 (red), Centrin (centriole marker, in green) and MAP2. Insets depict the indicated centriole areas (3x magnification). Scale bar is 10 μ m.

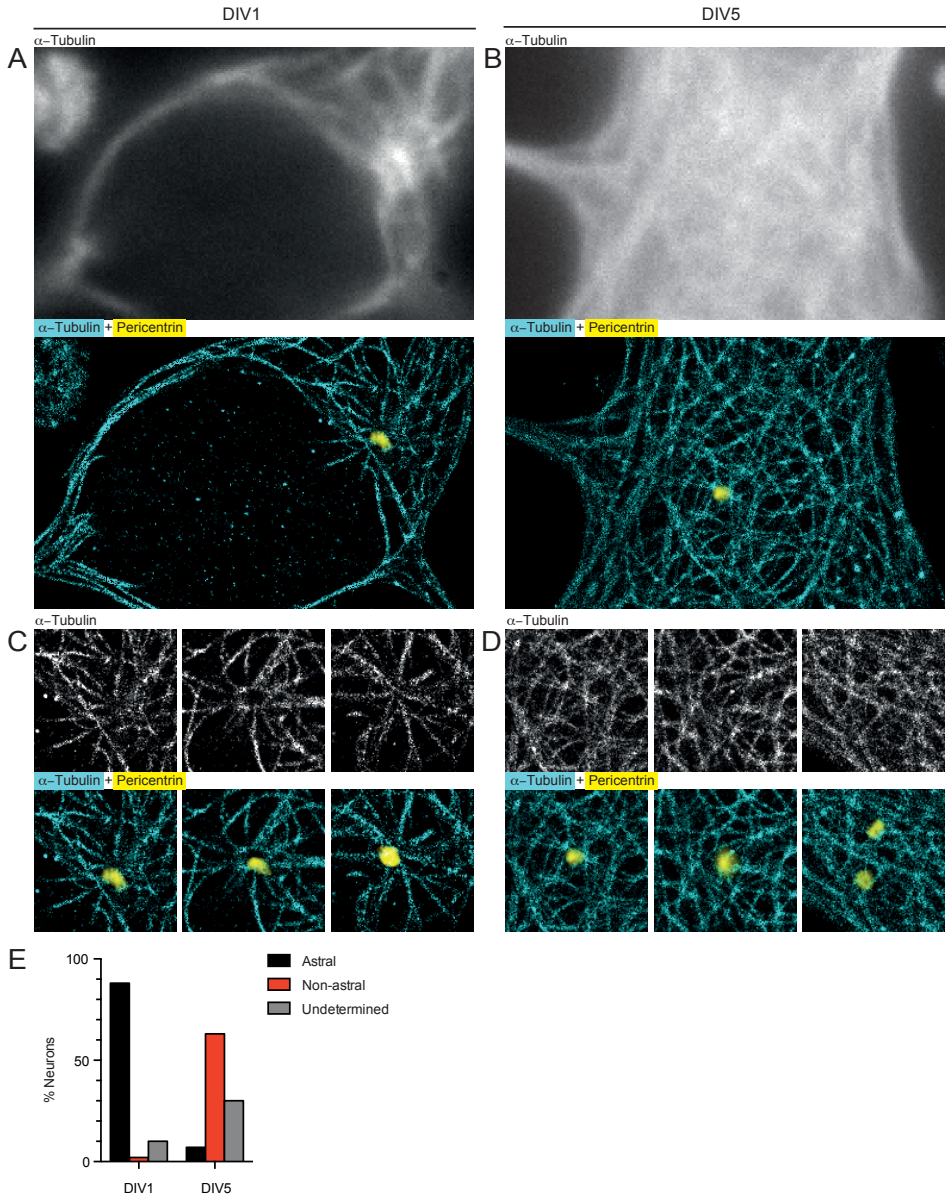


Figure S8 (related to Figure 7A): dSTORM analysis of microtubule organization in DIV1 and DIV5 neurons
A,B Conventional widefield image (top) and corresponding dSTORM reconstruction (bottom) of a neuron at DIV1 (A) and DIV5 (B), labeled with primary antibodies against α -tubulin and AlexaFluor647-labeled secondary antibodies. dSTORM image is overlaid with the conventional widefield image of Pericentrin staining to locate the centrosome (visualized using an AlexaFluor488-labeled secondary antibody). Scale bars are 2 μ m.

C,D Top: Three zooms of microtubule organization around the centrosome for three neurons at DIV1 (C) and DIV5 (D), including the neurons shown in A) and B). Bottom: Overlay of dSTORM microtubule image with conventional widefield image of pericentrin. Scale bars are 2 μ m.

E Occurrence of astral and non-astral microtubule organization for neurons at DIV1 (N=50 neurons) or DIV5 (N=43 neurons).

SUPPLEMENTARY MATERIALS AND METHODS

Antibodies and reagents

The following primary and secondary antibodies were used in this study: rabbit anti-EB3 (02-1005-07), mouse anti-MAP2 (HM-2, M 9942, Sigma), chicken polyclonal anti-MAP2 (Abcam), mouse anti-acetylated-Tubulin (6-11B-1, T7451, Sigma), rat anti-tyrosinated-Tubulin (YL1/2, ab6160, Abcam), rabbit anti-GFP (598, MBL), mouse anti-Nestin (611658, BD Transduction Laboratories), mouse anti-Tau (PC1C6, MAB3420, Chemicon), mouse anti-Bassoon (SAP7F407, VAM-PS003, Stressgen), mouse anti- γ -Tubulin (T6557, Sigma), mouse anti-Centrin (20H5, Milipore), rabbit polyclonal anti-Cep135 (Sigma), rabbit anti-CAMSAP1 (Novus Biologicals, NBP1-26645), rabbit anti-CAMSAP2 (17880-1-AP, Proteintech; NBP1-21402, Novus Biologicals; HPA0273, Sigma), rabbit anti-CAMSAP3 (Abgent, AP18323a), mouse anti-AFP (3E6, AFP5002), chicken anti- β -Galactosidase (BGL-1040, Aveslab), rabbit anti-EB3 [1], mouse anti-Ankyrin G (N106/36, NeuroMab, clone 4G3F8, Life Technologies), mouse anti-pan-Nav (S8809, Sigma), rabbit anti- β IV-Spectrin (gift from Dr. Rasband, [2]), Alexa-350-, Alexa 488-, Alexa 568- and Alexa 594- conjugated secondary antibodies (Invitrogen). Other reagents used in this study include: Nocodazole (M1404, Sigma), Taxol (T7402, Sigma), brain derived neurotrophic factor (rhBDNF G1491, Promega), DL-2-amino-5-phosphonopentanoic acid (APV), 6-cyano-7-nitroquinoline-2,3-dione (CNQX), N-methyl-D-aspartic acid (NMDA), 1-aminoinidan-1,5-dicarboxylic acid (AIDA). A recombinant single chain antibody against GFP, bio-VHHGFP, was derived from VVHGFP4 [3], subcloned into pMXB10-bio, and purified from bacteria using the intein system (IMPACT Kit, NEB).

DNA and shRNA constructs

The following mammalian expression plasmids have been described: pGW2-mRFP, pGW1-GFP, pbactin-HA- β -Galactosidase [4], pSuper vector [5], pCDNA3.1-mCherry- α -Tubulin [6]. All other constructs were created using PCR based strategy. For CAMSAP2 the human CAMSAP2 cDNA (IMAGE clone 40124603) was used to create CAMSAP2 fusion construct in pGW1-GFP. This construct was used to create all other CAMSAP2-mutant constructs and cloned into pGW1-GFP. For CAMSAP1 the human CAMSAP1 cDNA (IMAGE clone 40146611) was used to generate pGW1-GFP-CAMSAP1. For CAMSAP3 the mouse CAMSAP3 cDNA (IMAGE clone 6489361) was used to generate pGW1-GFP-CAMSAP3. The mCherry-MT+TIP construct contains the general microtubule tip localization signal, SxIP motif recognized by microtubule plus-end binding (EB) proteins [7] and was generated as follows. The two-stranded leucine zipper coiled-coil sequence corresponding to GCN4-p1 (RMKQLEDKVEELLSKNYHLENEVARLKKLVGER) was fused to N-terminal 43 amino acid peptide (ETVPQTHRPTPRAGSRPSTAKPSKIPTPQRKSPASKLKDSSKR) of human MACF2 (E5455-R5497; NP_899236) by PCR based strategy [7]. A glycine rich-linker sequence (GAGG) was inserted between GCN4-pl and MACF43 and subcloned in pbactin-16-pl expression vectors [4] to generate pbactin-mCherry-GCN4-MACF43. Since we use mCherry-GCN4-MACF43 as a general marker to analyze the dynamics of microtubule growing plus-ends, we named this construct mCherry-MT+TIP. The following shRNAs were created and used in this study: g-Tubulin-shRNA (5'-ggaggacatctcaaggac) [8], GCP2-shRNA (5'-tggcctgtctactgatta), GCP6-shRNA (5'-gaccatcaacctactgaag) CAMSAP2-shRNA1, (5'-ttgcatgtgctcaacagt), CAMSAP2-shRNA2 (5'-attcagaagaatcgggtg) and an additional mouse CAMSAP2-shRNA (5'-acacataatcagaatgct) used for *in utero* electroporation.

Lentivirus generation and transduction of neuron cultures

RNAi expression cassettes (H1 promoter + shRNA) from pSuper constructs were excised via BamHI and ClaI sites and inserted in pLVTHM-GFP lentivirus vector backbone (Addgene 12247) [9]. Lentiviral particles were produced in HEK293T cells by polyethylenimine (PEI) transfection of 100 μ g pLVTHM-GFP plasmid, 35 μ g env plasmid (pMD2.G) and 65 μ g packaging plasmid (pCMV Δ R8.2) in a 500 cm² dish. Cell culture medium was exchanged to Opti-MEM medium after 6h and viral particles were harvested 48 h after transfection. Virus containing supernatant was cleared from debris (centrifugation 4000g, 30 min) and reduced from 100ml to 300 μ l by tangential flow filtration (Amicon Ultra-15 100K). Concentrated virus solution was diluted 1:1 in PBS, snap frozen in liquid nitrogen, and stored at -80°C until further usage. For CAMSAP2 knockdown experiments, 20 μ l of virus stock was applied at DIV 15 and DIV 20.

Primary hippocampal neuron cultures, transfection and immunohistochemistry

Primary hippocampal cultures were prepared from embryonic day 18 rat brains. Cells were plated on coverslips coated with poly-L-lysine (30µg/ml) and laminin (2µg/ml) at a density of 75,000/well. Hippocampal cultures were grown in Neurobasal medium (NB) supplemented with B27, 0.5 µM glutamine, 12.5 µM glutamate and penicillin/streptomycin. Hippocampal neurons were transfected using Lipofectamine 2000 (Invitrogen). Briefly, DNA (1.8 µg/well, for a 12 wells plate) was mixed with 3.3 µl of Lipofectamine 2000 in 200µl NB, incubated for 30 min, and then added to the neurons in NB at 37°C in 5% CO₂ for 45 min. Next, neurons were washed with NB and transferred in their original medium at 37°C in 5% CO₂ for 2-4 days. For BDNF-induced dendritic growth experiments, mature neurons were treated with 50 ng/ml BDNF for 3 days [10]. For Taxol experiments, 10 nM Taxol was added to culture medium 1 day after plating and cells were further incubated for 48 hours at 37°C in the presence of the drug [11].

For general immunohistochemistry, neurons were fixed for 10 min with 4% paraformaldehyde (PFA)/4% sucrose in PBS at room temperature or 10 min with ice-cold methanol 100% containing 1mM EGTA at -20°C. For detection of CAMSAP2, γ -Tubulin, Cep135, and Centrin neurons were fixed in ice-cold methanol for 10 minutes at 100% containing 1 mM EGTA at -20°C. Fixing neurons to stain for EB3 comets required 2 min with ice-cold methanol 100% with 1mM EGTA at -20°C and subsequently 8 min with 4% paraformaldehyde/4% sucrose in PBS. After fixation cells were washed 3 times for 5 min in PBS at room temperature and incubated with the primary-antibody mix in GDB buffer (0.2% BSA, 0.8M NaCl, 0.5% Triton X-100, 30mM phosphate buffer, pH 7.4) overnight at 4°C. Next the neurons were washed 3 times for 5 min in PBS at room temperature and incubated with the secondary-antibody mix in GDB buffer for at most 1 hour at room temperature. Neurons were then washed 3 times for 5 min in PBS at room temperature and subsequently mounted on slides in Vectashield mounting medium (Vector Laboratories). To extract soluble cytoplasmic proteins before staining, neurons were fixed and extracted [12]. Confocal images were acquired using AR1-A1 confocal (Nikon), LSM510 (Zeiss), LSM 5 Pascal, or LSM 700 with a 20x (dry), 40x (oil), 63x (oil), or 100x (oil) objective. A total thickness of 10µm was scanned for each position and imaging settings were kept the same when pictures were compared for fluorescence intensity.

Primary cortical neuron cultures and nucleofection

Primary cortical neurons were isolated from E18 rat brain. Cells (1x10⁶) were transfected using the Amaxa Rat Neuron Nucleofector kit (Lonza) with 3µg of plasmid DNA and plated on coverslips coated with poly-L-lysine (37.5µg/ml) and laminin (5µg/ml) in 12-wells plates (2-6 x10⁴ cells/well) containing DMEM supplemented with 10% FBS [13]. Cells were allowed to recover and adhere to the surface at 37°C in 5% CO₂, after 4 hours the medium was replaced with Neurobasal medium supplemented with 2% B27, 0.5mM glutamine, 15.6µM glutamate, and 1% penicillin/streptomycin. Cells were grown for 4 days at 37°C in 5% CO₂ prior to fixation.

Cell culture heterologous cells

African Green Monkey SV40-transformed kidney fibroblast cells (COS7) and Human Embryonic Kidney 293 cells (HEK293) cells were cultured in DMEM/Ham's F10 (50%/50%) containing 10% Fetal Calf Serum (FCS) and 1% penicillin/streptomycin at 37°C and 5% CO₂. Prior to transfection, COS-7 cells were plated on 24mm glass coverslips for at least 2 days. COS-7 cells were transfected with Fugene6 (Roche) according to manufacturer's protocol, and incubated overnight. HEK293 cells were transfected for 48 hours with GFP-CAMSAP1, GFP-CAMSAP2 and GFP-CAMSAP3 constructs with polyethylenimine (PEI, Polysciences).

Cell extracts and Western blot

HEK293 whole cell lysates were prepared by resuspending cells in equal amounts of lysis buffer containing 25mM Tris-HCl pH 8.0, 50mM NaCl, 0.5% Triton X-100 supplemented with 1x protease inhibitors cocktail (Roche). The soluble fraction was separated by centrifugation at 14000 RPM for 10 minutes and supplemented with sample buffer 4x (8% SDS, 25% glycerol, 0.05M Tris pH 6.8, 400mM DTT and 40mg/l bromophenol blue).

Hippocampal homogenates of embryonic (E18) and adult (7 weeks) rats were prepared in ice cold extraction buffer containing 20mM Tris, pH 8.0, 150mM NaCl, 1% Triton-X100 and protease inhibitors cocktail (Roche) in a ratio of tissue and buffer 1:10. Rat primary hippocampal neurons (E18) were plated at a density of 20000 cells/cm² in 6-well dishes. After 1, 5 and 14 days in vitro (DIV), cells were lysed in hot denaturing sample buffer. Lysates prepared from 6 individual wells were pooled together. Single wells with lentiviral transduced

hippocampal cultures were lysed by the same method. Equal protein concentrations were adjusted before supplementing with 4x sample buffer. Samples were boiled at 99° C for 5 minutes and centrifuged at 16000 g before being analysed by SDS-PAGE. Proteins were transferred on PVDF membranes (Millipore) using a wet blotting system (Bio-Rad). Membranes were blocked and incubated with primary antibodies (overnight at 4°C) in PBST (0.1% Triton X-100, 2% BSA). Peroxidase-coupled secondary antibodies were applied for 1 hour. Following primary CAMSAP antibodies have been used for detection: CAMSAP1 rabbit antibody (Novus, NBP1-26645 at 1:500), CAMSAP2 (Proteintech/NBP1-21402 at 1:500 for endogenous or 1:50000 for overexpression) and CAMSAP3 rabbit antibody (Abgent, RB24779 at 1:250). For quantifying CAMSAP2 depletion, the relative intensities of CAMSAP2 for each sample were obtained by normalization to the actin loading control. The percentage of depletion for each CAMSAP KD sample was obtained by normalization of the relative intensities with the relative intensity of the control (KD1 92%, KD2 81%). Quantifications were performed with Image J.

Live-cell imaging and laser-induced severing

Total internal reflection fluorescence microscopy (TIRFM) was performed on an inverted microscope (Nikon Eclipse Ti with Perfect Focus System) with a CFI Apo TIRF 100x objective, 1.49 numerical aperture (NA), oil objective (Nikon) with an Evolve 512 EMCCD camera (Photometrics) and CoolSNAP HQ2 CCD (Photometrics). MetaMorph software is used to control the camera and all motorized parts. The microscope is further outfitted with an ASI motorized stage MS-2000-XY, Optosplit III, ILas2 system (Roper Scientific), Shutter LB10-3. For fluorescence excitation a Calypso 491 nm, 100mW laser and Jive 561, 100mW laser (Cobolt). A Teem Photonics 532 nm Q-switched pulsed laser is used for laser-induced severing [14,15]. ET-GFP/mCherry dichroic (59022 Chroma) and ET-mCherry (49008 Chroma) are used for wavelength selection. In order to perform laser-induced severing using the 532 nm Q-switched pulsed laser during simultaneous dual-color imaging, the filter cube containing mCherry dichroic was switched with ET-mCherry and switched back after laser-induced severing was successful. Frames recorded in the switched period were not taken into account for analysis of the intensity traces of CAMSAP2. No signs of toxicity or blebbing of cells was observed during laser-induced severing. All imaging was performed in full conditioned medium (for neurons) or Ringer's buffer (for COS-7 cells, 10mM Hepes, 155mM NaCl, 1mM CaCl₂, 1mM MgCl₂, 2mM NaH₂PO₄, 10mM glucose, pH 7.4). A Tokai Hit Stage Top Incubator (INUBG2E-ZILCS) was used to maintain an optimal environment for the cells. The FRAP experiments were performed on TIRF microscope system using the ILas2 system (Roper Scientific).

Ex vivo electroporation and organotypic slice cultures.

Pregnant C57Bl/6 mice were sacrificed by cervical dislocation and E14.5 embryos were rapidly removed and decapitated. CAMSAP2 shRNA1/2 (0.6µg/µl) and/or a GFP vector (0.4 or 1µg/µl) dissolved in 0,05% Fast Green was injected in the lateral ventricles using glass micro-pipettes (Harvard Apparatus). Heads were electroporated using an ECM 830 Electro-Square-Porator (Harvard Apparatus) set to three unipolar pulses at 30V (100ms interval and pulse length) and using gold-plated Genepaddles (Fisher Scientific). Brains were then isolated, collected in ice-cold cHBSS, embedded in 3% LMP-agarose (Fisher Scientific) in cHBSS and sectioned coronally into 350µm thick slices using a vibratome (Leica). Sections were collected on poly-D-lysine-laminin-coated culture membrane inserts (Falcon), placed on top of slice culture medium (70% v/v Basal Eagle Medium, 26% v/v cHBSS, 2% Horse Serum, 20mM D-glucose, 1mM L-glutamine, penicillin/streptomycin) and cultured for 3 days prior to fixation in 4% paraformaldehyde in PBS. Fixed slices were blocked and permeabilized in 3% BSA + 0.1% Triton X-100 in PBS followed by a primary antibody staining against GFP (rabbit, MBL international Cat. 598) and secondary antibody labeled with Alexa488 (Life Technologies). Slices were mounted in Vectashield containing DAPI (Vector Laboratories Cat. H-1200). Z-stack acquisitions were taken using conventional confocal microscopy using a LSM700 (Zeiss). The degree of neuronal migration was quantified as described previously [16].

In utero electroporation

Pregnant C57Bl/6 mice at E14.5 were deeply anaesthetized by Ketamin (75mg/kg)-Medetomidin (1.0mg/kg)-Atropin (0.04mg/kg)-injection and the abdominal cavity was opened. The uterus containing embryos was carefully exposed and the lateral ventricles of the embryo's were injected with GFP (1µg/µl), GFP (0,4µg/µl) + CAMSAP2 shRNA1/2 (0,6µg/µl), GFP (0,5µg/µl) + GFP-CAMSAP2 (0,5µg/µl), or GFP (0,2µg/µl) + CAMSAP2 shRNA1/2

(0.6 μ g/ μ l) + GFP-CAMSAP2 (0.2 μ g/ μ l) dissolved in 0.05% Fast Green was injected in the lateral ventricles using glass micro-pipettes (Harvard Apparatus). Brains were electroporated using an ECM 830 Electro-Square-Porator (Harvard Apparatus) set to three unipolar pulses at 30V (100ms interval and pulse length) and using gold-plated GenePaddles (Fisher Scientific). Embryos were placed back into the abdomen, abdominal muscles and skin were sutured separately and mother mice were injected with 0.05mg/kg Buprenorphinehydrochloride and awakened by injection of 1 mg/kg antipamezole. Embryos were collected at E17.5 and heads were fixed in 4% Paraformaldehyde in PBS and submerged in 30% Sucrose. 12 μ m cryosections were made and sections were blocked and permeabilized in 10% Normal Horse Serum + 0.2% Triton X-100 in PBS followed by a primary antibody staining against GFP (rabbit, MBL international Cat. 598). Secondary antibodies labeled with Alexa488 or Alexa568 (Life Technologies) were used following the primary antibodies. Sections were mounted in Vectashield containing DAPI (Vector Laboratories, H-1200). Z-stack acquisitions were taken using conventional confocal microscopy using a LSM700 (Zeiss).

Image analysis and quantification

Image processing was performed in ImageJ, MetaMorph, MatLab, Origin and or LabVIEW. Confocal images were projected using maximum projection. For all of the analysis background subtraction of the image was applied. As indicated in the figure legends, some images were processed by low pass filtering with a 3x3 kernel.

Analysis of laser-induced severing experiments. To determine the intensity of GFP-CAMSAP2 before and after laser-induced severing, a 10x10 pixel region was selected at the site of laser cutting and a second region of the same size was used to subtract the background. The intensity trace was then plotted in origin and fitted with a single exponent: $I(t) = A(1 - e^{-\lambda t})$. I, is the intensity (a.u.), A, is the amplitude, λ , is the time constant. The amplitude of the exponent was used to normalize the intensity trace.

Analysis of FRAP experiments. To analyze the recovery of fluorescence, 10x10 pixel regions including the bleached CAMSAP2 area were selected and background subtracted frame-by-frame by subtracting the average intensity of an empty, non-bleached area. Recovery R was then calculated as $R = (I(t) - I(\text{directly after bleaching})) / (I(\text{before bleaching}) - I(\text{directly after bleaching}))$, with I denoting total dendrite intensity. After normalization, the final recovery R_{final} for each individual trace was determined as the level at the end of the recording (800 s after bleaching). The immobile fraction was then calculated as 1-R_{final}. The values obtained were similar to the values obtained by fitting an exponential recovery ($R = R_{\text{final}}(1 - \exp(-t/\tau))$), to the trace obtained by averaging all individual traces.

Quantification of endogenous antibody staining in neurons. To determine intensities from endogenous staining in an image (acquired with LSM700 40x objective and 63x objective), ImageJ is used to manually draw regions of interest (ROI) around the soma and primary dendrites. From the ROI the mean intensity was measured. To avoid measuring staining intensity from surrounding and overlapping neurons, smaller regions of 20x20 pixels were used for analysis of staining intensities. This method has been used for measuring the protein depletion in CAMSAP2 and γ -Tubulin shRNA expressing neurons. Measurements of endogenous EB3 localization in fixed neurons were performed as described previously [17,18]. The number of EB3 comets per 10 μ m of soma or dendrite length was measured using MetaMorph software. The dendrites and axons of mRFP-expressing neurons were identified based on their morphology and by immunostaining for the dendritic marker MAP2. Statistical analysis was performed with Student's t-test assuming a two-tailed and unequal variation. N was defined as the number of neurons analyzed.

Quantification of γ -Tubulin at the centrioles. Confocal images of the Cep135 (centriolar marker) were thresholded and converted in binary images using ImageJ. Regions of interest (ROI) representing the location of each individual centriole were generated by applying the "Analyse particles" function. These ROIs were subsequently applied to the corresponding γ -Tubulin images and mean pixel intensities were quantified. Pericentrosomal signals were determined by measuring the mean pixel intensity within a 3 pixel radius encircling the ROI.

Quantification of number of positive axons per neuron. The Olympus BX53 upright microscope was used to quantify the number of axons per single neuron (stage 2 or stage 3 neurons), by counting the number of neurites positive for the axon specific marker tau, or axon initial segment markers pan-Nav or β IV-Spectrin. The counting was performed on neurons untreated and treated with 10 nM Taxol for 48 hours. The results of statistical analyses are performed using a Student's t-test assuming a two-tailed distribution and unequal variation. N was defined as the number of neurons analyzed

Analysis of dendrite morphology. For the morphometric analysis of dendrite morphology, we used β -Galactosidase, GFP, or mRFP as an unbiased cell fill. Images for dendritic morphology were performed with a 40x objective on the LSM510 and LSM5 Pascal. Morphometric analysis for dendrites was performed in MetaMorph. Quantification of the number of dendritic branches, primary dendrites, total dendrite length and Sholl analysis was done with the acquired images. For dendrite length all dendrites of a single neuron were traced in MetaMorph and the number of pixels was automatically converted to μm . For Sholl analysis concentric circles with 20 μm differences in diameter were drawn around the cell body, and the number of dendrites crossing each circle was manually counted. The results of statistical analyses are performed using a Student's t-test assuming a two-tailed distribution and unequal variation. N was defined as the number of neurons analyzed

Intensity profile analysis. Characterization of fluorescence intensity profile in initial segment was performed similar to [19]. For each neuron image, the intensity profile was traced along the axon in ImageJ using curves of appropriate thickness ($\sim 0.5 \mu\text{m}$). This produced an array of intensities $I(r_k)$ at discrete distances r_k from the initial point along the curve $k \in \{1, 2, \dots, N\}$. Further the smoothening of the profile was performed using moving average filter with the window equal to $\sim 3 \mu\text{m}$, giving profile $\tilde{I}(r_k)$. It was normalized with respect to its minimum and maximum values:

$$\hat{I}(r_k) = \frac{\tilde{I}(r_k) - \tilde{I}_{\min}}{\tilde{I}_{\max} - \tilde{I}_{\min}}$$

The result was used to locate points describing the shape of profile: maximum, minimum, “beginning” and “end”. Position of the “beginning” reference point r_{beg} corresponded to the normalized intensity value of 0.33 while moving in the direction to the cell body from the maximum. Position of the “end” r_{end} used the same threshold intensity value, but moving in the direction away from cell body.

Relative average alignment. Intensity profiles were traced along the same line in two-channel image of double labeled neurons, where one channel corresponded to the CAMSAP2 staining and the other one to the protein of interest. Each profile was characterized as described above. As a common reference point we chose the “end” point of CAMSAP2, since its intensity distribution represents monotonically decreasing function. To perform the averaging between different neurons, we aligned all profiles in such a way that the position of the CAMSAP2 “end” point for each staining became the origin of r axis. To overcome different sampling of fluorescent intensity along the curve we performed linear interpolation of discrete profile

$$\hat{I}(r) = \sum_{k=1}^{N-1} \hat{I}_k(r),$$

where

$$\hat{I}_k(r) = \begin{cases} \hat{I}(r_k) + \frac{\hat{I}(r_{k+1}) - \hat{I}(r_k)}{r_{k+1} - r_k} (r - r_k) & r \in [r_k, r_{k+1}] \\ 0, & r \notin [r_k, r_{k+1}] \end{cases}.$$

We used these linear interpolations to equidistantly sample each profile with the step of 0.1 μm . This allowed us to average normalized fluorescent intensity values from different neurons at the same points of r axis. All analysis routines were written using MATLAB software and are available at <https://github.com/ekatruxha/AIS>.

dSTORM imaging

dSTORM microscopy [20,21] was performed on a Nikon Ti microscope equipped with a 100x Apo TIRF objective (NA. 1.49), a Perfect Focus System and an additional 2.5x Optovar to achieve an effective pixel size of 64 nm. Evanescent or oblique laser illumination was achieved using a custom illumination pathway with a 15 mW 405 nm diode laser (Power Technology), a 50 mW 491 nm DPSS laser (Cobolt Calypso), and a 40 mW 640 nm diode laser (Power Technology). Fluorescence was detected using an Andor DU-897D EMCCD camera. To facilitate multicolor imaging, an image splitting device (Optosplit III, Cairn research) with ET series GFP, RFP, Cy5 filters (Chroma Technology) was placed between microscope and camera. All components were controlled by Micromanager software [22]

For dSTORM imaging of Alexa Fluor 647 and Atto 488, the sample was continuously illuminated with 640 nm and 491 nm light, respectively. In addition, the sample was illuminated with 405 nm light at increasing intensity to keep the number of fluorophores in the fluorescent state constant. Between 8000 and 13000 frames were recorded per acquisition with exposure times of 25-40 ms. For multi-color images, Alexa Fluor 647 was imaged before Atto 488.

Immunolabeling of endogenous CAMSAP2 required fixation using methanol, as no staining was observed after fixation with PFA, most likely due to epitope blocking. Unfortunately, whereas microtubules appeared normal using conventional microscopy after treatment with methanol, dSTORM imaging was unable to resolve individual neuronal microtubules in these conditions (as opposed to PFA fixation, see Figure 2D,E). To simultaneously resolve microtubule ends and CAMSAP2, we therefore overexpressed CAMSAP2-GFP, which could be immunolabeled using a single chain antibody against GFP (VHH_{GFP}) upon PFA fixation.

For optimal microtubule imaging, cells were first extracted with 0.3% glutaraldehyde (GA) in extraction buffer (0.3% Triton-X + 5mM MgCl₂ + 150mM NaCl + 5 mM glucose in PEM80-buffer (80 mM PIPES, 1 mM EGTA, 4 mM MgCl₂, pH 6.9) for one minute. After extraction, fixation was performed in 4% PFA for 10 minutes. After fixation, cells were washed 2 times 5 minutes in PBS and cells were further permeabilized 10 minutes in PBS + 0.2% Triton-X. Cells were then washed 3 times 5 minutes in PBS and incubated for 45 minutes in blocking solution (2% w/v BSA, 0.2% w/v gelatin, 10 mM glycine, 50 mM NH₄Cl in PBS, pH 7.4). Primary antibodies were incubated overnight at 4°C or 1.5 hours at RT and washed with PBS. Cells were post-fixed in 2% PFA for 10 minutes or stored at 4 °C. Primary antibodies were α -Tubulin (Sigma) conjugated to Alexa647 and VHH_{GFP} coupled to atto488, both diluted 1:100.

For Alexa647 only, imaging was performed using 50-100mM MEA, 5% w/v glucose, 560 μ g/ml glucose oxidase, 40 μ g/ml catalase in PBS. For Atto488 alone or together with Alexa Fluor 647, imaging was performed using 200mM MEA in 10mM Tris buffer (pH 10).

dSTORM Localization and Rendering Algorithms

Single-molecule localization software was written in Java as an ImageJ plugin. Each image in an acquired stack was convoluted with the two dimensional mexican hat kernel matching the microscope's point spread function (PSF) size. The intensity histogram of the convolved image was fitted to a Gaussian distribution and used to calculate the threshold intensity value (mean value of the fit plus three standard deviations). The maximum intensity values within individual spots were chosen as initial positions for the peaks' fitting performed on the original image. We used unweighted nonlinear least squares fitting with Levenberg-Marquardt algorithm to the assumed asymmetric two-dimensional Gaussian PSF.

Only fits with a calculated width within $\pm 30\%$ of the measured PSF's standard deviation were accepted. Localizations within one pixel distance in a number of successive frames were considered to arise from the same molecule. In this case the weighted mean was calculated for each coordinate, where weights were equal to inverse squared localization errors. The resulting table with molecule coordinates and errors was used to render the final localization image with 10 or 20 nm pixel size. Each molecule was plotted as a 2D Gaussian of the integrated intensity equal to one and with standard deviations of 32 nm.

For two color imaging, chromatic corrections obtained from scanning multichromatic beads were applied to the Alexa647 dataset. In cases where sample drift was observed during acquisition, a correction algorithm was applied [23]. In short, a set of localization images was built from consecutive subsets of frames corresponding to different times. Drift was determined by maximizing the spatial normalized cross-correlation between these intermediate reconstructions.

Stretch Analysis

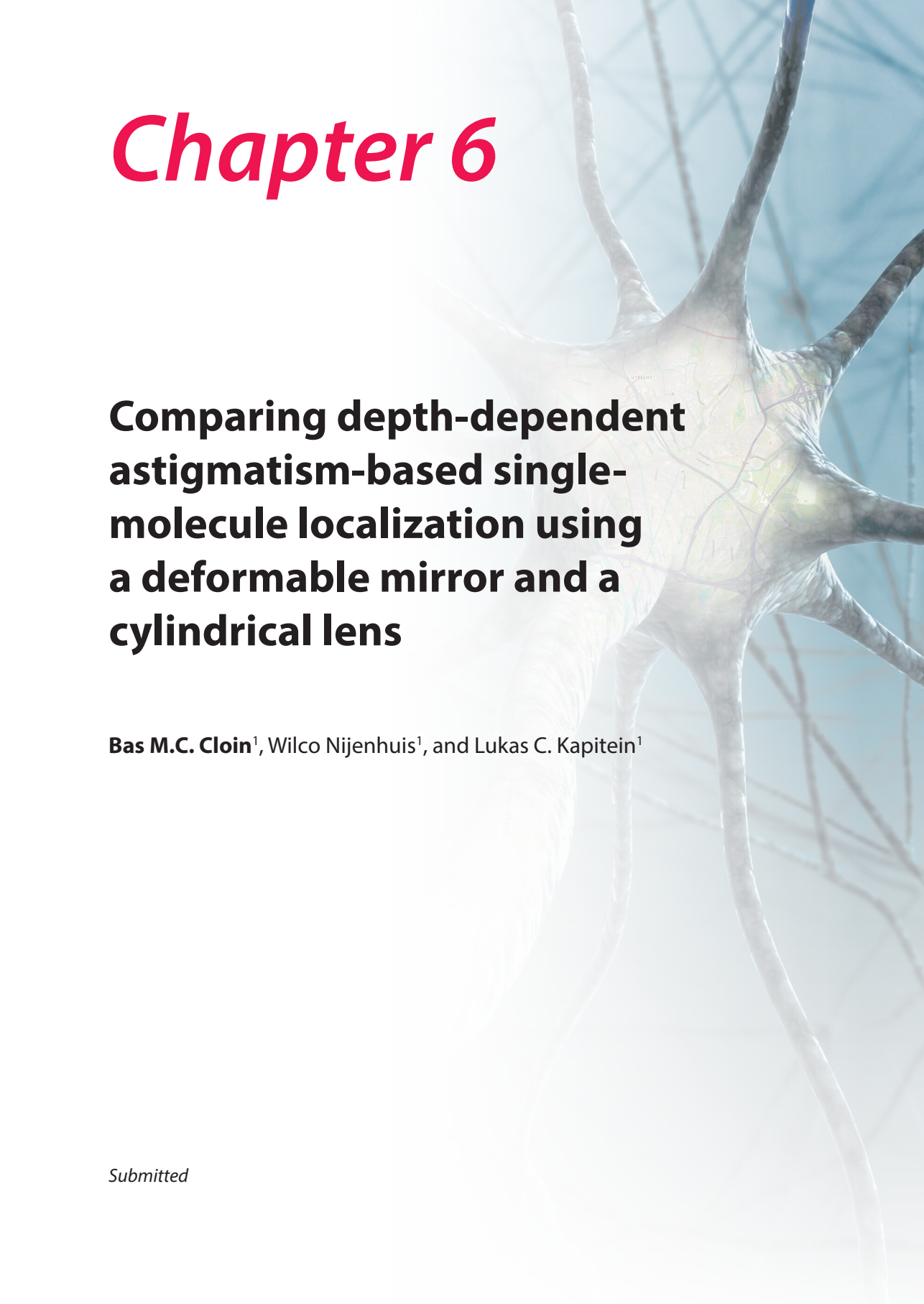
Super-resolution images were thresholded at two standard deviations above the average pixel intensity and stretches and their length were detected using a custom ImageJ routine, with a threshold minimal stretch length of 250 nm. The width of a stretch was determined by fitting the intensity profile perpendicular to the length of the stretch with a Gaussian. The Full Width at Half Maximum (FWHM) of a stretch was determined from the standard deviation σ of the Gaussian fit.

SUPPLEMENTARY REFERENCES

- 1 Stepanova, T. et al. Visualization of microtubule growth in cultured neurons via the use of EB3-GFP (end-binding protein 3-green fluorescent protein). *The Journal of neuroscience : the official journal of the Society for Neuroscience* 23, 2655-2664 (2003).
- 2 Ogawa, Y. et al. Spectrins and ankyrinB constitute a specialized paranodal cytoskeleton. *The Journal of neuroscience : the official journal of the Society for Neuroscience* 26, 5230-5239 (2006).
- 3 Caussinus, E., Kanca, O. & Affolter, M. Fluorescent fusion protein knockout mediated by anti-GFP nanobody. *Nature structural & molecular biology* 19, 117-121.
- 4 Kapitein, L. C., Yau, K. W. & Hoogenraad, C. C. Microtubule dynamics in dendritic spines. *Methods in cell biology* 97, 111-132 (2010).
- 5 Brummelkamp, T. R., Bernards, R. & Agami, R. A system for stable expression of short interfering RNAs in mammalian cells. *Science* 296, 550-553 (2002).
- 6 Shaner, N. C. et al. Improved monomeric red, orange and yellow fluorescent proteins derived from *Discosoma* sp. red fluorescent protein. *Nature biotechnology* 22, 1567-1572 (2004).
- 7 Honnappa, S. et al. An EB1-binding motif acts as a microtubule tip localization signal. *Cell* 138, 366-376 (2009).
- 8 Alvarado-Kristensson, M., Rodriguez, M. J., Silio, V., Valpuesta, J. M. & Carrera, A. C. SADB phosphorylation of gamma-tubulin regulates centrosome duplication. *Nature cell biology* 11, 1081-1092 (2009).
- 9 Wiznerowicz, M. & Trono, D. Conditional suppression of cellular genes: lentivirus vector-mediated drug-inducible RNA interference. *Journal of virology* 77, 8957-8961 (2003).
- 10 Cheung, Z. H., Chin, W. H., Chen, Y., Ng, Y. P. & Ip, N. Y. Cdk5 is involved in BDNF-stimulated dendritic growth in hippocampal neurons. *PLoS biology* 5, e63 (2007).
- 11 Witte, H., Neukirchen, D. & Bradke, F. Microtubule stabilization specifies initial neuronal polarization. *The Journal of cell biology* 180, 619-632 (2008).
- 12 Zhou, F. Q., Zhou, J., Dedhar, S., Wu, Y. H. & Snider, W. D. NGF-induced axon growth is mediated by localized inactivation of GSK-3beta and functions of the microtubule plus end binding protein APC. *Neuron* 42, 897-912 (2004).
- 13 Kaech, S. & Banker, G. Culturing hippocampal neurons. *Nature protocols* 1, 2406-2415 (2006).
- 14 Botvinick, E. L., Venugopalan, V., Shah, J. V., Liaw, L. H. & Berns, M. W. Controlled ablation of microtubules using a picosecond laser. *Biophysical journal* 87, 4203-4212 (2004).
- 15 Colombelli, J., Reynaud, E. G., Rietdorf, J., Pepperkok, R. & Stelzer, E. H. In vivo selective cytoskeleton dynamics quantification in interphase cells induced by pulsed ultraviolet laser nanosurgery. *Traffic (Copenhagen, Denmark)* 6, 1093-1102 (2005).
- 16 Hand, R. et al. Phosphorylation of Neurogenin2 specifies the migration properties and the dendritic morphology of pyramidal neurons in the neocortex. *Neuron* 48, 45-62 (2005).
- 17 Jaworski, J. et al. Dynamic microtubules regulate dendritic spine morphology and synaptic plasticity. *Neuron* 61, 85-100 (2009).
- 18 Kapitein, L. C. et al. NMDA receptor activation suppresses microtubule growth and spine entry. *The Journal of neuroscience : the official journal of the Society for Neuroscience* 31, 8194-8209 (2011).
- 19 Grubb, M. S. & Burrone, J. Activity-dependent relocation of the axon initial segment fine-tunes neuronal excitability. *Nature* 465, 1070-1074.
- 20 Heilemann, M. et al. Subdiffraction-resolution fluorescence imaging with conventional fluorescent probes. *Angewandte Chemie (International ed)* 47, 6172-6176 (2008).
- 21 Rust, M. J., Bates, M. & Zhuang, X. Sub-diffraction-limit imaging by stochastic optical reconstruction microscopy (STORM). *Nature methods* 3, 793-795 (2006).
- 22 Edelstein, A., Amodaj, N., Hoover, K., Vale, R. & Stuurman, N. Computer control of microscopes using microManager. *Current protocols in molecular biology / edited by Frederick M. Ausubel ... [et al.] Chapter 14, Unit 14.20* (2010).
- 23 Mlodzianoski, M. J. et al. Sample drift correction in 3D fluorescence photoactivation localization microscopy. *Optics express* 19, 15009-15019 (2011).

¹Department of Biology, Utrecht University, Padualaan 8, 3584 CH Utrecht, The Netherlands

Chapter 6

A stylized neuron with a map overlay on its cell body. The neuron is rendered in a light blue and white color scheme, with its cell body and dendrites appearing as a complex network of fibers. A semi-transparent map of a city is overlaid on the central cell body, showing streets and green spaces. The background is a light blue gradient with faint, overlapping geometric patterns.

Comparing depth-dependent astigmatism-based single-molecule localization using a deformable mirror and a cylindrical lens

Bas M.C. Cloin¹, Wilco Nijenhuis¹, and Lukas C. Kapitein¹

Submitted

SUMMARY

Single-molecule localization microscopy (SMLM) enables imaging of fluorescently labeled biological samples with nanometric resolution. Localizing molecules close to the coverslip in the lateral directions is relatively straightforward, and the z-direction can be encoded by introducing astigmatism with a cylindrical lens (CL). However, performing SMLM deeper in watery samples is impeded by increased optical aberrations, arising from both the setup and the sample, resulting in decreased localization precisions. Adaptive optics (AO) can be used to correct these aberrations, and can simultaneously be used to induce precise levels of astigmatism. How astigmatism-based z-encoding by a CL and AO deep in watery samples compare has not been systematically addressed. Moreover, a comparison of water immersion, which is more suited for deeper imaging in watery samples because of the similar refractive index, with oil immersion in combination with AO is lacking. Here we compare SMLM using oil and water immersion objectives and assess the use of a deformable mirror (DM) to compensate aberrations and induce z-encoding. We find that adaptive optics enable deep ($> 15 \mu\text{m}$) 3D localization with oil immersion by providing aberration correction and tunable astigmatism, but does not improve localization accuracy beyond the performance of water immersion-based imaging in combination with a cylindrical lens.

INTRODUCTION

In Single Molecule Localization Microscopy (SMLM) the diffraction limit is circumvented by analyzing the Point Spread-Function (PSF) of single fluorescent molecules to obtain precise information about the molecule's position in x and y [1,2]. Subsequently localizing large numbers of fluorophores provides information about the structure under investigation with a resolution in the order of nanometers. Information about the z -position of fluorophores can be encoded in the PSF by inducing astigmatism, either by introducing a cylindrical lens [3] (CL) or an adaptive optical element [4] in the detection path. Inducing astigmatism creates slightly separate focal planes for the x - and y -direction, with the average focal plane (AFP) situated halfway in between them. The PSF of a fluorophore positioned in the AFP appears round, while the PSFs of fluorophores not in the AFP appear elliptical. The orientation of the major and minor axis of an elliptical PSF indicates whether a fluorophore is positioned above or below the AFP and the distance to the AFP can be determined from the amount of ellipticity.

When imaging deeper into a sample, aberrations induced by both the optical setup and the sample distort the PSF and will decrease the localization precision. Sources of setup-induced aberrations are for instance imperfections in the objective, other lenses, and dichroic mirrors. High NA oil immersion objectives, often used for SMLM, provide optimal imaging close to the coverslip, but focusing deeper into a water-based sample results in large, mainly spherical aberrations because of the mismatch in refractive index between the immersion oil (~ 1.51) and the sample (~ 1.33). The use of water immersion objectives limits this mismatch at the expense of a lower NA and, as a result, lower photon counts and a decreased resolution. Deeper imaging also increases the distance light has to travel through the sample, increasing scattering and refraction of the fluorescence emission due to inhomogeneities in the sample.

Aberrations induced by both setup and sample can be corrected using an adaptive optical element, such as an LCD-based spatial light modulator (SLM) or a deformable mirror (DM). In SMLM applications DMs are preferred because they reflect $>95\%$ of the incoming light and are not sensitive to the polarization of the light, implying less photon loss compared to SLMs. Since in SMLM the excitation pattern is not critical, implementing a DM only in the detection path is sufficient. In addition, a DM can also be used to induce a tunable amount of astigmatism for 3D-SMLM[4]. Previous work has shown that correction of system-induced aberrations and the simultaneous induction of astigmatism using a DM can result in high-quality 3D-SMLM images of structures close to the coverslip [4]. Additionally, it was shown that the amount of induced astigmatism influences the x -, y - and z -accuracy [4,5], but the settings for optimal x -, y -, and z -resolution have not been systematically explored.

Correction of setup- and sample-induced aberrations becomes more important when imaging deeper into a sample, especially when using an oil immersion objective. At a depth of $6\ \mu\text{m}$ in cultured COS-7 cells, correction of aberrations resulted in improved 2D-SMLM as measured in amount of localizations and degree of structure reconstruction [6]. Additionally, using a DM for aberration correction and induction of astigmatism for 3D-SMLM increased

the amount of localizations by a factor of 2-3 resulting in an improved FRC-resolution, although localization precisions did not clearly improve [6]. Despite this evidence that DM-based adaptive optics can improve 2D- and 3D-SMLM when imaging deeper into a biological sample, a thorough investigation of the effect of aberration correction on SMLM performance as function of imaging depth is lacking. Additionally, a comparison of astigmatism-based 3D-SMLM either induced by adaptive optics or a CL as function of imaging depth has not been reported.

Here we first explored how localization precision as a function of imaging depth in 2D-SMLM is affected by DM-based aberration correction. The performance of a 60x water immersion objective was also included in the comparison. Secondly, astigmatism-based PSF z-encoding as function of imaging depth was compared between a CL and a DM. Thirdly, we experimentally addressed the optimal value of induced astigmatism to achieve the highest x-, y-, and z-localization precisions. Lastly, we show that 3D-SMLM using a DM to correct aberrations and induce astigmatism at high imaging depth in a biological sample can provide high-quality super-resolved reconstructions.

MATERIAL AND METHODS

Microscopy

SMLM microscopy was performed on a Nikon Ti-E microscope equipped with a 100x Apo TIRF oil immersion objective (NA. 1.49), a 60x Plan Apo IR water immersion objective (NA 1.27), and Perfect Focus System 3. Excitation was achieved with a mercury lamp or via a custom illumination pathway with a Lighthub-6 (Omicron) containing a 638 nm laser (BrixX 500 mW multimode, Omicron), a 488nm laser (Luxx 200 mW, Omicron), and a 405 nm laser (Luxx 60 mW, Omicron). Emission light was separated from excitation light with a quad-band polychroic mirror (ZT405/488/561/640rpc, Chroma), a quad-band emission filter (ZET405/488/561/640m, Chroma), and an additional single-band emission filter (ET525/50m for green emission and ET655lp for far-red emission, Chroma). Fluorescence was detected via either a pathway containing a removable Nikon CL (left port), or a pathway containing the MicAO™ adaptive optics system (Imagine Optic, right port). The latter pathway used a relay system of two lenses with equal focal length to conjugate the back focal plane of the objective to a DM (MIRAO 52-e, Imagine Optic) and project the front focal plane onto the sCMOS camera (Hamamatsu Flash 4.0v2). A removable mirror was used to optionally deflect the light to a Shack-Hartmann wavefront sensor (HASO3, Imagine Optic). The camera had an effective pixel size of 65 nm (100x objective) or 107 nm (60x objective) and the camera output was converted to photons using the calibration factor supplied by the manufacturer. Samples were positioned in the x- and y-direction with an M-687 PILine stage (PI) and in the z-direction with either the Perfect Focus System or a P-736 PInano stage (PI). The DM and wavefront sensor were controlled by Imagine Optic software, all other components by Micromanager [7].

Aberrations were corrected using the image-based 3N algorithm [6,8] as implemented in the Imagine Optic software, with maximum contrast as optimization metric. In short, per Zernike mode three images of a 100 nm fluorescent bead were acquired with a zero, negative, and positive amplitude bias of that Zernike mode applied to the DM. The optimization metric is measured in the three images and a fit is used to determine the amount of applied Zernike mode corresponding to the maximum of the metric. This is done for per Zernike mode, and the sum of Zernike modes with corresponding amplitudes is subsequently applied to the mirror to correct aberrations. The amplitude of astigmatism is reported as μm RMS roughness of the DM when the corresponding Zernike mode is applied.

For SMLM, the sample was continuously illuminated with 638 nm light. In addition, the sample was illuminated with 405 nm light at increasing intensity to keep the number of fluorophores in the fluorescent state constant. Typically 5,000 frames for in-vitro MTs and 10,000 frames for CACO-cells were recorded per acquisition with exposure times of 30-40 ms.

In vitro imaging of fluorescent beads and MTs

HiLyte™ Fluor 647 labeled MTs were prepared from stabilized seeds as described earlier [9] and stored at -80°C . HiLyte™ Fluor 647 (HF647)-tubulin was purchased from Cytoskeleton. Before sample preparation seeds were kept at 37°C for 2-4 h and stabilized by 1% glutaraldehyde. Agarose gel was prepared by adding 4% agarose (A9539, Sigma Aldrich) to 100 mM Tris at pH 8. MT seeds and 100 nm green fluorescent beads (final dilution 1/2000; F8803, ThermoFisher) were added to heated agarose, gently mixed, and put on a microscope slide between two pieces of double sided tape. For SMLM, mercaptoethylamine and an oxygen scavenging system consisting of glucose, glucose oxidase and catalase were additionally added to the heated agarose (final concentrations: 50 mM MEA, 5% w/v glucose, 560 $\mu\text{g}/\text{ml}$ glucose oxidase, 40 $\mu\text{g}/\text{ml}$ catalase). A coverslip was pressed onto the tape and the sample was cooled under running water to quickly solidify the agarose.

When focusing into a water-based sample with an oil immersion objective, the imaging depth has to be corrected for the refractive index mismatch. Reported depths for data obtained with the oil immersion objective were corrected by multiplying the measured depth with a constant factor equal to the ratio between the refractive index of water (1.33) and the immersion oil (1.515) [10].

Single molecule localization precisions at depths of 0, 4.4, 8.8, 17.6, and 25.5 μm (oil immersion; OI) and 0, 5, 10, 20, and 30 μm (water immersion; WI) were determined using the previously described ImageJ plugin Detection of Molecules (DoM) [11]. Localizations with an uncertainty above 32.5 nm in either the x- or y-coordinate were discarded. The total localization precision was calculated as $\sigma_{\text{tot}} = \sqrt{\sigma_x^2 + \sigma_y^2}$. The median localization precision was determined by binning localization precisions into 50 bins between 0 and 65 nm, and taking the middle of the bin with maximum number of counts. Mean and median localization precision were calculated from three acquisitions per depth.

OI without AO		
depth (μm)	N	n (sum of N acquisitions)
0	3	45326
4.4	3	188384
8.8	3	62536
17.6	3	63783
25.5	3	41288

OI with AO		
depth (μm)	N	n (sum of N acquisitions)
0	3	52278
4.4	3	98835
8.8	3	68797
17.6	3	96655
25.5	3	128260

WI		
depth (μm)	N	n (sum of N acquisitions)
0	1	13045
5	3	95799
10	3	126592
20	3	70258
30	3	151894

Data for histograms in figures 1D and 1G is binned into 46 bins of 1 nm. Data for the histogram in 1E is binned in 50 bins of 120 photons. In figure 1F only every 5th point is shown for clarity. The histogram in figure 1G shows data for localizations with an integrated intensity between 1700 and 2000 photons.

Comparison of 3D calibration curves

Calibration curves are obtained by making z-stacks with 20 nm steps of 100 nm green fluorescent beads suspended in the agarose gel. For each z-step, the x-width and y-width of the PSF (as determined from a Gaussian fit using DoM) are subtracted and plotted against the z-position. This is done at depths of 0.0, 0.9, 3.5, 8.8, and 17.6 μm (OI) and 0.0, 5.0, 10, 15, and 20 μm (WI). Astigmatism is induced with the CL or the DM. The amount of astigmatism induced with the DM was increased with increasing imaging depth, from 0.060 μm RMS at the coverslip to 0.120 μm RMS at a depth of 17.6 μm , to obtain similar calibration curves. For figures 2A-C, beads were imaged at stage positions of -250 nm, 0 nm, and 250 nm with induced astigmatism, at depths of 0 and 17.6 μm (oil immersion) and 0 and 18 μm (water immersion).

Comparison of field-of-view distortion

A small sample volume was created by adhering a coverslip to a microscope slide using double-sided tape. 100 nm green fluorescent beads were diluted in PBS (1/100,000) and incubated for 10 minutes in the sample volume to allow nonspecific adsorption. Free beads were then washed away with PBS and the volume sealed with vacuum grease.

An image was made of beads within the field of view of the camera with and without astigmatism using the CL, and at another position using AO (0.00 and 0.06 μm RMS astigmatism). To assess the distortion of the field-of-view, a custom MATLAB-script was used that for each particle in the image without astigmatism finds the highest-intensity particle in the image with astigmatism within a certain area around the first. Based on a first assessment of positional shift, this area was set to be an ellipse with longer y-axis to account for the mostly y-shifted positions. Ellipse radii of 0.67 pixels in x and 6.7 pixels in y were used for CL images, and of 1.0 pixels in x and 3.2 pixels in y for AO images. First, the overall shift was determined and subtracted from the individual shifts to account for non-ideal alignment. Then, the leftover positional shifts were decomposed in the x- and the y-direction. Shifts in the y-direction were averaged over particles with positions within a 50 pixel windows in the y-direction in the images without astigmatism. After shifts more than 2 times the standard deviation from the mean were removed, the mean and standard deviation were recalculated to produce the graph in figure 3D. In total 522 and 501 shifts were used for CL and AO, respectively.

Tuning of astigmatism

Samples with green fluorescent beads on a coverslip were prepared as described above, with a bead dilution of 1/50,000. Z-stacks were made with 50 nm steps with astigmatism between 0.00 and 0.10 μm RMS with steps of 0.01 μm RMS, induced with the DM (Figure 4A). PSF widths were determined using DoM. The offset between the x-focal plane and the y-focal plane was determined from 3rd order polynomial fits to the bottom part (x- and y-width < 8 pixels) of the curves of x- and y-width as function of the z-position of the stage (Figure 4B). The focal plane offset was calculated by dividing the difference in z-position between the minima of the two fits by two. The focal plane offset was determined for different amounts of induced astigmatism (Figure 4C) and for each setting, a linear fit to the z-position of the stage versus the difference between x-width and y-width resulted in a slope α , used to calculate the z-position of localized particles based on their PSF widths (Figure 4D, E).

To determine how the localization uncertainties in x, y and z depend on the amount of induced astigmatism, beads immobilized on the coverslip were imaged in focus for ten frames per astigmatism value (ranging from 0.000 to 0.100 μm RMS) and localized using DoM. From this, we could directly estimate the uncertainties in x and y (Figure 4H) as a function of focal plane offset, as well as the uncertainty in determining the width of the PSF as a function of the width of the PSF for beads in focus (Figure 4F). From this, we could

then estimate the z localization error for particles close to the focus as

$$\sigma_z = \sqrt{\alpha^2 (\sigma_{x\text{-width}}^2 + \sigma_{y\text{-width}}^2)}$$

where α is the slope of the calibration curve and $\sigma_{x\text{-width}}$ the error in determining the x- and y-widths, as determined from the Gaussian fits.

Next, the localization uncertainty for z-positions away from the objective focal plane were calculated based on the expected PSF width in x and y (Figure 4B) and corresponding uncertainties in the widths (Figure 4F). To robustly estimate how the x- and y-width depended on z-position, we measured the width of focused beads for different focal plane offsets and fit the data with a 4th order polynomial. For a given amount of astigmatism, corresponding to a given focal plane offset, we could now estimate the x- and y-width at a distance z from the focus, by calculating the width at (z - focal plane offset) and (z + focal plane offset), respectively.

SMLM imaging of Caco2-BBE cells

Caco2-BBE cells (a gift from S.C.D. van IJzendoorn, University Medical Center Groningen, The Netherlands) were maintained in DMEM supplemented with 9% FBS, 50 $\mu\text{g}/\mu\text{l}$ penicillin/streptomycin and 2 mM L-glutamine. For immunofluorescent imaging, cells were seeded on 18 mm coverslips at a density of $1 \times 10^5/\text{cm}^2$ and cultured for 10-12 days to allow for spontaneous polarization and brush border formation. Cells were fixed with 4% paraformaldehyde in PBS for 10 min, washed with PBS, permeabilized with 0.5% Triton X-100 in PBS for 15 min and blocked with 3% BSA in PBS for at least 1 h. Cells were incubated with primary antibodies, either Mouse-anti-Ezrin (610602; BD Biosciences; 1 $\mu\text{g}/\text{ml}$) or Mouse-anti-Villin (610358; BD Biosciences; 1 $\mu\text{g}/\text{ml}$), for 6 h at room temperature, washed with PBS, incubated with secondary antibodies, Goat-anti-mouse Alexa 647 (A21236; Life Technologies; 6.7 $\mu\text{g}/\text{ml}$), for an additional hour at room temperature and washed with PBS.

RESULTS AND DISCUSSION

To test how the use of a DM alters localization precision in single-molecule localization microscopy, we embedded HF647-labeled microtubules and fluorescent beads in an agarose gel. After optimizing the DM shape using the fluorescent beads, we compared localization accuracies with and without adaptive optics at imaging depth between 0-30 μm using the two exit ports of the microscope. The DM shape was optimized before every acquisition for optimal aberration correction. In addition, we used a water immersion objective to measure localization accuracies in the absence of a refractive index mismatch.

The DM clearly improved localization accuracies when using the oil immersion objective at depths beyond 5 μm (Figures 1B,C), up to a factor of 1.7 for the mode localization accuracy at 25 μm depth. Although the number of photons collected per event increased only slightly (Figure 1E), for molecules with the same integrated intensity localization accuracies were significantly better when using the DM (Figures 1F,G) due to a better match between the PSF shape and our

fitting function, a two-dimensional Gaussian. Nevertheless, at depths over 5 μm , the precisions achieved with an oil objective plus deformable mirror were never better than the performance of the water objective. These data demonstrate that wavefront shaping can improve the localization precision at large imaging depth, but that precision does not improve beyond what is achievable with a water immersion objective used without further corrections at depths over 5 μm .

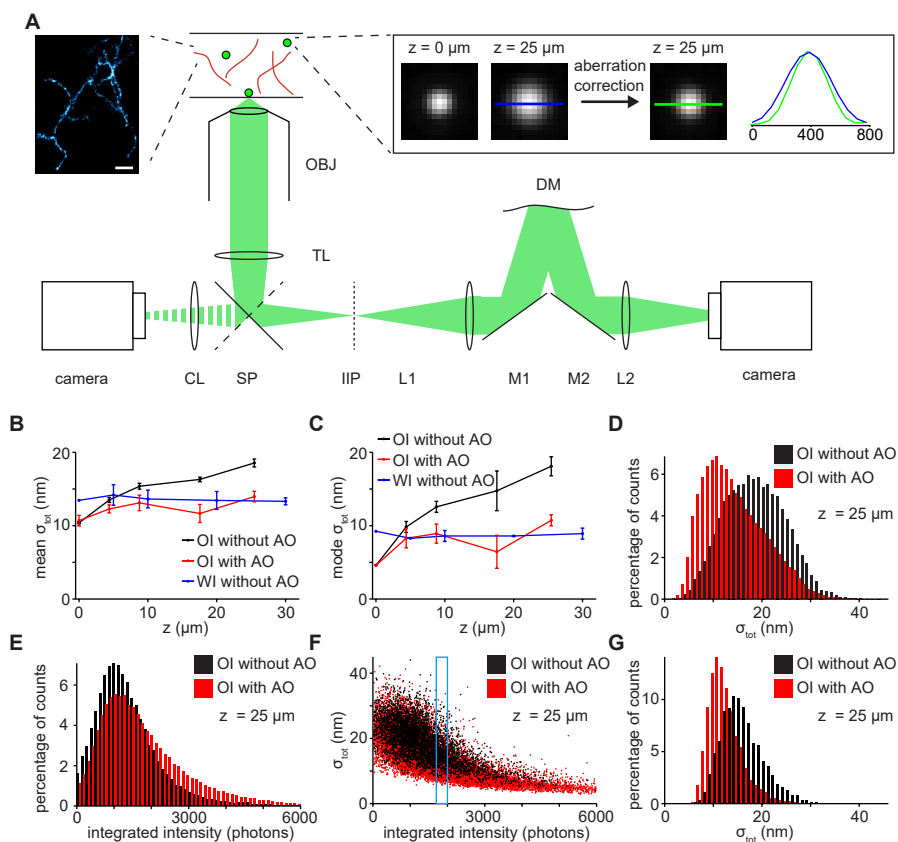


Figure 1: Use of Adaptive optics improves 2D SMLM away from the coverslip

A) Schematic representation of the imaging setup. Fluorescence from the sample, consisting of green fluorescent beads and stabilized HiLyte647-conjugated microtubules suspended in agarose gel, is collected via a water immersion or oil immersion objective and projected on a camera either directly (left side; optionally through a CL) or via a DM. Left inset shows a representative SMLM reconstruction of the HiLyte647-MTs, scalebar is 1 μm . Right inset shows images and cross sections of a fluorescent bead at the coverslip (left panel) and at 25 μm depth without (middle panel) and with aberration correction (right panel). Cross sections at the drawn lines are shown on the right.

B, C) Mean (B) and mode (C) objective localization error of AF647 molecules as function of distance from the coverslip, imaged with the oil immersion (OI) objective with and without adaptive optics (AO), and with the water immersion (WI) objective. Error bars represent standard deviation.

D, E) Histogram of localization errors (D) and integrated intensities (E) at a depth of 25 μm imaged with the OI objective without (black) and with (red) AO.

F) Scatterplot of localization errors as function of integrated intensities at a depth of 25 μm imaged with the OI objective without (black) and with (red) AO.

G) Histogram of localization errors of localizations inside the blue box in F.

Next, we compared the use of either a CL or a DM to induce astigmatism for z-localization at different imaging depth. After insertion of the CL, the PSF of fluorescent beads close to the coverslip (depth < 5 μm) showed clear ellipticity. At larger imaging depth, however, the PSF remained largely symmetric and could not be used to encode the z-position (Figure 2A). This is reflected in the calibration curves obtained by plotting the difference in PSF width in the x and y direction as a function of z-position (Figure 2B).

Similarly, even after optimizing the DM to correct for increased spherical aberrations, the degree of astigmatism sufficient for z-encoding near the coverslip did not induce strong ellipticity at larger imaging depth. Nevertheless, more astigmatism could easily be added, resulting in consistent ellipticity and corresponding calibration curves at depths up to 18 μm (Figure 2C,D; S1). When the water immersion objective was used in combination with the cylindrical lens, the induced ellipticity was less pronounced (Figure 2E), but the calibration curve remained unaltered for depths from 0-20 μm (Figure 2F). These results demonstrate that, in contrast to oil immersion objectives, water immersion objectives can be used for fixed-lens astigmatism-based z-encoding at all imaging depth, and that the combined use of an oil objective and DM can also result in robust depth-independent z-encoding, but requires recalibration at every depth.

When using the CL, we noted that its insertion into the optical path induced a deformation of the image in one direction (Figure 3A). To quantify this, we imaged

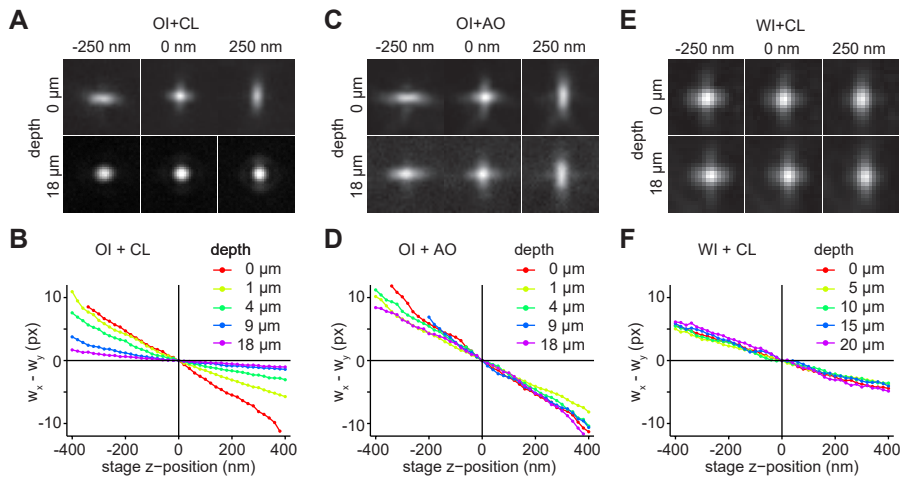


Figure 2: Adaptive optics allow z-encoding away from the coverslip

A) PSF with astigmatism of a 100 nm green fluorescent bead in agarose gel on the coverslip (top panels) and at 18 μm depth (bottom panels) at stage z-positions of -250 nm (left), 0 nm (middle) and 250 nm (right panel) with respect to the focal plane of the oil immersion objective. Astigmatism was induced with the CL.

B) Curves of the difference between PSF x-width and y-width as function of the stage z-position with respect to the objective focal plane, at increasing distance from the coverslip for the 100x oil immersion objective.

C,D) Same as A) and B) but adaptive optics was used to both correct aberrations and induce astigmatism.

E,F) Same as A) and B), but imaged with the 60x water immersion objective.

fluorescent particles immobilized on the coverslip and measured how the position of their imaged altered upon insertion of the lens. This revealed a lateral displacement that increased linearly with the distance from the center of the field of view, consistent with a decrease in magnification of 3.6 % (Figure 3B-D). In contrast, inducing astigmatism using the DM did not induce a change in magnification (Figure 3C,D)

Next, we wanted to explore the optimal amount of astigmatism to encode the x,y,z -location with minimal uncertainty. In contrast to inducing astigmatism with a CL, deformable-mirror induced astigmatism did not alter the imaging depth at which the point spread function was symmetric. Instead, the DM shifted both the x - and y -focal points, both in opposite directions away from the initial focus. This displacement away from the original focus, called the focal plane offset, increased nearly linearly from 0 to 300 nm when increasing the astigmatism from 0.00 to 0.10 μm RMS. For all these different focal plane offsets, we created calibration curves that could be linearly approximated to yield a calibration slope α (nm/px).

At first sight, a higher calibration slope might seem favorable for precise z -encoding, because it would give a more pronounced change in the PSF for the same change in z . Nevertheless, increasing astigmatism will also increase PSF width at $z = 0$, which could lead to a decreased precision in estimating both x and y position and in the PSF width in x and y , w_x and w_y , respectively. Indeed, the uncertainties in x and y , σ_x and σ_y , rapidly

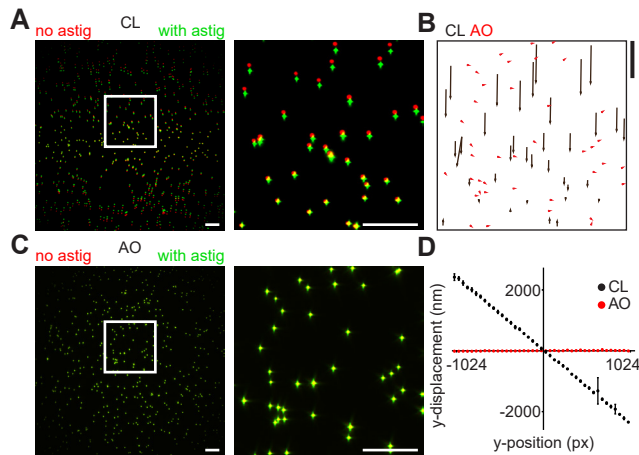


Figure 3: Inducing astigmatism with AO does not distort the field of view

A) Overlaid images of green fluorescent beads without (red) and with (green) CL inserted in the optical path (left) and a zoom of the region in the white box (right). Scalebar is 10 μm .

B) Displacement of bead locations when astigmatism is induced with the CL (black arrows) and with adaptive optics (red arrows). Scalebar for shifts is 1 μm .

C) Overlaid images of green fluorescent beads without (red) and with (green) astigmatism induced with the DM (left) and a zoom of the region in the white box (right). Scalebar is 10 μm .

D) Graph showing y -displacement when astigmatism is induced using the CL (black) and adaptive optics (red) as function of y -position with respect to the center of the field of view.

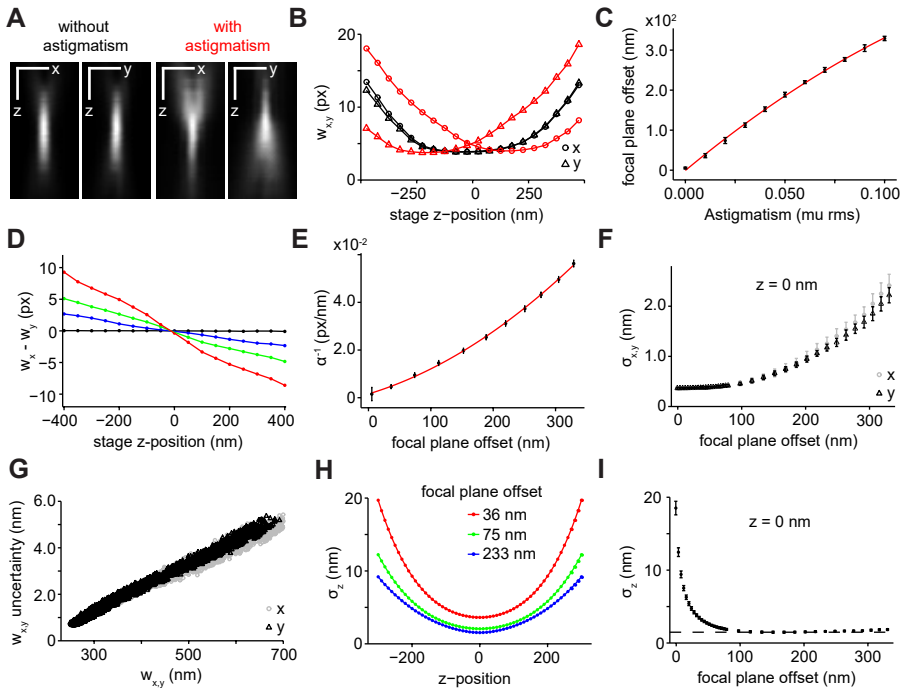


Figure 4: Tunability of astigmatism

A) Cross sections in x and y of a PSF of a 100 nm green fluorescent bead without astigmatism (left panels) and with 0.05 μm RMS astigmatism induced with the DM (right panels). Pixel size in z is 20 nm.

B) PSF width of a 100 nm green fluorescent bead in x (circles) and y (triangles) as function of the z -position of the stage, without astigmatism (red) and with 0.05 μm RMS astigmatism induced with the DM.

C) Focal plane offset as function of the amount of induced astigmatism (mean \pm sd, $N = 5$ beads). Red line represents a least squares fit with a second order polynomial.

D) Difference between PSF x -width and y -width as function of the z -position of the stage, for focal plane offsets of 0 nm (red), 116 nm (blue), 218 nm (green), and 331 nm (red).

E) Absolute values of the inverse of calibration slope α as function of the focal plane offset (mean \pm sd, $N = 5$). A 2nd order polynomial was fit to the data.

F) Localization error in x (gray circles) and y (black triangles) of 100 nm green fluorescent beads in the objective focal plane as function of the focal plane offset (mean \pm sd, $N = 5$). Focal plane offset was altered by changing the amount of astigmatism and the exact value inferred from C. Localization errors were determined with DoM.

G) Uncertainty in PSF width as function of the PSF width as determined from Gaussian fits, for x (gray circles) and y (black triangles) ($n = 240$, $N = 5$).

H) Calculated localization error in z of 100 nm green fluorescent beads as function of the z -position with respect to the focal plane, for focal plane offsets of 36 nm (red), 75 nm (green), and 233 nm (blue). Localization errors were calculated using the known dependence of uncertainty in width versus width (F), the different calibration constants (E), and the dependence of the width on focal plane offset (Figure S2).

I) Localization error in z of 100 nm green fluorescent beads in objective focal plane as function of the focal plane offset (mean \pm sd, $N = 5$).

increased for focal plane offsets above 100 nm (Figure 4F). In addition, plotting the uncertainty in w_x and w_y versus w_x and w_y , revealed a fivefold increase in uncertainty when the PSF width increased from 300 to 700 nm (Figure 4G). Propagating the uncertainty in w_x and w_y allowed us to calculate the uncertainty in z as a function of z and as function of focal plane offset (Figure 4H, I). This revealed that the uncertainty in z decreased rapidly when the focal plane offset increased from 0 to 100 nm, but did not improve any further beyond 100 nm. Given that σ_x and σ_y rapidly increased for focal plane offsets above 100 nm, we conclude that the ideal focal plane offset is around 100 nm for imaging close to the coverslip.

Finally, we tested whether using the DM for aberration correction and astigmatism-based z -encoding would allow three-dimensional nanoscopic imaging of the epithelial brush border of Caco2 cells, which consists of actin-rich protrusion called microvilli. Microvilli were stained using antibodies against the actin interacting proteins villin (Figure 5A,B) and ezrin (Figure 5C,D). Indeed, using the DM increased the number of successful localizations by 1.5-2 fold, as well as the overall localization precision. In addition, using astigmatism-based z -detection we could clearly resolve tilted microvilli that could not be resolved in the two-dimensional image. Thus a DM in combination with a high NA oil immersion objective enables three-dimensional nanoscopy deep in watery samples.

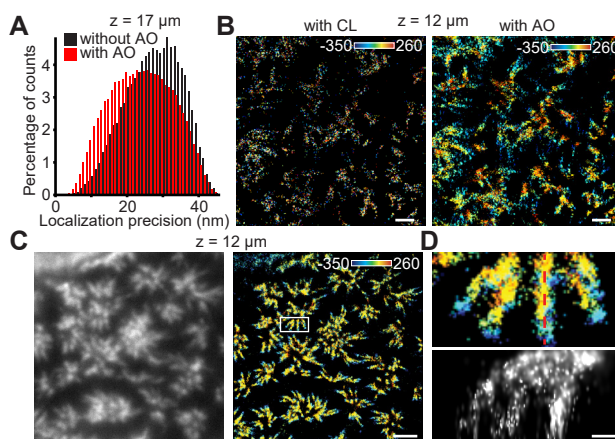


Figure 5: Adaptive optics improve 2D and 3D SMLM in CACO-cell monolayers

A) Histogram of localization errors of Villin-AF647 in a monolayer of Caco-2 cells at a depth of 17 μm without (black) and with (red) AO ($n = 240126$ and 132069 localizations with and without AO, respectively).

B) 3D SMLM reconstructions of a villin-AF647 immunostaining in a CACO-cell at a depth of 12 μm using a CL to introduce astigmatism (left panel) or AO to correct aberrations and introduce astigmatism (right panel). Scalebars are 1 μm .

C) Widefield image (left panel) and 3D SMLM reconstruction (right panel) of Ezrin-AF647 in a monolayer of Caco-2 cells at a depth of 12 μm . Astigmatism was induced with AO (0.11 μm RMS). Scalebar is 2 μm .

D) Zoom of the area in the white box in the right panel of C) (top panel) and cross section at the red dotted line (bottom panel). Scalebar is 500 nm.

Here we have tested the 2D- and 3D-SMLM performance of an oil immersion objective with and without adaptive optics as function of imaging depth and compared it to a water immersion objective without adaptive optics. For 2D-SMLM, we found that with an oil immersion objective at imaging depths over $5\ \mu\text{m}$ the use of a DM to correct aberrations improves localization precisions, up to a factor of 1.7 for the mode localization precision at $25\ \mu\text{m}$ depth. The localization precision achieved with a water immersion objective without aberration correction at depths between $5\ \mu\text{m}$ and $30\ \mu\text{m}$ is, however, comparable or better than in the case of the oil immersion objective with aberration correction. The use of adaptive optics results in a more complicated and less stable optical setup that has to be optimized for every sample/acquisition, implying that 2D-SMLM imaging further than $5\ \mu\text{m}$ from the coverslip is preferentially done using a water immersion objective. However, the purely sample-induced aberrations can be higher in more inhomogeneous thick biological samples than in the agarose samples used here making the effect of aberration correction more pronounced.

To encode the z-position for 3D-SMLM, astigmatism was induced using either a CL or the DM. We found that using a CL in combination with an oil immersion objective resulted in quickly deteriorating z-encoding at greater imaging depth. In contrast, combined aberration correction and astigmatism induction using the DM resulted in robust z-encoding for imaging depths up to at least $18\ \mu\text{m}$, although the amount of astigmatism needed to be tuned at each imaging depth. Strikingly, a CL in combination with water immersion also results in constant z-encoding over the same depth-range. An advantage of the DM is that a tunable amount of astigmatism can be induced. This could be used for optimizing the amount of astigmatism for each imaging application [6]. However, we found that there is an optimal amount of astigmatism as determined from the changes in x, y and z localization precisions as function of astigmatism. This implies that a well-chosen CL combined with a water immersion objective would perform equally well. Nonetheless, when imaging in more inhomogeneous samples the increased importance of aberration correction might necessitate adaptive optics for optimal imaging.

Furthermore we show that using an oil objective with a DM for 3D-SMLM in biological samples results in superior images compared to using a CL. The number of localizations is 1.5-2 fold higher, resulting in denser reconstructed structures, and the robust DM-induced z-encoding results in discrimination of microvilli lying on top of each other. A comparison using a water immersion objective and a well-chosen CL should clarify the need for aberration correction of sample-induced aberrations in these biological samples. The depth-dependent performance of other methods for achieving 3D-SMLM could also be explored. The saddle-point PSF [12], for instance, theoretically has a better x- y- and z-resolution than the astigmatic PSF at the same amount of signal and background photons over a range of $3\ \mu\text{m}$, and can be created using a DM. With a relatively small change to the optical setup bi-plane imaging can be implemented and its behavior explored when imaging deeper into samples. Other PSFs, such as the double helix [13] and the self-bending PSF [14], can be achieved with an SLM instead of a DM because of the necessary abrupt phase changes and might be worth investigating further for 3D performance deep in samples.

ACKNOWLEDGEMENTS

We thank Amol Aher for providing microtubule seeds. This research is supported by the Dutch Technology Foundation STW, which is part of the Netherlands Organisation for Scientific Research (NWO). Additional support came from the European Research Council (ERC Starting Grant to L.C.K.).

AUTHOR CONTRIBUTIONS

B.M.C.C. and L.C.K. designed the study. B.M.C.C. performed experiments and analyzed data. W.N. prepared specimen. B.M.C.C. and L.C.K. wrote the manuscript. L.C.K. supervised the project.

REFERENCES

- 1 Betzig, E. et al. Imaging Intracellular Fluorescent Proteins at Nanometer Resolution. *Science* 313, 1642-1645 (2006).
- 2 Rust, M. J., Bates, M. & Zhuang, X. Sub-diffraction-limit imaging by stochastic optical reconstruction microscopy (STORM). *Nat Meth* 3, 793-796 (2006).
- 3 Huang, B., Wang, W., Bates, M. & Zhuang, X. Three-Dimensional Super-Resolution Imaging by Stochastic Optical Reconstruction Microscopy. *Science* 319, 810-813 (2008).
- 4 Izeddin, I. et al. PSF shaping using adaptive optics for three-dimensional single-molecule super-resolution imaging and tracking. *Optics express* 20, 4957-4967 (2012).
- 5 Mlodzianoski, M. J., Juette, M. F., Beane, G. L. & Bewersdorf, J. Experimental characterization of 3D localization techniques for particle-tracking and super-resolution microscopy. *Optics express* 17, 8264-8277 (2009).
- 6 Burke, D., Patton, B., Huang, F., Bewersdorf, J. & Booth, M. J. Adaptive optics correction of specimen-induced aberrations in single-molecule switching microscopy. *Optica* 2, 177-185 (2015).
- 7 Stuurman, N., Edelstein, A. D., Amodaj, N., Hoover, K. H. & Vale, R. D. Computer Control of Microscopes using μ Manager. *Current protocols in molecular biology* (2010).
- 8 Booth, M. J., Neil, M. A. A., Juškaitis, R. & Wilson, T. Adaptive aberration correction in a confocal microscope. *Proceedings of the National Academy of Sciences* 99, 5788-5792 (2002).
- 9 Mikhaylova, M. et al. Resolving bundled microtubules using anti-tubulin nanobodies. *Nature communications* 6 (2015).
- 10 Visser, T. D. & Oud, J. L. Volume measurements in three-dimensional microscopy. *Scanning* 16, 198-200 (1994).
- 11 Yau, K. W. et al. Microtubule Minus-End Binding Protein CAMSAP2 Controls Axon Specification and Dendrite Development. *Neuron* 82, 1058-1073 (2014).
- 12 Shechtman, Y., Sahl, S. J., Backer, A. S. & Moerner, W. E. Optimal Point Spread Function Design for 3D Imaging. *Physical review letters* 113, 133902 (2014).
- 13 Pavani, S. R. P. et al. Three-dimensional, single-molecule fluorescence imaging beyond the diffraction limit by using a double-helix point spread function. *Proceedings of the National Academy of Sciences of the United States of America* 106, 2995-2999 (2009).
- 14 Jia, S., Vaughan, J. C. & Zhuang, X. Isotropic three-dimensional super-resolution imaging with a self-bending point spread function. *Nat Photon* 8, 302-306 (2014).

SUPPLEMENTARY FIGURES

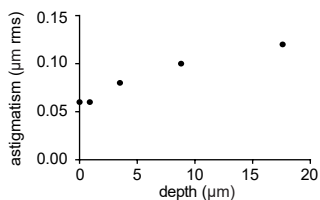


Figure S1: Induced astigmatism as function of depth in the sample

The amount of induced astigmatism to maintain a constant calibration curve slope when imaging deeper into a watery sample with an OI objective.

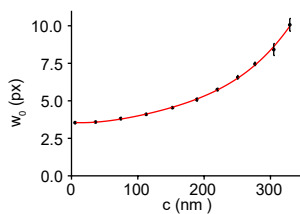
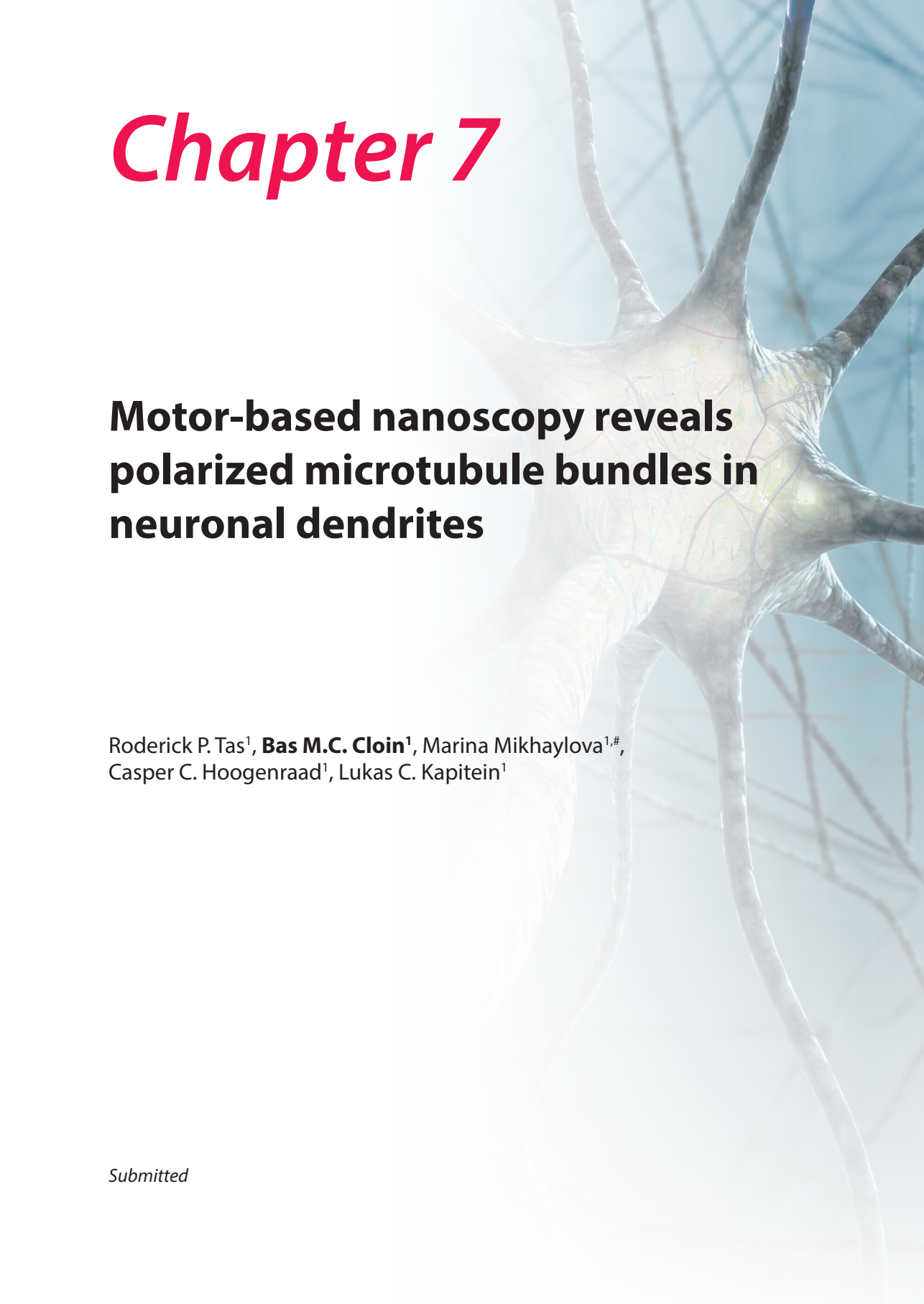


Figure S2: PSF width in the average focal plane as function of focal plane offset c

The width of the PSF at $z=0$ increases for increasing focal plane offset.

¹Division of Cell Biology, Department of Biology, Faculty of Science, Utrecht University, 3584 CH Utrecht, the Netherlands.#present address: University Medical Center Hamburg-Eppendorf, UKE, Center for Molecular Neurobiology, ZMNH, Falkenried 94, 20251 Hamburg, Germany

Chapter 7



Motor-based nanoscopy reveals polarized microtubule bundles in neuronal dendrites

Roderick P. Tas¹, **Bas M.C. Cloin**¹, Marina Mikhaylova^{1,#},
Casper C. Hoogenraad¹, Lukas C. Kapitein¹

Submitted

ABSTRACT

The intrinsic structural polarity of microtubules determines the directionality of motor proteins, which move selectively towards either the microtubule plus or minus end. However, precisely resolving microtubule orientations within dense cytoskeletal structures has remained challenging. Here we use nanometric tracking of motor proteins running over an extracted cytoskeleton to super-resolve microtubules and determine their polarity. In hippocampal neurons, we find that axonal microtubules are uniformly oriented, whereas microtubules in dendrites have mixed orientations with no overall polarization throughout the entire dendrite. However, within dendrites different bundles often have a preferred polarity and are spatially separated from bundles of opposite polarity. The existence of such multilane highways reveals an unanticipated local order within dendritic microtubules arrays, with immediate implications for models of neuronal transport.

MAIN TEXT

The structural polarity of microtubules determines the directionality of motor proteins, which move selectively towards either the microtubule plus (most kinesins) or minus end (dynein) to control the transport and positioning of proteins, RNAs and organelles [1,2]. Understanding transport on higher-level microtubule arrays, such as mitotic spindles or neuronal microtubule bundles, therefore requires knowledge of microtubule orientations within these structures. For example, on uniformly oriented microtubule arrays, such as found in the axons of most neurons, cargoes driven by a specific motor will move unidirectionally, whereas arrays with mixed microtubule orientations, such as found in neuronal dendrites or in the mitotic spindle, will lead to directional switching [3,4]. It has been proposed that spatially defined microtubule orientations contribute to organelle patterning, but experimental validation has been hampered by the difficulty to robustly assess microtubule orientations within dense networks.

Microtubule polarity can be assessed by combining electron microscopy of microtubule cross sections with a specialized preparation technique during which tubulin is added to permeabilized cells, the so-called hook decoration technique [5,6]. Using this labor-intensive, low throughput technique, it was reported that microtubules are equally mixed between both orientations in the first half of the dendrite, but that plus-end are predominantly oriented outwards in the distal dendrite [7,8]. More recently, proteins that mark either the plus or minus end of microtubules have been used to assign microtubule polarity [9,10], but these techniques cannot reliably report the overall polarization of microtubule arrays, as they only label (a subset of) dynamic ends, irrespective of their length. Experiments that combine imaging of end targeting proteins with laser-based microtubule severing can locally sample microtubule orientations [11,12], but suffer from potential artifacts due to damage-induced calcium transients that alter microtubule dynamics. Finally, second-harmonic generation microscopy can be used to estimate overall microtubule polarization in dense bundles [13,14], but proper calibration typically requires prior knowledge [15]. Thus, robustly resolving microtubule orientations within dense cytoskeletal structures has remained a central challenge.

Because most motor proteins move unidirectionally, using them as transient binding probes for single-molecule localization microscopy [16,17] would provide a diffraction-unlimited image and also report the orientation of the microtubules. Nevertheless, completely sampling a dense microtubule array requires detecting thousands of single-molecule events over the course of several minutes, and any concurrent microtubule rearrangement will blur the final image and obscure structural information. To overcome this challenge, we tested whether motor proteins could still move over microtubules after chemical fixation of the cytoskeleton [18] (Figure 1A). COS7 cells were permeabilized using detergent, extracted and fixed using paraformaldehyde. Using real-time imaging to carefully optimize buffer conditions for extraction and fixation (Figure S1) resulted in a procedure to successfully preserve microtubule organization without any noticeable rearrangements or depolymerization (Figure 1A). Subsequent addition of purified and fluorescently labeled kinesin-1 molecules resulted in numerous transient events in which a motor bound to the microtubule and ran over it for hundreds of nanometers with a speed of $7.5 \pm 3.0 \cdot 10^2$ nm/s (average \pm SD) (Figure 1B-C, S2, Movie S1).

Next, we analyzed these binding events using single-molecule localization and tracking techniques to construct a diffraction-unlimited image of the microtubule array in which the absolute orientation of each microtubule is known (Figure 1B-E, S2, S3). Line scans across individual microtubules revealed a full width at half maximum (FWHM) of 52 ± 5 nm (mean \pm SD for $n=30$ profiles, Figure 1D), suggesting a lateral resolution of the same magnitude, because microtubule FWHM is a good predictor of lateral resolution in case of sufficient labeling density [19]. As expected for this cell type, most microtubules were oriented with their plus end directed outwards, whereas a subset of microtubules was oriented oppositely (Figure 1C-D).

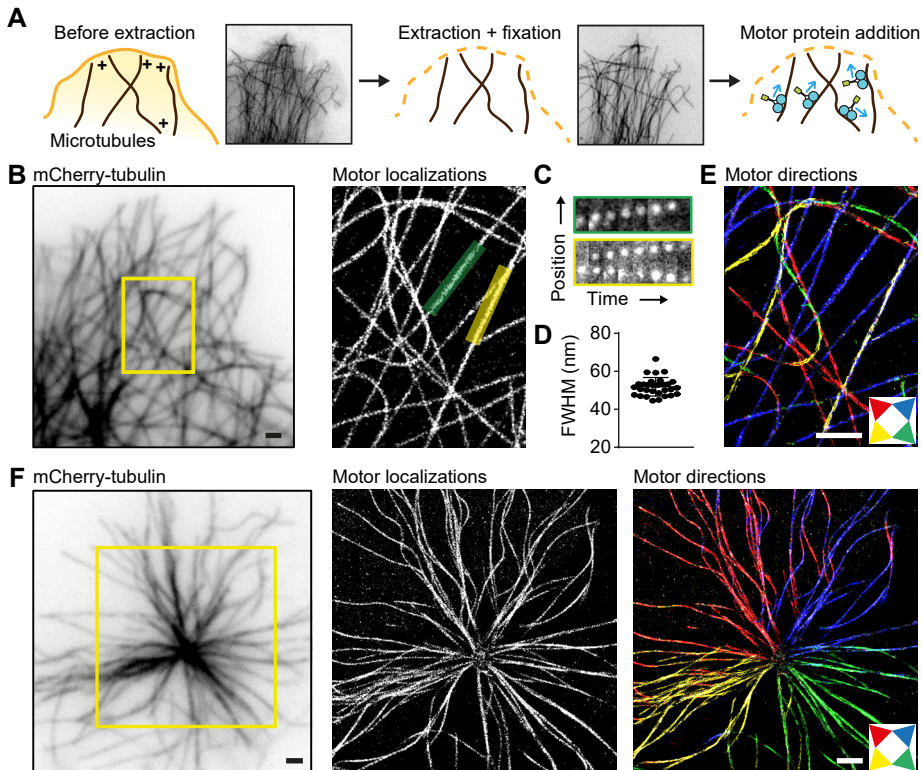


Figure 1: motor-PAINT: super-resolution imaging of microtubules and their orientations

- A) Assay: after extraction and fixation, purified and fluorescently labeled motors are added and map out the microtubule array by unidirectional runs.
- B) Extracted COS7 cell expressing mCherry-tubulin (left) and corresponding super-resolved image obtained by subpixel localization of thousands of motor binding events (right, 21841 localizations).
- C) Stills demonstrating directional movements along the microtubules highlighted in B).
- D) FWHM of cross sections of microtubule imaged by motor tracking (mean \pm s.d.: 52 ± 1 nm, $n=30$ profiles).
- E) Super-resolution reconstruction with all microtubule segments colored according to their absolute orientation. Legend arrows point in the direction of the plus end. Imaged obtained from 6250 motor localizations (~ 1600 tracks) and using track interpolation (see methods).
- F) Orientation mapping of a centrosomal microtubule array obtained after nocodazole washout in a COS7 cell expressing mCherry-tubulin.
- Scale bars: 1 μ m.

In occasional cases, movements in opposite directions were detected along a single line (Figure 1C,E), reflecting either erratic motor motility or the presence of two or more closely spaced microtubules of opposite polarity. To validate the motors trajectories as reliable readout of microtubule polarity, we treated cells with the microtubule destabilizing agent nocodazole, followed by washout 6 minutes prior to extraction and fixation. This procedure induced rapid regrowth of microtubules nucleated by the centrosome, resulting in a well-defined radial array of microtubules with all plus ends oriented outward (Figure 1F). Indeed, the motor-based super-resolution image obtained for these cells unambiguously confirmed this organization, with 100% of centrosome-associated microtubules attached with their minus end (Figure 1G, 141 microtubules in 3 cells). Thus, motors moving over an extracted cytoskeleton reliably report the polarity of microtubules and can be used to reconstruct a super-resolved image. Because our method is conceptually related to transient binding approaches that can be classified as PAINT variants (point-accumulation-for-imaging-in-nanoscale-topography) [17,20-23], we termed it motor-PAINT.

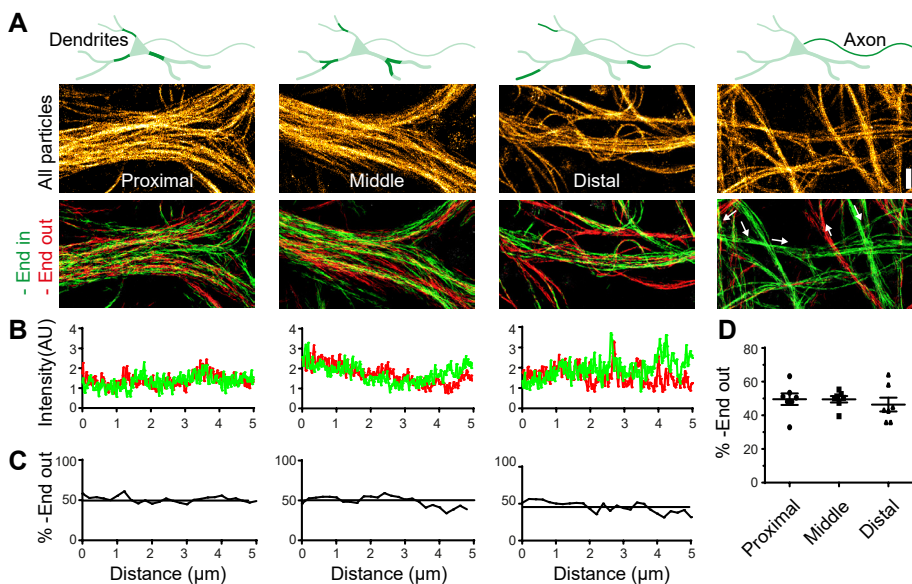


Figure 2: Dendritic microtubules have mixed orientations throughout the entire dendrite

A) Motor-based super-resolution reconstruction of microtubules in dendrites and axons of cultured rat hippocampal neurons (DIV 16-17). Top images are based on all binding events (> 42405 events per image). Bottom images are color coded for absolute orientation. Track interpolation was used for all run-based images.

B) Quantification of inward and outward moving kinesins in 5 μm long proximal, middle and distal dendritic segments, reflecting the number minus-end outward and inward oriented microtubules, respectively.

C) Percentage of minus-end out oriented microtubules in proximal, middle and distal dendritic segments, based on the graphs shown in B).

D) Average percentage of minus-end out oriented microtubules in proximal, middle and distal dendritic segments ($N=7$ segments from 7 neurons for every category).

Scale bar: 1 μm .

We next used our methodology to explore the microtubule organization in the dendrites and axons of rat hippocampal neurons. Consistent with earlier reports [7,10,12], microtubules in axons were uniformly oriented, whereas microtubules in dendrites were oriented both ways (Figure 2A). Comparing the number of outward and inward runs in 5- μm stretches in proximal, middle and distal regions of dendrites revealed that 50% of the microtubules were oriented minus-end out throughout the dendrite (Figure 2B-D). Interestingly, the separate images created for minus-end outward and minus-end inward oriented microtubules were not entirely identical. Often, spatially separated bundles of microtubules in dendrites would be enriched for one orientation, indicating local orientational order (Figure 3A-C). Quantification revealed that individual bundles displayed 2-4 fold enrichment in either outward or inward runs, suggesting a 66/33% - 80/20% ratio between microtubules of opposing orientations (Figure 3C). Thus, the dendritic microtubule array is comprised of bundles of preferred polarity, while overall both orientations are equally abundant.

To further quantify the dissimilarity between microtubule networks of opposing orientations and estimate its spatial extent, we calculated the spatial correlation between the two images as a function of reconstruction pixel size, i.e. $C_{in/out}$. If both images were identical, the correlation would be 1, whereas it would be zero if all non-zero pixels in one image would be zero in the other. As a control, we also calculated the spatial correlation $C_{odd/even}(p)$ between

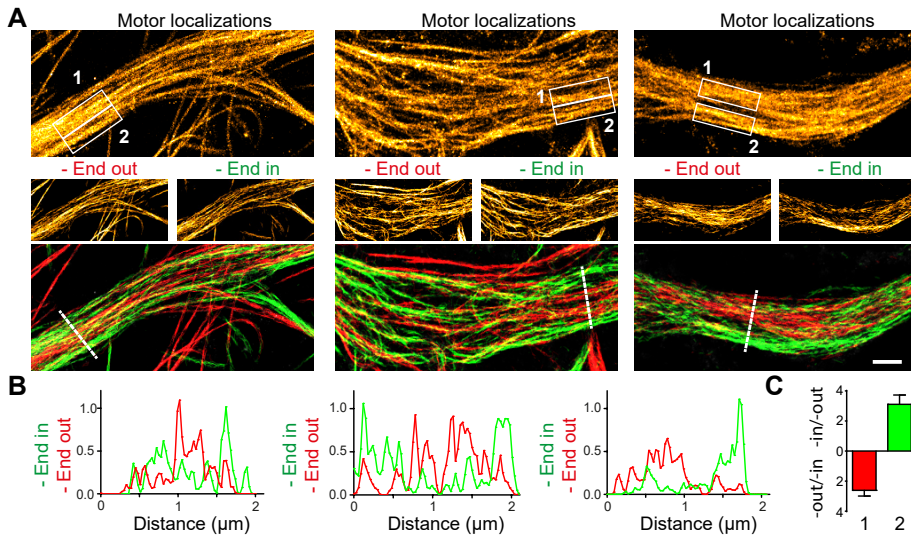


Figure 3: Local orientational order in dendritic microtubule arrays

A) Three examples of dendrites demonstrating bundles of preferred polarity (left-right). Motor-based super-resolution reconstructions, based on either all binding events (top), inward runs (middle right), outward runs (middle left) or runs of both directions (bottom). Track interpolation was used for the run-based images.

B) Intensity profiles for inward and outward pointing microtubules along the lines indicated in A).

C) Ratio between outward and inward runs or inverse for regions marked with 1 or 2 in A).

Scale bar: 1 μm

two reconstructions obtained from either odd or even localizations, irrespective of orientation (Figure 4, S3, S4). These control correlations were close to 1 for pixel sizes above 100 nm, but decreased at lower pixel sizes. Fitting an exponential saturation function revealed that the control images were non-identical at length scales below 51 nm ($n=10$ different images for 10 different neurons). This reflects the pointillistic nature of the images, which are composed of individual points that correspond to single localizations. When rendered at pixel sizes smaller than the average distance between localizations, non-zero pixel values mostly emerge from individual localizations, which are divided between the two reconstructions and do not overlap. In our case, the length scale of 51 nm suggests an average spacing between points on a labeled structure of ~ 25 nm.

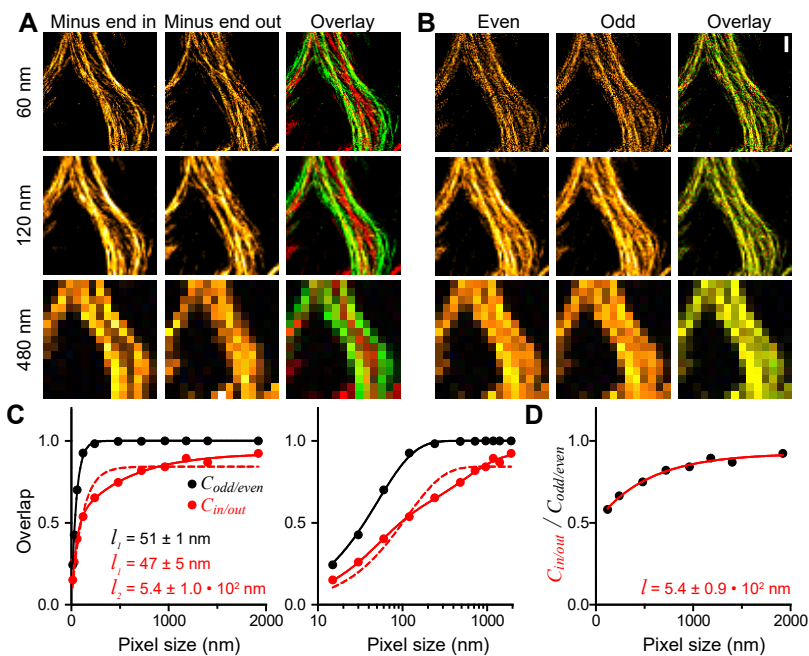


Figure 4: Correlation-based analysis of local orientational order

A) Motor-based super-resolution reconstructions of a dendritic segment, based on inward runs (left) or outward runs (middle) and rendered at different pixel sizes. Right images show the overlay of the left and middle images. See Figure S4 for more renderings.

B) Motor-based super-resolution reconstructions of the same segment, based on all even (left) or odd (right) localizations, irrespective of direction, and rendered at different pixel sizes. Right images show the overlay of the left and middle images.

C) Degree of overlap as a function of reconstruction pixel size, obtained by calculating the correlation coefficient between reconstructions of minus-end in and minus-end out tracks ($C_{m/out}$), or reconstructions of even and odd localizations, irrespective of direction ($C_{odd/even}$). Solid black and dotted red lines are fits of $C = A(1-\exp(-p/l))$, whereas the solid red line is a fit with $C = A(1-B\exp(-p/l_1) - (1-B)\exp(-p/l_2))$. Error bars of SE fall within symbol size.

D) Ratio between $C_{m/out}$ and $C_{odd/even}$ for pixel sizes >100 nm and fitted with . Error bars of SE fall within symbol size. Scale bar: 1 μ m.

Similar to the control curve, $C_{in/out}(p)$ also rapidly increased when increasing pixel size from 15 to 120 nm. However, at 120 nm, $C_{in/out}$ was still only 54% of $C_{odd/even}$, indicating non-random dissimilarity between minus-end outward and inward oriented microtubule arrays. The ratio between $C_{in/out}$ and $C_{odd/even}$ increased slowly to > 85% for pixel sizes above 1000 nm and fitting a bi-exponential saturation function to $C_{in/out}(p)$ revealed an additional length scale of $5.4 \pm 1.0 \times 10^2$ nm (Figure 4C-D). These results demonstrate that at lateral length scales below 600 nm dendritic microtubules are enriched for a specific orientation.

By nanometric tracking of motors that move over an extracted and fixed cytoskeleton, we have established a method to create diffraction-unlimited images of microtubules in which all orientations are known. This method, termed motor-PAINT, confirmed that both microtubule orientations are equally abundant throughout the dendrite, as recently reported by analyzing the movement of microtubule plus end binding proteins upon laser-induced microtubule severing [12]. In addition, our experiments revealed unanticipated local orientational order in dendrites where microtubules are organized in multiple polarized bundles. The existence of such multilane highways has immediate consequences for understanding active transport in dendrites, because the motility of cargoes drive by specific motors over these bundles will no longer be random, as expected for a random distribution of microtubule orientations [3], but biased. As such, our results help to explain the observation of long directional cargo movements in dendrites [24]. Our earlier mathematical modeling revealed that even a small asymmetry will create a directional bias for motors [3] (Figure S5). For example, when plus-end out microtubules are twofold enriched, 50% of kinesin-driven cargoes would accumulate in the last 20% or 9% of the bundle for a bundle length of 20 or 50 μ m, respectively (Figure S5B-C). We anticipate that our method will be an important starting point to further explore how microtubule organization guides intracellular transport in different cellular contexts.

ACKNOWLEDGMENTS

This research was supported by the Netherlands Organisation for Scientific Research (NWO) (NWO-ALW-VICI to C.C.H., NWO-ALW-VIDI to L.C.K.), the Dutch Technology Foundation STW, which is part of the NWO (NWO-NANO to C.C.H and L.C.K), and the European Research Council (ERC Starting Grant to L.C.K., ERC Consolidator Grant to C.C.H).

AUTHOR CONTRIBUTIONS

LCK conceived research and supervised the project. MM and BMCC established proof-of-principle and initial protocols. RPT optimized procedures, purified motors, designed and performed experiments and analyzed data. BMCC (partially) performed experiments and analyzed data for figures 1, 2, 3, and S2. CCH provided neuronal cultures and gave advice during the project. RPT and LCK wrote the paper with input from all other authors.

REFERENCES

- 1 Vale, R. D. The molecular motor toolbox for intracellular transport. *Cell* 112, 467-480 (2003).
- 2 Li, R. & Gundersen, G. G. Beyond polymer polarity: how the cytoskeleton builds a polarized cell. *Nat Rev Mol Cell Biol* 9, 860-873 (2008).
- 3 Kapitein, L. C. et al. Mixed microtubules steer dynein-driven cargo transport into dendrites. *Curr Biol* 20, 290-299 (2010).
- 4 Derivery, E. et al. Polarized endosome dynamics by spindle asymmetry during asymmetric cell division. *Nature* 528, 280-285 (2015).
- 5 Heidemann, S. R. & McIntosh, J. R. Visualization of the structural polarity of microtubules. *Nature* 286, 517-519 (1980).
- 6 Baas, P. W. & Lin, S. Hooks and comets: The story of microtubule polarity orientation in the neuron. *Developmental neurobiology* 71, 403-418 (2011).
- 7 Baas, P. W., Deitch, J. S., Black, M. M. & Banker, G. A. Polarity orientation of microtubules in hippocampal neurons: uniformity in the axon and nonuniformity in the dendrite. *Proc Natl Acad Sci U S A* 85, 8335-8339 (1988).
- 8 Baas, P. W., Black, M. M. & Banker, G. A. Changes in microtubule polarity orientation during the development of hippocampal neurons in culture. *J Cell Biol* 109, 3085-3094 (1989).
- 9 Yau, K. W. et al. Microtubule Minus-End Binding Protein CAMSAP2 Controls Axon Specification and Dendrite Development. *Neuron* 82, 1058-1073 (2014).
- 10 Stepanova, T. et al. Visualization of microtubule growth in cultured neurons via the use of EB3-GFP (end-binding protein 3-green fluorescent protein). *J Neurosci* 23, 2655-2664 (2003).
- 11 Bragues, J., Nuzzo, V., Mazur, E. & Needleman, D. J. Nucleation and transport organize microtubules in metaphase spindles. *Cell* 149, 554-564 (2012).
- 12 Yau, K. W. et al. Dendrites In Vitro and In Vivo Contain Microtubules of Opposite Polarity and Axon Formation Correlates with Uniform Plus-End-Out Microtubule Orientation. *J Neurosci* 36, 1071-1085 (2016).
- 13 Kwan, A. C., Dombeck, D. A. & Webb, W. W. Polarized microtubule arrays in apical dendrites and axons. *Proc Natl Acad Sci U S A* 105, 11370-11375 (2008).
- 14 Dombeck, D. A. et al. Uniform polarity microtubule assemblies imaged in native brain tissue by second-harmonic generation microscopy. *Proc Natl Acad Sci U S A* 100, 7081-7086 (2003).
- 15 Yu, C. H. et al. Measuring microtubule polarity in spindles with second-harmonic generation. *Biophys J* 106, 1578-1587 (2014).
- 16 Patterson, G., Davidson, M., Manley, S. & Lippincott-Schwartz, J. Superresolution imaging using single-molecule localization. *Annu Rev Phys Chem* 61, 345-367 (2010).

- 17 Molle, J. et al. Superresolution microscopy with transient binding. *Curr Opin Biotechnol* 39, 8-16 (2016).
- 18 Sivaramakrishnan, S. & Spudich, J. A. Coupled myosin VI motors facilitate unidirectional movement on an F-actin network. *J Cell Biol* 187, 53-60 (2009).
- 19 Mikhaylova, M. et al. Resolving bundled microtubules using anti-tubulin nanobodies. *Nature communications* 6, 7933 (2015).
- 20 Sharonov, A. & Hochstrasser, R. M. Wide-field subdiffraction imaging by accumulated binding of diffusing probes. *Proc Natl Acad Sci U S A* 103, 18911-18916 (2006).
- 21 Giannone, G. et al. Dynamic superresolution imaging of endogenous proteins on living cells at ultra-high density. *Biophys J* 99, 1303-1310 (2010).
- 22 Jungmann, R. et al. Multiplexed 3D cellular super-resolution imaging with DNA-PAINT and Exchange-PAINT. *Nat Methods* 11, 313-318 (2014).
- 23 Kiuchi, T., Higuchi, M., Takamura, A., Maruoka, M. & Watanabe, N. Multitarget super-resolution microscopy with high-density labeling by exchangeable probes. *Nat Methods* 12, 743-746 (2015).
- 24 Esteves da Silva, M. et al. Positioning of AMPA Receptor-Containing Endosomes Regulates Synapse Architecture. *Cell reports* 13, 933-943 (2015).
- 25 Chazeau, A., Katrukha, E. A., Hoogenraad, C. C. & Kapitein, L. C. in *Methods in Cell Biology* Vol. 131 (ed K. Pfister) in press (2015).
- 26 Edelstein, A., Amodaj, N., Hoover, K., Vale, R. & Stuurman, N. in *Current Protocols in Molecular Biology* (John Wiley & Sons, Inc., 2001).
- 27 Sharma, A. et al. Centriolar CPAP/SAS-4 Imparts Slow Processive Microtubule Growth. *Dev Cell* 37, 362-376 (2016).

LEGENDS TO SUPPLEMENTARY MOVIES

Movie S1

Video demonstrating motor movements on the extracted microtubule cytoskeleton of a COS7 cell. This video corresponds to the cell in Figure 1B-E and Figure S2. Imaged at 10 frames per seconds, total time is 16 seconds. Scale bar is 2 μm . 4 x sped up.

Movie S2

Video demonstrating motor movements on the extracted dendritic microtubule cytoskeleton of a hippocampal neuron. This video corresponds to Figure 3. Imaged at 10 frames per seconds, total time is 16 seconds. Scale bar is 2 μm . 4 x sped up.

SUPPLEMENTARY FIGURES

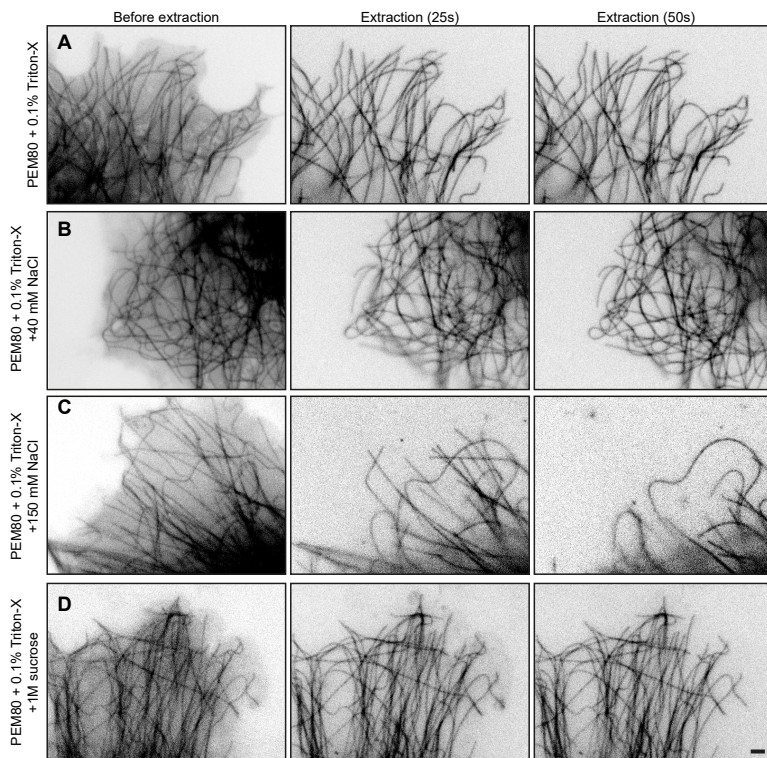


Figure S1: Preservation of the microtubule cytoskeleton during extraction

Optimization of the extraction protocol to preserve microtubule organization in COS7 cells expressing cherry-tubulin. Images shown were obtained before extraction (left), 25 seconds after extraction (middle), or 50 seconds after extraction and before fixation (right). Extraction was performed in the presence of 0.1-0.15% Triton-X in PEM80 buffer (A), supplemented with NaCl (B,C) or sucrose (D). The conditions in D) were used for all subsequent experiments.

Scale bar: 2 μm

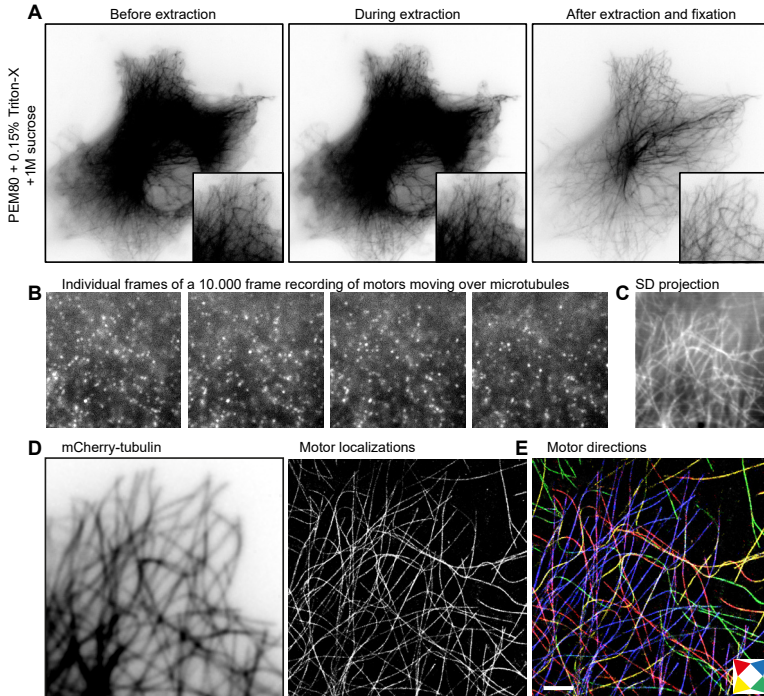


Figure S2: Super-resolution imaging of microtubules and their orientations

A) COS7 cell expressing *mCherry-tubulin* shown before extraction (left), during extraction (middle) and after fixation (right). Zoom indicates the region of interest for which the microtubule orientations are determined in **B)** (similar as figure 1B-C).

B) Four subsequent frames from a 10.000 frame recording of the zoom region in **A)**.

C) Median filtered (0.3 pixel size) standard deviation projection of the complete 10.000 frame recording of the zoom region in **A)** (also see Movie S1).

D) Zoom of cell shown in **A)** expressing *mCherry-tubulin* (left) and corresponding super-resolved image obtained by subpixel localization of thousands of motor binding events (middle, 255466 localizations).

E) Super-resolution reconstruction with all microtubule segments colored according to their absolute orientation.

Legend arrows point in the direction of the plus end. Directional image obtained from 19511 motor trajectories with 72846 localizations and created using track interpolation (see methods).

Scale bar: 2 μm

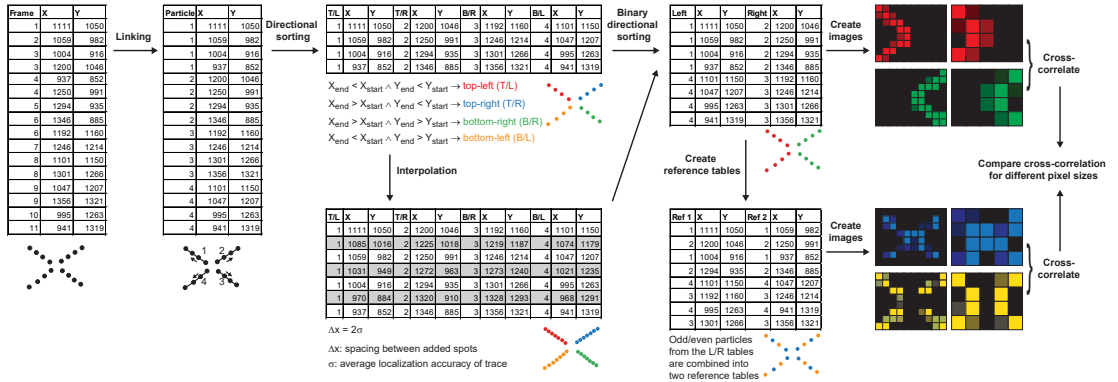


Figure S3: Analysis workflow

Particle tables containing single molecule information are linked to generate tracks and the resulting tracks are sorted based on the orientation. Optionally, tracks are interpolated to enhance visualization. For neuronal acquisitions tracks are sorted in two bidirectional tables. To analyze the overlap, control particle tables are created by sorting even and odd localizations, irrespective of orientations. Subsequently, the correlation coefficient is calculated for the orientation images or the reference images.

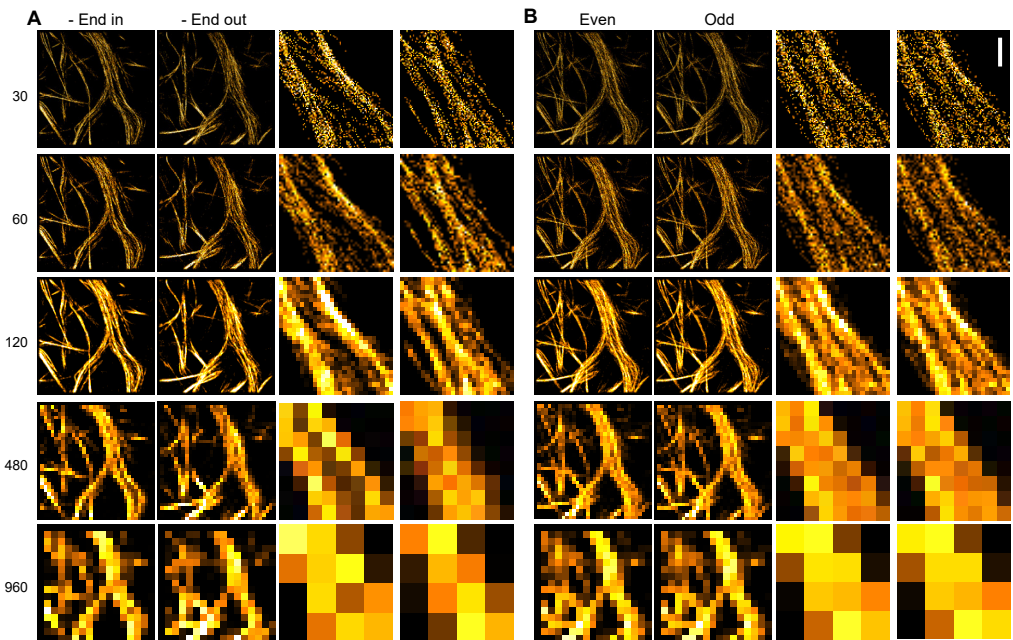


Figure S4: Correlation-based analysis of the spatial extent of orientational order

A) Motor-based super-resolution reconstructions of a dendritic segment, based on inward runs (left and left zoom) or outward runs (right and right zoom) and rendered at different pixel sizes. These pictures augment Figure 4A).

B) Motor-based super-resolution reconstructions of the same segment, based on all even (left and left zoom) or odd (right and right zoom) localizations, irrespective of direction, and rendered at different pixel sizes. These pictures augment Figure 4B).

Scale bar: $1\mu\text{m}$

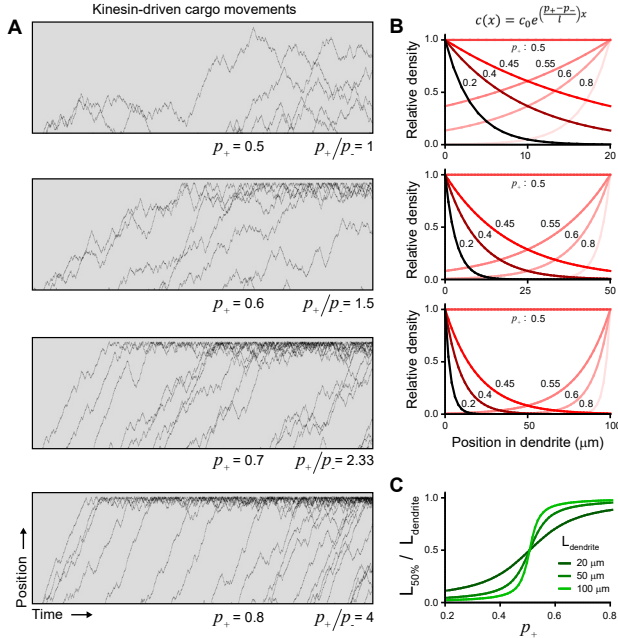


Figure S5: Orientational order and directional transport

A) Simulated kymographs of kinesin-driven transport on microtubule arrays with different fractions of plus-end out oriented microtubules p_+ , as indicated. A small asymmetry in orientations results in a strong directional bias. Total dendrite length $L_{dendrite}$ is $100 \mu\text{m}$ and average run length l before selecting a new direction is $2 \mu\text{m}$.

B) Expected distributions of kinesin-driven cargoes for different fractions of plus-end out oriented microtubules p_+ and for three different dendrite length ($20, 50, 100 \mu\text{m}$). Distributions follow the stated equation and are normalized to maximum density. Numbers indicated in the graph denote the specific p_+ for each curve.

C) Graph of the relative dendritic coordinate, $L_{50\%}/L_{dendrite}$, at which the number of particles before that position equals the number of particles beyond that position. $L_{50\%}/L_{dendrite}$ is shown against p_+ for three dendritic lengths. Except for $p_+ = 0.5$, where $L_{50\%}/L_{dendrite} = 0.5$, the functional form plotted is $L_{50\%}/L_{dendrite} = \frac{1}{\alpha} \ln(\frac{1}{2} e^{\alpha L_{dendrite}} + \frac{1}{2}) / L_{dendrite}$, with $\alpha = \frac{p_+ - p_-}{l}$.

SUPPLEMENTARY MATERIALS AND METHODS:

DNA constructs and Protein purification

To generate DmKHC(1-421)-GFP-6xHis, amino acids 1-421 of the *Drosophila* kinesin heavy chain were inserted in a pET28a-GFP-6xHis expression vector in the NcoI and EcoRI site. GFP was previously inserted between the EcoRI and XhoI sites. The construct was verified by sequencing and transformed in the BL21DE3 bacterial strain.

To express the DmKHC(1-421)-GFP-6xHis, a 2L culture was grown until OD0.6. Expression was induced with 1mM of IPTG and cells were grown for 0.5 hours at 37°C and 3.5 hours at 20 °C. Cells were then pelleted by centrifugation and resuspended on ice in resuspension buffer (20mM Pipes, 150mM NaCl, 4 mM MgSO₄, pH7.0) supplemented with lysozyme and protease inhibitor cocktail (Roche). Subsequently, cells were lysed through 5 rounds of 30 seconds sonication. The soluble fraction containing the expressed protein was separated through 40 minutes centrifugation at 20000g and incubated with NiNTA beads (Roche) for 1 hour at 4°C.

Beads were washed 3 times in resuspension buffer supplemented with 50 µM ATP and in the last wash 60mM imidazole was added. Recombinant protein was eluted for 15 minutes in Elution buffer (80mM Pipes, 4mM MgSO₄, 300mM imidazole, 50µM ATP, pH7.0). The supernatant was concentrated to 0.5 ml and recombinant protein was further purified and buffer exchanged through gel filtration on a superdex75 column (GE Healthcare, Superdex 75 10/300) equilibrated with PEM80 buffer (80 mM Pipes, 4mM MgCl₂, 1 mM EGTA). Fractions containing DmKHC(1-421)-GFP-6xHis were identified by SDS-page, collected and stored at -80 °C in 10% glycerol after snap-freezing in liquid nitrogen.

Cell cultures and transfection

COS-7 cells were cultured in DMEM/Ham's F10 (1:1) medium containing 10% FCS and penicillin/streptomycin. Cells were plated on 18-mm diameter coverslips 2–4 days before transfection. Cells were transfected with Eugene6 transfection reagent (Roche) according to the manufacturer's protocol and imaged one day after transfection.

Primary hippocampal cultures were prepared from embryonic day 18 (E18) rat brains. Cells were plated on coverslips coated with poly-L-lysine (30 mg ml⁻¹) and laminin (2 mg ml⁻¹). Hippocampal cultures were grown in Neurobasal medium (NB) supplemented with B27 (Invitrogen), 0.5 mM glutamine, 12.5 mM glutamate, and penicillin plus streptomycin. Transfections of hippocampal neurons were performed 24 h before imaging with lipofectamine 2000 (Invitrogen). DNA (1.8 µg per well) was mixed with 3.3 µl lipofectamine 2000 in 200 ml NB, incubated for 30 min, and added to the neurons in NB supplemented with 0.5 mM glutamine at 37 °C in 5% CO₂. After 60-90 min neurons were washed with NB and transferred to the original medium at 37 °C in 5% CO₂ for 1 day.

Kinesin motility assay

To prepare cellular microtubule cytoskeletons for the kinesin motility assays, the cytoplasm of COS7-cells or hippocampal neurons was extracted for 1 minute in extraction buffer (1M sucrose + 0.15% Triton-X in PEM80) at 37 °C. Subsequently, an equal amount of fixation buffer (2% PFA in PEM80 at 37 °C) was added and the solution was gently mixed by pipetting for 1 minute. The extraction and fixation buffer were then replaced by washing solution (PEM80 + 100nM Taxol 37°C) for 1 minute. After three more 1-minute washes imaging buffer (1.7% w/v glucose, 185 µg/ml glucose oxidase, 40 µg/ml catalase, 5mM ATP, 1mM DTT, 100mM Taxol in PEM80 buffer at 37 °C) was added.

mCherry-tubulin expressing cells were selected for imaging and after a conventional preacquisition of cherry-tubulin, 1 µl of approximately 30nM DmKHC(1-421)-GFP-His was added above the location of acquisition and 10000-20000 frames were acquired at 10 Hz using stream acquisition. Because the concentration of visible kinesins at the selected position gradually decreased because of diffusion and photobleaching, recombinant kinesin was supplemented during imaging to increase the number of localizations of motile kinesins.

For the Nocodazole washout experiments (Figure 1F), COS-7 cells were treated with 10 µM nocodazole for 1 hour at 37°C followed by 1 hour incubation at 4°C. Samples were washed 6x times with cold culturing medium. Subsequently, microtubules were allowed to polymerize for ~6 minutes at 37°C. Finally, extracted microtubule cytoskeletons were prepared as described earlier.

Most samples were imaged on a Nikon Ti-E microscope equipped with a 100x Apo TIRF oil immersion objective (NA. 1.49) and Perfect Focus System 3. Excitation was achieved with a mercury lamp or via a custom illumination pathway starting with a Lighthub-6 (Omicron) containing a 638 nm laser (BrixX 500 mW multimode, Omicron), a 488nm laser (Luxx 200 mW, Omicron) and using an optical configuration that allowed tuning the angle of incidence. In most instances, total internal reflection or highly inclined laser illumination was used. Emission light was separated from excitation light with a quad-band polychroic mirror (ZT405/488/561/640rpc, Chroma), a quad-band emission filter (ZET405/488/561/640m, Chroma), and an additional single-band emission filter (ET525/50m for GFP emission, Chroma), and detected using a sCMOS camera (Hamamatsu Flash 4.0v2). In some cases, a very similar microscope that has been previously described [1] was used in the same configuration, but using an Andor DU-897D EMCCD camera with an additional 2.5x Optovar to achieve an effective pixel size of 64 nm. All components were controlled by Micromanager software[2].

Single molecule localization and track orientation analysis

Images were analyzed using our custom ImageJ plugin called DoM (Detection of Molecules, https://github.com/ekatrukha/DoM_Utrecht), which has been described in detail previously [1,3]. Briefly, each image in an acquired stack was convoluted with a two dimensional Mexican hat-type kernel that matches the microscope's point spread function (PSF) size. Spots were detected by thresholding the images and their sub-pixel positions were determined by fitting a 2D Gaussian function using unweighted nonlinear least squares fitting with the Levenberg-Marquardt algorithm. Drift correction was applied by calculating the spatial cross-correlation function between intermediate super-resolved reconstructions.

To link localizations into motor trajectories, the linking function of DoM was used as described previously [4]. Briefly, linking was performed using a nearest neighbor algorithm where the maximum permitted distance between detected molecules in two subsequent frames, was 3 pixels (~192 nm). No frame gap was permitted within a track. Only individual tracks that could be observed for at least 3 subsequent frames were included for further analysis. In addition, trajectories in which the angle between two segments was larger than 75 degrees were discarded.

Next, trajectories were separated into different tables based on their direction. For non-neuronal cells, localizations belonging to validated tracks were separated into four different particle tables defined by four criteria for the total displacement in x and y coordinates of the track (i.e. $Dx > 0 \wedge Dy > 0$; $Dx > 0 \wedge Dy < 0$; $Dx < 0 \wedge Dy > 0$; $Dx < 0 \wedge Dy < 0$). For neuronal cells, particle tables were separated into two particle tables corresponding to the axis of the dendrite. The resulting particle tables were subsequently reconstructed using DoM into different super-resolved images that represented all microtubules with similar orientations.

Because the average frame-to-frame displacement of motors was 75 ± 30 nm, tracks appeared as a series of dots when rendered at small pixel sizes. To better visualize these tracks, additional localizations were inserted with a spacing of 15 nm by interpolating between two subsequent localizations within tracks. The localization precision was set as the average of the two observed localizations. Nevertheless, to avoid potential artefacts, all quantifications were performed on the non-interpolated data sets and images.

Correlation analysis

To determine the degree of overlap between images obtained from the retrograde and anterograde runs, the correlation coefficient $C_{in/out}$ was calculated as

$$C_{n/out} = \frac{\sum_{x=1}^X \sum_{y=1}^Y i_n(x,y) i_{out}(x,y)}{\sqrt{\sum_{x=1}^X i_n^2(x,y) \sum_{y=1}^Y i_{out}^2(x,y)}}$$

where $i_{in}(x,y)$ and $i_{out}(x,y)$ are the intensities of the images based on anterograde and retrograde runs at pixel (x,y) , respectively. Similarly, the correlation coefficient $C_{odd/even}$ was calculated from the intensities $i_{odd}(x,y)$ and $i_{even}(x,y)$ of the images based on odd and even localizations within tracks (see Figure S3). The curves of C against different pixel sizes were fitted in Graphpad Prism 5 using the functions described in the legends.

Simulations

Simulations of motors on microtubule orientations with different ratios of plus and minus end out oriented microtubules were performed as described previously [5]. In the same reference, we also derived the mathematical expression for the distributions of kinesin-propelled cargoes on different arrays as a function of the fractional orientation probabilities p_+ and p_- and the average run length before switching microtubules l :

$$c(x) = c_0 e^{\alpha x}, \text{ with } \alpha = \frac{p_+ - p_-}{l}.$$

Integrating this to calculate the number of particles n at x_n gives:

$$n = \frac{1}{\alpha} (e^{\alpha x_n} - 1)$$

From this, the dendritic coordinate $L_{50\%}$ at which the number of particles before that position equals the number of particles beyond that position can be found by solving

$$\frac{1}{\alpha} (e^{\alpha L_{50\%}} - 1) = \frac{1}{2\alpha} (e^{\alpha L_{dendrite}} - 1), \text{ which gives } L_{50\%} / L_{dendrite} = \frac{1}{\alpha} \ln \left(\frac{1}{2} e^{\alpha L_{dendrite}} + \frac{1}{2} \right) / L_{dendrite}.$$

SUPPLEMENTARY REFERENCES

- 1 Chazeau, A., Katrukha, E. A., Hoogenraad, C. C. & Kapitein, L. C. in *Methods in Cell Biology* Vol. 131 (ed K. Pfister) in press (2015).
- 2 Edelstein, A., Amodaj, N., Hoover, K., Vale, R. & Stuurman, N. in *Current Protocols in Molecular Biology* (John Wiley & Sons, Inc., 2001).
- 3 Yau, K. W. et al. Microtubule Minus-End Binding Protein CAMSAP2 Controls Axon Specification and Dendrite Development. *Neuron* 82, 1058-1073 (2014).
- 4 Sharma, A. et al. Centriolar CPAP/SAS-4 Imparts Slow Processive Microtubule Growth. *Dev Cell* 37, 362-376 (2016).
- 5 Kapitein, L. C. et al. Mixed microtubules steer dynein-driven cargo transport into dendrites. *Curr Biol* 20, 290-299 (2010).



Chapter 8

General discussion



INTRODUCTION

Described in this thesis are the development and use of novel single molecule localization technologies to gain new insights into (neuronal) MT organization. After a recapitulation of the results from previous chapters, these results will be placed in a broader perspective.

The image quality of SMLM depends on a sound optical setup. Aberrations introduced by optical components, or by the sample, result in a distorted PSF, lower photon counts, and a decreased localization precision. Avoiding aberrations or correcting them (Chapter 6) is therefore of great importance. However, optimized fixation protocols and fluorescent probes are just as important for high quality images. The immunostaining protocol described in Chapter 2 allows SMLM of MTs and MAPs with low background signal and high labeling density. It was used in Chapter 5 to show that MT organization drastically changes during neuronal development, and that CAMSAP2 decorates MT minus-ends in neurons. Optimization of fluorescent probes in terms of brightness, return percentage, and size also leads to higher quality SMLM imaging. The commonly used bright monomeric red fluorescent protein mCherry turned out to be a high quality SMLM probe when exploiting a purely chemical caging mechanism with a return percentage up to 80%, as described in Chapter 3. In Chapter 4, novel tubulin nanobodies were shown to enable investigation of individual MTs in dense bundles, which is not possible with conventional antibodies. A property of MTs that cannot be determined with immunostaining is their orientation. We showed in Chapter 7 using a processive kinesin motor protein as a probe for SMLM that the orientation of MTs can be determined in fixed cells and, surprisingly, that there is local orientational order in the dendritic MT array. In the following, I will discuss these results and give recommendations for future research.

INSTRUMENTATION

With the focus in this thesis on SMLM to study MT organization, one wonders how other super-resolution (SR) methods compare. In general, there is a trade-off between spatial and temporal resolution. While SMLM provides the highest spatial resolution among SR methods, it requires acquiring thousands of camera frames. This corresponds to acquisition times in the order of 5 - 30 minutes, an order of magnitude longer than for other SR methods such as stimulated emission depletion (STED) microscopy and structured illumination microscopy (SIM). Although live-cell SMLM has been demonstrated[1-4], the time resolution was in the order of tens of seconds (although subsecond time resolution was also reported[3]), and only a few snapshots could be made. Moreover, the relatively high laser powers associated with SMLM increase the risk of photo-induced toxicity. Other SR methods are therefore more suited for the high resolution study of dynamics in living cells, with advanced SIM approaches appearing to conquer the field in all regards[5].

In fixed specimens, acquisition times and photo-toxicity are less important and its unmatched spatial resolution among SR methods makes SMLM an attractive option. However, imaging in fixed samples is also the domain of electron microscopy (EM) providing

an order of magnitude higher resolution. Established advantages of fluorescence microscopy (FM) over EM, including the extremely high molecular specificity, larger field of view, ease of imaging, and (relatively) high throughput, also apply to SMLM. These advantages over EM leave a substantial role for SMLM in fixed cell imaging. Combining the strengths of EM and FM in correlative light and electron microscopy (CLEM), with SMLM as the FM method, is a very promising approach to further our understanding of cellular organization[6-10].

NOVEL SMLM PROBES

Given the great interest in, and potential of SMLM, specifically designed probes have been rapidly emerging. The properties of both the fluorescent labels and the targeting mechanisms are important parameters for SMLM image quality.

Fluorescent proteins

Photoconvertible and photoswitchable FPs are being developed and improved continuously[11,12]. The use of these FPs in cellular assays lags behind, however, partially because an in-depth characterization is needed to assess any influence of the probe on the investigated system that could result in erroneous interpretations. The possibility to use established conventional FPs for SMLM is therefore of considerable interest. Moreover, it renders knock-in animal models with these FPs directly suitable for SMLM. Recently, the use of conventional RFPs for high quality SMLM has been reported, exploiting thiols in the buffer to induce illumination dependent[13] and independent dark states (Chapter 3). These thiol-based buffers are not compatible with live-cell imaging, however, restricting the use of conventional RFPs for SMLM to fixed samples. The question then arises how RFP SMLM compares to immunostaining with organic dyes. Compared to popular organic dyes, RFPs are less bright resulting in lower localization precisions. However, the small size of FPs (~4 nm) results in a small spacing between the protein of interest (POI) and the fluorophore. We noticed that the width of MTs immunostained with secondary-labeled antibodies and the width of mCherry-tubulin containing MTs were similar in SMLM reconstructions. This implies that the effect of lower photon yield is negated by the closer proximity of the fluorophore when using the RFP. Using labeled primary antibodies or nanobodies tips the scale towards immunostaining for single-color SMLM. Also for hard to detect structures immunostaining is preferred because of signal amplification through multiple dyes per antibody and multiple secondary antibodies per primary antibody.

For multi-color SMLM, the combination of immunostaining with a far-red dye and expression of an RFP can conveniently be used because the thiol-based buffers allow SMLM with both. In fixed cells, it is advantageous to use RFPs over popular green-to-red convertible FPs, such as mEos3.2, since localization precision is similar (Chapter 3) but the green channel is not occupied. Additionally, mCherry is brighter and matures faster compared to popular dark-to-red switchable FPs[14,15], making it a viable option for multi-color SMLM.

Organic dyes

Positioning organic dyes closer to the protein of interest (POI), for instance using nanobodies, increases resolution of SMLM reconstructions as evidenced by smaller apparent MT widths, lower Fourier ring correlation-based resolution, and higher resolving power of individual MTs in bundles (Chapter 4). Other advantages of nanobodies include straightforward production and the possibility to easily obtain cDNA libraries for a POI. A disadvantage is that coupling different dyes to nanobodies is not trivial as it can easily disrupt the binding capacity.

As shown in Chapter 4, the use of nanobodies allows individual MTs to be resolved in tight neuronal bundles in dendrites. However, as can be seen in figure 2i, not all dendritic bundles can be resolved, and more closely spaced axonal MTs, with a 20 nm wall-to-wall distance[16], are still out of reach. Two ways to further increase the resolving power of SMLM are using even smaller probes and increasing localization accuracy. In addition, resolving bundled microtubules often also requires a good resolution in the *z*-direction.

Probes smaller than nanobodies (~3-3.5 nm) are not abundant. Frequently used polypeptide-tags for labeling with organic dyes without immunoprobes, such as the SNAP-tag[17] (~3.6 nm), CLIP-tag[18] (~3.6 nm), and HaloTag[19] (~4.2 nm) are of similar size. Aptamers, single strand oligonucleotides able to bind specifically to all kinds of target molecules after folding into a 3D shape[20], potentially reduce probe-size by a nanometer. Aptamers are used for diagnostics[21], staining of tissue[22], and drug delivery[23], and staining for SR microscopy has also been reported[24]. The potential resolution gain over nanobodies is limited, however, and it is not clear if smaller probes can and will be developed.

Improving localization precision has greater potential to increase SMLM image resolution. Every fluorophore is localized with a certain precision, resulting in a distribution of localization precisions for a SMLM acquisition. Usually, a localization is only added to the super-resolved image if it is localized more precise than a certain threshold, or cut-off, determined from the distribution of localization precisions. There is a tradeoff between the number of localizations contributing to the final image and the localization precision cut-off; a stringent cut-off results in better overall localization precision but allows less localizations to contribute to the SMLM reconstruction, resulting in a lower Nyquist resolution.

Improvement of localization precision could come from development of new, brighter dyes, although no dyes have been developed that outperform the popular far-red dyes used from the very beginning of SMLM. However, optimized buffers improve localization precision of these dyes up to a factor of two[25,26]. A screen for new buffer components might reveal chemicals further improving localization precision.

Localization precision can also be improved indirectly by increasing the number of localizations, allowing a more stringent precision cut-off. The number of localizations for immunostained samples is mostly limited by the amount of dyes attached to each POI. Coupling more dyes per anti- or nanobody might be possible although this can interfere

with their binding capacity. Moreover, with more fluorophores present in a diffraction limited area, the duty ratio needs to be decreased, either by prolonging the dark-state or by shortening the fluorescent-state, to allow single molecule imaging. Shorter times spent in the fluorescent state imply either lower photon yields, or the use of higher laser powers resulting in more irreversible photobleaching. Dark state control can be achieved by caging approaches resulting in very stable dark-states[27,28]. Interestingly though, a theoretically unlimited number of localizations can be obtained by using transiently binding probes, for instance by using the kinesin motor protein as a probe (Chapter 7), or with the more generic DNA-PAINT approach[29]. In the latter approach, a protein-binding probe is labeled with a short oligonucleotide strand, the docking-strand, with a length in the order of 20 bases. The complementary imaging-strand, conjugated to a dye, is added to the imaging medium and dynamically binds to the docking strand with on-off kinetics determined by the strand length and sequence. During a binding-event, the immobilized dye can be localized with high precision. Every docking-strand can sequentially bind a theoretically unlimited number of imaging-strands, resulting in many localizations. This allows an extremely stringent localization cut-off while retaining enough localizations for a high resolution image.

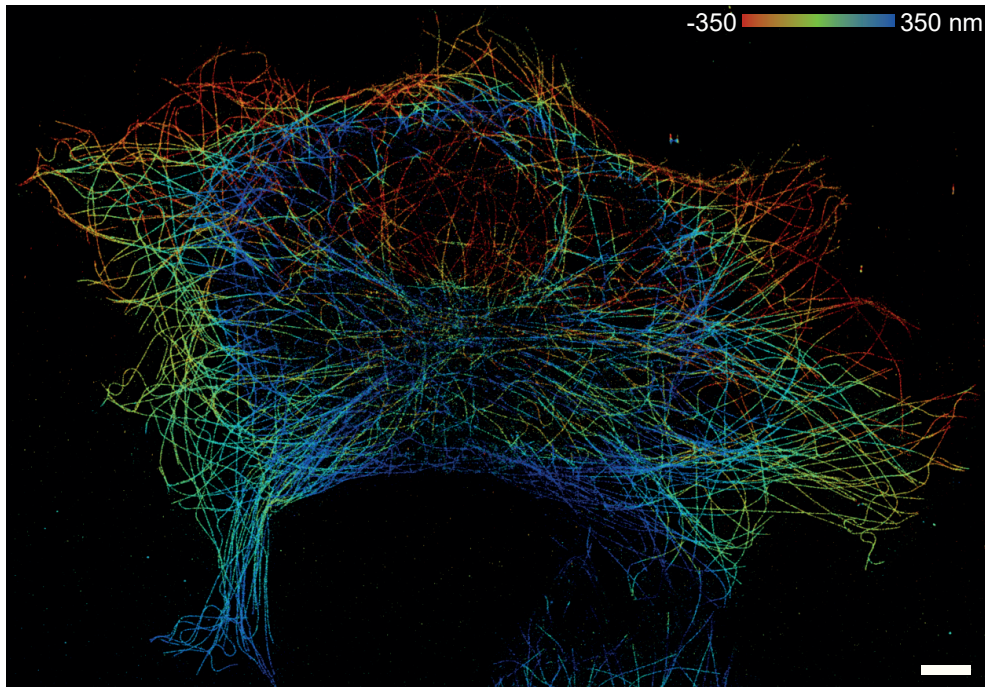


Figure 1: 3D-SMLM reconstruction of the MT network of a COS-7 cell

Large field-of-view 3D-SMLM of the MT network was performed using adaptive optics, to correct aberrations and induce astigmatism, and the DNA-PAINT approach. Color indicates z-position from -350 nm to 350 nm. Scalebar is 5 μm .

Microscopy setup

A disadvantage of transiently binding probes is the high background fluorescence of the large non-bound fraction, and illumination of only a slice of the sample, either by TIRF microscopy or by selective plane illumination microscopy (SPIM), is necessary to achieve SMLM. Only SPIM enables imaging of thicker samples, such as spheroids and (brain) tissue slices, further from the coverslip. The combination of SPIM and SMLM has been reported with a 1.8 μm thick Gaussian light sheet in spheroids using PAmCherry[30] and with a thinner ~ 1 μm lattice light sheet (LLS), better matched to the depth of field of a high numerical aperture (NA) objective and thus resulting in less out of focus background fluorescence, using Dendra2[31] or transiently binding probes[32]. The optical setups used in these experiments are not trivial to build, however, and the intricate imaging geometry restricts the use of objectives to NAs under 1.1 and necessitates special sample preparation. An attractive alternative is single objective SPIM (soSPIM)[33] where the same objective is used for generating a lightsheet and collecting fluorescence. soSPIM was shown to be compatible with SMLM using a 1.1 - 1.6 μm thick light sheet and a 1.2 NA water immersion objective[33,34]. The combination of soSPIM and DNA-PAINT could lead to high image quality in a relatively easy to manage optical setup.

Imaging deeper in samples

Aberrations induced by both the optical setup and the sample become more apparent when imaging deeper into the sample. High NA oil immersion objectives provide very high localization precisions for fluorophores close to the coverslip, but depth-dependent PSF distortion reduces the localization precision when focusing further away from the coverslip (Chapter 6). Moreover, the z-accuracy of 3D SMLM with a cylindrical lens and an oil immersion objective quickly deteriorates (Chapter 6). Adaptive optics in the form of a deformable mirror (DM) can correct aberrations induced by the setup[35] and by the sample[36]. Additionally, a DM can induce a tunable amount of astigmatism resulting in high precision 3D SMLM[35,36]. Since an increasing amount of astigmatism is necessary to retain optimal z-encoding when using an oil immersion objective to image deeper into samples (Chapter 6), a DM is better suited for astigmatism-based 3D SMLM in thick samples than a fixed cylindrical lens.

For imaging in thick samples often water immersion objectives are used. Although these objectives have a lower (maximum) NA than oil immersion objectives, the better match between the refractive index of the immersion medium and the sample greatly reduces depth dependent aberrations. The combination of lower NA and less depth-dependent aberrations results in lower localization precision at the coverslip but higher localization precision already at 5 μm into the sample (Chapter 6). Additionally, astigmatism-based z-encoding remains constant over a depth of at least 20 μm (Chapter 6). Depth-dependent aberrations are still an issue, however. Light refraction by the sample induces aberrations regardless of immersion medium, and spherical aberrations still result in a depth-dependent decrease of localization

precision of 20% between depths of 5 μm and 40 μm [33]. When imaging more than 5 μm into a sample, a combination of a water immersion objective and adaptive optics to correct sample-induced and spherical aberrations and to introduce astigmatism would provide the best means for 3D SMLM.

High throughput imaging

An advantage of SMLM with respect to EM is the relatively high imaging throughput, allowing collection of sufficient data to draw conclusions on cellular organization. For instance, as shown in Chapter 5, 90 neurons were imaged in a short timespan to provide the statistics needed for a well-underpinned conclusion about MT organization during neuronal development. Moreover, for years, knowledge about MT orientations in neurons was based on EM images of a few neurites, while using an SMLM approach we can base our conclusions about MT orientations on in total tens of dendritic segments of multiple neurons (Chapter 7). Automation of SMLM imaging can greatly further this advantage. In most imaging setups the microscope and translation stage are already controlled via a PC, and real-time control of laser powers based on the number of fluorophores localized per imaging frame is routinely implemented. Further optimization could be achieved with an automated perfusion system to refresh SMLM buffer components, including thiols, oxygen scavenging system components, and transiently binding probes. Still, using such an automated imaging system, either interesting positions have to be searched for and saved by hand before starting the automated imaging sequence, or a large area of the coverslip has to be imaged completely resulting in unnecessary long acquisition times and large amounts of data and images to sift through. This could be improved by seeding cells on coverslips with patterned adhesion sites. It has been shown that neurons can be grown on these patterns and, moreover, by adapting pattern shape and size the position of axon and dendrites can be predetermined[37,38]. Uniformly distributing these patterns over a coverslip would allow completely automated imaging of large numbers of neurons, and even of specific subcellular parts such as the axon initial segment, or perhaps interneuron connections using overlaying patterns.

MT ORGANIZATION

The technology described in this thesis was used to study neuronal MT organization. In Chapter 5 we showed using SMLM that CAMSAP2 localizes to MT minus-ends in neurons and that the neuronal MT organization drastically changes during development. This was not possible with conventional FM because of the high density of the MT network in neurons. In Chapter 7, SMLM was used to investigate MT orientations in neurons with high spatial resolution. In the following will be discussed how SMLM could further contribute to the investigation of the neuronal MT network.

Non-centrosomal MTs

The centrosome loses its role as central MTOC during neuronal development[39,40] and the majority of MTs is not connected to the centrosome at later developmental stages [41] (Chapter 5). The minus-ends of non-centrosomal MTs need to be stabilized to prevent fast depolymerization, and CAMSAP2 plays a major role in this (Chapter 5). CAMSAP is present on minus-ends of MTs in puncta in young neurons and in small stretches in older neurons due to slow minus-end growth (Chapter 5). This points towards a correlation between CAMSAP2 stretch length and the age of the MT minus-end. Testing for a correlation between CAMSAP2 stretch length and, for instance, levels of acetylation could shed more light on this. It would also be interesting to see whether there are non-centrosomal MT minus-ends in mature neurons that are not stabilized by CAMSAP2, for instance by combining the method for determination of MT orientation described in Chapter 7 with subsequent immunostaining and SMLM of CAMSAP2.

Although non-centrosomal MTs are an important part of dendritic morphology in mammalian hippocampal neurons, their origin remains unclear. It has been shown that in *Drosophila* class IV dendritic arborization neurons Golgi outposts in dendritic branches are capable of γ -tubulin dependent MT nucleation[42], consistent with earlier reports of MT nucleation from the Golgi in RPE cells[43]. It is still under debate, however, what the role of Golgi outposts is in regulating dendritic MT nucleation[44]. It would be interesting to further investigate the role of Golgi outposts in dendritic MT organization in mammalian hippocampal neurons, for instance using SMLM to see whether MT nucleation factors are present on them and whether they are directly associated with CAMSAP2 stretches.

Another ways of creating non-centrosomal MTs throughout dendrites are the severing of existing MTs and the transport of MTs from nucleation sites in the cell body or in the dendrites themselves by motor proteins. In case the age of the MT minus-end and CAMSAP stretch length are correlated, it might be possible to make a distinction between these mechanisms for individual MTs based on the length of the associated CAMSAP stretch. Fresh MT minus-ends created by MT severing are probably associated with smaller CAMSAP2 stretches than MTs transported into dendrites.

MT orientations, PTMs, and selective transport

Selective cargo transport is essential to establish and maintain the polarized neuronal morphology. Properties of MTs, such as their orientations in specific compartments and PTMs, are implicated to play a role in steering motor proteins towards their destination, although the exact mechanisms have remained unclear.

Effects of tubulin PTMs on cargo transport by motor proteins have been extensively studied, but black and white mechanisms seem elusive[45-52]. It is now thought that PTMs, in combination with tubulin isotypes, provide probabilistic signals that tune motor protein behavior rather than completely enable or block it, a hypothesis called the 'tubulin code'[51,53]. Interestingly, a recent study reported that the less studied tubulin PTM polyamination is the

cause of axonal MT stability[54], instead of being a consequence as seems to be the case for the also predominantly axonally localized PTMs acetylation and detyrosination[54,55]. Polyamination could therefore be an important cue for the specific axonal targeting of, for instance, KIF5. Treatment with the MT stabilizing agent Taxol results in targeting of KIF5 to both axon and dendrites[56], possibly exploiting the same mechanism as polyamination to attract KIF5 to MTs. However, polyamination adds positive charge to MTs[54] which is thought to interfere with kinesin-1 processivity[51]. It is not clear how KIF5's preference for (polyamination-stabilized) axonal MTs can be reconciled with the added positive charge by polyamination. A possible mechanism is that recruitment of other PTMs, such as polyglutamylation, adds negative charge resulting in net zero or negative charge. In line with the idea of the tubulin code, a combination of signals then results in the preferential motor recruitment to certain MTs. Multicolor SMLM of multiple PTMs on individual MTs could shed light on this.

Another factor influencing selective transport is MT orientation. It was shown that MTs in axons are oriented uniformly plus-end out, while in dendrites MT orientations are mixed[57,58]. More recent reports indicated that overall dendritic MT orientations are distributed equally in both directions along the whole length of dendrites[59] (Chapter 7). Surprisingly, also bundles of MTs with a preferred polarity are found in dendrites, spatially separated from bundles with opposite polarity (Chapter 7). As shown by our modeling (Chapter 7), a randomly mixed microtubule array in dendrites would result in an even distribution of cargo along the whole dendrite. In contrast, a more uniform MT array would result in biased, long range transport.

An interesting idea is that opposite polarity MT bundles might differ in stability and motor selectivity. KIF5, specifically targeting cargo to the axon, has a preference for stabilized MTs. If the bundles of minus-end out MTs are more stable, this could prevent KIF5 from entering dendrites explaining its inability to transport cargo into them. It could also clarify why KIF1 is not axon-selective since it preferentially moves over dynamic MTs, mediated by doublecortin-like kinase 1[60], and would therefore be able to enter dendrites.

Additionally, a bias in orientation of stabilized MTs implies that motor proteins are involved preferentially in antero- or retrograde dendritic transport. For instance, KIF5, moving preferentially over stable MTs, would be mostly involved in retrograde dendritic transport. A recent study showed a strong bias for dynein processivity over tyrosinated MTs versus detyrosinated MTs[61]. Assuming more stable MT are also more detyrosinated, dynein would preferentially move over plus-end out MTs, also contributing preferentially to retrograde dendritic transport. KIF1, on the other hand, would be more likely to be involved in anterograde transport.

The stability of MTs in orientationally biased bundles could be assessed using the motorPAINT approach, either using MT depolymerization protocols to depolymerize the less stable MTs before motorPAINT, or staining for MT acetylation or detyrosination after motorPAINT.

CONCLUDING REMARKS

Investigating (neuronal) MT organization is a multidisciplinary field. In Chapter 5, for instance, a multitude of techniques was used to show the important role of CAMSAP2 in structuring the MT array during neuronal development. Among these techniques super-resolution microscopy, including SMLM, is relatively new. Although not yet developed to its full potential, super-resolution microscopy already provided valuable insights into cellular functioning, and its development was awarded with the Nobel Prize in Chemistry in 2014. It is evident that super-resolution microscopy will continue to play an important role in the study of cellular functioning in general, and MT organization in particular, within the multidisciplinary cell biological landscape. Further improvements, technical innovations, and the widespread availability of super-resolution microscopes are expected to result in an even higher applicability and new insights in the coming years.

REFERENCES

- 1 Shroff, H., Galbraith, C. G., Galbraith, J. A. & Betzig, E. Live-cell photoactivated localization microscopy of nanoscale adhesion dynamics. *Nat Meth* 5, 417-423 (2008).
- 2 Biteen, J. S. et al. Super-resolution imaging in live *Caulobacter crescentus* cells using photoswitchable EYFP. *Nat Meth* 5, 947-949 (2008).
- 3 Shim, S.-H. et al. Super-resolution fluorescence imaging of organelles in live cells with photoswitchable membrane probes. *Proceedings of the National Academy of Sciences of the United States of America* 109, 13978-13983 (2012).
- 4 Jones, S. A., Shim, S. H., He, J. & Zhuang, X. Fast, three-dimensional super-resolution imaging of live cells. *Nature methods* 8, 499-508 (2011).
- 5 Li, D. et al. Extended-resolution structured illumination imaging of endocytic and cytoskeletal dynamics. *Science (New York, N.Y.)* 349, aab3500-aab3500 (2015).
- 6 Watanabe, S. et al. Protein localization in electron micrographs using fluorescence nanoscopy. *Nature methods* 8, 80-84 (2011).
- 7 Kopek, B. G., Shtengel, G., Xu, C. S., Clayton, D. A. & Hess, H. F. Correlative 3D superresolution fluorescence and electron microscopy reveal the relationship of mitochondrial nucleoids to membranes. *Proceedings of the National Academy of Sciences of the United States of America* 109, 6136-6141 (2012).
- 8 Suleiman, H. et al. Nanoscale protein architecture of the kidney glomerular basement membrane. *eLife* 2, e01149 (2013).
- 9 Löschberger, A., Franke, C., Krohne, G., van de Linde, S. & Sauer, M. Correlative super-resolution fluorescence and electron microscopy of the nuclear pore complex with molecular resolution. *Journal of Cell Science* 127, 4351-4355 (2014).
- 10 Johnson, E. et al. Correlative in-resin super-resolution and electron microscopy using standard fluorescent proteins. *Scientific reports* 5, 9583 (2015).
- 11 Zhou, X. X. & Lin, M. Z. Photoswitchable Fluorescent Proteins: Ten Years of Colorful Chemistry and Exciting Applications. *Current opinion in chemical biology* 17, 682-690 (2013).
- 12 Shcherbakova, D. M., Sengupta, P., Lippincott-Schwartz, J. & Verkhusha, V. V. Photocontrollable fluorescent proteins for superresolution imaging. *Annual review of biophysics* 43, 303-329 (2014).
- 13 Winterflood, C. M. & Ewers, H. Single-Molecule Localization Microscopy using mCherry. *Chemphyschem : a European journal of chemical physics and physical chemistry* 15, 3447-3451 (2014).
- 14 Subach, F. V. et al. Photoactivatable mCherry for high-resolution two-color fluorescence microscopy. *Nat Meth* 6, 153-159 (2009).
- 15 Shaner, N. C. et al. Improved monomeric red, orange and yellow fluorescent proteins derived from *Discosoma* sp. red fluorescent protein. *Nat Biotech* 22, 1567-1572 (2004).

- 16 Chen, J., Kanai, Y., Cowan, N. J. & Hirokawa, N. Projection domains of MAP2 and tau determine spacings between microtubules in dendrites and axons. *Nature* 360, 674-677 (1992).
- 17 Keppler, A. et al. A general method for the covalent labeling of fusion proteins with small molecules in vivo. *Nat Biotech* 21, 86-89 (2003).
- 18 Gautier, A. et al. An Engineered Protein Tag for Multiprotein Labeling in Living Cells. *Chemistry & biology* 15, 128-136 (2008).
- 19 Los, G. V. et al. HaloTag: A Novel Protein Labeling Technology for Cell Imaging and Protein Analysis. *ACS Chemical Biology* 3, 373-382 (2008).
- 20 Hermann, T. & Patel, D. J. Adaptive Recognition by Nucleic Acid Aptamers. *Science* 287, 820-825 (2000).
- 21 Zhang, J. et al. SELEX Aptamer Used as a Probe to Detect Circulating Tumor Cells in Peripheral Blood of Pancreatic Cancer Patients. *PLoS ONE* 10, e0121920 (2015).
- 22 Zeng, Z. et al. Using oligonucleotide aptamer probes for immunostaining of formalin-fixed and paraffin-embedded tissues. *Modern pathology : an official journal of the United States and Canadian Academy of Pathology, Inc* 23, 1553-1558 (2010).
- 23 Sun, H. et al. Oligonucleotide Aptamers: New Tools for Targeted Cancer Therapy. *Mol Ther Nucleic Acids* 3, e182 (2014).
- 24 Opazo, F. et al. Aptamers as potential tools for super-resolution microscopy. *Nat Meth* 9, 938-939 (2012).
- 25 Lee, S. F., Vérolet, Q. & Fürstenberg, A. Improved Super-Resolution Microscopy with Oxazine Fluorophores in Heavy Water. *Angewandte Chemie International Edition* 52, 8948-8951 (2013).
- 26 Olivier, N., Keller, D., Gönczy, P. & Manley, S. Resolution Doubling in 3D-STORM Imaging through Improved Buffers. *PLoS ONE* 8, e69004 (2013).
- 27 Vaughan, J. C., Jia, S. & Zhuang, X. Ultrabright photoactivatable fluorophores created by reductive caging. *Nat Meth* advance online publication (2012).
- 28 Vaughan, J. C., Dempsey, G. T., Sun, E. & Zhuang, X. Phosphine quenching of cyanine dyes as a versatile tool for fluorescence microscopy. *J Am Chem Soc* 135, 1197-1200 (2013).
- 29 Jungmann, R. et al. Multiplexed 3D cellular super-resolution imaging with DNA-PAINT and Exchange-PAINT. *Nat Meth* 11, 313-318 (2014).
- 30 Cella Zanacchi, F. et al. Live-cell 3D super-resolution imaging in thick biological samples. *Nature methods* 8, 1047-1049 (2011).
- 31 Chen, B.-C. et al. Lattice Light Sheet Microscopy: Imaging Molecules to Embryos at High Spatiotemporal Resolution. *Science (New York, N.Y.)* 346, 1257998-1257998 (2014).
- 32 Legant, W. R. et al. High-density three-dimensional localization microscopy across large volumes. *Nat Meth* 13, 359-365 (2016).

- 33 Galland, R. et al. 3D high- and super-resolution imaging using single-objective SPIM. *Nat Meth* 12, 641-644 (2015).
- 34 Meddens, M. B. M. et al. Single objective light-sheet microscopy for high-speed whole-cell 3D super-resolution. *Biomedical optics express* 7, 2219-2236 (2016).
- 35 Izeddin, I. et al. PSF shaping using adaptive optics for three-dimensional single-molecule super-resolution imaging and tracking. *Optics express* 20, 4957-4967 (2012).
- 36 Burke, D., Patton, B., Huang, F., Bewersdorf, J. & Booth, M. J. Adaptive optics correction of specimen-induced aberrations in single-molecule switching microscopy. *Optica* 2, 177-185 (2015).
- 37 Roth, S. et al. How Morphological Constraints Affect Axonal Polarity in Mouse Neurons. *PLoS ONE* 7, e33623 (2012).
- 38 Tomba, C., Braini, C., Wu, B., Gov, N. S. & Villard, C. Tuning the adhesive geometry of neurons: length and polarity control. *Soft matter* 10, 2381-2387 (2014).
- 39 Stiess, M. et al. Axon Extension Occurs Independently of Centrosomal Microtubule Nucleation. *Science* 327, 704-707 (2010).
- 40 Nguyen, M. M., Stone, M. C. & Rolls, M. M. Microtubules are organized independently of the centrosome in *Drosophila* neurons. *Neural Development* 6, 38-38 (2011).
- 41 Baas, P. W. & Lin, S. Hooks and Comets: The Story of Microtubule Polarity Orientation in the Neuron. *Developmental Neurobiology* 71, 403-418 (2011).
- 42 Ori-McKenney, K. M., Jan, L. Y. & Jan, Y.-N. Golgi outposts shape dendrite morphology by functioning as sites of acentrosomal microtubule nucleation in neurons. *Neuron* 76, 921-930 (2012).
- 43 Efimov, A. et al. Asymmetric CLASP-dependent nucleation of non-centrosomal microtubules at the trans-Golgi network. *Developmental Cell* 12, 917-930 (2007).
- 44 Nguyen, M. M. et al. γ -Tubulin controls neuronal microtubule polarity independently of Golgi outposts. *Molecular biology of the cell* 25, 2039-2050 (2014).
- 45 Larcher, J.-C., Boucher, D., Lazereg, S., Gros, F. & Denoulet, P. Interaction of Kinesin Motor Domains with α - and β -Tubulin Subunits at a Tau-independent Binding Site: regulation by polyglutamylation. *Journal of Biological Chemistry* 271, 22117-22124 (1996).
- 46 Konishi, Y. & Setou, M. Tubulin tyrosination navigates the kinesin-1 motor domain to axons. *Nat Neurosci* 12, 559-567 (2009).
- 47 Reed, N. A. et al. Microtubule Acetylation Promotes Kinesin-1 Binding and Transport. *Current Biology* 16, 2166-2172 (2006).
- 48 Ikegami, K. et al. Loss of α -tubulin polyglutamylation in ROSA22 mice is associated with abnormal targeting of KIF1A and modulated synaptic function. *Proceedings of the National Academy of Sciences of the United States of America* 104, 3213-3218 (2007).
- 49 Dunn, S. et al. Differential trafficking of Kif5c on tyrosinated and detyrosinated microtubules in live cells. *Journal of Cell Science* 121, 1085-1095 (2008).

- 50 Hammond, J. W. et al. Posttranslational Modifications of Tubulin and the Polarized Transport of Kinesin-1 in Neurons. *Molecular biology of the cell* 21, 572-583 (2010).
- 51 Sirajuddin, M., Rice, L. M. & Vale, R. D. Regulation of microtubule motors by tubulin isoforms and posttranslational modifications. *Nature cell biology* 16, 335-344 (2014).
- 52 Kapitein, Lukas C. & Hoogenraad, Casper C. Building the Neuronal Microtubule Cytoskeleton. *Neuron* 87, 492-506 (2015).
- 53 Janke, C. The tubulin code: Molecular components, readout mechanisms, and functions. *The Journal of cell biology* 206, 461-472 (2014).
- 54 Song, Y. et al. Transglutaminase and Polyamination of Tubulin: Posttranslational Modification for Stabilizing Axonal Microtubules. *Neuron* 78, 109-123 (2013).
- 55 Schulze, E., Asai, D. J., Bulinski, J. C. & Kirschner, M. Posttranslational modification and microtubule stability. *The Journal of cell biology* 105, 2167-2177 (1987).
- 56 Kapitein, L. C. et al. Mixed Microtubules Steer Dynein-Driven Cargo Transport into Dendrites. *Current Biology* 20, 290-299 (2010).
- 57 Baas, P. W., Black, M. M. & Banker, G. A. Changes in microtubule polarity orientation during the development of hippocampal neurons in culture. *The Journal of cell biology* 109, 3085-3094 (1989).
- 58 Dombeck, D. A. et al. Uniform polarity microtubule assemblies imaged in native brain tissue by second-harmonic generation microscopy. *Proceedings of the National Academy of Sciences of the United States of America* 100, 7081-7086 (2003).
- 59 Yau, K. W. et al. Dendrites In Vitro and In Vivo Contain Microtubules of Opposite Polarity and Axon Formation Correlates with Uniform Plus-End-Out Microtubule Orientation. *The Journal of Neuroscience* 36, 1071-1085 (2016).
- 60 Lipka, J., Kapitein, L. C., Jaworski, J. & Hoogenraad, C. C. Microtubule-binding protein doublecortin-like kinase 1 (DCLK1) guides kinesin-3-mediated cargo transport to dendrites. *The EMBO Journal* 35, 302-318 (2016).
- 61 McKenney, R. J., Huynh, W., Vale, R. D. & Sirajuddin, M. Tyrosination of α -tubulin controls the initiation of processive dynein-dynactin motility. *The EMBO Journal* (2016).



Addendum

A stylized neuron with a map of a city overlaid on its cell body, set against a background of a blue sky with a grid pattern.

Lay summary

Lekensamenvatting

Curriculum vitae

List of publications

Dankwoord

LAY SUMMARY

Just like any plant or animal you are composed of cells, trillions of them. Approximately 90 billion of your cells are brain cells, also called neurons. To be able to think, act, and experience memories, your neurons have to work in perfect harmony, relaying signals from neuron to neuron all over the brain. To fulfill this function neurons have a highly specialized shape. They consist of a cell body from which protrusions grow that can reach lengths of more than a meter. All throughout these long protrusions building blocks are needed for proper functioning of the neuron. The building blocks are often generated in the cell body and then transported by motor proteins towards their destination in the cell. Motor proteins transport their cargo over long distances by moving over microtubules, the roads of the cell. This microtubule-based transport has emerged as a process involved in several neurological and neurodevelopmental disorders. A better understanding of active microtubule-based transport can therefore further our understanding of these diseases and speed up the development of cures or treatments.

The protrusions of neurons are classified either as dendrites, that receive signals from other neurons, or as axons that send out signals. Axons and dendrites need different building blocks to function properly, and therefore the transport of building blocks has to be somehow regulated. It is thought that properties of the microtubules, such as their orientation and their modifications, play an important part in this. To get a better understanding of the role of microtubule properties in the regulation of active transport, the distribution of these properties over the microtubule network has to be mapped. Since the neuronal microtubule network is very dense and crowded, recently developed *super-resolution microscopy* methods with a spatial resolution in the order of nanometers (one nanometer is one millionth of a millimeter), are well suited to study it.

The work described in this thesis focuses on the super-resolution method with the highest spatial resolution, *Single Molecule Localization Microscopy* (SMLM), and its use to investigate the neuronal microtubule network. SMLM is a *fluorescence* microscopy method which per definition involves making images of fluorescent, light-emitting molecules, also called fluorophores. These fluorophores are attached to the structure under investigation that by itself is not (clearly) visible. In the case of microtubules, you could compare this to mapping the roads in a city at night based on the light coming from lampposts 'attached' to the roads. Usually all fluorophores are imaged simultaneously. For SMLM, however, hundreds of thousands of light-emitting molecules are imaged one-by-one and the precise location of each one is determined. These locations are then used to reconstruct a *super-resolved* image of the structure they are attached to. So, instead of using all the light coming from the lampposts to map the roads, only the precise locations of the lampposts are used and this results in a greatly improved resolution.

We demonstrated that SMLM is well suited to study the neuronal microtubule network, for instance by showing that the microtubule associated protein CAMSAP2 is found specifically on one of the ends of microtubules, playing an important role in protecting these ends from breaking down. Additionally we showed that during neuronal development the microtubule

network changes from a radial array originating from a central microtubule organizing center to a non-radial array, implying that the organizing center loses its function. These observations were not possible with normal fluorescence microscopy.

To further increase the capabilities of SMLM to study the neuronal microtubule network, we developed new and improved *fluorescent labels*. A fluorescent label consists of a fluorophore (the lamp) and a way of attaching it to the structure of interest (the post). Properties of both the lamp and the post influence the performance of SMLM.

The fluorophores have to exhibit a (semi-)controllable on-off behavior, often called blinking, to image them one-by-one. We found that an often used fluorophore, the red fluorescent protein mCherry, can be turned off by a reaction with the chemical β -mercaptoethanol (β ME). Importantly, the mCherry-molecules can then be sequentially turned on again by illumination with violet light, allowing them to be imaged one-by-one. Because mCherry is often used as a fluorescent label, this discovery opens up a whole range of existing cell lines and cells from model organisms for direct investigation with SMLM.

The size of a label (analogous to the length of the lamppost) also influences the quality of SMLM images. The closer fluorophores are to the structure of interest, the clearer the image of this structure will be. Often a cascade of two *antibodies* is used to attach fluorophores to, for instance, microtubules, resulting in a spacing between fluorophore and microtubule in the order of 20 – 30 nanometer. We developed smaller labels, microtubule specific *nanobodies*, with a size of only 5 nanometer. Using these nanobodies for SMLM, we were able to resolve microtubules that were only approximately 50 nanometer apart. This allowed individual microtubules to be resolved in the dense microtubule network in dendrites that could not be resolved with conventional antibodies, giving a clearer view of the organization of these microtubules.

Another fluorescent label we developed consists of a shortened motor protein fused to a fluorophore. These motor proteins can then be precisely localized while they move over the microtubules, providing direct information about the orientation of the microtubules. Microtubule orientation is a property that directly influences active transport, but is not well investigated in neurons because of a lack of tools. We named the technique *motor-PAINT*, and used it to confirm previous reports that in dendrites the same amount of microtubules are oriented towards and away from the cell body. Surprisingly, however, we also found bundles of microtubules mostly oriented in the same direction that for instance could act as cellular highways. The next step is to find out how exactly the active transport is influenced by the presence of these bundles.

Next to developing and using new and improved labels, we also investigated the performance of SMLM in more demanding situations. Imaging of cells is often done close to the objective lens of the microscope. However, there is a trend in cell biology towards the investigation of cells deeper in samples (and thus further from the objective lens), for instance in multicellular structures. Imaging in these structures can be problematic due to optical distortions. However, these distortions can be reduced by installing a *deformable mirror*,

a reflective membrane of which the shape of the surface can be controlled. Interestingly, a deformable mirror can be used simultaneously to extend SMLM from two dimensions (x and y) to three dimensions (x , y and z). We compared the performance of a microscope with and without a deformable mirror, and found that using a deformable mirror results in enhanced SMLM images in two as well as in three dimensions when imaging deeper into samples. On the other hand, we also found that using a different objective lens resulted in the same image quality without the use of a deformable mirror. The samples we used were quite homogenous, however, and imaging in even more demanding samples could still benefit from the use of a deformable mirror to reduce sample-induced distortions.

In conclusion, the work in this thesis describes the development of novel SMLM methods and labels, as well as their use to investigate the neuronal microtubule network. This resulted in new and interesting findings that improve our understanding of the microtubule network in neurons possible speeding up the development of treatments for neurological and neurodevelopmental disorders.

LEKENSAMENVATTING

Net zoals elke plant en elk dier ben jij opgebouwd uit cellen, biljoenen ervan. Ongeveer 90 miljard van je cellen zijn hersencellen, ook wel neuronen genoemd. Om te kunnen denken, doen en herinneringen te hebben, moeten al je neuronen samenwerken bij het verspreiden van signalen van neuron tot neuron door je hele brein. Om dit te kunnen doen hebben neuronen een zeer speciale vorm. Ze bestaan uit een cellichaam waaruit verschillende lange uitlopers groeien die meer dan een meter lang kunnen worden. Over de hele lengte van deze uitlopers zijn bouwstenen nodig om het neuron goed te laten functioneren. Bouwstenen worden vaak aangemaakt in het cellichaam en daarna door motoreiwitten naar hun bestemming gebracht. Motoreiwitten transporteren hun lading over microtubuli, de wegen van de cel. Het is gebleken dat dit actieve transport over microtubuli betrokken is bij verschillende neurologische aandoeningen. Een beter begrip van de werking van dit transport kan daarom bijdragen aan een beter inzicht in deze aandoeningen en kan het vinden van behandelmethodes versnellen.

De uitlopers van neuronen worden onderverdeeld in dendrieten, voor het ontvangen van signalen van andere neuronen, en axonen die de signalen uitzenden. Dendrieten en axonen hebben verschillende bouwstenen nodig, dus het transport van deze bouwstenen moet gereguleerd worden. Er zijn indicaties dat eigenschappen van de microtubuli waarover de bouwstenen vervoerd worden een belangrijke rol in spelen in deze regulatie. Om meer inzicht te krijgen in hoe de eigenschappen van de microtubuli het actieve transport beïnvloeden, moet eerst in kaart gebracht worden waar welke eigenschappen zich bevinden in het microtubuli netwerk. Omdat het microtubuli netwerk in neuronen erg druk en vol is, zijn de recent ontwikkelde *super-resolutiemicroscopie* methoden, met een resolutie in de ordegrootte van nanometers (een nanometer is een miljoenste van een millimeter) zeer geschikt om het te bestuderen.

De focus van dit proefschrift ligt op de super-resolutiemicroscopie techniek met de hoogste resolutie, genaamd *Single Molecule Localization Microscopy* (SMLM) en het gebruik daarvan om het netwerk van microtubuli in neuronen te bestuderen. SMLM is een *fluorescentie* microscopie techniek wat inhoudt dat (bijna) onzichtbare structuren beter zichtbaar gemaakt worden door er lichtgevende moleculen, genaamd fluoroforen, aan te koppelen. In het geval van microtubuli zou je dit kunnen vergelijken met het 's nachts in kaart brengen van de wegen in een stad door te kijken naar de lantaarnpalen die 'gekoppeld' zijn aan de wegen. Bij normale fluorescentie microscopie worden alle fluoroforen tegelijkertijd afgebeeld. Echter, bij SMLM worden er honderdduizenden lichtgevende moleculen een-voor-een bekeken en wordt de precieze locatie van elk molecuul bepaald. Deze locaties worden dan gebruikt om een plaatje van de onderliggende structuur te reconstrueren met een zeer hoge resolutie. Dus in plaats van te kijken naar het licht van de lantaarnpalen langs een weg, gebruik je alleen de precieze locaties van de lantaarnpalen om de wegen in kaart te brengen en dit verhoogt de resolutie met ongeveer een factor tien.

We hebben gedemonstreerd dat SMLM zeer geschikt is om het microtubuli netwerk in neuronen te bestuderen, bijvoorbeeld door te laten zien dat het eiwit CAMSAP2 alleen te vinden is op één van de uiteinden van microtubuli waar het een belangrijke rol speelt in

de bescherming van dit einde tegen afbraak. Ook hebben we laten zien dat tijdens de ontwikkeling van een neuron de organisatie van het microtubuli netwerk overgaat van een radiële organisatie vanuit een centraal punt naar een niet-radiële organisatie. Dit impliceert dat de organisator van het radiële netwerk zijn functie verliest. Deze bevindingen waren niet mogelijk met normale fluorescentie microscopie.

Om de mogelijkheden van SMLM voor het onderzoeken van het neuronale microtubuli netwerk verder uit te breiden, ontwikkelden we nieuwe en verbeterde *fluorescente labels*. Een fluorescent label bestaat uit een fluorofoor (de lantaarn) en een deel dat bindt aan de te onderzoeken structuur (de paal). De eigenschappen van zowel de lantaarn als de paal hebben invloed op de kwaliteit van een SMLM plaatje.

De fluoroforen moet (semi-)controleerbaar aan en uit te zetten zijn om ze een-voor-een te kunnen bekijken. Wij ontdekten dat een veelgebruikte fluorofoor, het rood-lichtgevende eiwit mCherry, uitgezet kan worden door een reactie met de chemische stof β -mercaptoethanol (β ME). En even belangrijk, de mCherry moleculen kunnen ook weer om de beurt aangezet worden door ze te beschijnen met violet licht. Zo kunnen ze een-voor-een afgebeeld en gelokaliseerd worden en dit maakt dus SMLM mogelijk. mCherry is een veelgebruikte fluorofoor en daardoor maakt deze ontdekking een groot aantal bestaande cellijnen en cellen van modelorganismen direct geschikt om onderzocht te worden met SMLM.

De grootte van een label (vergelijkbaar met de lengte van de lantaarnpaal) heeft ook invloed op de kwaliteit van SMLM plaatjes. Hoe dichter de fluoroforen bij de te onderzoeken structuur zitten, hoe scherper het plaatje van deze structuur wordt. Vaak wordt een combinatie van twee antilichamen gebruikt om fluoroforen aan bijvoorbeeld microtubuli te koppelen. Dat resulteert in een afstand tussen de fluorofoor en de microtubulus van 20-30 nanometer. Wij ontwikkelden een label, een *nanobody* dat specifiek bindt aan microtubuli, met een grootte van slechts 5 nanometer. Toen we deze nanobodies gebruikten voor SMLM konden we microtubuli los van elkaar zien wanneer ze slechts 50 nanometer uit elkaar lagen. Dit zorgde ervoor dat we individuele microtubuli konden onderscheiden in het drukke microtubuli netwerk in de dendrieten van neuronen, die niet te onderscheiden waren wanneer we gewone antilichamen gebruikten. Hierdoor krijgen we een duidelijker beeld van de microtubuli organisatie in neuronen.

Een ander fluorescent label dat we ontwikkelden bestaat uit een ingekort motoreiwit gekoppeld aan een fluorofoor. Deze motoreiwitten kunnen daardoor zeer precies gelokaliseerd worden terwijl ze over microtubuli bewegen en verschaffen zo directe informatie over de richting waarin de microtubuli liggen. De richting waarin microtubuli liggen heeft directe invloed op het actieve transport, maar is niet goed onderzocht omdat er geen geschikte methoden waren. Met onze techniek, die we *motor-PAINT* noemden, konden we de eerdere bevinding bevestigen dat microtubuli in dendrieten globaal evenveel naar het cellichaam toe wijzen als er vanaf. Verrassend genoeg vonden we echter ook bundels van microtubuli met grotendeels dezelfde richting die bijvoorbeeld de snelwegen van de cel zouden kunnen vormen. De volgende stap is om te onderzoeken hoe het bestaan van deze bundels het actieve

transport precies beïnvloedt.

Behalve het ontwikkelen van nieuwe en verbeterde fluorescente labels voor SMLM, onderzochten we ook de prestaties van SMLM in meer veeleisende situaties. Meestal worden cellen bekeken die zich dichtbij het objectief van de microscoop bevinden. Er is echter een *trend* in cel biologie om cellen te bekijken die dieper in de preparaten liggen (en dus verder van het objectief), bijvoorbeeld cellen middenin veelcellige structuren. Dit is problematisch omdat het beeld vervormd wordt wanneer je dieper in een preparaat kijkt. Deze vervormingen kunnen verminderd worden door een *vervormbare spiegel*, een reflecterend membraan waarvan het oppervlak controleerbaar vervormd kan worden, in de microscoop te installeren. Interessant genoeg kan een vervormbare spiegel tegelijkertijd gebruikt worden om SMLM uit te breiden van twee dimensies (x en y) naar drie dimensies (x , y en z). Toen we een opstelling met en zonder vervormbare spiegel vergeleken, vonden we dat we met een opstelling met een vervormbare spiegel inderdaad betere SMLM plaatjes konden maken wanneer we dieper in een preparaat keken. Aan de andere kant vonden we ook dat wanneer we een ander objectief gebruikten dit resulteerde in dezelfde verbetering van de SMLM plaatjes. De preparaten die wij bekeken waren echter vrij homogeen; bij het maken van SMLM plaatjes in meer inhomogene preparaten zou het gebruik van een vervormbare spiegel nuttig kunnen zijn om door het preparaat geïntroduceerde vervormingen te corrigeren.

In conclusie, in dit proefschrift beschrijven we de ontwikkeling van vernieuwende SMLM methoden en labels en het gebruik ervan om het microtubuli netwerk in neuronen in kaart te brengen. Dit resulteerde in nieuwe en interessante bevindingen die de zoektocht naar behandelmethoden voor neurologische aandoeningen zouden kunnen versnellen.

CURRICULUM VITAE

Bas M.C. Cloin was born on December 21st in Eindhoven, The Netherlands. After receiving his high school diploma in 2001 (Gymnasium β , Trevianum Scholengroep, Sittard), he studied applied physics at the Eindhoven University of Technology. During his studies he spend a year as full time member of the board of the study association for applied physics and took place in various committees. As part of his master program, Bas performed a research internship in the group of prof.dr. Bernardo Neves at the Universidade General de Minas Gerais (Belo Horizonte, Brazil) and a graduation project in the group of prof.dr.ir. Menno Prins at the Eindhoven University of Technology. In 2008 he received his master diploma with a specialization in medical physics. In the same year, Bas started studying psychology at the Open University of the Netherlands and received his bachelor diploma *cum laude* in 2011. Bas then started his PhD in the group of prof.dr. Casper Hoogenraad and dr. Lukas Kapitein, the results of which are described in this thesis.

LIST OF PUBLICATIONS**Comparing depth-dependent astigmatism-based single-molecule localization using a deformable mirror and a cylindrical lens**

Bas M.C. Cloin, Wilco Nijenhuis, and Lukas C. Kapitein

Submitted

Motor-based nanoscopy reveals polarized microtubule bundles in neuronal dendrites

Roderick P. Tas, Bas M.C. Cloin, Marina Mikhaylova, Casper C. Hoogenraad, Lukas C. Kapitein

Submitted

Efficient mCherry-based localization microscopy using a novel caging mechanism

Bas M. C. Cloin, Elke De Zitter, Vincent Gielen, Gert E. Folkers, Marina Mikhaylova, Bartosz Krajnik, Casper C. Hoogenraad, Luc Van Meervelt, Peter Dedecker, Lukas C. Kapitein.

Submitted

Resolving bundled microtubules using anti-tubulin nanobodies.

Mikhaylova M, Cloin BM, Finan K, van den Berg R, Teeuw J, Kijanka MM, Sokolowski M, Katrukha EA, Maidorn M, Opazo F, Moutel S, Vantard M, Perez F, van Bergen en Henegouwen PM, Hoogenraad CC, Ewers H, Kapitein LC.

Nature Communications (2015); 6:7933

Single Molecule Localization Microscopy to Study Neuronal Microtubule Organization

Bas M. Cloin, Casper C. Hoogenraad, Marina Mikhaylova, Lukas C. Kapitein

Immunocytochemistry and Related Techniques (2015); 101 Neuromethods; 389-408

Microtubule minus-end binding protein CAMSAP2 controls axon specification and dendrite development.

Yau KW, van Beuningen SF, Cunha-Ferreira I, Cloin BM, van Battum EY, Will L, Schätzle P, Tas RP, van Krugten J, Katrukha EA, Jiang K, Wulf PS, Mikhaylova M, Harterink M, Pasterkamp RJ, Akhmanova A, Kapitein LC, Hoogenraad CC.

Neuron (2014); 82(5); 1058-1073

Always on a Friday: referral pattern for metastatic spinal cord compression.

Koiter E, Poortmans P, Cloin B.

Radiotherapy and Oncology (2013); 107(2); 259-260

DANKWOORD

Een proefschrift maak je niet alleen. Veel mensen hebben eraan bijgedragen dat mijn promotie-periode zo leuk geweest is als het was, en dit proefschrift geworden is wat het nu is. Ik wil graag iedereen bedanken die op wat voor manier dan ook een bijdrage heeft geleverd aan de fantastische ervaring die promoveren voor mij geweest is.

Allereerst wil ik mijn promotor Casper Hoogenraad en co-promotor Lukas Kapitein bedanken. Ondanks dat ik in pak aankwam bij de eerste sollicitatie heb ik van jullie de kans gekregen om in een geweldige groep mijn promotieonderzoek uit te voeren.

Beste Casper, ik vind het uitzonderlijk dat jij ondanks alle drukte zo toegankelijk bent. Terwijl iedereen weet hoe vol je leven zit, wakte je de indruk alle tijd van de wereld te hebben voor een praatje, zowel over mijn promotie als over minder belangrijke zaken. Je hebt meteen door hoe de vork in de steel zit en ook waar mijn onderzoek niet direct in jouw straatje lag wist je waardevolle tips te geven. The best of luck with your latest endeavour en hartelijk dank voor de fijne begeleiding!

Beste Lukas, een van de dingen die me het meest bij zal blijven is jouw grenzeloze en aanstekelijke enthousiasme. Wanneer je weer vertelde over een nieuw project of een nieuw idee leek het elke keer of het het beste project of idee ooit was. Ik heb veel van je geleerd op het gebied van het kort, krachtig en precies verwoorden van resultaten en aandacht te hebben voor de kleinste details. Bovendien neem ik mee dat er zo goed als altijd een passende verklaring is voor alle (merkwaardigheden in) experimenten en data. Jij gaat er zomaar niet vanuit dat iets toeval is of dat er 'gewoon iets niet klopt'. Ik vond het leuk om mee te maken hoe jouw lab is gegroeid van een paar man naar een volwassen onderzoeksgroep. Hartelijk dank voor de goede, soms intensieve begeleiding en veel succes in de toekomst.

Ik wil ook de andere leden van mijn promotiecommissie, Erwin Peterman, Sjoerd Stallinga, Judith Klumperman, Allard Mosk en Hans Gerritsen, hartelijk bedanken voor het lezen en beoordelen van mijn proefschrift. Beste Anna, voor mijn gevoel is dit ook de plaats om jou te bedanken. Altijd scherp, kritisch en doelgericht met een flinke dosis humor. Je vragen en suggesties tijdens meetings en daarbuiten hebben veel bijgedragen aan de vorming van mijn proefschrift. Bedankt voor alles.

Eugene and Max, thank you for being my paranymphs! Eugene, I think you are a skilled, relaxed, and very friendly guy. Your work greatly contributed to get super-resolution in Lukas lab to the high level it is today, and I liked working and collaborating with you on that. I thoroughly enjoyed the outings and dance parties we went to together. Keep up the good work and see you soon for a drink! Max, wetenschapper en party-animal eersteklas, zowel binnen als buiten het lab hebben we veel lol gehad. Van PhD retreats tot chupitos, van vroege zwempartijen tot paragliding, jij bent van de partij. En je maakt er altijd een feestje van. Bedankt voor de mooie tijd en tot binnenkort!

Samen met Eugene en Max was ik deel van het Kapitein-lab. De goede sfeer in het Kapitein-lab was een belangrijk ingrediënt van het plezier in mijn promotie, en ik ben alle leden daarvoor veel dank verschuldigd. With you, Marina, I think I had most interaction.

You are the best example of work hard play hard that I know, and it was a delight to work and play with you. Your knowledge and experimental skills are amazing, as was the fun we often had behind the microscope. Always cheerful, smiling and helpful, you are an example for me. I cannot thank you enough. See you soon. Petra, met jou heb ik de eerste stappen gezet in het celbiologisch werk. Met veel geduld probeerde jij een natuurkundige uit te leggen hoe je met cellen om moet gaan. Ik vond het erg fijn en gezellig om met je te werken en wens je al het beste in de toekomst. Anaël, you certainly made a lasting impression. I liked your kindness and humor in the office a lot. What I will remember most though are your crazy cool dancing moves, and your scarily lifelike Samantha performance. Thanks and all the best! Roderick, ik heb je meegemaakt als master student en als collega PhD, en in beide gevallen ging jij als een speer. Het is mooi om te zien hoe snel je dingen oppikt en hoe je opgaat in het onderzoek. Bedankt voor de samenwerking en voor de leuke gesprekken. Jaap, ook jij bedankt voor je grote inzet tijdens je master stage. Anne, bedankt voor de samenwerking en voor de gezelligheid. Ik wens je veel succes met je promotie. Wilco, jij bracht een hoop kennis mee waar heel het lab van profiteerde. Je heldere uitleg en to-the-point vragen blijven me bij. Bedankt en veel succes in het vervolg van je carrière. Desirée, as my successor I wish you all the best with bringing the super-resolution imaging to new heights. Chiung-Yi, I also wish you a very fruitful future in the lab.

Mijn nog niet genoemde *roomies* hebben ook veel bijgedragen aan de beleving van mijn promotie. Vanaf het begin heb ik tegenover jou gezeten Marleen. We hebben heel wat serieuze, soms filosofische zaken besproken, waarin je lekker fel en vaak humoristisch uit de hoek kon komen. Ook hebben we flink wat lief en leed gedeeld in de afgelopen 4 jaar. Bedankt voor de leuke tijd! Ik hoop snel een uitnodiging voor jouw promotie te ontvangen. Catia, a.k.a. best roomie ever, I love your energy and your enthusiasm. You often filled the office with your laughter, jokes and delicious Portuguese food. I also learned some Portuguese words from you that I cannot repeat here. I wish you lots of luck with finishing your PhD and all the best for your future!

I would like to thank all other (past) members of the department of Cell Biology that I had the pleasure to meet and work with during my PhD. Esther, Corette, Paul en Jan Andries, zeer bedankt voor jullie vragen tijdens meetings en waardevolle input. Esther, jouw veerkracht is bewonderenswaardig. Ik kwam altijd graag een praatje met je maken. Ik wens je alle geluk in het werk en daarbuiten. Paul, jouw lach schalt vaak door de gangen van het Kruytgebouw. Bedankt voor de discussies over koetjes, kalfjes, muziekapparatuur en politiek. Corette, bedankt voor de gezellige woon-werk fietsritjes. Jan Andries, bedankt voor het meedenken met het mCherry-verhaal.

Amol, handen bij je oren! You are an amazing guy. I admire your working attitude and enjoyed your cheerfulness in the lab. Also during outings and paragliding trips you are a joy to be with. The best of luck with finishing your PhD and see you soon. Sam, gezellige vent, altijd zin in een feestje, vol goede adviezen, ontzettend behulpzaam, kortom je bent een echte topgozer. We zien elkaar snel weer voor een pilsje of zo'n lekker kopje koffie.

Benjamin, I liked it a lot that your emails about the almost daily occurring anonymous spillings, broken things, and lost stuff often had a humoristic touch. And there was the soup of course, and some even weirder jokes. The best of luck in the future. Josta, master van planning en organisatie, zowel jouw scherpe humoristische opmerkingen als je dansmoves waren altijd goed voor vermaak. Tot het volgende feestje! Joanna, thank you very much for the good times in and outside the lab, and for one of the best weddings ever! Good luck with the squash and I hope to see you soon. Phebe, ik heb even aan je moeten wennen, en jij waarschijnlijk aan mij, maar ik heb je leren kennen als iemand die erg begaan is met het lab en een grote rol speelt in de dagelijkse gang van zaken. Bedankt voor de gezellige tijd in het lab en tijdens uitjes en borrels, en voor alle bloed, zweet en tranen die jij in het lab steekt. Jingchao, you are a genuinely very nice and helpful person and I enjoyed our many conversations in the lab. I wish you the best of luck! Ilya, you seemed quite harsh at first but turned out to be a very gentle guy. I enjoyed the sometimes weird, often a bit awkward, but always funny interactions with you. Keep up the amazing work running the imaging facility. Kah Wai, volgens mij ben jij de enige die, als er in een protocol staat vijf minuten wachten, ook echt vijf minuten wacht. Ook jij bedankt voor de gezelligheid. Marijn, ik vond het erg leuk om je paranimf te zijn. Veel succes met je avonturen in Berlijn! Robert, ik vond het plezierig om met je samen te werken. Heel veel succes met de laatste loodjes van je promotie. Mariëlla, goedhartig en gezellig, ik wens je al het beste. Marta and Andrea, I enjoyed watching football matches and dancing at Queens/Kings day with you. Ricardo, thanks for the time we spent together at parties, and all the conversations about which parties to go to next. Hai Yin, ik vind je een leuke gast met een ijzersterk doorzettingsvermogen. Ga zo door. Ines, best of luck investigating the thingies. Ivar, mede-organisator van een zeer geslaagd labuitje, bedankt voor de gezellige tijd in het lab en veel succes met het afronden van je PhD. Helma, ook met jou heb ik heel wat besproken tijdens de afgelopen 4 jaar. Veel succes met het afronden van je thesis en het vinden van een leuke baan! Maud, thanks for playing squash with me. Ruddi, thanks for the tips for my Cuba trip. Diedonné, altijd leuk om een praatje met je te maken bij de koffieautomaat of op kantoor. Qingyang, I hope you still use your acquired R skills. Dusan, keep it cool man. Kai and Shasha, I cannot believe how hard you work in the lab. Thank you for the advice and the laughs. Bart, van jou kun je altijd de droogste opmerkingen van het lab verwachten. Martin, vol kennis en altijd te vinden op feestjes. Harold, bedankt voor je input tijdens de uitverkoren Lukas-lab meetings waar je aanwezig was. Peter Jan, succes met de belangrijke taak van ICT-wizard van de afdeling. Feline, bedankt voor de tips voor mijn Amerika-reis. Gabi, I really like your cheerfulness. Yujie, thanks for the information about cheeses. Also all other (past) members of Cell Biology, Laura, Philipp, Karin, Amélie, Elena, Lena, Dennis, Michael, René, Bram, Margriet, Hari, Renu, Raimond, Alex, , Cilia, Carol, Marta, Olga, Eliana, Sybren, Ankit, Chao, York, Xingxiu, Ruben, Katerina, Sabrina, Rachid, Sofia, Smiriti, Jarno, Purvi, thank you all for the enjoyable and friendly atmosphere! I wish you all the best!

Frits and Fons, geniet van jullie welverdiende pensioen! Laurens, succes met het voortzetten van het onderwijs.

I would also like to thank all members of the department of Developmental Biology. Thanks for your contribution to the pleasant atmosphere on the fifth floor and for the input during meetings. Sander en Inge, naast de wetenschappelijke input vond ik de omgang en koffieautomaat-gesprekjes met jullie erg plezierig. Ook jullie moves op labfeestjes blijven me bij. Ik wens jullie al het beste. Mike, op basis van jouw adviezen zijn de eerste Z-wave gestuurde apparaten in mijn huis een feit. Bedankt voor de leuke tijd.

Lars-Erik, naast een gezellige, vrolijke, bijdehante collega, heb ik je ook buiten het werk leren kennen als een leuke, zorgzame, bijdehante vent. Ik vind het knap dat jij bij bijna elke presentatie een doordachte vraag kunt stellen en altijd geïnteresseerd overkomt. We zien elkaar snel weer! Suzanne, we zijn toch wel regelmatig op pad geweest, vaak ook samen met Marina, en dat was altijd gezellig. Zonde dat je blessure ervoor zorgde dat je niet mee kon op de paragliding trips. Ik wens je heel veel succes met het afronden van je promotie! Vincent, op het lab en op weg naar en van de CSnD uitjes hebben we heel wat verhalen uitgewisseld. Bedankt en veel succes met je promotie. Thijs, de volgende keer als Cosmic Gate in de buurt is gaan we weer! Veel succes in de VS. Selma, João, Suzan, Aniek, Juliane, Janine, en Molley, the best of luck to all of you!

Ook buiten het lab ben ik veel mensen dankbaar voor hun bijdrage aan mijn promotie. Dat kan zijn in de vorm van steun en advies, van ontspanning, van een drankje op z'n tijd, van een feestje, of gewoon van een praatje of een berichtje. Een aantal mensen wil ik hier graag extra voor bedanken.

Lieve ouders, dankzij jullie ben ik opgegroeid in een warm gezin waar de mogelijkheden voor het oprapen lagen. Jullie motivatie om het beste uit je zelf te halen, al dan niet op prijs gesteld door mij, heeft mij gevormd en gebracht naar waar ik nu ben. Vanuit de grond van mijn hart bedankt voor alles.

Eveline en Reinder, wij zien elkaar slechts bij verplichte familieaangelegenheden en jullie hebben helaas nooit kunnen onthouden wat de titel van mijn proefschrift was. Toch bedankt voor de warme deken van humor, scherpe opmerkingen en felle discussies waarin ik me tijdens mijn jeugd heb mogen wentelen. Ik weet dat jullie er voor me zijn als het nodig is. Joost en Richard, mijn zus en broertje hebben het goed getroffen met jullie, en daarmee ik ook. Bedankt voor de gezelligheid tijdens de al dan niet verplichte familie aangelegenheden.

Lieve Bondjes, met jullie heb ik een van de belangrijkste en leukste periodes van mijn leven doorlopen. Lachen, huilen, studeren, feestjes en brakke ochtenden, het zijn mooie herinneringen. Onze Bonddates smaken altijd naar meer en jullie nieuwsgierigheid naar mijn onderzoek, en waarom dat nou nuttig is, zorgt dat ik er graag over vertel. Bedankt!

Paul, ik heb genoten van de dingen die we samen hebben ondernomen, van legendarische tafelvoetbal-overwinningen en avonturen in Brazilië tot gewoon lekker op de bank voor de tv hangen. In de zomer een potje beachballen en een biertje drinken in het park, ik heb er al weer zin in. We zien elkaar binnenkort.

Steen, joe dulln, we herinneren allebei onze ontmoeting op de tennisbaan zo'n 18 jaar geleden als de dag van gisteren. Sindsdien zijn we de beste vrienden en dat blijft de rest van ons leven zo. Met jouw humoristische en verrassende opmerkingen kun je mij altijd aan het lachen maken. Bedankt en tot snel.

Tinus, mijn eerste studentenhuus ervaring was een succes dankzij jou. Bedankt voor de leuke tijd in Eindhoven en de prachtige tripjes naar Barcelona. Ik kom je binnenkort weer opzoeken.

Squash is altijd een uitlaatklep geweest voor de opgebouwde spanning van mijn promotie. Bart, Ramsi, Rob, met jullie heb ik leuke trainingen gehad, een spannende onderlinge strijd uitgevochten, en verschillende kampioenschappen in de wacht gesleept. Ik hoop dat we elkaar snel weer treffen op de squashbaan en daarbuiten. Ook mijn huidige teamgenoten in Utrecht, bedankt voor de uitdagende squashpartijen en de gezelligheid aan de bar!

Lieve Marije, het laatste lood van een promotie weegt het zwaarst en daar heb jij me in bijgestaan. Met je lieve woorden, leuke kaartjes, de ontelbare keren dat jij het eten maakte, je begrip als ik weinig tijd had en ga zo maar door. Bedankt dat je altijd voor me klaar staat.

Dat is het dan, *Hora est.*

